THE PORPHYRIN TRIPLET STATE: FROM PORPHYRIN-2,2':6',2''-TERPYRIDINE CONJUGATES TO PHOTOCATALYSIS

Inauguraldissertation

zur
Erlangung der Würde eines Doktors der Philosophie
vorgelegt der
Philosophisch-Naturwissenschaftlichen Fakultät
der Universität Basel

von
Angelo Lanzilotto

aus Italien

Basel, 2018

Genehmigt von der Philosophisch-Naturwissenschaftlichen Fakultät
auf Antrag von

Prof. Dr. Catherine Housecroft und Prof. Dr. Oliver Wenger

Basel, den 12.12.2017

Prof. Dr. Martin Spiess

Dekan

Table of Contents

Introductory remarks

The doctoral work we present consists of three separate parts, each dealing with a different project, each is linked to the others by a main theme: porphyrins. Each part is structured to be independent, with its own introduction, results and discussion sections. Introductions are written for a general readership with academic knowledge of chemistry; it is therefore possible to read each of the three parts without previous specific knowledge of porphyrin spectroscopy or catalysis. All the analytical data are shown in figures, so that it is easier for the reader to rely on NMR and absorption/emission spectra while reading.

Part I is relative to the synthesis of a new porphyrin-terpyridine conjugate and its application in the preparation of homo- and heteroleptic transition metal complexes. Particularly, attention is focused on a heteroleptic ruthenium complex, which was tested as a light harvester in regards to dye-sensitized solar cell applications. Homoleptic complexes were prepared to study their spectroelectrochemical behaviour.

Part II moves the focus onto photocatalysis. A water-soluble free-base porphyrin catalyst has been prepared and employed to sensitize molecular oxygen to its singlet state. Singlet oxygen is active against a wide selection of substrates, among which we decided to work on two: thiols and sulfides. Studies against simple aminoacids made us interested in assessing whether photocatalytic activity would be retained in polypeptides *in vitro*. We stepped into photodynamic therapy by applying our photocatalyst to *E. coli* liquid cultures and following the population change over exposure to singlet oxygen. From a pure synthetic point of view, we screened the photocatalyst on aliphatic and aromatic sulfides. We collected examples on commercial substrates, both symmetric and asymmetric, of natural or pharmaceutical origin. The main goals were the assessment of catalyst's site-specificity, tolerance to coexisting functional groups and action on diverse structures.

Part III arises from a purely academic interest: is it possible to record the emission spectrum of a redox species, electrochemically generated *in situ*? In fact, spectroelectrochemistry is widely applied to absorption spectroscopy, where detection of the transmitted light greatly increases sensitivity. It is indeed possible to record such a signal, with the main problem being that reduced or oxidized species mainly show quenching of the emission. For a reversible redox couple, reversing the potential results in the recovery of the original fluorescence band. It remains a challenge to find a molecule whose redox behaviour is associated with emission at different wavelengths or variation in the vibrational pattern of the emission band.

Publications

[1] A. Lanzilotto, L. A. Büldt, H. C. Schmidt, A. Prescimone, O. S. Wenger, E. C. Constable and Catherine E. Housecroft, "Improved light absorbance does not lead to better DSC performance: studies on a ruthenium porphyrin–terpyridine conjugate", *RSC Adv.*, 2016, 6, 15370.

[2] C. E. Housecroft, C. G. Palivan, L. Gademann, W. Meier, M. Calame, V. Mikhalevich, X. Zhang, E. Piel, M. Szponarski, A. Wiesler, A. Lanzilotto, E. C. Constable, A. Fanget, R. Stoop, " 'Active Surfaces' as Possible Functional Systems in Detection and Chemical (Bio) Reactivity", *CHIMIA*, Volume 70, Number 6, 2016, 402.

[3] A. Lanzilotto, M. Kuss-Petermann, O. S. Wenger, E. C. Constable and C. E. Housecroft, "Homoleptic complexes of a porphyrinatozinc(II)-2,2':6',2''-terpyridine ligand", *Photochem. Photobiol. Sci.*, 2017, 16, 585.

[4] Y. M. Klein, A. Lanzilotto, A. Prescimone, K. W. Krämer, S. Decurtins, S.-X. Liu, E. C. Constable, C. E. Housecroft, "Coordination behavior of 1-(3,2':6',3"-terpyridin-4'-yl)ferrocene: Structure and magnetic and electrochemical properties of a tetracopper dimetallomacrocycle", *Polyhedron*, 129, 2017, 71.

[5] A. Lanzilotto, M. Kyropoulou, E. C. Constable, C.E. Housecroft, W. P. Meier, C. G. Palivan, "Porphyrin-polymer nanocompartments: singlet oxygen generation and antimicrobial activity", 2017, (accepted by the *Journal of Biological Inorganic Chemistry*).

Acknowledgments

I am indebted to Catherine and Ed, who took me despite, or maybe because of, my totally different background. We have come a long way in these four years and we make a good team. I could simply thank you for being my supervisors, but that can be said about every single one of them. The reason for my thanks and the reason why I will strongly recommend working for you is because you have been the best supervisors a PhD student could long for.

At times, it still surprizes me how you just sit in group-meetings listening to how I started a collaboration or performed a synthesis, basically because it was of interest to me and not necessarily for the group. You always took the challenge and we discussed as they were not 'undercover' projects. Well, they were until I presented an NMR spectrum, to which point there was not much to do about it anyway. At least, the 'parallel' chemical knowledge could be used to teach students in the practical courses. For the specific case of the Tollens reaction, I wonder if they were more surprized from the experiment or from the fact that they brought home actual silver.

I do remember as if it was yesterday one of my very first days. I and Catherine walked down the corridor to the labs in Spitalstrasse; Catherine was searching an older PhD student that could help me getting started with synthesis. Inadvertently, my colleague Cathrin walked out lab 219 as we were approaching. That was it. Catherine asked her if she would be up to it, to which she replied that she had never prepared porphyrins before. Personally, I tried to be of comfort and I added that I never did synthesis at all. If only words could describe Cathrin's expression as she looked at me. Probably words could describe it, but I am going to hide behind the I'm-not-a-native-speaker pretence. It doesn't take mind-reading to glimpse that her thoughts were bouncing back and forth between 'how did we get someone with no experience in synthesis?' and 'why has he been assigned to porphyrins?'; add a bit of 'does he know what he just signed up for?'. I didn't. I should have known better, but probably that is precisely the reason why I accepted.

Another subtle signal could have been considering that only another PhD student (Patrick) does porphyrins in the whole department. It took eleven months to prepare and purify the porphyrin-terpyridine conjugate, and a total of two years until the solar cell dye. Looking back, it has been worth it; chemistry doesn't have to be easy, it has to be interesting.

I would still sign up for it.

My thanks go as well to Oliver for accepting to co-examine my dissertation. Since it takes one to know one, it comes without saying that I turned to a photochemist. Your help has been important long before this moment, and the two publication we share are a sign of that. I look forward to the examination day. If you are reading this, see you soon.

Thanks to Cornelia for having accepted to chair the examination. Our collaboration started as part of the NCCR and it was quite prolific. This bring me to Μυρτώ, my best collaborator. A friend, indeed, but I have somehow the impression that she prefers the term collaborator. You did put a lot of effort in our joint project and it recently paid out. Think that in twenty years you will go through your publication record and all of the co-authors will remind you of a specific time of your life.

Daniel, I will miss you. Will you? Surely not the emails in which I ask for NMR experiments or tell you the machine has a problem. A pleasure to learn from the best.

P.S. You made my 2016 summer party.

Bea and Audrey, you have been a great help. I could write something like 'are thanked for handling bureaucratic and administrative stuff', but at the end of the day that is work. What I am most grateful for is that you represent the human side of this department. You make a good job; do not underestimate your value, especially the support you provide to a PhD student.

Bernhard, it was a pleasure teaching in the Practicum of General Chemistry. Thanks for the freedom of doing stuff outside of the usual experiments, something I always appreciate. And who knows, maybe I did manage to teach something to our students; we'll have to wait and see what they grow up to be.

Next in line is my 'welcome committee' composed of Srboljub, Biljana, Kiril and Kristina. You were the first people to welcome me here and if moving to a new city did not feel that abrupt it had to do with your friendship. Srboljub is specially thanked for having the patience to correct my English when necessary. You never gave up and the burden grew little by the day; a good investment, if I may. You also showed me that it is possible to retain five languages in one head, an experiment I try to repeat as a grownup.
Contacts may loosen over time, but the core feeling is there.

Martina, you do have a compromising video of me singing, I believe. That's not good. Alexandra could use it as proof of alcohol in my veins, a thing we both know to be unrealistic. Apart from that, thanks for the moments spent together; more recently, for the help you provided me.

A research group represents a second family, especially when you move somewhere new. A lot of people has come and gone over the course of four years and if on one side I extend a general thank to my whole research group, a special one goes to some colleagues that grew into becoming friends. They will be mentioned as they appear on the group website (excellent work with the pictures Fredi).
Sarah ti scrivo in italiano perchè tanto lo so che capisci. Mi ricordo ancora il nostro viaggio a Napoli e la tua guida turistica che ci avvertiva di essere finiti nella parte malfamata della città. Ti sei resa conto da te che non avevamo nulla da temere. Ci siam divertiti a fare i turisti in giro per la Campania e se da un lato posso dire di averti portata nella migliore pizzeria di Napoli (tu non sarai d'accordo), dall'altro puoi essere orgogliosa di avermi trascinato al cinese. Non succede tutti i giorni. Solid achievement, my dear.
Max I already started writing in Italian so I am considering to keep going. I'm switching back just because it's you. Somehow when I think of the time spent together, sharing the room in Castiglione della Pescaia comes to mind first. I refer particularly to the 'invasion' we suffered the farewell night. I will say no more, at the end of the day this documents stays and you are a father now. I need to give an immaculate image of you. Your child will grow up to read this…
Alexandra! How many times have you heard your name being called with my suave voice? Never enough is the answer you are looking for. Isn't it impressive how far we have come from our first day? We have our differences, especially when it comes to animals. And piercings. And tattoos. And horses. And sitting in a plane without engine. Isn't' it fantastic how we get along nevertheless? It must be because of throwing incandescent disk into the Black Forest. It binds.

Nathalie, potrei sciverti in francese, ma poi è capace che mi scappa l'errore e mi tocca beccarmi le correzioni. Perciò applico anche a te il sistema tanto-mi-capisci. Ne abbiam passate tante in quel dipartimento, come quando andavamo a fare shopping. È solo una mia impressione o si finiva con le braccia cariche di vetreria che poi manco la porta dell'ascensore aprivi? Mannaccia tua... Ci siam anche divertiti al di fuori di quelle quattro mura; son bei ricordi.

Alessandro, sarei pronto a scommettere che toccherà a te tradurre le parti in italiano di questa tesi, perciò cercherò di scriverne molte. Tieni alto il buon nome degli italiani nel gruppo e sii orgoglioso di quello che abbiam combinato insieme. Lo so benissimo che hai la gigantografia della porfirina in camera.

Tommaso, buon vecchio Tommaso. Chissà se ci sarai il 18. Sei la ragione principale per cui abbia imparato ad andare in bici. La senti la responsabilità sulle spalle? Dai, scherzo, lo sappiamo entrambi che ho appositamente aspettato che te andassi per imparare. Quante ne abbiam passate in Tristonia? Un peccato te ne sia andato, non se ne trovano molte di persone come te. Ci rivediam giù.

Valerio, Marinko e Daniele, i basilesi per caso. E Theresa; eh sì, pure lei ne fa parte. Ora Daniele attacca con la storia della notte a Steinervorstadt (che ricorda solo lui, e Marinko, che se ne era già andato...). Valerio controbatte che in bici viro a sinistra invece di tirar dritto e Marinko suggerisce scenari in cui il conte si risveglia col suo bagno occupato al mattino.

Che belli che siete, non cambiate mai. Magari Marinko sì, che lui deve diventare come il nemico. Valerio ci piace così com'è; uno che va a compleanni, ma intanto te lo ritrovi in dolce compagnia al Café des Arts, sul piedistallo. Daniele, il cui francese gli guadagnò un posto alla griglia durante l'ultimo summer party. Quest'anno come farete ad imbucarvi?

Stefano... son contento che tu sia finito qua. Poi tu sei crucco dentro, dove saresti voluto finire, ad Amburgo? Beata a Tiziana che ti sopporta, la distanza deve aiutare...

Concludo con l'Orsi, il Ferdi, la Mary, il Gigi e l'Oli. Chissà che un giorno aprirete questa tesi a questa pagina. Ringrazio i miei genitori per tutto il supporto ricevuto; in pratica vuol dire che non ho mai dovuto lavorare durante gli studi. Vuol dire più di questo, ovviamente. Grazie di tutto.

Siam arrivati alla fine.

Potete anche chiuder qui.

Quello che avevo da dire l'ho detto.

Il resto è chimica.

Abbreviations

|	
BrTPP	7-bromo-5,10,15,20-tetraphenyl-21H-23H-porphyrin
CFU	colony forming units
CLSM	confocal laser scanning microscopy
COSY	correlation spectroscopy (NMR)
DLS	dynamic light scattering
DSCs	dye-sensitized solar cells
ESI	electro-spray ionization
LUMO	lowest unoccupied molecular orbital
HMBC	heteronuclear multiple bond correlation (NMR)
HMQC	heteronuclear multiple quantum correlation (NMR)
HOMO	highest unoccupied molecular orbital
IC	internal conversion
LC	ligand-centred
MLCT	metal-to-ligand charge transfer
MO	molecular orbital
NBS	N-bromosuccinimide
NIR	near infra-red
NMR	nuclear magnetic resonance
NOESY	nuclear Overhauser effect (NMR)
OTTLE	optical thin-layer electrochemical cell
TA	transient absorption
H_2TPP	5,10,15,20-tetraphenyl-21H-23H-porphyrin
SLS	static light scattering
TEM	Transmission electron microscopy
tpy	2,2':6',2"-terpyridine
TPyCP	5,10,15,20-Tetrakis(1-(6-ethoxy-6-oxohexyl)-4-pyridin-1-io)-21H,23H-porphyrin tetrabromide
TPyMP	5,10,15,20-tetra(N-methylpyridin-4-yl)-21H,23H-porphyrin tetrachloride
[Zn(TPP)]	5,10,15,20-tetraphenyl-21H-23H-porphyrinato zinc(II)

Part I

Heteroleptic and homoleptic complexes of a porphyrin-2.2':6',2''-terpyridine conjugate

1 INTRODUCTION

1.1 State of the art and motivation

The present work stems from the fact that porphyrin- and ruthenium-based sensitizers are widely used in the field of dye-sensitized solar cells (DSCs)[1-12]. Surprisingly, not many examples exist of molecules containing both units, and few of the ones present in the literature have been prepared within the scope of application in DSCs[13-15]. A class of molecules containing a tetraphenylporphyrin moiety covalently linked to a terpyridine domain has been reported previously and members of this class are summarized in Scheme 1.1. The most common point of connection is represented by the *meso* position of the porphyrin core (Scheme 1.1 (b) to (d))[16-29], while one example exists of a connection involving the beta position of the pyrrole rings (Scheme 1.1 (a))[16]. We decided therefore to base our synthetic strategy on substitution of the pyrrole ring. Apart from the use of terpyridines, functionalization can be performed with 2,2'-bipyridine[30-36] or 1,10-phenanthroline[37-40], giving access to tris(chelate) metal complexes, and a number of multinuclear arrays[41-45]. An alternative approach predicates upon axial coordination of metalloporphyrins, for example by 4'-(4-pyridyl)-2,2':6',2"-terpyridine[46-48].

Porphyrin-polypyridylruthenium conjugates have found applications as sensitizers in dye-sensitized solar cells (DSCs); in fact, by looking at the respective absorption spectra, it appears clear that the two units are complementary. The porphyrin core absorbs in the blue and in the orange-red part of the spectrum, with virtually no absorption in the green. On the other hand, ruthenium-polypyridine complexes possess a broad band in the green part, due to the metal-to-ligand charge transfer transition. In sight of achieving better conversion efficiencies, coupling of the two moieties holds promises for the realization of a panchromatic dye.

(a) (b) (c) (d)
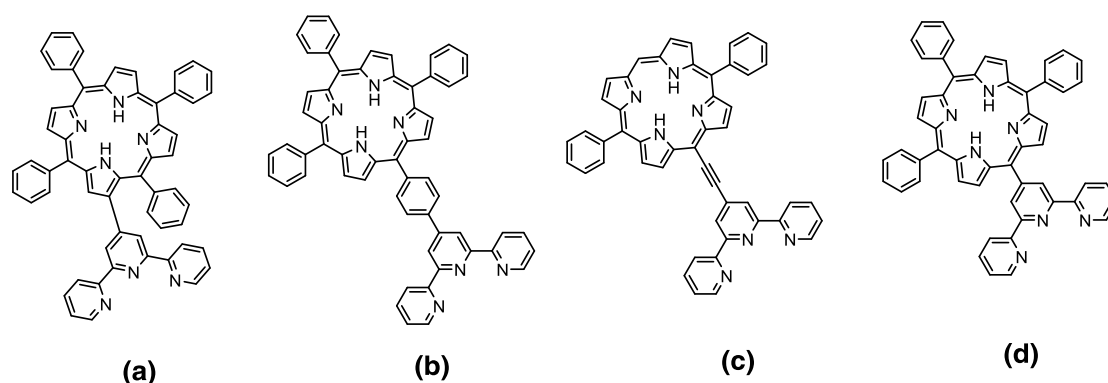
Scheme 1.1 Porphyrin derivatives bearing terpyridine previously prepared by (a) ref [16], (b) refs [17-22], (c) refs [23-27] and (d) refs [28, 29].

In addition to their use as sensitizers, porphyrin-2,2':6',2"-terpyridine (tpy) ligands have been combined with late transition metals to prepare dyads and triads. These kinds of complexes constitute the benchmarks for energy- and electron-transfer studies[20, 21, 28, 49-52].

1.2 Spectroscopy of porphyrins

A brief introduction on porphyrin spectroscopy is given, focusing on absorption and emission properties. Later on, where appropriate for the discussion of the experimental results, we will discuss specific spectroscopic properties as: ^{1}H-NMR and ^{13}C-NMR (section 2.1), spectroelectrochemical behaviour (section 3), triplet-triplet absorption spectrum (section 4.3).

1.2.1 Absorption

In 1961, Gouterman developed what has become known as the four-orbital model: the simplest model to explain the absorption spectra of a variety of porphyrins[53]. By simply considering the last two filled orbitals (nowadays termed the HOMO-1 and HOMO) and the first two empty ones (LUMO and LUMO+1), he predicted how intensity and position of the bands vary upon substitution of the porphyrin core. He collected the main experimental evidences that physical chemists had been gathering in the previous years. We will briefly introduce these evidences before entering into the detail of Gouterman's model.

Stern and coworkers[54] published between 1934 and 1937 a number of papers in which they reported the absorption spectrum of 40 porphyrins. Empirically, they were classified in three categories: etio-, rhodo- and phylloporphyrins, according to the relative intensities of the bands in the visible region. *meso*-Tetrasubstituted porphyrins and porphyrins containing alkyl chains on the pyrrole beta-positions possess an etio-like spectrum, a rhodo-spectrum is displayed in porphyrins containing electron-withdrawing groups attached to the pyrrole ring and phyllo-spectra are characteristic of porphyrins which contain one or two substituents in the *meso*-positions[55]. The difference can be easily understood if we number the set of four visible bands from I to IV, assigning number I to the most redshifted. Fig. 1.1 shows the difference in appearance of spectra of etio-, rhodo and phylloporphyrins. An etio-type follows the order IV > III > II > I, a rhodo- III > IV > II > I and a phyllo- IV > II > III > I. A second important observation was that if the two hydrogens in the central cavity are replaced with a metal cation, the four-band system reduces to a two-band system. Noticeably, the effect of the metal consists in a variation of intensity and positions of the visible bands[54, 56].
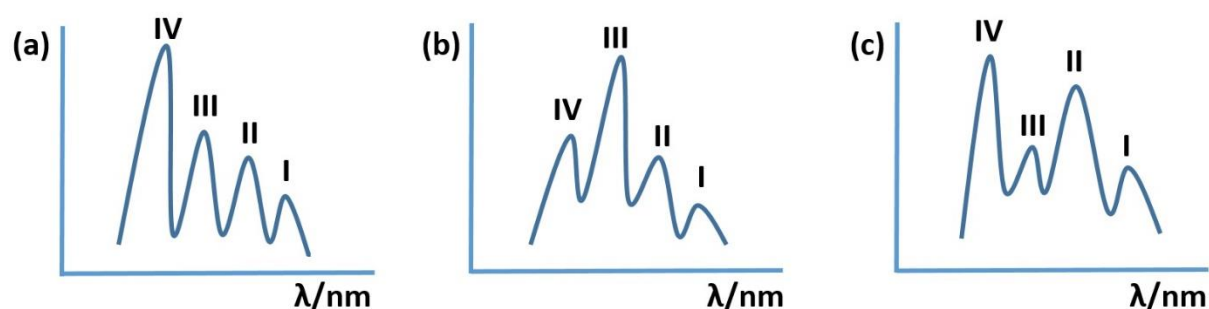

Figure 1.1 Schematic representation of the Q bands region (a) etio- (b) rhodo- and (c) phyllo-spectrum.

As Gouterman states in his paper, his model has received many inputs from publications of other authors. He lists Simpson[57], who first related porphyrins to an 18-membered cyclic polyene; Longuet-Higgins et al.[58] for giving the first molecular orbital (MO)

treatment of the system; Platt[59, 60] for developing a vector model to explain substituent effects; the theory of alternating hydrocarbons[61]; Moffitt theory of cyclic polyenes[62]; Parisier and Parr[63, 64] and Ham and Ruedenberg[65, 66] treatments of configuration interaction in aromatic hydrocarbons. Fig. 1.2 shows the absorption spectrum of H_2TPP (5,10,15,20-tetraphenyl-21H-23H-porphyrin) and [Zn(TPP)] (5,10,15,20-tetraphenyl-21H-23H-porphyrinato zinc(II)); they can be taken as reference spectra for free base and metallated porphyrins, respectively. From here on, we will refer to the intense band in the blue part of the spectrum as the Soret band or B band ($S_2 \leftarrow S_0$ transition), and to the weaker bands on the right side as Q bands ($S_1 \leftarrow S_0$ transition). The Q bands have been classified as a set of vibrational bands on the basis of their constant energetic separation[59]. Together, B and Q bands provide a set of two transitions, which can be further divided if we consider polarization issues. In fact, H_2TPP possesses D_{2h} symmetry; this detail implies that the transition dipole along the x-axes (defined as the axes connecting the nitrogen atoms which bear protons) is different from that along y (Fig 1.3). Polarization requires B and Q bands to split into B_x, B_y, Q_x and Q_y. Only in a metallated porphyrin does the symmetry rise to D_{4h} and such distinction is no longer applicable. Fig 1.4 shows the orbitals involved in the four-orbital model, as obtained from MO calculations[58].
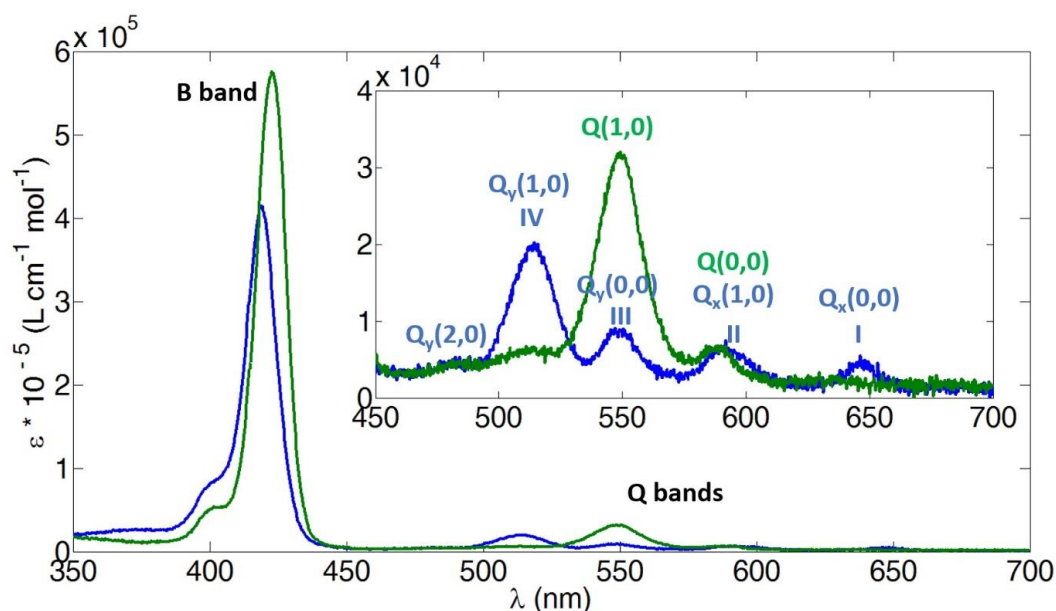

Figure 1.2 Solution absorption spectra of (blue) H_2TPP and (green) [Zn(TPP)] in toluene, fully assigned. The inset shows a zoom of the Q bands region.
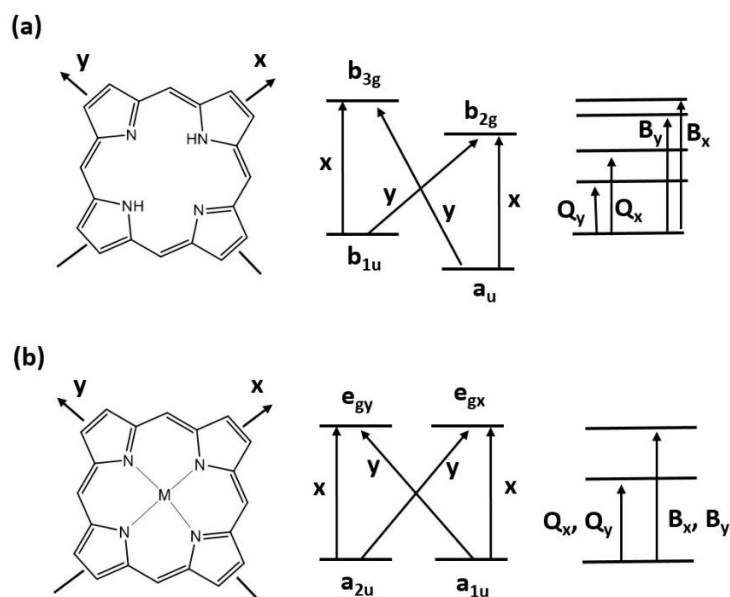
Figure 1.3 Polarization axes for (a) free base and (b) metal porphyrins. The possible transitions are displayed. Level symbols are the ones used by Gouterman in ref [53].
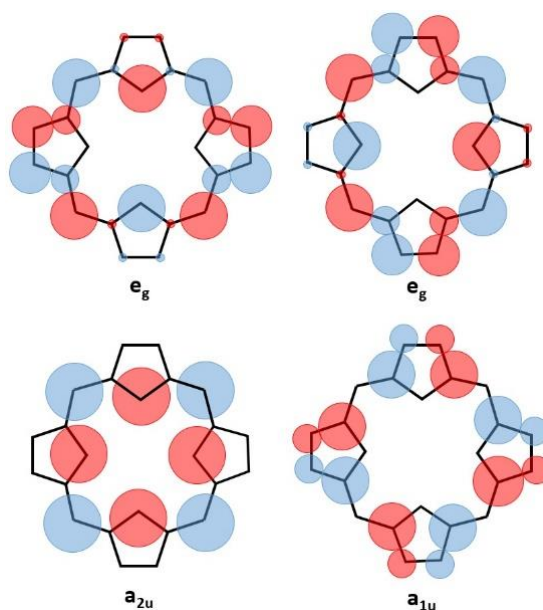
Figure 1.4 HOMO and HOMO-1 (a_{1u} and a_{2u}), LUMO (e_g) and LUMO+1 (e_g) of H_2TPP. The atomic orbital coefficients are proportional to the size of the circles; blue or red circles indicate sign. Note that the two e_g MO are degenerate because one is the simple rotation of the other.

In 1957, Weigl[67] confirmed that H_2TPP possesses a set of Q bands in which Q_x is polarized perpendicularly to Q_y, by performing fluorescence depolarization experiments. Noticeably, the B band showed a different degree of polarization at different wavelengths, a possible indication that two bands with opposite polarization (B_x and B_y) coexist under what appears to be a unique B band. The first experimental evidence in this sense came in 1958 from Rimington et al.[55] who found a 0.03 eV (250 cm^{-1}) split in the B band of H_2TPP when measuring at -180 °C in ethanol.

1.2.2 Emission

In the wake of Haurowitz's observation that porphyrins containing diamagnetic metals are fluorescent and those containing paramagnetic ones are not[68], Allison and Becker conducted the first systematic study of emission spectra of porphyrins upon metal substitution[69]. They divided the effect according to whether the metal falls in one of the following categories: closed shell, open paramagnetic shell or open diamagnetic shell configuration. For closed shell metals, as in d^{10} [Zn(TPP)], they found that the strength of the spin-orbit coupling heavily depends on the atomic number, i.e. late transition metals more efficiently promote the conversion of singlet states to triplets, lowering the fluorescence quantum yield (QY) and increasing the phosphorescence QY. [Zn(TPP)] shows both fluorescence and phosphorescence, so its intersystem crossing efficiency is moderate. In the case of open paramagnetic shells, as d^9 [Cu(TPP)], the degree of spin-orbit coupling is such that fluorescence is quenched in favor of triplet emission. Finally, it is interesting to discuss d^8 [Ni(TPP)] as an open diamagnetic shell example. Square planar Ni(II) is diamagnetic, therefore a behavior similar to that of [Zn(TPP)] is expected. Experimentally, [Ni(TPP)] shows no fluorescence, with all the energy being accumulated into the phosphorescence band, even though the atomic number of Ni is less than that of Zn. The authors hypothesized that the porphyrin exerts a ligand field effect which alters the disposition of the metal d-orbitals. This term was found to be greater than spin-orbit coupling and was given as an explanation for the quenching of fluorescence. They concluded that the coordination geometry for Ni(II) is not square-planar but rather distorted towards tetrahedral, which causes the excited state potential energy curve to cross with the ground state one and to deactivate through internal conversion (IC). The IC mechanism lowers the triplet population as well, accounting for the low phosphorescence quantum yield. Fig. 1.5 and 1.6 show the overlap between absorption and emission spectra of H_2TPP and [Zn(TPP)], respectively.

Figure 1.5 Solution absorption (blue) and emission (green) spectra of H_2TPP in toluene, vibrational structure of the bands is displayed. Normalization made with respect to the Q bands.

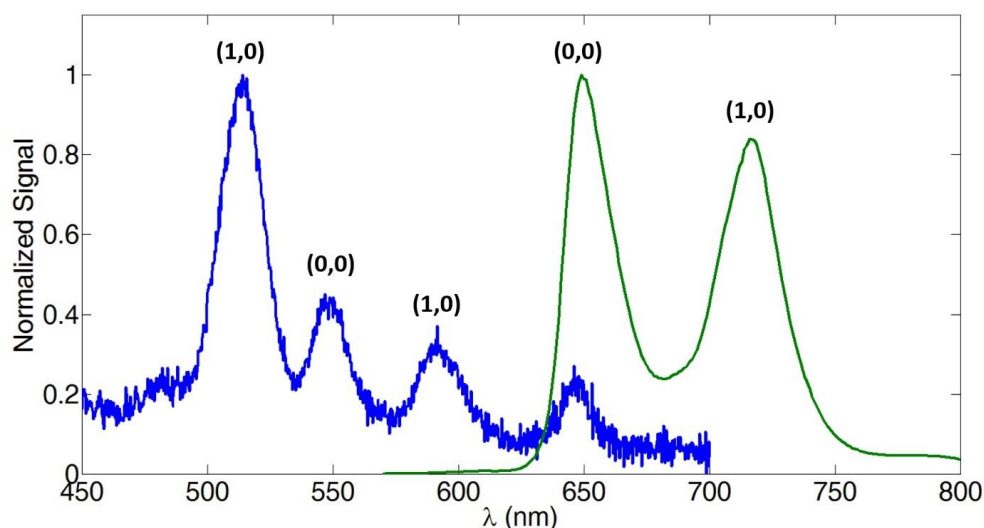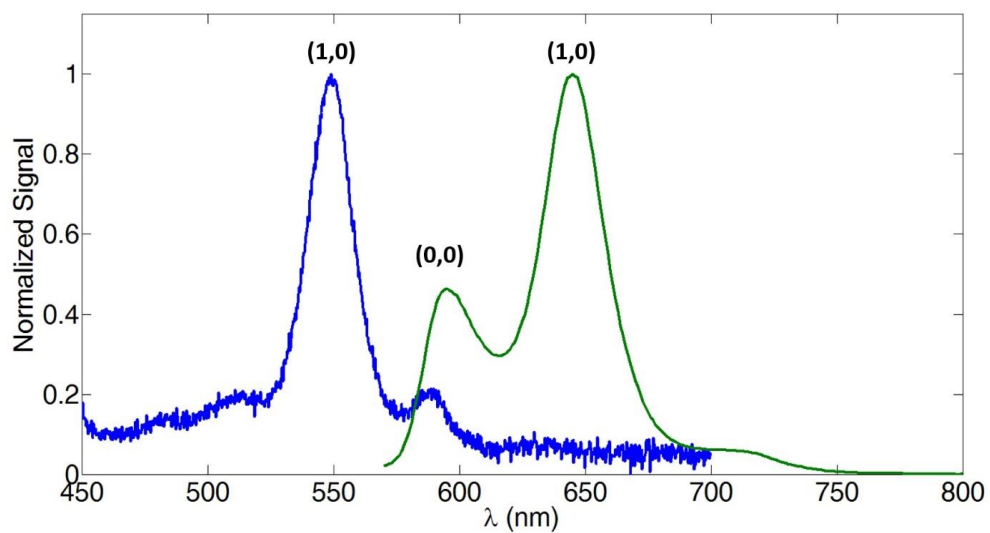Figure 1.6 Solution absorption (blue) and emission (green) spectra of [Zn(TPP)] in toluene, vibrational structure of the bands is displayed. Normalization made with respect to the Q bands.

References

[1] T. Higashino and H. Imahori, *Dalton Trans.*, 2015, 44, 448.

[2] A. Hagfeldt, G. Boschloo, L. Sun, L. Kloo and H. Pettersson, *Chem. Rev.*, 2010, 110, 6595.

[3] A. Hagfeldt and M. Grätzel, *Acc. Chem. Res.*, 2000, 33, 269.

[4] Y. Xie, Y. Tang, W. Wu, Y. Wang, J. Liu, X. Li, H. Tian and W.-H. Zhu, *J. Am. Chem. Soc.*, 2015, 137, 14055.

[5] A. Mishra, M. Fischer and P. Bäuerle, *Angew. Chem. Int. Ed.*, 2009, 48, 2474.

[6] A. Yella, H.-W. Lee, H. N. Tsao, C. Yi, A. K. Chandiran, M. K. Nazeeruddin, E. W.-G. Diau, C.-Y. Yeh, S. M. Zakeeruddin and M. Grüäzel, *Science*, 2011, 334, 629.

[7] C.-Y. Chen, M. Wang, J.-Y. Li, N. Pootrakulchote, L. Alibabaei, C.-h. Ngoc-le, J.-D. Decoppet, J.-H. Tsai, C. Grätzel, C.-G. Wu, S. M. Zakeeruddin and M. Grätzel, *ACS Nano*, 2009, 3, 3103.

[8] H. Ozawa, Y. Okuyama and H. Arakawa, *ChemPhysChem*, 2014, 15, 1201.

[9] S. Mathew, A. Yella, P. Gao, R. Humphry-Baker, B. F. E. Curchod, N. Ashari-Astani, I. Tavernelli, U. Rothlisberger, M. K. Nazeeruddin and M. Grätzel, *Nat. Chem.*, 2014, 6, 242.

[10] M. K. Panda, K. Ladomenou and A. G. Coutsolelos, *Coord. Chem. Rev.*, 2012, 256, 2601.

[11] W. M. Campbell, A. K. Burrell, D. L. Officer and K. W. Jolley, *Coord. Chem. Rev.,* 2004, 248, 1363.

[12] M. Urbani, M. Grätzel, M. K. Nazeeruddin and T. Torres, *Chem. Rev.*, 2014, 114, 12330.

[13] C. Stangel, K. Ladomenou, G. Charalambidis, M. K. Panda, T. Lazarides and A. G. Coutsolelos, *Eur. J. Inorg. Chem.*, 2013, 1275.

[14] I. Jung, H. Choi, J. K. Lee, K. H. Song, S. O. Kang and J. Ko, *Inorg. Chim. Acta*, 2007, 360, 3518.

[15] A. L. A. Parussulo, B. A. Iglesias, H. E. Toma and K. Araki, *Chem. Commun.*, 2012, 48, 6939.

[16] N. M. M. Moura, M. A. F. Faustino, M. G. P. M. S. Neves, F. A. Almeida Paz, A. M. S. Silva, A. C. Tomé, J. A. S. Cavaleiro, *Chem. Commun.*, 2012, **48**, 6142.

[17] A. Harriman, F. Odobel and J.-P. Sauvage, *J. Am. Chem. Soc.*, 1995, 117, 9641.

[18] T. J. Cho, C. D. Shreiner, S.-H. Hwang, C. N. Moorefield, B. Courneya, L. A. Godìnez, J. Manrìquez, K.-U. Jeong, S. Z. D. Cheng and G. R. Newkome, *Chem. Commun.*, 2007, 4456.

[19] A. C. Benniston, G. M. Chapman, A. Harriman and M. Mehrabi, *J. Phys. Chem. A*, 2004, 108, 9026.

[20] A. C. Benniston, A. Harriman, C. Pariani and C. A. Sams, *J. Phys. Chem. A*, 2007, 111, 8918.

[21] A. C. Benniston, A. Harriman, C. Pariani and C. A. Sams, *Phys. Chem. Chem. Phys.*, 2006, 8, 2051.

[22] T.-Z. Xie, K. Guo, J.-Y. Li, B. Zhang, K. Zheng, C. N. Moorefield, M. J. Saunders, K. J. Endres, S. Sallam, C. Wesdemiotis and G. R. Newkome, *J. Inorg. Organomet. Polym.*, 2016, 26:907.

[23] H. T. Uyeda, Y. Zhao, K. Wostyn, I. Asselberghs, K. Clays, A. Persoons and M. J. Therien, *J. Am. Chem. Soc.*, 2002, 124, 13806;

[24] T. V. Duncan, T. Ishizuka and M. J. Therien, *J. Am. Chem. Soc.*, 2007, 129, 9691.

[25] T. Ishizuka, L. E. Sinks, K. Song, S.-T. Hung, A. Nayak, K. Clays and M. J. Therien, *J. Am. Chem. Soc.*, 2011, 133, 2884.

[26] A. Nayak, J. Park, K. De Mey, X. Hu, T. V. Duncan, D. N. Beratan, K. Clays and M. J. Therien, *ACS Cent. Sci.*, 2016, 2, 954.

[27] T. Jiang, N. F. Polizzi, J. Rawson and M. J. Therien, *J. Am. Chem. Soc.*, 2017, 139, 8412.

[28] I. M. Dixon and J.-P. Collin, *J. Porphyrins Phthalocyanines*, 2001, 5, 600.

[29] L. Flamigni, F. Barigelletti, N. Armaroli, J.-P. Collin, J.-P. Sauvage and J. A. G. Williams, *Chem. Eur. J.*, 1998, 4, 1744;

[30] X. Liu, J. Liu, K. Jin, X. Yang, Q. Peng and L. Sun, *Tetrahedron*, 2005, 61, 5655.

[31] J. L. Allwood, A. K. Burrell, D. L. Officer, S. M. Scott, K. Y. Wild and K. C. Gordon, *Chem. Commun.*, 2000, 747.

[32] D. LeGourriérec, M. Andersson, J. Davidsson, E. Mukhtar, L. Sun and L. Hammarström, J. *Phys. Chem. A*, 1999, 103, 557.

[33] I. Hamachi, S. Tsukiji, S. Shinkai and S. Oishi, *J. Am. Chem. Soc.*, 1999, 121, 5500.

[34] A. Harriman, M. Hissler, O. Trompette and R. Ziessel, *J. Am. Chem. Soc.,* 1999, 121, 2516.

[35] K. Araki, P. Losco, F. M. Engelmann, H. Winnischofer and H. E. Tona, *J. Photochem. Photobiol. A*, 2001, 142, 25.

[36] J. M. Lintuluoto, V. V. Borovkov, G. A. Hembury and Y. Inoue, *Bull. Chem. Soc. Jpn.,* 2003, 76, 309.

[37] J. Liu, J.-W. Huang, B. Fu, P. Zhao, H.-C. Yu and L.-N. Li, *Spectrochim. Acta, Part A*, 2007, 67, 391.

[38] J. X. Zhang, K.-L. Wong, W.-K. Wong, N.-K. Mak, D. W. J. Kwong and H.-L. Tam, *Org. Biomol. Chem.*, 2011, 9, 6004.

[39] K. P. Birin, Y. G. Gorbunova and A. Y. Tsivadze, *RSC Adv.*, 2015, 5, 67242.

[40] C.-T. Poon, P.-S. Chan, C. Man, F.-L. Jiang, R. N. S. Wong, N.-K. Mak, D. W. J. Kwong, S.-W. Tsao and W. K. Wong, *J. Inorg. Biochem.*, 104, 2010, 62.

[41] M. Morone, L. Beverina, A. Abbotto, F. Silvestri, E. Collini, C. Ferrante, R. Bozio and G. A. Pagani, *Org. Lett*., 2006, 8, 2719.

[42] H. Kon, K. Tsuge, T. Imamura, Y. Sasaki, S. Ishizaka and N. Kitamura, *Inorg. Chem*., 2006, 45, 6875.

[43] K. Araki and H. E. Toma, *J. Photochem. Photobiol. A*, 1994, 83, 245.

[44] H. E. Toma and K. Araki, *Coord. Chem. Rev*., 2000, 196, 307.

[45] G. Santosh and M. Ravikanth, *Inorg. Chim. Acta*, 2005, 358, 2671.

[46] K. Chichak and N. R. Branda, *Chem. Commun*., 1999, 523.

[47] D. R. Martir, M. Averardi, D. Escudero, D. Jacquemin and E. Zysman-Colman, *Dalton Trans.***,** 2017**,** 46**,** 2255**.**

[48] I. Beletskaya, V. S. Tyurin, A. Y. Tsivadze, R. Guilard and C. Stern, *Chem. Rev.,* 2009, 109, 1659.

[49] L. Flamigni, F. Barigelletti, N. Armaroli, B. Ventura, J.-P. Collin, J.-P. Sauvage and J. A. G. Williams, *Inorg. Chem*., 1999, 38, 661.

[50] A. C. Benniston, A. Harriman and P. Li, *J. Am. Chem. Soc*., 2009, 132, 26.

[51] A. Quaranta, G. Charalambidis, C. Herrero, S. Margiola, W. Leibl, A. Coutsolelos and A. Aukauloo, *Phys. Chem. Chem. Phys*., 2015, 17, 24166.

[52] L. Flamigni, *Chem. Rec.*, 2016, 16, 1067.

[53] M. Gouterman, *J. Mol. Spectrosc.* 6, 138, 1961.

[54] (a) A. Stern and H. Wenderlein, series of paper entitled: *über die Lichtabsorption der Porphyrine* I to *über die Lichtabsorption der Porphyrine* XII, *Zeitschrift für Physicalische Chemie*, 1934. (b) A. Stern and M. Dezelic, *Z . physik. Chem.* 180A, 131, 1937.

[55] C. Rimington, S. F. Mason, O. Kennard, *Spectrochim. Acta*, 1958, 12, 65.

[56] G. D. Dorough, J. R. Miller and F. M. Huennekens, *J. Am. Chem. Soc.* 73, 4315, 1951.

[57] W. T. Simpson, *J. Chem*. *Phys.* 17, 1218, 1949.

[58] H. C. Longuet-Higgins , C. W. Rector and J. R. Platt, *J. Chem. Phys.* 18, 1174, 1950.

[59] J. R. Platt, "Radiation Biology," A. Hollaender, ed. Vol. III, chapter 2. McCraw Hill, New York, 1956.

[60] M. Gouterman, *J. Chem. Phys*. 30, 1139, 1959.

[61] M. J. S. Dewar and H. C. Longuet-Higgins, *Proc. Phys. Soc. A* 67, 795, 1954.

[62] W. Moffitt, *J. Chem. Phys.* 22, 320, 1954.

[63] R. Parisier and R. Parr, *J. Chem. Phys.* 21, 767, 1953.

[64] R. Parisier, *J. Chem. Phys.* 24, 250, 1956.

[65] N. S. Ham and K. Ruedenberg, *J. Chem. Phys*. 25, 1, 13, 1956.

[66] N. S. Ham and K. Ruedenberg, *J. Chem. Phys*. 29, 1199, 1958.

[67] J. W. Weigl, *J. Mol. Spectrosc.* 1, 133, 1957.

[68] F. Haurowitz, *Ber. Deut. Chem. Ges*., 68, 1795, 1935.

[69] J.B. Allison, R. S. Becker, *J. Chem. Phys.* 32, 1410, 1960.

2 SYNTHESIS AND CHARACTERIZATION

2.1 Synthesis of the heteroleptic complex [Ru(3)(4)][PF$_6$]$_2$

2.1.1 Synthesis of ligand 3

Our synthetic strategy to a porphyrin-terpyridine conjugate is illustrated in scheme 2.1, while scheme 2.2 shows how to obtain the corresponding heteroleptic ruthenium(II) complex. The presence in the literature of a procedure that allows the selective bromination in position 7 (beta pyrrole position) of H$_2$TPP[1] opens the way to our synthetic approach. H$_2$TPP is an electron-rich aromatic molecule, thus activated towards bromination; if molecular bromine were to be used, it would result in multiple bromination of the porphyrin core. It was found that treating H$_2$TPP with *N*-bromosuccinimide (NBS) yields mono- and dibromo compounds, separable by column chromatography. Metalation of BrTPP is performed with excess of zinc acetate, which yields quantitatively the corresponding neutral complex 1. In principle, the bromination and metalation steps could be done in either order. From our experience, if the bromination is conducted on [Zn(TPP)] and not on H$_2$TPP, a mixture of brominated compounds is obtained, which is harder to separate by column chromatography. We decided to proceed in the order bromination then metalation. Compound 1 was coupled to boronic acid 2 in a Suzuki-Miyaura cross-coupling reaction, yielding 3 in moderate yield (70%) after optimization of the reaction conditions. Even though BrTPP could be successfully coupled to 2, our experience indicates that metalation post-coupling proves difficult since the terpyridine domain acts as a metal ion binder, leading to competition towards the complexation of zinc(II). The structure of 3 was confirmed by 2D-NMR experiments (Fig. 2.1 to 2.4) and single crystal determination (Fig. 2.5). A first evidence comes from the fact that the four phenyl rings of [Zn(TPP)] are desymmetrized: *ortho*-positions H^{D2}, H^{E2} and H^{G2} (see Scheme 2.1 for labelling scheme) are magnetically different, and *meta*- and *para*-protons in the ring D (H^{D3} and H^{D4}) are well separated from those of rings E and G due to the interaction with ring C (figure 2.29).
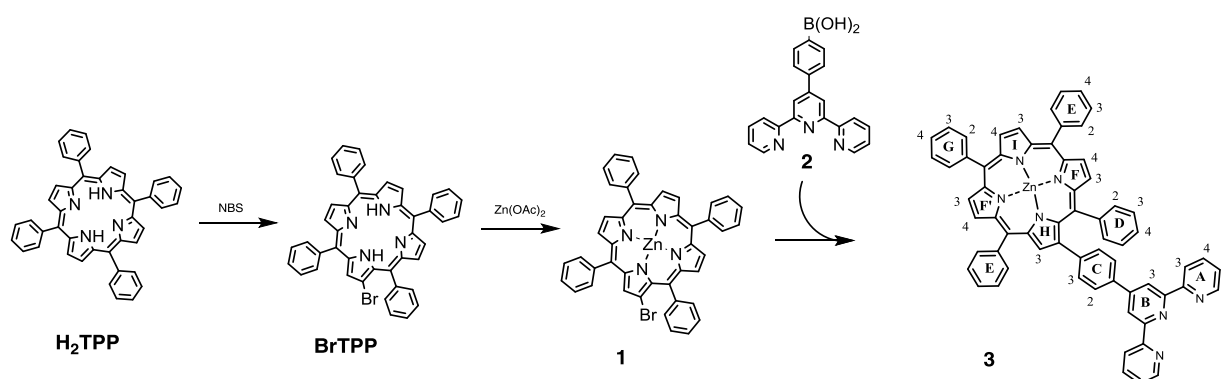
Scheme 2.1 Synthetic route to 3. Conditions are described at the end of the chapter. Ring labels are those used in the NMR spectroscopic assignment.
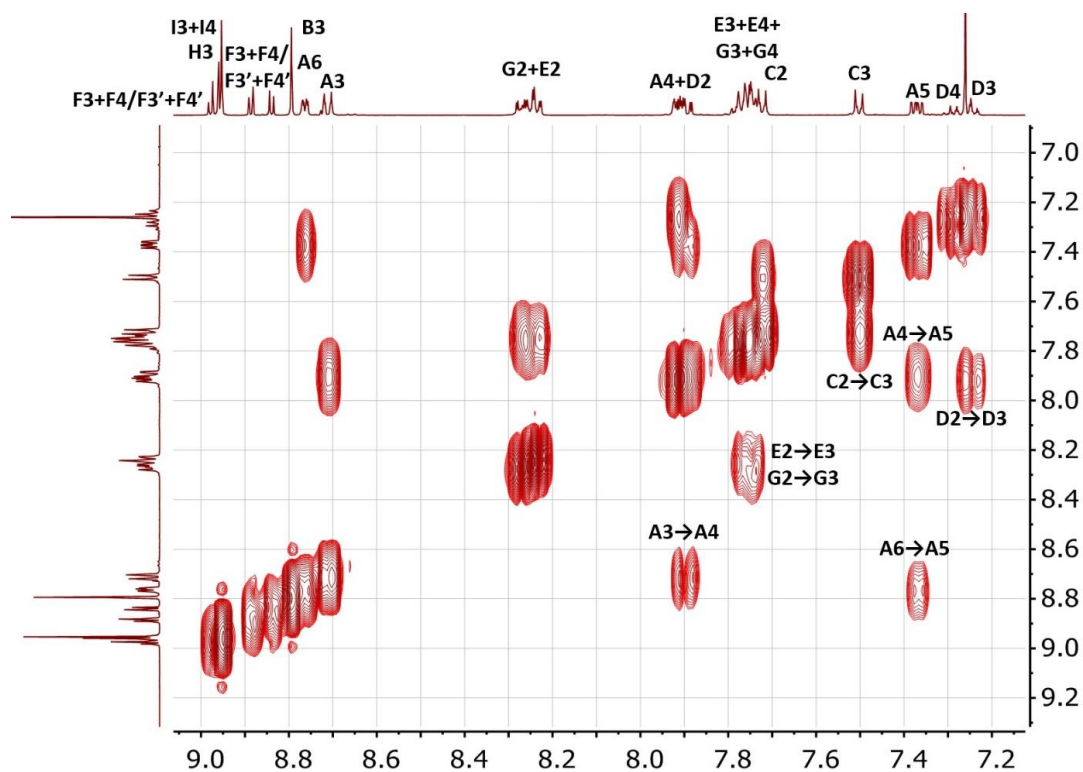
Fig 2.1 500 MHz COSY spectrum of a CDCl$_3$ solution of **3** (295 K). δ = 7.26 ppm residual solvent peak. COSY peaks are assigned.
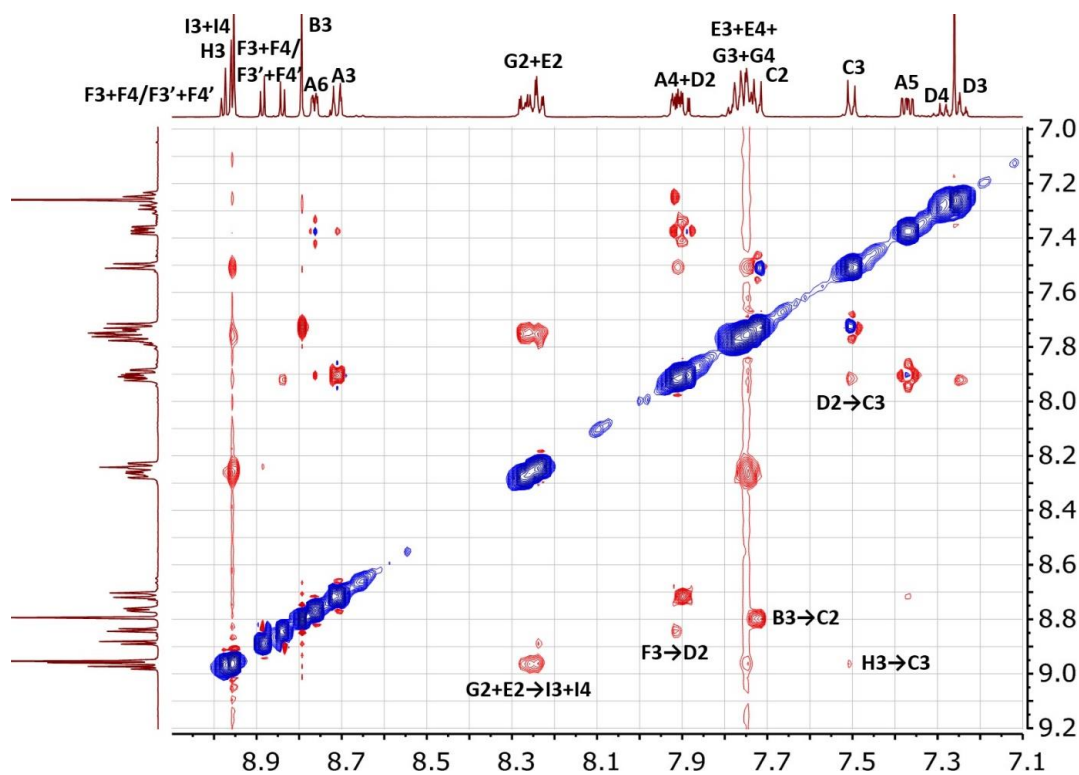

Fig 2.2 500 MHz NOESY spectrum of a CDCl$_3$ solution of **3** (295 K). δ = 7.26 ppm residual solvent peak. NOESY peaks are assigned.
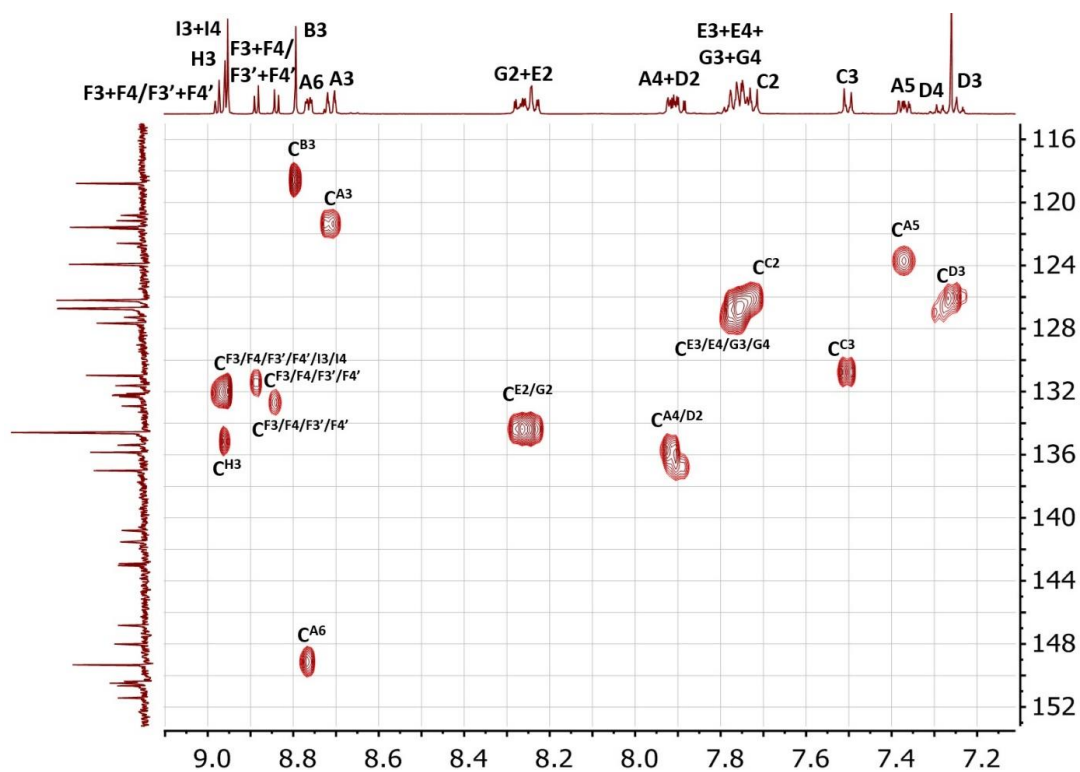
Fig 2.3 HMQC spectrum (^{1}H, 500 MHz; ^{13}C, 126 MHz) of a CDCl$_3$ solution of **3** (295 K). δ = 7.26 ppm residual solvent peak. Hydrogen-bearing carbon atoms are assigned.
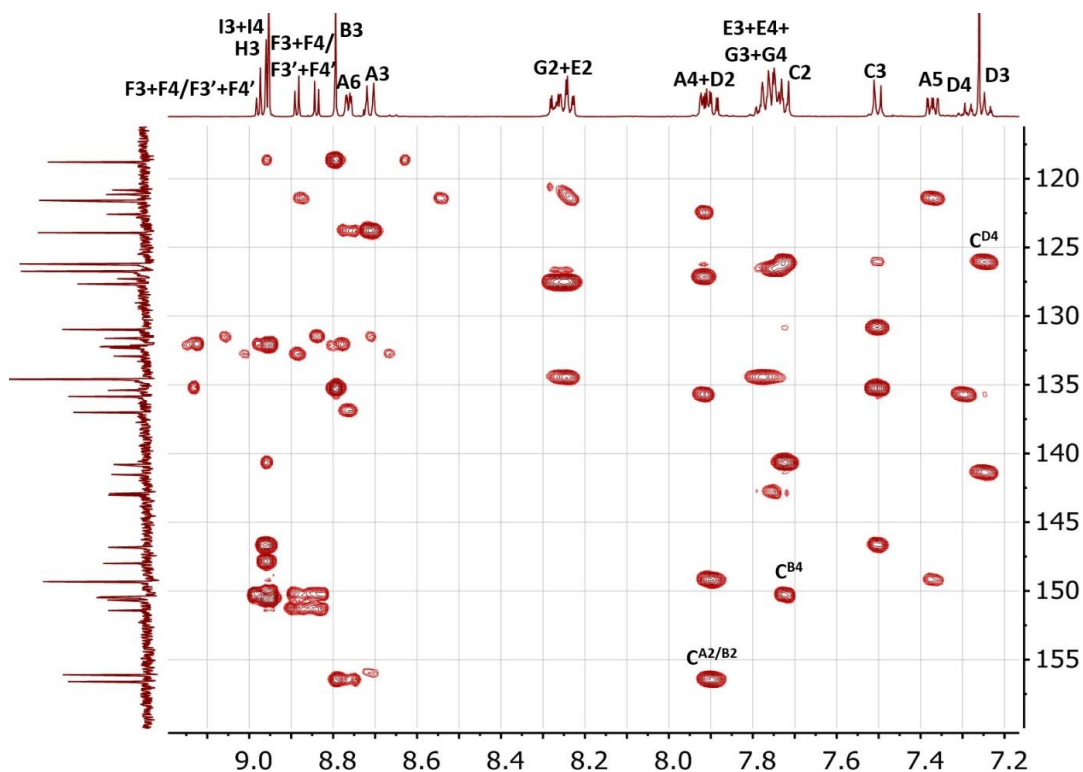

Fig 2.4 HMBC spectrum (^{1}H, 500 MHz; ^{13}C, 126 MHz) of a CDCl$_3$ solution of **3** (295 K). δ = 7.26 ppm residual solvent peak. Quaternary carbon atoms are assigned whether assignment could be unambiguous.

2.1.2 Crystal structure of **3**

Single crystals of **3**•Me$_2$CO were grown by slow evaporation of solvent from a saturated acetone solution of **3**. **3**•Me$_2$CO (Fig. 2.5) crystallizes in the monoclinic space group *P*2$_1$/*c*. The {Zn(TPP)} unit consists of a planar arrangement of four pyrrole rings and a central zinc ion, which lies only 0.14 Å out of the plane. Zn-N bond distances and N–Zn–N bond angles are as follows: Zn1–N1 = 2.034(3), Zn1–N2 = 2.062(3), Zn1–N3 = 2.042(3), Zn1–N4 = 2.062(3) Å, N1–Zn1–N2 = 89.69(14), N2–Zn1–N3 = 89.27(13), N1–Zn1–N4 = 89.52(13), N3–Zn1–N4 = 90.51(13)°. The acetone molecule is axially coordinated and the Zn–O bond distance is 2.345(4) Å. The angles between the square planar ZnN$_4$ system and the axial acetone molecule are: N1–Zn1–O1 = 82.10(16), N2–Zn1–O1 = 88.43(16), N3–Zn1–O1 = 106.45(16), N4–Zn1–O1 = 98.11(16)°. The twist angles between the planes of the phenyl rings with C3, C14, C25 and C36 and the porphyrin core are in the range 59.8 and 67.4°; for the phenyl ring containing C45, the corresponding angle is 61.9°, and the pyridine ring with N6 is twisted through 32.5° with respect to the plane of the phenyl spacer. The plane described by the tpy unit is tilted of 81.6° with respect to the porphyrin one.
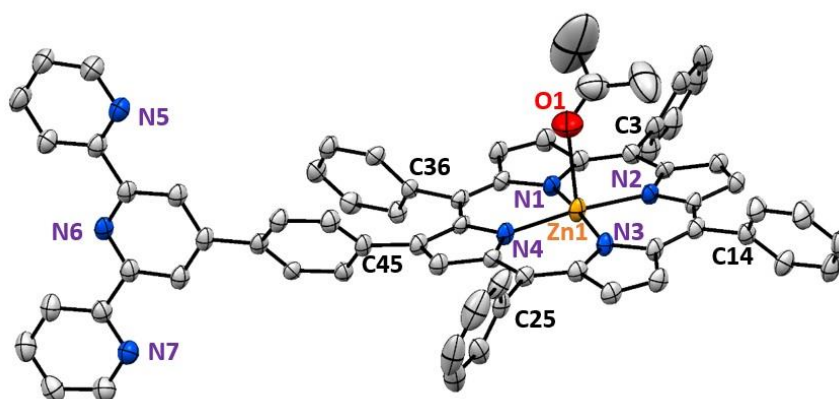
Fig 2.5 Structure of **3**•Me$_2$CO with H atoms omitted for clarity. Thermal ellipsoids plotted at 30% probability level.

The similar twist angles for the arene rings containing C36 and C45 permit the rings to engage in a π-stacking interaction although the 16.2° angle between their planes is not ideal; the centroid-centroid distance is 3.51 Å. The tpy unit is virtually planar (angles between planes of adjacent pyridine rings are 2.7 and 6.2°). The planarity is associated with a face-to-face π-interaction between centrosymmetric pairs of tpy units, which are parallel (Fig. 2.6). The centrosymmetric pairing of the {Zn(TPP)} units (Fig. 2.7) is typical and the distance Zn-Zn is 6.903 Å.

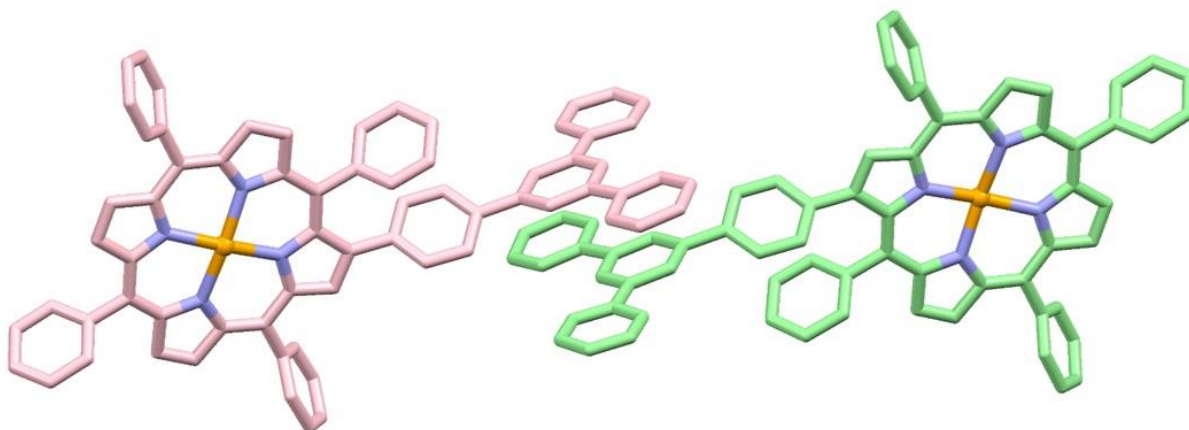Fig 2.6 Stacking of centrosymmetric pairs of tpy domains in **3**•Me$_2$CO. Separation of the central pyridine rings = 3.30 Å and centroid-centroid distance = 3.71 Å. H atoms omitted for clarity.
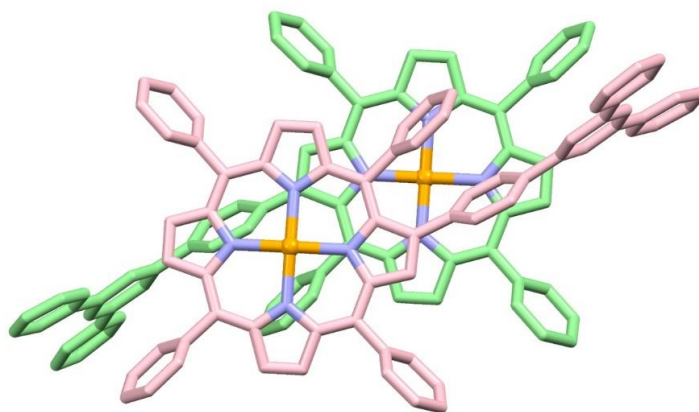

Fig 2.7 Stacking of centrosymmetric pairs of {Zn(TPP)} units in **3**•Me$_2$CO. Zn1-Zn1^i = 6.903(1) Å (symmetry code *i* = 2 − x, 1 − y, 2 − z). H atoms omitted for clarity.

2.1.3 Incorporation of **3** into [Ru(**3**)(**4**)][PF$_6$]$_2$

A second terpyridine (compound **4** in scheme 2.2) was prepared[2]. The phosphonic ester substituent was chosen to ultimately act as a anchoring domain (after deprotection) in a DSC. Ligand **4** was reacted with RuCl$_3$ yielding the intermediate to a heteroleptic complex. From this point, reaction between Ru(**4**)Cl$_3$ and compound **3** in the presence of a reducing agent (*N*-ethylmorpholine) leads to [Ru(**3**)(**4**)][PF$_6$]$_2$ after anion exchange. Again, the order in which reactions are performed is important. It is true that compound **3** reacts with RuCl$_3$ to give the corresponding complex Ru(**3**)Cl$_3$, but when this is followed by treatment with **4** in the presence of the reducing agent *N*-ethylmorpholine, cleavage of the porphyrin unit from the tpy unit was observed.
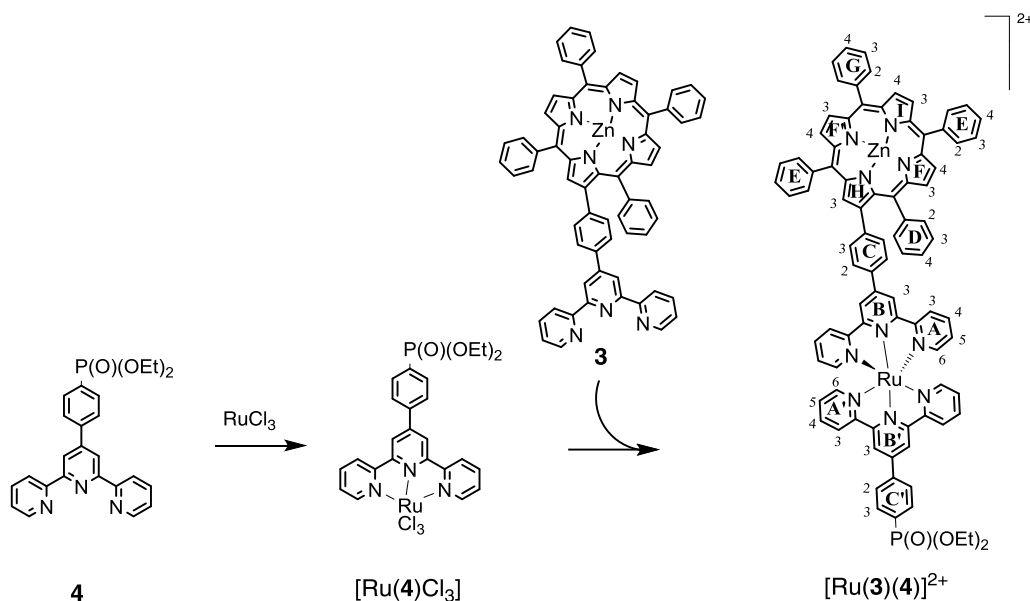
Scheme 2.2 Synthetic route to [Ru(**3**)(**4**)]²⁺. Conditions are described in the chapter.

The integral of the resonances in the aliphatic region of [Ru(**3**)(**4**)][PF$_6$]$_2$ fit with the presence of two ethyl groups, and this is a sign that no cleavage occurred upon complexation. Looking at the aromatic region, two sets of terpyridine signals are present (figure 2.8 bottom). It was possible to tell apart which terpyridine was which by using 2D-NMR experiments (Fig. 2.9 to 2.12). Specifically, we started looking for the *ipso*-C atom directly connected to the phosphorus atom (C$^{C4'}$), which is expected to be a doublet due to its coupling to phosphorous atom. ^{1}H-NMR spectra of both compound **3** and [Ru(**3**)(**4**)][PF$_6$]$_2$, are shown for comparison in figure 2.8. Another piece of evidence supporting the formation of the heteroleptic complex is the presence of a bisterpyridine domain, whose characteristic sign is the highfield shift of proton H^{A6}. This position is considered to be deshielded in compound **3**, since it lies next to a nitrogen atom in a pyridine unit. Things change when two terpyridines form an octahedral domain. In this specific configuration, H^{A6} find itself under the ring current of its counterpart, an effect that results in a shielding effect. The resonance of H^{A6} in an octahedral complex is therefore expected at lower chemical shift than that belonging to a non-coordinating terpyridine.
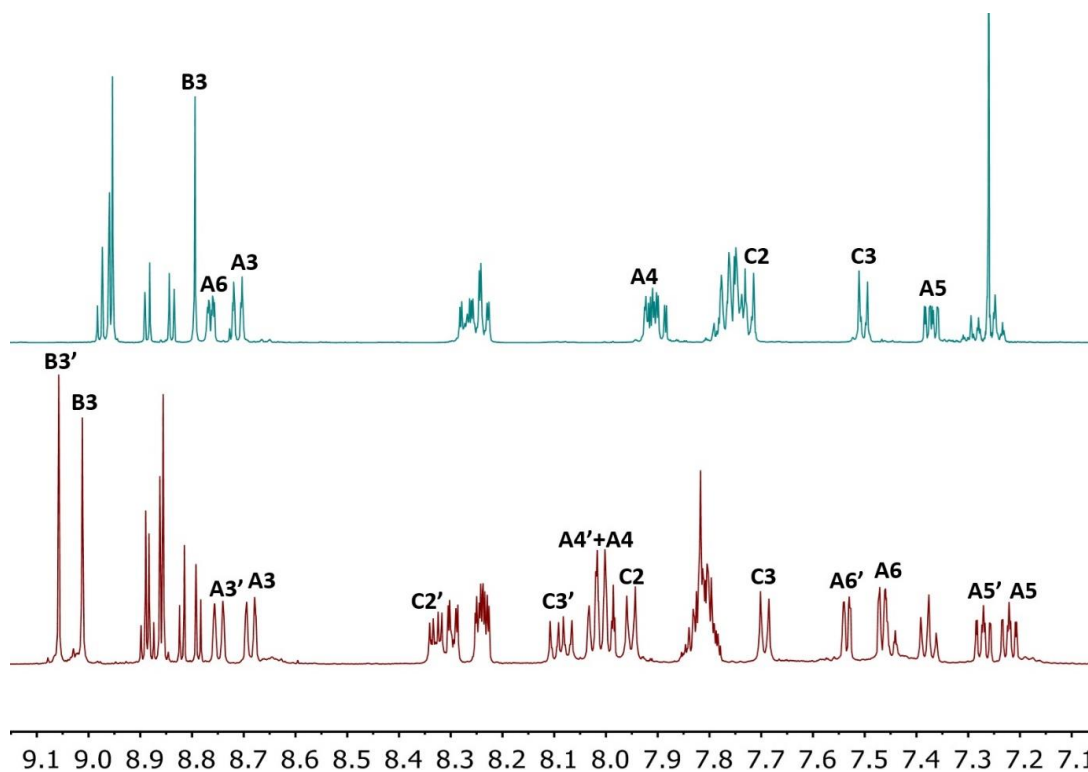
Fig 2.8 Aromatic region of the 500 MHz ^{1}H-NMR spectra of **3** in CDCl$_3$ (top) and [Ru(**3**)(**4**)][PF$_6$]$_2$ in CD$_3$CN (bottom). Chemical shifts in δ/ppm. Only terpyridine signals are assigned for clarity.
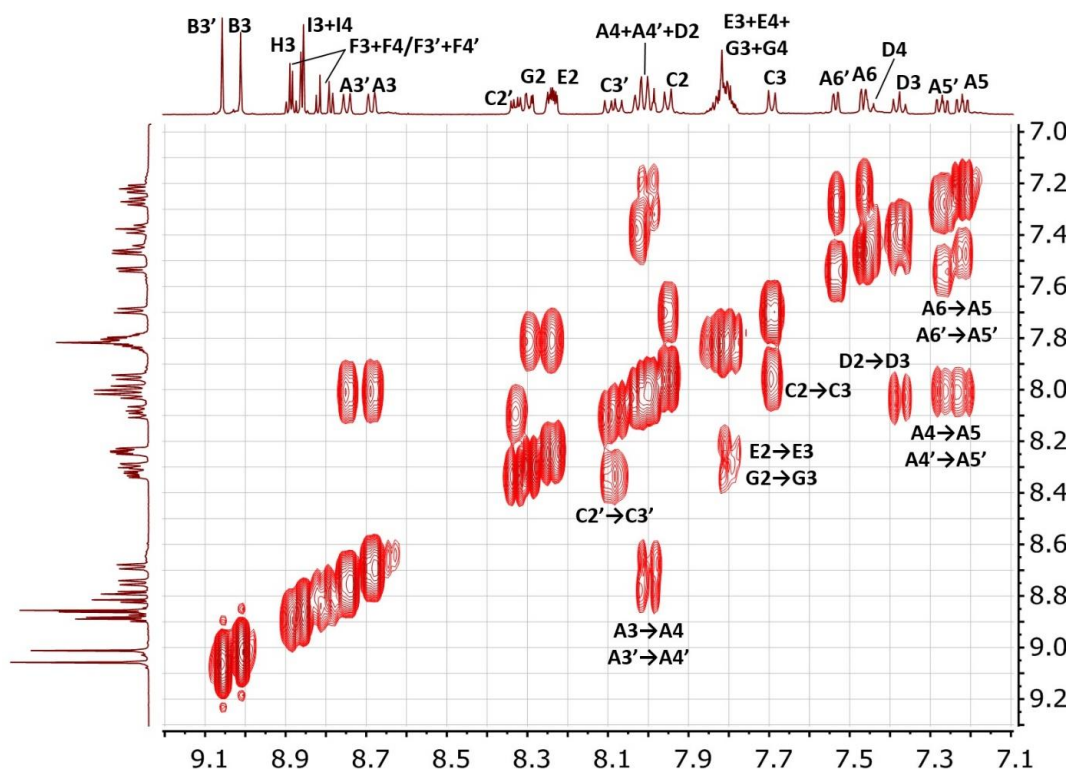
Fig 2.9 500 MHz COSY spectrum of a CD$_3$CN solution of [Ru(**3**)(**4**)][PF$_6$]$_2$ (295 K). COSY peaks are assigned.
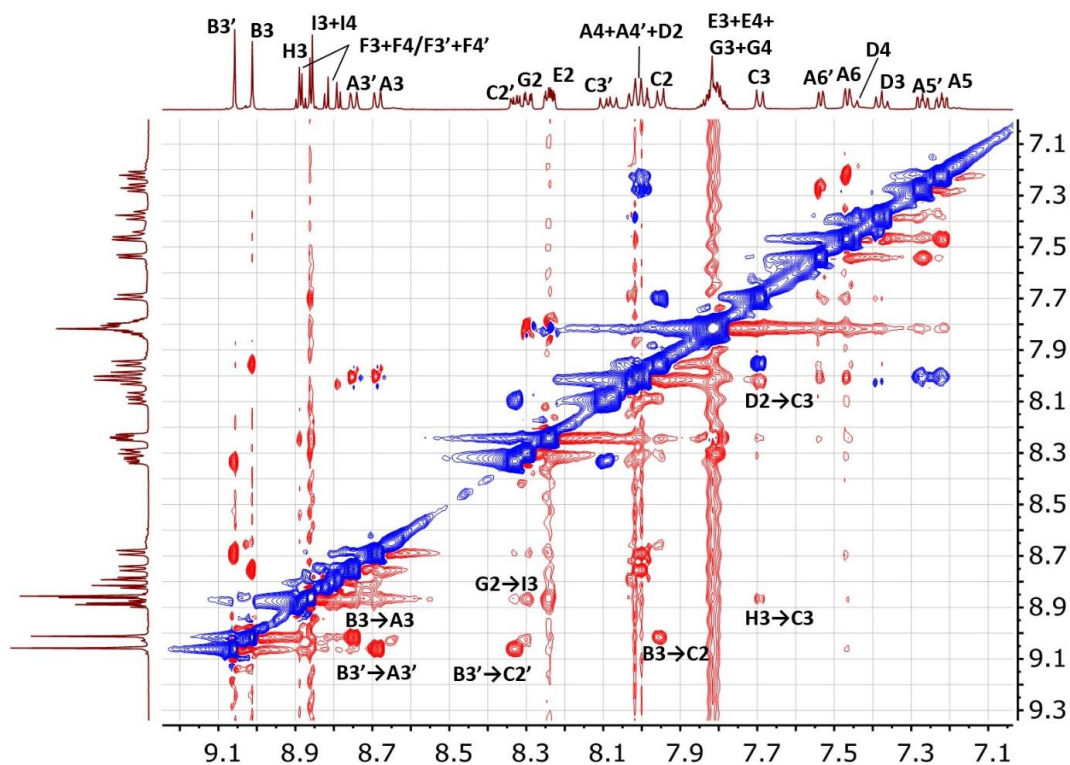
Fig 2.10 500 MHz NOESY spectrum of a CD₃CN solution of [Ru(**3**)(**4**)][PF₆]₂ (295 K). NOESY peaks are assigned.
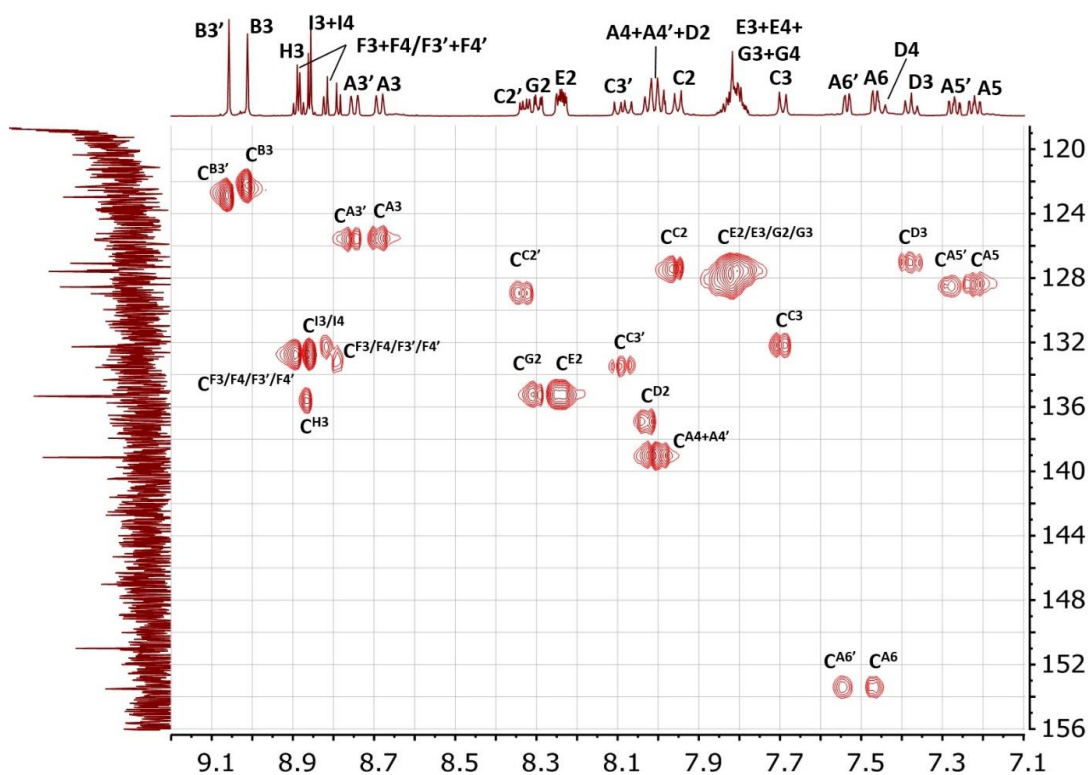
Fig 2.11 HMQC spectrum (¹H, 500 MHz; ¹³C, 126 MHz) of a CD₃CN solution of [Ru(**3**)(**4**)][PF₆]₂ (295 K). Hydrogen-bearing carbon atoms are assigned.
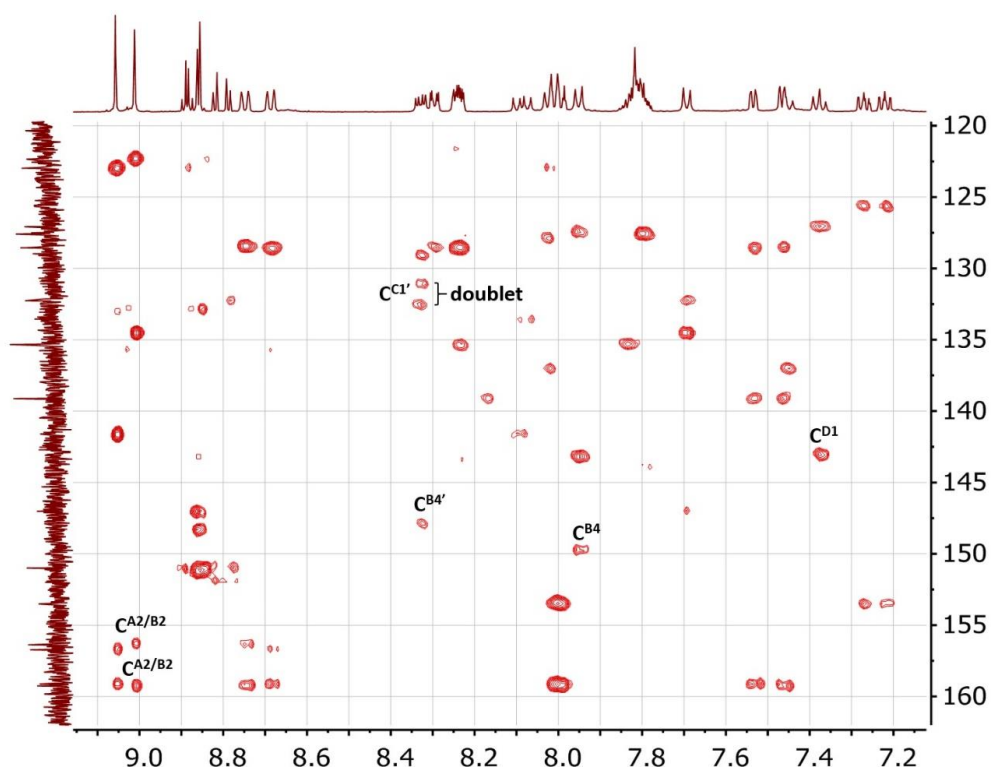
Fig 2.12 HMBC spectrum (^{1}H, 500 MHz; ^{13}C, 126 MHz) of a CD$_3$CN solution of [Ru(**3**)(**4**)][PF$_6$]$_2$ (295 K). Quaternary carbon atoms are assigned only when the assignment was unambiguous.

2.2 Synthesis of homoleptic complexes [M(3)$_2$][PF$_6$]$_2$, with M = Fe^{II}, Zn^{II}, Ru^{II}.

Having established a synthetic pathway to ligand **3** and prepared heteroleptic [Ru(**3**)(**4**)][PF$_6$]$_2$ for DSC applications, we decided to study in depth the coordination behaviour of **3** by obtaining a series of homoleptic complexes, as illustrated in Scheme 2.3. In case of Zn^{II} and Fe^{II}, reactions of one equivalent of a metal salt to two equivalents of tpy ligand led to the formation of the corresponding homoleptic complex, which was then precipitated and isolated by anion exchange. For Ru^{II}, a two-step approach was preferred. The protocol was analogous to that used for the preparation of heteroleptic [Ru(**3**)(**4**)]$^{2+}$. Compound **3** was initially reacted with RuCl$_3$ and the crude Ru(**3**)Cl$_3$ was reacted with another equivalent of **3** in the presence of a reducing agent. The [Ru(**3**)$_2$]$^{2+}$ complex (at this stage as the chloride salt) was then isolated as the hexafluorophosphate salt by ion exchange.

3
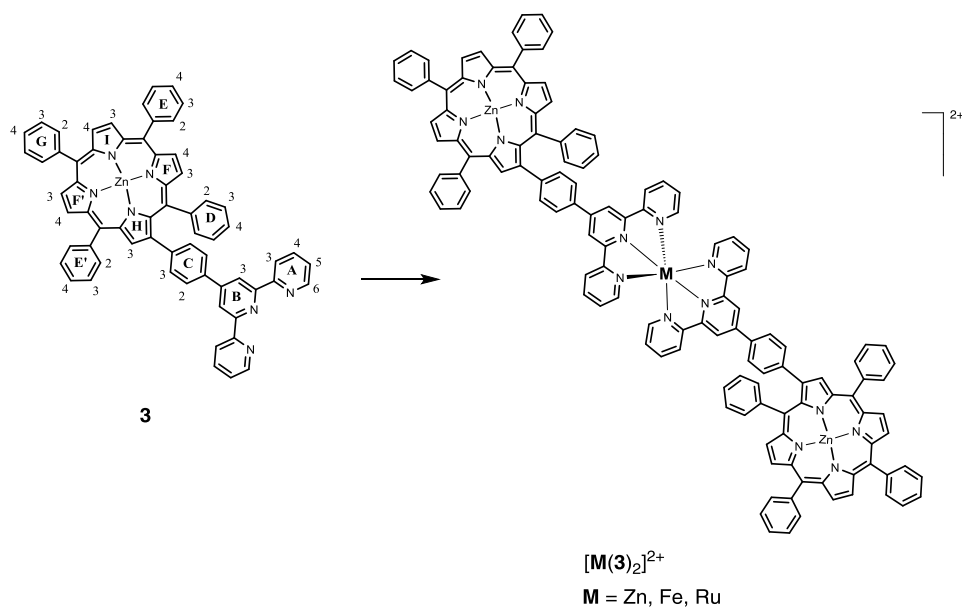
$[\textbf{M}(\textbf{3})_2]^{2+}$

$\textbf{M} = \text{Zn, Fe, Ru}$

Scheme 2.3 Synthetic route to $[\textbf{M}(\textbf{3})_2]^{2+}$, $\textbf{M}$ = Zn, Fe, Ru. Conditions are described later on in the chapter.

^{13}C- and ^{1}H-NMR spectra were fully assigned by means of COSY, NOESY, HMBC and HMQC techniques, the full set of NMR-experiments is reported for $[\text{Zn}(\textbf{3})_2][\text{PF}_6]_2$ (Fig. 2.19 to 2.22), while only the ^{1}H-NMR is shown for $[\text{Fe}(\textbf{3})_2][\text{PF}_6]_2$ (Fig. 2.33) and $[\text{Ru}(\textbf{3})_2][\text{PF}_6]_2$ (Fig. 2.31). The main hallmark that evidences the formation of the $\{\text{M(tpy)}_2\}$ core in each homoleptic complex is the chemical shift of proton H^{A6} upon complexation, as already discussed for $[\text{Ru}(\textbf{3})(\textbf{4})]^{2+}$. Figure 2.18 gives the position of all the terpyridine signals in compound **3** and in its three homoleptic complexes. Starting from a chemical shift of δ 8.76 ppm for H^{A6} in **3**, H^{A6} appears at δ 8.31 ppm in $[\text{Zn}(\textbf{3})_2]^{2+}$, δ 7.32 ppm in $[\text{Fe}(\textbf{3})_2]^{2+}$ and δ 7.56 ppm in $[\text{Ru}(\textbf{3})_2]^{2+}$, an effect solely due to the nature of the coordinated metal. Contrary to the d^{10} configuration for Zn$^{\text{II}}$, Fe$^{\text{II}}$ and Ru$^{\text{II}}$ exhibit partially occupied shells. This leads to the appearance of a metal-to-ligand charge transfer band in the absorption spectrum of $[\text{Fe}(\textbf{3})_2]^{2+}$ and $[\text{Ru}(\textbf{3})_2]^{2+}$ (Fig. 2.25) to wavelengths characteristic of $[\text{Fe(tpy)}_2]^{2+}$ and $[\text{Ru(tpy)}_2]^{2+}$.
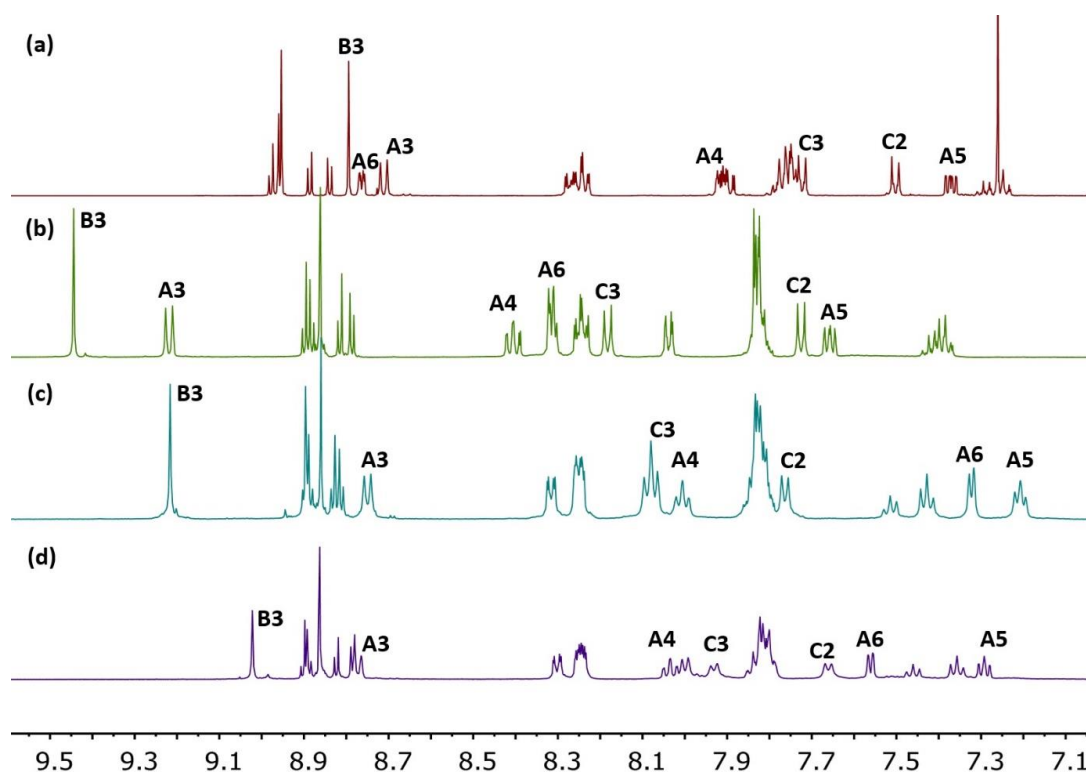
Fig. 2.18 500 MHz ^{1}H NMR spectra of (a) **3** in CDCl$_3$ (b) [Zn(**3**)$_2$][PF$_6$]$_2$ in (CD$_3$)$_2$CO (c) [Fe(**3**)$_2$][PF$_6$]$_2$ in CD$_3$CN (d) [Ru(3)$_2$][PF$_6$]$_2$ in CD$_3$CN. Only terpyridine signals are assigned for clarity. See Scheme 2.3 for NMR labelling.
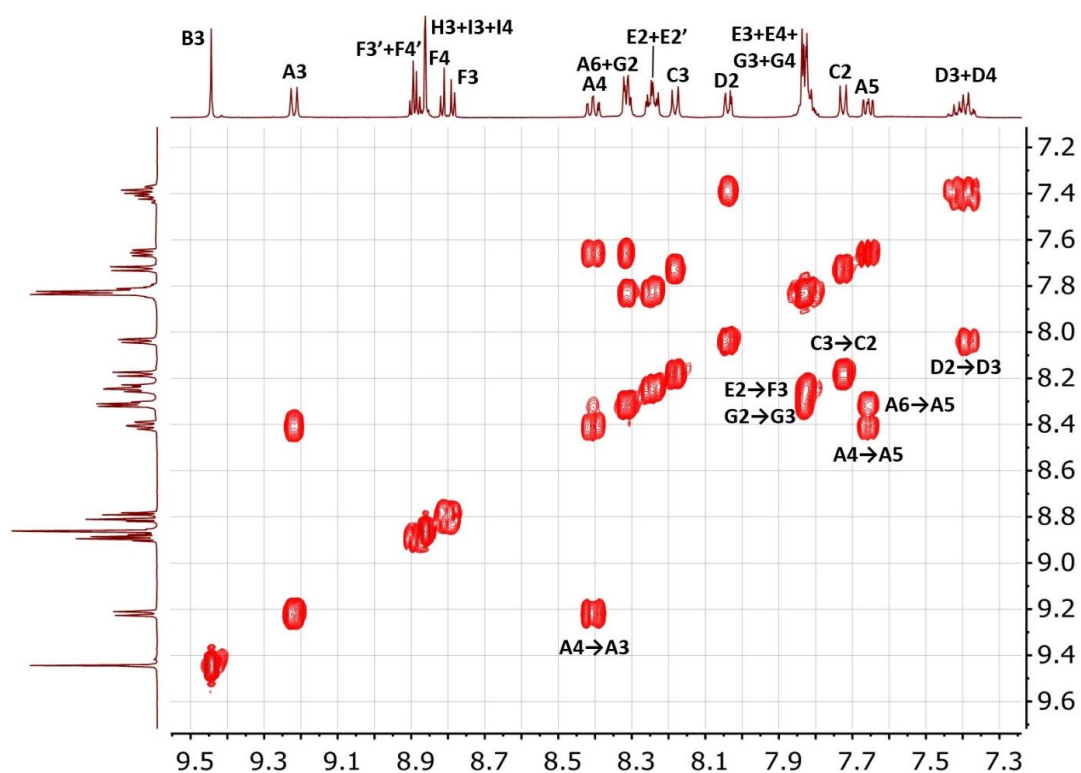
Fig 2.19 500 MHz COSY spectrum of a (CD$_3$)$_2$CO solution of [Zn(**3**)$_2$)][PF$_6$]$_2$ (295 K). COSY peaks are assigned.
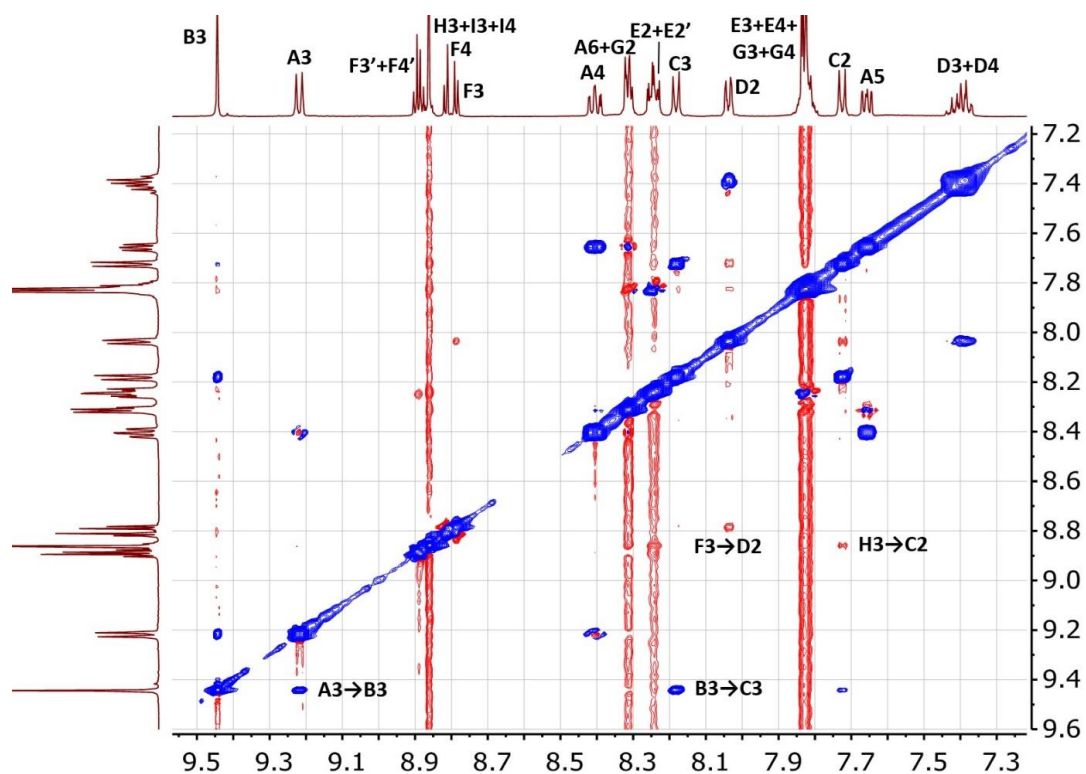
Fig 2.20 500 MHz NOESY spectrum of a $(CD_3)_2CO$ solution of $[Zn(\mathbf{3})_2)][PF_6]_2$ (295 K). NOESY peaks are assigned.
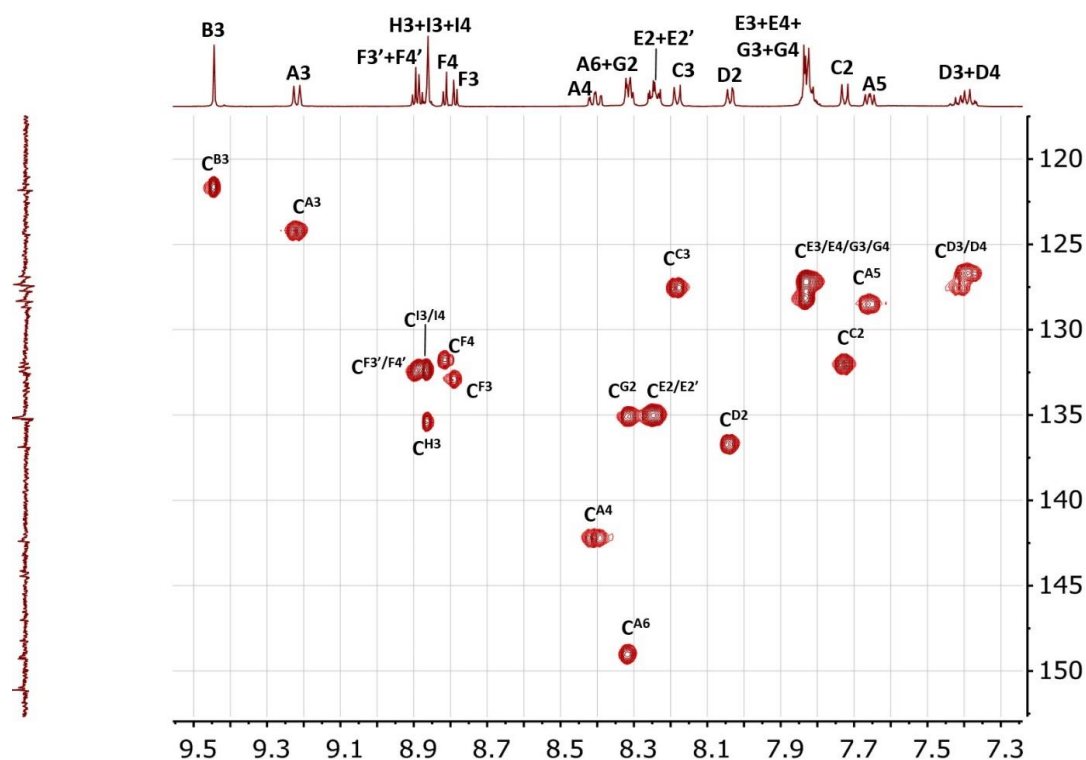
Fig 2.21 HMQC spectrum (^{1}H, 500 MHz; ^{13}C, 126 MHz) of a $(CD_3)_2CO$ solution of $[Zn(\mathbf{3})_2][PF_6]_2$ (295 K). Hydrogen-bearing carbon atoms are assigned.
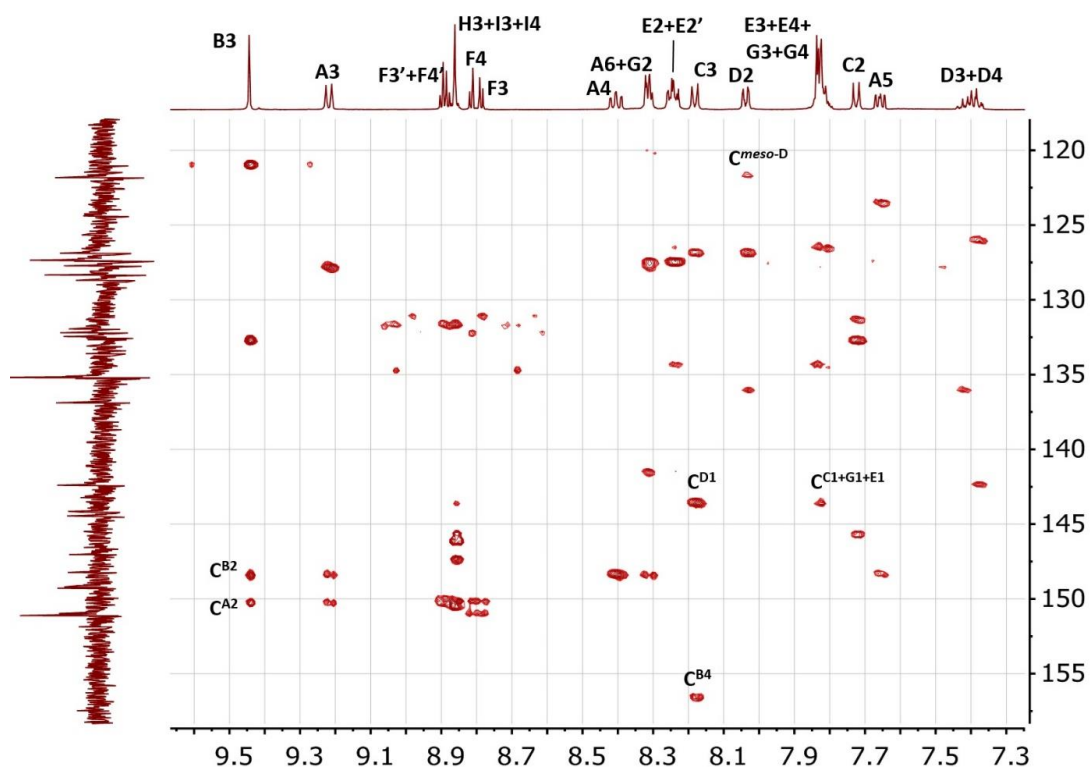
Fig 2.22 HMBC spectrum (^{1}H, 500 MHz; ^{13}C, 126 MHz) of a $(CD_3)_2CO$ solution of $[Zn(\mathbf{3})_2][PF_6]_2$ (295 K). Quaternary carbon atoms are assigned only when the assignment was unambiguous.

2.3 Cyclic voltammetry

All of the complexes prepared contain the sub-unit [Zn(TPP)], whose electrochemical behaviour has already been established[3]. [Zn(TPP)] undergoes up to two reversible one-electron oxidations and one reversible one-electron reduction, with oxidation processes involving abstraction from porphyrinic π-orbitals and injection into π*-orbitals upon reduction. In Table 2.1 and Fig. 2.23 we report the electrochemical data collected for our series of compounds, referenced with respect to the Fc/Fc$^+$ couple. The first oxidative processes involving [Zn(TPP)] is mostly affected by the presence of the terpyridine in **3** (E^{ox} goes from +0.42 to +0.34 V), while once in a complex, not the first nor the second oxidation potential are significantly affected. More interestingly, while the first reduction process is reversible for simple [Zn(TPP)], all the reductions are irreversible when it comes to complexes. When an electroactive metal centre is present, an additional oxidation wave appears in the voltammogram. The Ru^{II} centre in [Ru(**3**)$_2$][PF$_6$]$_2$ oxidizes at +0.89 V and at +0.88 V in [Ru(**3**)(**4**)][PF$_6$]$_2$, values that well compare to that of a model compound ([Ru(Phtpy)$_2$][PF$_6$]$_2$, +0.895 V)[4]. The Fe^{II} centre in [Fe(**3**)$_2$][PF$_6$]$_2$ behaves peculiarly, since its oxidation overlaps with that of the process [Zn(TPP)]$^+$/[Zn(TPP)]$^{2+}$ at +0.65 V. Differential pulse voltammetry confirmed that the oxidation band at +0.65 V is responsible for a three-electron process, meaning that while a total of two electrons come from the porphyrins, a third comes from the redox couple Fe^{II}/Fe^{III}. This value is lower than that of a model compound ([Fe(tpy)$_2$][PF$_6$]$_2$, +0.77 V)[5], an evidence that is rationalized if we take into account the electron-releasing effect of the electron-rich porphyrin core[3].

Table 2.1 Redox potentials for [Zn(TPP)] and **3** in CH_2Cl_2, and for [Zn(**3**)$_2$][PF$_6$]$_2$, [Fe(**3**)$_2$][PF$_6$]$_2$, [Ru(**3**)$_2$][PF$_6$]$_2$ and [Ru(**3**)(**4**)][PF$_6$]$_2$ in MeCN measured using cyclic voltammetry. Potentials are referenced to Fc/Fc$^+$ with 0.1 M [^{n}Bu$_4$N][PF$_6$] as supporting electrolyte and a scan rate of 0.1 V/s. Values in parentheses = E_{pe} - E_{pa} in mV (ir = irreversible).

Compound	$E^{ox}_{1/2}$ /V	$E^{red}_{1/2}$ /V	$E^{ox}_{1/2} - E^{red}_{1/2}$ /V
[Zn(TPP)]	+0.42 (82)	-1.79 (79)	2.21
	+0.71 (81)		
3	+0.34 (57)	-1.76^{ir}	2.10
	+0.66 (84)	-1.97^{ir}	
		-2.09^{ir}	
		-2.27^{ir}	
[Zn(**3**)$_2$][PF$_6$]$_2$	+0.38 (56)	-1.26^{ir}	1.64
	+0.67 (92)	-1.89^{ir}	
[Fe(**3**)$_2$][PF$_6$]$_2$	+0.37 (83)	-1.35^{ir}	1.72
	+0.65 (92)	-1.92^{ir}	
		-2.43^{ir}	
[Ru(**3**)$_2$][PF$_6$]$_2$	+0.39 (74)	-1.30^{ir}	1.69
	+0.67 (65)	-1.92^{ir}	
	+0.89 (65)		
[Ru(**3**)(**4**)][PF$_6$]$_2$	+0.39 (56)	-1.56^{ir}	1.95
	+0.67 (56)	-1.87^{ir}	
	+0.88 (65)	-2.21^{ir}	
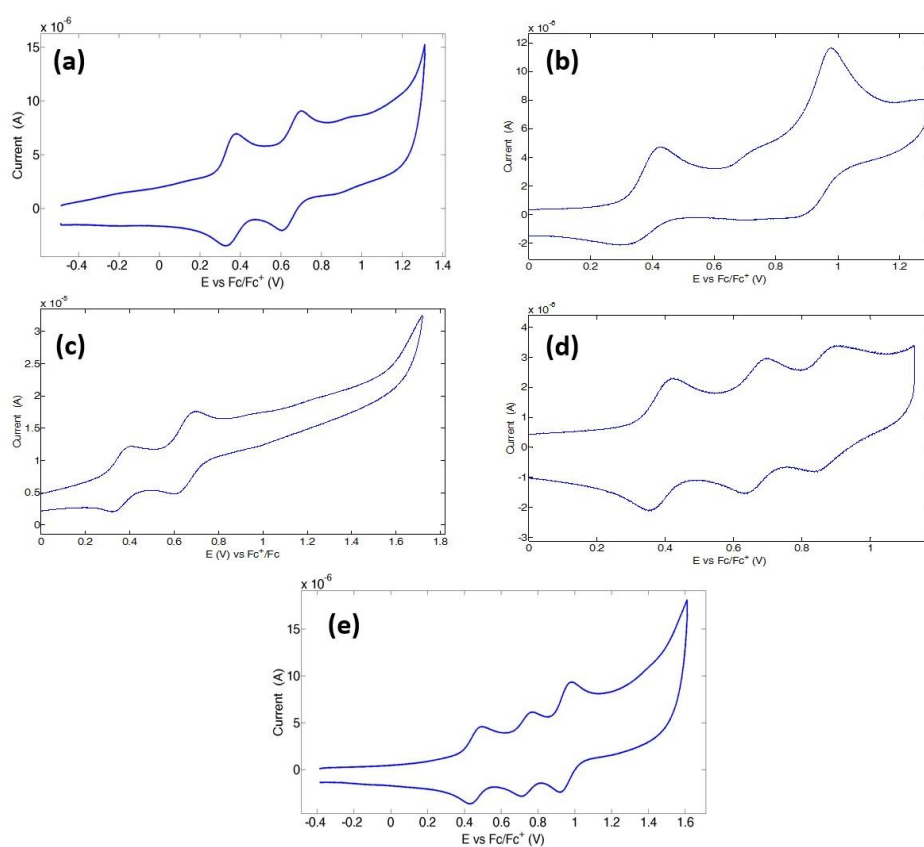
Fig. 2.23 Oxidative cyclic voltammograms of (a) **3** (b) [Zn(**3**)$_2$][PF$_6$]$_2$ (c) [Fe(**3**)$_2$][PF$_6$]$_2$ (d) [Ru(**3**)$_2$][PF$_6$]$_2$ € [Ru(**3**)(**4**)][PF$_6$]$_2$. For conditions, see Table 2.1.

2.4 Absorption Spectroscopy

Due to the aromatic character, to the presence of heteroatoms and to the extensive conjugation in-between the pyrrole rings, absorption spectrum of porphins and porphyrins consists of many transitions, covering most of the visible range. This can be put in evidence by analyzing the spectrum of the model compound H_2TPP. As discussed in the introduction section (Section 2.1), porphyrins display one intense absorption in the blue part of the spectrum, independently on the presence or not of a coordinated atom in the centre. It is when we move our attention to the red part of the spectrum that the coordination state matters. Gouterman rationalized how free base porphyrins (symmetry D_{2h}) possess a transition $S_0 \leftarrow S_1$ characterized by a set of four bands, consequence of the polarization direction (transition dipole along x and y axes) coupled to vibrational structure ((0,0) and (0,1) per dipole)[6]. On the other hand, the number of Q-bands lowers to two if an element is present in the core. This is due to symmetry reasons: the disappearance of two hydrogen atoms from the center render all four nitrogen atoms equivalent and increases the symmetry to D_{4h}. Therefore it is not possible to distinguish anymore between an x- and y-polarization axes and the two Q-bands simply reflect the vibrational structure (0,0) and (0,1).

In Fig. 2.24 we compare the absorption spectra of **1**, **3** and [Ru(**3**)(**4**)][PF$_6$]$_2$. This allows us to rationalize, in terms of absorption, what happens passing from compound **1** (the closest stucturally to [Zn(TPP)]), to compound **3** (whose aromatic surface is increased by being coupled to the terpyridine unit) and then to the heteroleptic complex [Ru(**3**)(**4**)][PF$_6$]$_2$. The spectrum of compound **1** is that of a metallated porphyrin[3, 7], an intense Soret band at 425 nm (ε = 660 000 dm^3 mol^{-1} cm^{-1}) arising from the $S_2 \leftarrow S_0$ transition, and weaker Q bands whose separation reflects that of the vibrational levels ((0, 0) and (0, 1)) from the $S_0 \leftarrow S_1$ transition (558 and 597 nm, ε = 22 000 and 7600 dm^3 mol^{-1} cm^{-1}, respectively). On going to compound **3**, the additional π-conjugated system moves slightly the Soret band and decreases its intensity (427 nm, ε = 520 000 dm^3 mol^{-1} cm^{-1}), while the Q bands change little (560 and 599 nm, ε = 26 000, 9500 dm^3 mol^{-1} cm^{-1}, respectively). Transitions in the ultraviolet part (around 285 nm, green trace in Fig. 2.24) are thought to have π* ← π ligand centred (LC) nature and to be localized on the phenyltpy domain. Upon formation of [Ru(**3**)(**4**)][PF$_6$]$_2$, the UV bands (below 350 nm) approximately double in intensity with respect to the absorptions in **3** (blue trace in Fig. 2.24), consistent with the presence of two tpy domains. The Soret band again decreases in intensity (ε = 370 000 dm^3 mol^{-1} cm^{-1}) but is little shifted from the free ligand **3** (425 versus 427 nm), providing evidence for electronic communication between the porphyrin and tpy domains. Fig. 2.24 shows that there is also little difference in the Q bands comparing **3** with [Ru(**3**)(**4**)][PF$_6$]$_2$, (in the complex, 559 and 599 nm, ε = 28 000, 10 000 dm^3 mol^{-1} cm^{-1}, respectively). Confirmation of the presence of the {Ru(tpy)$_2$}$^{2+}$ chromophore comes from the appearance of the broad band at 492 nm arising from the ^{1}MLCT absorption of this chromophore[8].
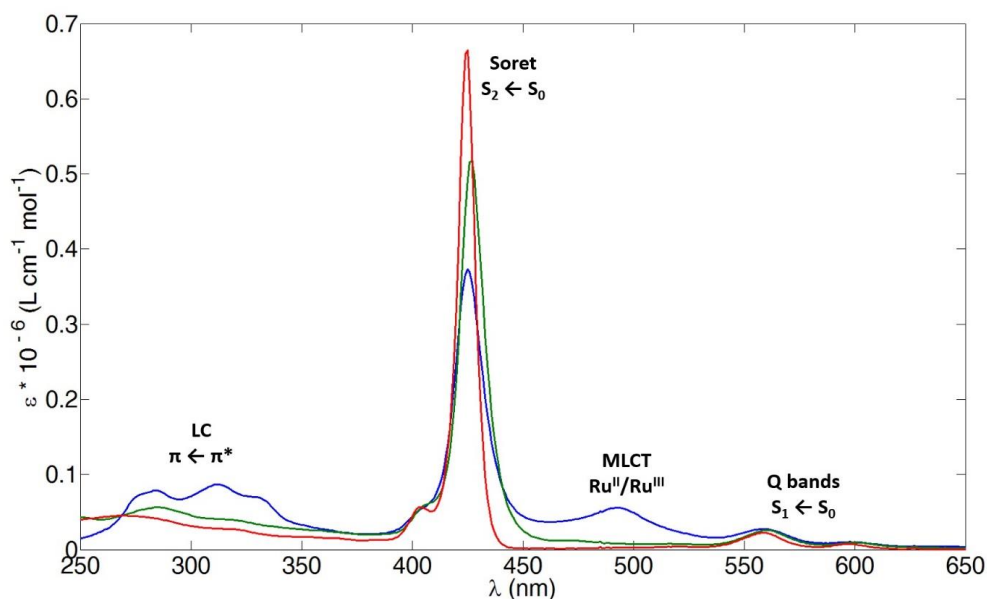
Fig. 2.24 Absorption spectra of **1** (red line, EtOH, 1•10^{-6} mol dm^{-3}), **3** (green line, EtOH, 1•10^{-6} mol dm^{-3}) and [Ru(**3**)(**4**)][PF$_6$]$_2$ (blue line, MeCN, 1•10^{-6} mol dm^{-3}).

Absorption spectra of the homoleptic series are collected in Fig. 2.25, and the spectroscopic data are presented in Table 2.2. The observed set of Soret and Q bands are typical of a metallated porphyrin[3]. The absorption spectrum of [Zn(**3**)$_2$][PF$_6$]$_2$ exhibits only these bands, as expected for a complex containing a d^{10} metal ion. In contrast, a metal-to-ligand charge-transfer (MLCT) band is also present in the spectra of [Fe(**3**)$_2$][PF$_6$]$_2$ and [Ru(**3**)$_2$][PF$_6$]$_2$. In the latter, the MLCT band is clearly visible at 495 nm, but for [Fe(**3**)$_2$][PF$_6$]$_2$, it overlaps with the Q bands (Table 2.2). The presence of an MLCT band relative to the redox couple Fe^{II}/Fe^{III} was verified by the results of the spectroelectrochemical investigations described in the next section.

Fig. 2.25 Absorption spectra of [Zn(**3**)$_2$][PF$_6$]$_2$ (red line, MeCN, 4•10^{-7} mol dm^{-3}), [Fe(**3**)$_2$][PF$_6$]$_2$ (green line, MeCN, 1•10^{-6} mol dm^{-3}), [Ru(**3**)$_2$][PF$_6$]$_2$ (blue line, MeCN, 7•10^{-7} mol dm^{-3}).
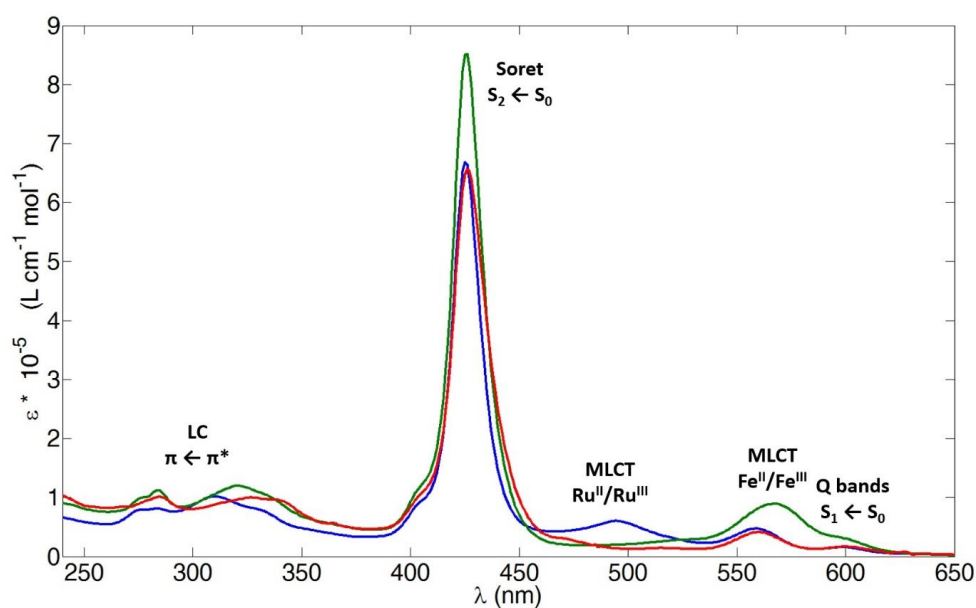
Table 2.2 Absorption spectra of **1** (EtOH, 4.5*10-6 mol dm-3), **3** (EtOH, $1 \cdot 10^{-6}$ mol dm^{-3}), [Zn(**3**)$_2$][PF$_6$]$_2$ (MeCN, $4 \cdot 10^{-7}$ mol dm^{-3}), [Fe(**3**)$_2$][PF$_6$]$_2$ (MeCN $1 \cdot 10^{-6}$ mol dm^{-3}), [Ru(**3**)$_2$][PF$_6$]$_2$ (MeCN, $7 \cdot 10^{-7}$ mol dm^{-3}), [Ru(**3**)(**4**)][PF$_6$]$_2$ (MeCN, $1 \cdot 10^{-6}$ mol dm^{-3}).

Compound	λ_{max}/nm (ε_{max}/dm^3 mol^{-1} cm^{-1}) tpy-centred	Soret	Q1	Q2	MLCT
1		425 (420 000)	559 (17 000)	598 (6000)	
3	285 (56 000)				
	315 (41 000)	427 (520 000)	560 (26 000)	599 (9500)	
[Zn(**3**)$_2$][PF$_6$]$_2$	285 (100 000)	426 (660 000)	560 (41 000)	600 (17 000)	
	327 (99 000)				
	337 (96 000)				
[Fe(**3**)$_2$][PF$_6$]$_2$	284 (105 000)	426 (840 000)	568 (88 000)	597 (35 000)	573 (88 000)
	321 (115 000)				
[Ru(**3**)$_2$][PF$_6$]$_2$	283 (82 000)	425 (670 000)	559 (47 000)	599 (16 000)	495 (62 000)
	310 (102 000)				
[Ru(**3**)(**4**)][PF$_6$]$_2$	284 (79 000)	425 (370 000)	559 (28 000)	599 (10 000)	492 (56 000)
	312 (87 000)				

2.5 Experimental

2.5.1 Synthesis of 7-bromo-5,10,15,20-tetraphenyl-21H-23H-porphyrin
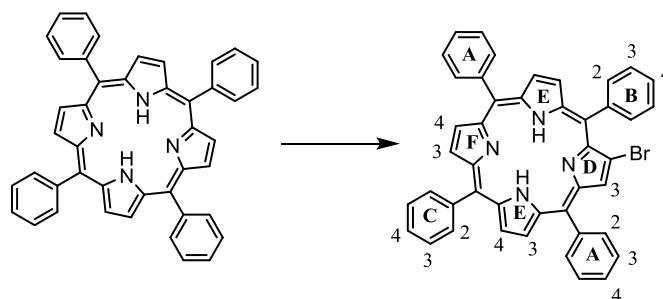
H$_2$TPP (184 mg, 0.3 mmol, 1 eq.) was dissolved in 180 mL chloroform in a three-necked 500 mL round bottom flask. A reflux condenser was mounted on the central neck. Pyridine (3 mL) was added and the mixture was brought to reflux (80 °C). NBS (108 mg, 0.6 mmol, 2 eq.) was dissolved in 90 mL chloroform and poured into a dropping funnel connected to the side arm of the flask. The dropping funnel was covered with aluminium foil to prevent light from photo-dissociating NBS (a yellow colour develops over time if this precaution is not taken). When the mixture was refluxing, the addition was started in such a way that all of the volume was added over the course of four hours. After the addition was completed, the mixture was let reflux for other 30 minutes before quenching the reaction by addition of 90 mL acetone.

The solvent was removed under reduced pressure and the crude (dull purple powder) was redissolved in a minimum amount of toluene. The crude was purified on a silica column (at least 500 mL dry silica was required to pack the column); a mixture 1:1 toluene/cyclohexane was chosen as eluent and the separation was performed gravitationally (no pressure was

applied). The first band was discarded (pale purple), while the second band was collected (dark purple). All of the bands that eluted after the second contained a mixture of isomers of the dibromo derivative. BrTPP was recovered as a dull purple powder (150 mg, 0.22 mmol, 0.7 eq.) in 70 % yield. ^{1}H-NMR matched that reported in literature (Fig 2.26)[1].
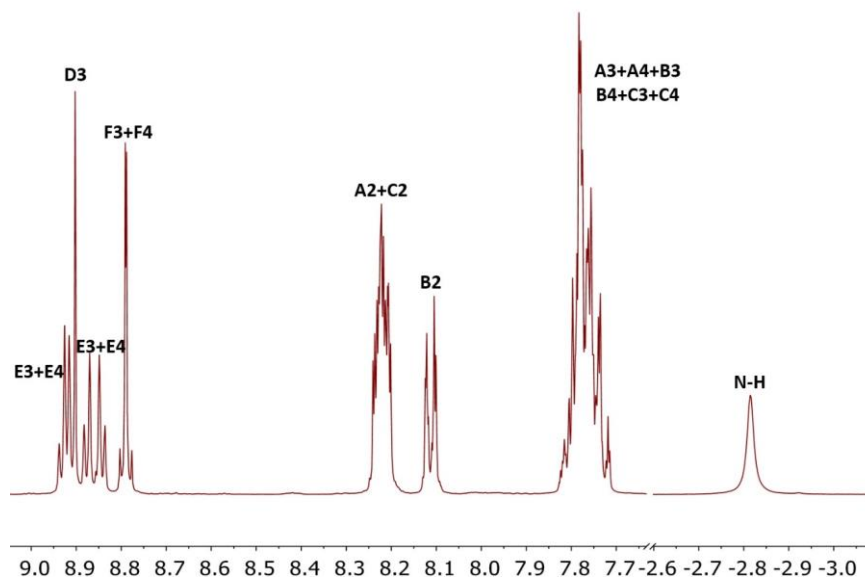
Fig 2.18 400 MHz ^{1}H-NMR of a CDCl$_3$ solution of BrTPP.

^{1}H (CDCl$_3$, 400 MHz): 8.93 (d, 1H, J_{HH} = 4.92 Hz, H$^{E3/E4}$), 8.92 (d, 1H, J_{HH} = 4.92 Hz, H$^{E3/E4}$), 8.90 (s, 1H, H^{D3}), 8.88 (d, 1H, J_{HH} = 4.96 Hz, H$^{E3/E4}$), 8.84 (d, 1H, J_{HH} = 4.93 Hz, H$^{E3/E4}$), 8.79 (d, 2H, J_{HH} = 1.22 Hz, H^{F3+F4}), 8.22 (m, 4H, H^{A2+C2}), 8.11 (m, 2H, H^{B2}), 7.77 (m, 9H, H$^{A3+A4+B3+B4+C3+C4}$), -2.81 (m, 2H, H^{NH}).

3.5.2 Synthesis of 7-bromo-5,10,15,20-tetrapehnylporphyrinatozinc(II) (1)
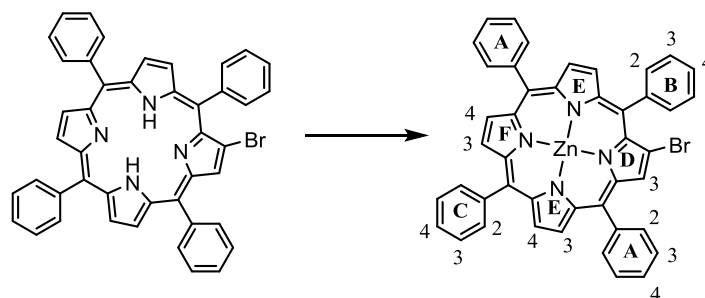
BrTPP (150 mg, 0.22 mmol, 1 eq.) was dissolved in 20 mL chloroform and mixed to a solution of Zn(OAc)$_2$•2H$_2$O (72 mg, 0.33 mmol, 1.5 eq.) in 2 mL methanol. The mixture was stirred at room temperature overnight. The mixture was washed with water and the two phases were separated by means of a separatory funnel. The organic phase was evaporated under reduced pressure yielding compound **1** (166 mg, 0.22 mmol, 1 eq.) in quantitative yield. ^{1}H-NMR matched that reported in literature (Fig 2.27)[9].
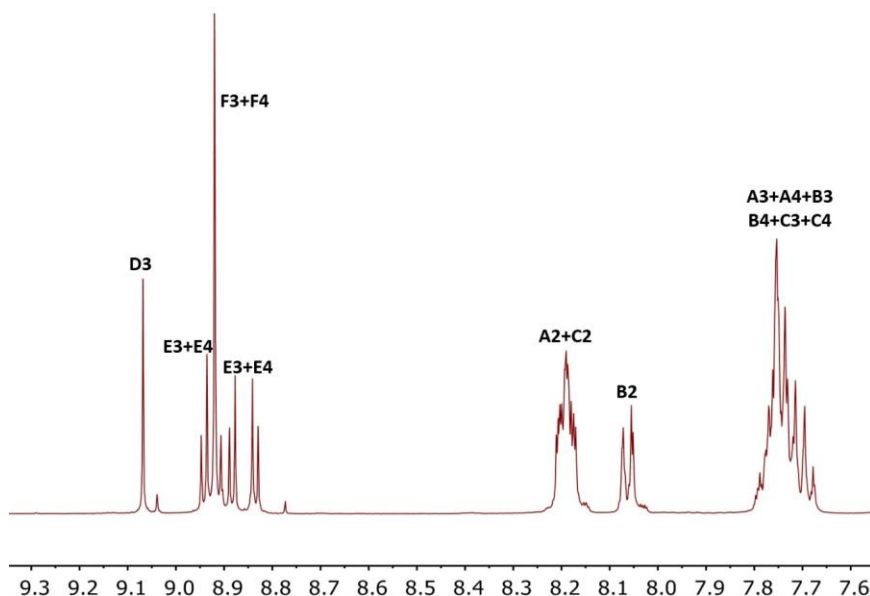
Fig 2.27 400 MHz ^{1}H-NMR of a CDCl$_3$ solution of **1**.

^{1}H (CDCl$_3$, 400 MHz): 9.08 (s, 1H, H^{D3}), 8.95 (d, 1H, J$_{HH}$ = 4.70 Hz, H$^{E3/E4}$), 8.93 (s, 2H, H^{F3+F4}), 8.92 (d, 1H, J$_{HH}$ = 4.70 Hz, H$^{E3/E4}$), 8.90 (d, 1H, J$_{HH}$ = 4.70 Hz, H$^{E3/E4}$), 8.85 (d, 1H, J$_{HH}$ = 4.70 Hz, H$^{E3/E4}$), 8.20 (m, 4H, H^{A2+C2}), 8.08 (m, 2H, H^{B2}), 7.75 (m, 9H, H$^{A3+A4+B3+B4+C3+C4}$).

2.5.3 Synthesis of (4-([2,2':6',2''-terpyridin]-4'-yl)phenyl)boronic acid (**2**)
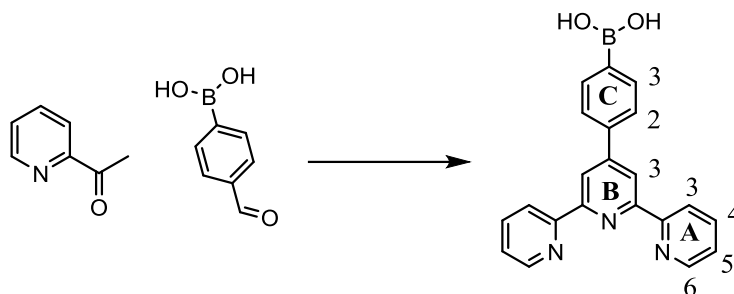
Potassium hydroxide (1.7 g, 30 mmol, 3 eq.) was dissolved in 60 mL absolute ethanol. 4-Formylphenylboronic acid (1.5 g, 10 mmol, 1 eq.) and 2-acetylpyridine (3.33 mL, 30 mmol, 3 eq.) were added and the yellow mixture was stirred overnight under nitrogen. The solution turned orange, at which point ammonium hydroxide (32% ammonia solution, 30 mL, excess) was added dropwise. The mixture was heated at 65 °C for 7 hours and then stirred at room temperature for 18 hours. A white precipitate formed, which was separated by filtration and washed with cold ethanol. Compound **2** was obtained as soft white fibers (1.6 g, 4.5 mmol, 0.45 eq.) in 45 % yield. ^{1}H-NMR matched that reported in literature (Fig 2.28)[10].
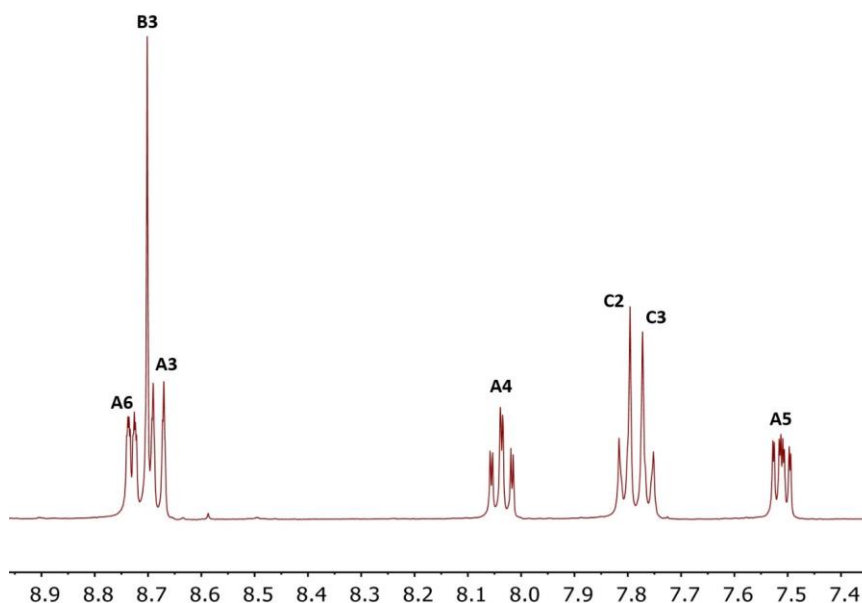
Fig 2.28 400 MHz ^{1}H-NMR of a MeOD solution of **2**.

^{1}H (MeOD, 400 MHz): 8.73 (ddd, 2H, J_{HH} = 4.88, 1.78, 0.90 Hz H^{A6}), 8.70 (s, 2H, H^{B3}), 8.68 (dd, 2H, J_{HH} = 7.99, 1.10 Hz, H^{A3}), 8.04 (td, 2H, J_{HH} = 7.91, 7.77, 1.80 Hz, H^{A4}), 7.81 (d, 2H, J_{HH} = 8.35 Hz, H^{C2}), 7.76 (d, 2H, J_{HH} = 8.30 Hz, H^{C3}), 7.51 (ddd, 2H, J_{HH} = 7.50, 4.88, 1.23 Hz, H^{A5}).

2.5.4 Synthesis of 7-(4-([2,2':6',2''-terpyridin]-4'-yl)phenyl)-5,10,15,20-tetraphenylporphyrinatozinc(II) (**3**)
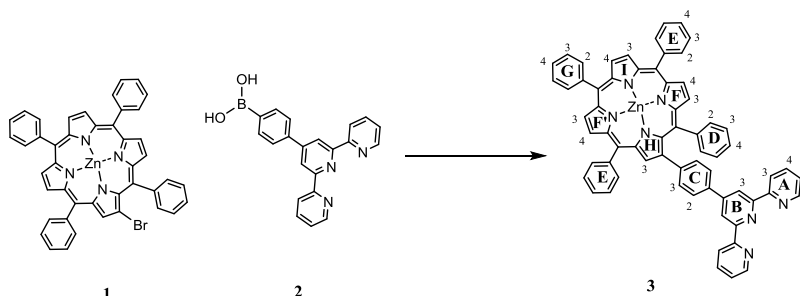
Compound **1** (100 mg, 0.13 mmol, 1 eq.), compound **2** (53 mg, 0.15 mmol, 1.2 eq.) and potassium carbonate (72 mg, 0.52 mmol, 4 eq.) were placed in a 20 mL microwave vial and dissolved in 9.5 mL toluene and 0.6 mL deionized water. The solution was degassed by bubbling nitrogen for 30 minutes and then [Pd(PPh$_3$)$_4$] (15 mg, 0.013 mmol, 0.1 eq.) was added and the vial sealed. The vial was heated at 120 °C for 4 hours in a microwave reactor. When the reaction was completed, the solution was pipetted in a round bottomed flask paying attention to leave the solid material in the vial. The solvent was evaporated and the crude underwent column chromatography (silica, pure chloroform as eluent). The first fraction run with the solvent and consisted of [Zn(TPP)], while compound **3** was contained in the slow moving (R$_f$ = 0.1) band. To the tail of compound **3**'s band, a dark brown band eluted consisting of not-identifiable aromatic compounds. Compound **3** was isolated as a cherry solid (89 mg, 0.09 mmol, 0.7 eq.) equivalent to a 70% yield. ^{1}H-NMR is shown is Fig 2.29, and the complete set of 2D-NMR experiments is shown in Fig. 2.1 (COSY), Fig. 2.2 (NOESY), Fig. 2.3 (HMQC), Fig. 2.4 (HMBC).
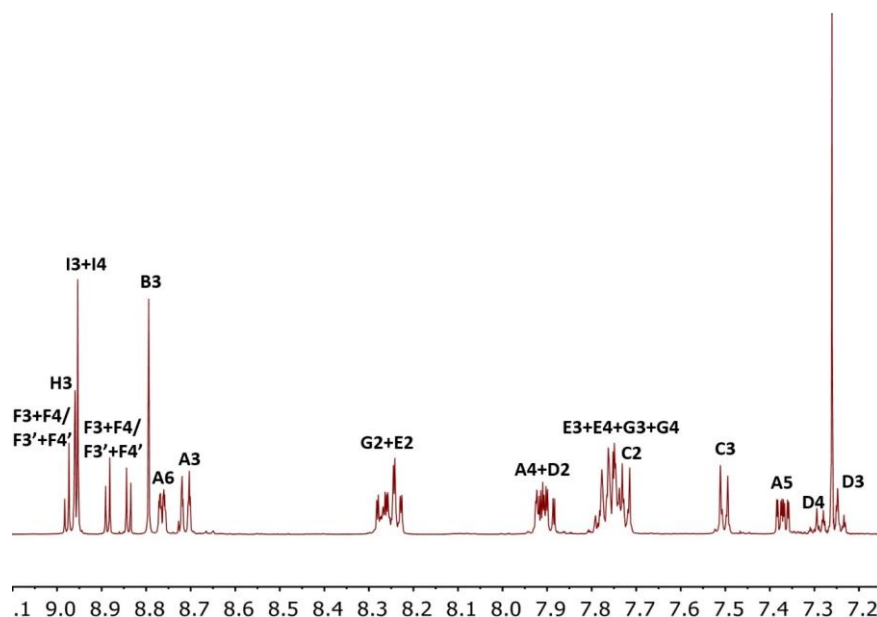
Fig 2.29 500 MHz ^{1}H-NMR of a CDCl$_3$ solution of **3**. δ = 7.26 ppm residual solvent peak.

^{1}H (CDCl$_3$, 500 MHz): δ/ppm 8.97 (m, 2H, H$^{F3+F4/F3'+F4'}$), 8.96 (s, 1H, H^{H3}), 8.95 (s, 2H, H^{I3+I4}), 8.89 (d, J$_{HH}$ = 4.5 Hz, 2H, H$^{F3/F4/F3'/F4'}$), 8.84 (d, J$_{HH}$ = 4.5 Hz, 2H, H$^{F3/F4/F3'/F4'}$), 8.79 (s, 2H, H^{B3}), 8.76 (ddd, J$_{HH}$ = 4.7, 1.8, 0.9 Hz, 2H, H^{A6}), 8.71 (dt, J$_{HH}$ = 8.0, 1.1 Hz, 2H, H^{A3}), 8.26 (m, 6H, H^{E2+G2}), 7.91 (m, 4H, H^{A4+D2}), 7.76 (m, 11H, H$^{E3+E4+G3+G4+C3}$), 7.50 (m, 2H, H^{C2}), 7.37 (ddd, J$_{HH}$ = 7.5, 4.7, 1.2 Hz, 2H, H^{A5}), 7.28 (m, 1H, H^{D4}), 7.24 (m, 2H, H^{D3}). ^{13}C NMR (126 MHz, CDCl$_3$) δ/ppm: 156.6 (C$^{A2/B2}$), 156.1 (C$^{A2/B2}$), 151.4 (C^Q), 150.7 (C^Q), 150.49 (C^Q), 150.47 (C^Q), 150.43 (C^Q), 150.42 (C^Q), 150.4 (C^{B4}), 149.3 (C^{A6}), 148.0 (C^Q), 146.85 (C^Q), 146.8 (C^Q), 143.0 (C^Q), 142.91 (C^Q), 142.89 (C^Q), 141.5 (C^Q), 140.8 (C^Q), 137.0 (C$^{D2/A4}$), 135.8 (C$^{D2/A4}$), 135.4 (C$^{H3/Q}$), 135.35 (C$^{H3/Q}$), 134.6 (C$^{E2/G2}$), 134.55 (C$^{E2/G2}$), 132.9 (C$^{F3/F4/F3'/F4'/I3/I4}$), 132.3 (C$^{F3/F4/F3'/F4'/I3/I4}$), 132.25 (C$^{F3/F4/F3'/F4'/I3/I4}$), 132.2 (C$^{F3/F4/F3'/F4'/I3/I4}$), 132.1 (C$^{F3/F4/F3'/F4'/I3/I4}$), 131.6 (C$^{F3/F4/F3'/F4'/I3/I4}$), 131.0 (C^{C3}), 127.7 (C$^{E3/E4/G3/G4}$), 127.65 (C$^{E3/E4/G3/G4}$), 127.3 (C^{D4}), 126.8 (C$^{E3/E4/G3/G4}$), 126.2 (C^{D3+C2}), 123.9 (C^{A5}), 122.6, 121.7 (C^Q), 121.6 (C^{A3}), 121.2 (C^Q), 120.8 (C^Q), 118.8 (C^{B3}) (C^Q = quaternary C, not unambiguously assigned). ESI MS *m/z* (positive mode) 984.7 [M+H]$^+$ (calc. 984.3). UV-Vis (EtOH, 9.7 * 10^{-7} M) λ/nm (ε/M^{-1} cm^{-1}) 285 (56 000), 315 (41 000), 427 (520 000), 560 (26 000), 599 (9500). Found C 75.89, H 4.41, N 9.49 ; C$_{65}$H$_{41}$N$_7$Zn•3H$_2$O: C 75.10, H 4.56, N 9.43.

2.5.5 Synthesis of diethyl (4-([2,2':6',2''-terpyridin]-4'-yl)phenyl)phosphonate (**4**)
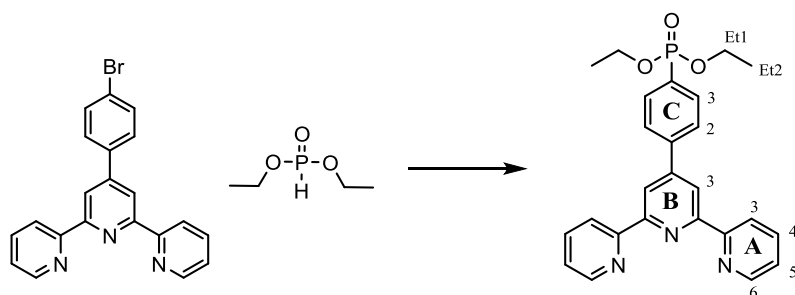
In a 100 mL two-neck round-bottomed flask 4'-(4-bromophenyl)-2,2':6',2''-terpyridine (1.94 g, 5 mmol, 1 eq.) was dissolved in 50 mL anhydrous toluene. The solution was purged with nitrogen, and under a nitrogen atmosphere diethyl phosphite (0.71 mL, 5.5 mmol, 1.1 eq.), triethylamine (0.77 mL, 5.5 mmol, 1.1 eq.) and [1,1-bis-(diphenylphosphino)ferrocene] dichloropalladium(II) complex with dichloromethane (1:1) (204 mg, 0.25 mmol, 0.05 eq.) were sequentially added. The reaction mixture was heated at 90 °C and stirred for 24 hours. Upon solvent removal by rotary evaporation, a violet oil was obtained, which was crystallized from acetonitrile (10 mL) yielding the pure compound as a white powder (500 mg, 1.12 mmol, 22%). ^{1}H-NMR matched that reported in literature (Fig 2.30)[2].
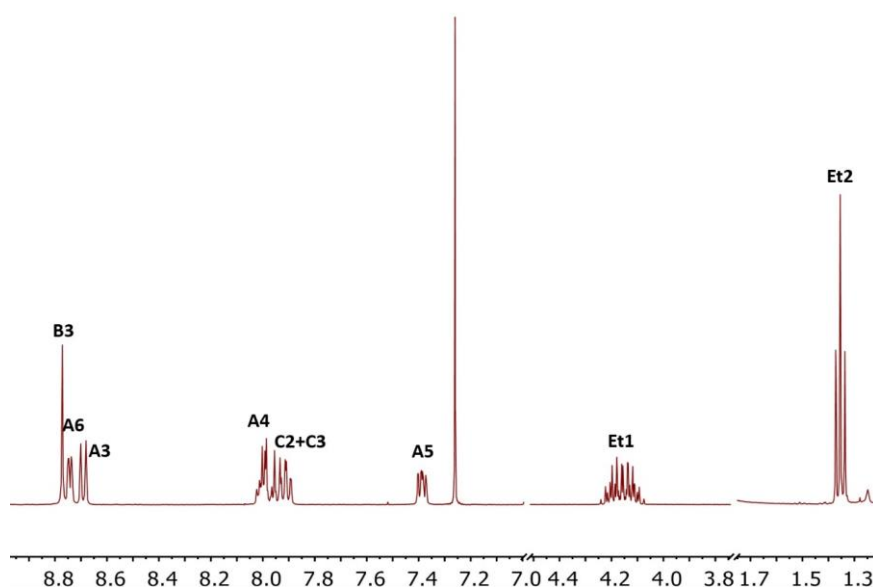
Fig 2.30 400 MHz ^{1}H-NMR of a CDCl$_3$ solution of **4**. δ = 7.26 ppm residual solvent peak.

[1]H (CDCl$_3$, 400 MHz): 8.77 (s, 2H, H^{B3}), 8.74 (ddd, 2H, J$_{HH}$ = 4.84, 1.82, 0.92 Hz, H^{A3}), 8.69 (dt, 2H, J$_{HH}$ = 8.03, 1.09 Hz, H^{A3}), 8.00 (m, 2H, H^{A4}), 7.93 (m, 4H, H^{C2+C3}), 7.39 (ddd, 2H, J$_{HH}$ = 7.47, 4.82, 1.18 Hz, H^{A5}), 4.16 (m, 4H, H^{Et1}), 1.35 (t, 6H, J$_{HH}$ = 7.07 Hz, H^{Et2}).

2.5.6 Synthesis of [Ru(**3**)(**4**)][PF$_6$]$_2$
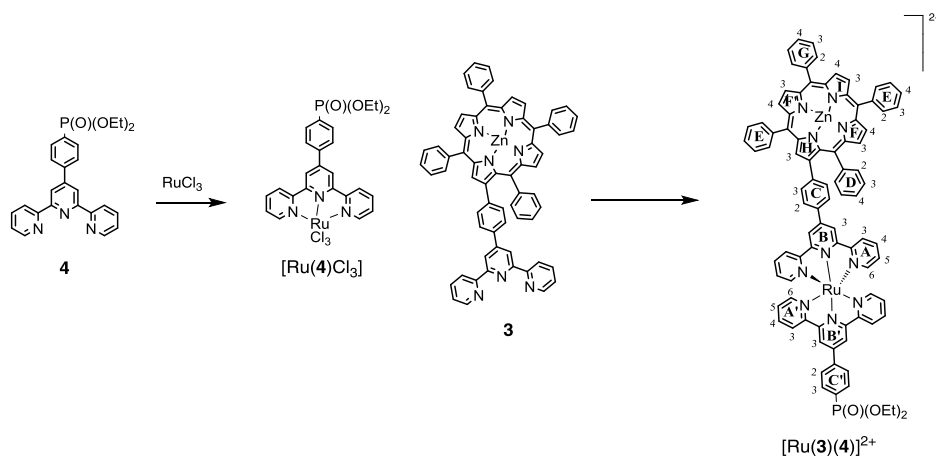
Compound **4** (27 mg, 0.06 mmol, 1 eq.) and $RuCl_3 \cdot 3H_2O$ (16 mg, 0.06 mmol, 1 eq.) were suspended in 10 mL ethanol and refluxed for 3.5 hours. A brown precipitate formed, which was centrifuged, washed with ethanol and diethyl ether. [Ru(**4**)Cl₃] (28 mg, 0.043 mmol, 0.7 eq.) was used for the next step without further characterization.

In a 5 mL microwave vial, [Ru(**4**)Cl₃] (28 mg, 0.043 mmol, 1 eq.), compound **3** (42 mg, 0.043 mmol, 1 eq.) and *N*-ethylmorpholine (2 drops) were suspended in dry ethanol. The vial was sealed and the mixture was heated in a microwave reactor at 140 °C for 20 min and the resulting dark red solution was poured in 50 mL saturated aqueous NH_4PF_6. The precipitate was collected by centrifugation and washed with water and diethyl ether (3 x 5 mL). The residue was dissolved in acetonitrile and eluted on silica gel using a mixture MeCN/saturated aq. KNO_3/water 7 : 1 : 0.5 by volume as eluent. The first fraction (orange, R_f = 0.67), corresponding to the desired product, was collected, concentrated to a volume of 3 ml and poured into 25 mL saturated aqueous NH_4PF_6. The precipitate was once again washed with water and ethanol (3 x 5 mL). [Ru(**3**)(**4**)][PF_6]₂ was isolated as brown powder (20 mg, 0.011 mmol, 0.26 eq.) in 26 % yield. ^{1}H-NMR is shown is Fig 2.31, and the complete set of 2D-NMR experiments is shown in Fig. 2.9 (COSY), Fig. 2.10 (NOESY), Fig. 2.11 (HMQC), Fig. 2.12 (HMBC).

Fig 2.31 500 MHz ^{1}H-NMR of a CD_3CN solution of [Ru(**3**)(**4**)][PF_6]₂.

^{1}H NMR (500 MHz, CD_3CN) δ/ppm: 9.06 (s, 2H, H$^{B3'}$), 9.01 (s, 2H, H^{B3}), 8.89 (m, 2H, H$^{F3+F4/F3'+F4'}$), 8.86 (s, 1H, H^{H3}), 8.85 (s, 2H, H^{I3+I4}), 8.82 (d, J_{HH} = 4.5 Hz, 2H, H$^{F3/F4/F3'/F4'}$), 8.79 (d, J_{HH} = 4.5 Hz, 2H, H$^{F3/F4/F3'/F4'}$), 8.75 (m, 2H, H$^{A3'}$), 8.69 (m, 2H, H^{A3}), 8.33 (m, 2H, H$^{C3'}$), 8.30 (m, 2H, H^{G2}), 8.24 (m, 4H, H^{E2}), 8.09 (m, 2H, H$^{C2'}$), 7.98-8.05 (m, 6H, H$^{A4'+A4+D2}$), 7.95 (d, J_{HH} = 8.5 Hz, 2H, H^{C3}), 7.77-7.86 (m, 9H, H$^{E3+E4+G3+G4}$), 7.70 (d, J_{HH}=8.5 Hz, 2H, H^{C2}), 7.53 (m, 2H, H$^{A6'}$), 7.47 (m, 2H, H^{A6}), 7.44 (m, 1H, H^{D4}), 7.38 (m, 2H, H^{D3}), 7.27 (m, 2H, H$^{A5'}$), 7.22 (m, 2H, H^{A5}), 4.14 (m, 4H, H^{P1}), 1.35 (t, J_{HH} = 7 Hz 6H, H^{P2}). ^{13}C NMR (126 MHz, CD_3CN) δ/ppm: 159.3 (C$^{A2'/B2'}$), 159.0 (C$^{A2/B2}$), 156.8 (C$^{A2'/B2'}$), 156.3 (C$^{A2/B2}$), 153.4 (C$^{A6+A6'}$), 151.9 (C^Q), 151.0 (C^Q), 148.5 (C^Q), 147.9 (C^{B4}), 147.1 (C$^{B4'}$), 147.0 (C^Q), 144.0 (C^Q), 143.8 (C^Q), 143.2 (C^Q), 143.0 (C^Q), 141.5 (C^Q), 139.0 (C$^{A4+A4'}$), 136.9 (C^{D2}), 135.7 (C^{H3}), 135.3 (C^{E2}), 135.2 (C^{G2}), 134.4 (C^Q), 133.4 (C$^{C3'}$), 133.1 (C$^{F3/F4/F3'/F4'}$), 132.7 (C$^{I3+I4+two of F3/F4/F3'/F4'}$), 132.2 (H$^{F3/F4/F3'/F4'}$), 132.1 (C^{C3}), 131.8 (C$^{C4'}$, J_{PC} = 189 Hz), 129.0 (C$^{C2'}$), 128.5 (H$^{A5+A5'}$), 127.8 (C$^{E3+E4+G3+G4+D4}$), 127.4 (C^{C2}), 127.0 (C^{D3}),

125.5 ($C^{A3+A3'}$), 123.0 ($C^{B3'}$), 122.2 (C^{B3}),), 63.2 (C^{Et}), 16.6 (C^{Et}). (C^Q = quaternary C, not unambiguously assigned). ESI MS *m/z* (positive mode) 765.6 $[M]^{2+}$ (calc. 765.7), negative mode 144.8 $[PF_6]^-$ (calc.. 145.0). UV-Vis (MeCN, $1*10^{-6}$ mol dm^{-3}) λ/nm (ε/dm^3 mol^{-1} cm^{-1}) 284 (79 000), 312 (87 000), 425 (370 000), 492 (56 000), 559 (28 000), 599 (10 000). Found: C 57.38, H 4.07, N 8.01; $C_{90}H_{65}F_{12}N_{10}O_3P_3$-RuZn*2H$_2$O requires C 58.18, H 3.74, N 7.54.

2.5.7 Synthesis of [Zn(**3**)$_2$][PF$_6$]$_2$

Compound **3** (53 mg, 0.054 mmol, 1 eq.) and Zn(OAc) $_2$·2H$_2$O (6 mg, 0.027 mmol, 0.5 eq.) were dissolved in 15 mL dry MeOH under nitrogen and the solution was stirred overnight at room temperature. An excess of saturated aqueous NH$_4$PF$_6$ was then added. A precipitate formed, which was collected by centrifugation. The solid was washed with water (3 × 5 mL) and diethyl ether (3 × 5 mL), and then dissolved in MeCN; the solvent was removed under vacuum. [Zn(**3**)$_2$][PF$_6$]$_2$ was isolated as a dark-purple solid (56 mg, 0.024 mmol, 90%). ^{1}H-NMR is shown is Fig 2.32, and the complete set of 2D-NMR experiments is shown in Fig. 2.19 (COSY), Fig. 2.20 (NOESY), Fig. 2.21 (HMQC), Fig. 2.22 (HMBC).
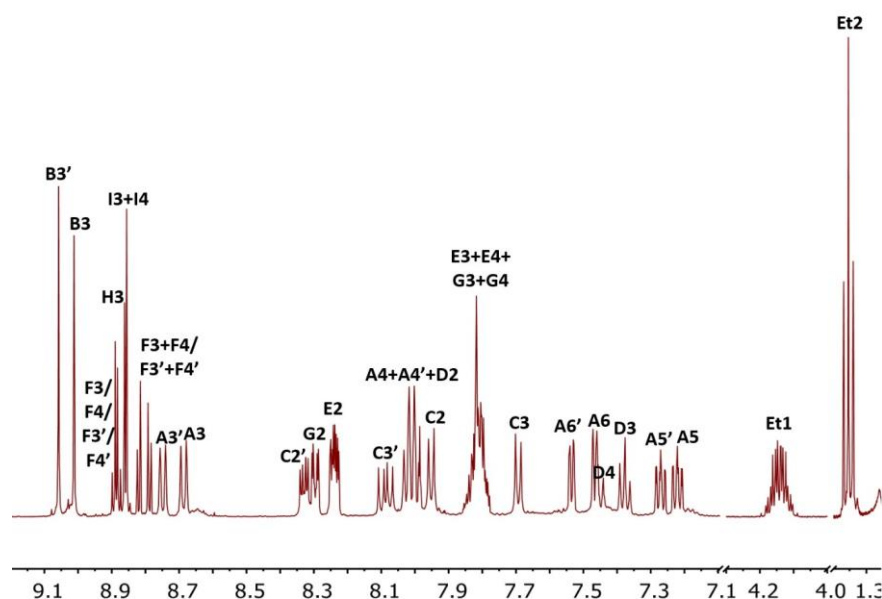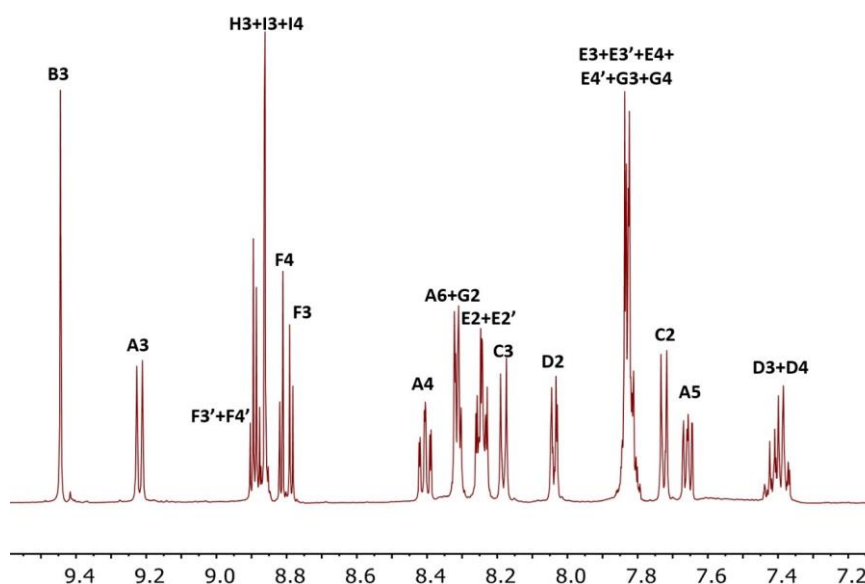

Fig. 2.32 500 MHz ^{1}H-NMR of a (CD$_3$)$_2$CO solution of [Zn(**3**)$_2$)][PF$_6$]$_2$. See Scheme 2.3 for NMR labelling.

^{1}H NMR (500 MHz, (CD$_3$)$_2$CO) δ/ppm: 9.44 (s, 4H, H^{B3}), 9.22 (m, 4H, H^{A3}), 8.90 (d, J_{HH} = 4.5 Hz, 2H, H$^{F3'/F4'}$), 8.88 (d, J_{HH} = 4.5 Hz, 2H, H$^{F3'/F4'}$), 8.86 (s, 2H, H^{H3}), 8.86 (s, 4H, H^{I3+I4}), 8.82 (d, J_{HH} = 4.6, 2H, H$^{F3/F4}$), 8.79 (d, J_{HH} = 4.6, 2H, H$^{F3/F4}$), 8.41 (ddd, J_{HH} = 8.1, 7.4, 1.6 Hz, 4H, H^{A4}), 8.31 (m, 8H, H^{A6+G2}), 8.24 (m, 8H, H$^{E2+E2'}$), 8.18 (m, 4H, H^{C2}), 8.04 (m, 4H, H^{D2}), 7.79–7.86 (m, 18H, H$^{E3+E3'+E4+E4'+G3+G4}$), 7.72 (m, 4H, H^{C3}), 7.66 (ddd, J_{HH} = 7.4, 5.2, 1.0 Hz, 4H, H^{A5}), 7.36–7.44 (m, 6H, H^{D3+D4}). ^{13}C NMR (126 MHz, (CD$_3$)$_2$CO) δ/ppm: 156.6 (C^{B4}), 150.2 (C^{A2}), 151.0/150.5/150.2/147.4/146.0 ($C^{F2+F5+F2'+F5'+H2+H4+H5+I2+I5}$), 149.0 ($C^{A6}$), 148.4 ($C^{B2}$), 143.6 ($C^{C1+G1+E1+E1'}$), 142.3 ($C^{D1}$), 142.2 ($C^{A4}$), 136.7 ($C^{D2}$), 135.4 ($C^{I3+I4}$), 135.35 ($C^{H3}$), 135.1 ($C^{G2+E2+E2'}$), 133.8 ($C^{C4}$), 132.9 ($C^{F3}$), 132.4 ($C^{F3'/F4'}$), 132.0 ($C^{C3}$), 131.8 ($C^{F4}$), 128.5 ($C^{A5}$), 128.2 ($C^{E3+E3'+E4+E4'+G3+G4}$), 127.5 ($C^{C2}$), 127.5 ($C^{D3+D4}$), 124.2 ($C^{A3}$), 121.7 ($C^{meso-D}$), 121.0 ($C^{B3}$), 120.9

(C^{meso-E}), 120.2 (C^{meso-G}). ESI MS *m/z* 1017.1 $[M]^{2+}$ (calc. 1016.7). Satisfactory elemental analysis was not obtained.

2.5.8 Synthesis of [Fe(**3**)$_2$][PF$_6$]$_2$

Compound **3** (56 mg, 0.057 mmol, 1 eq.) and FeCl$_2$ (7.2 mg, 0.057 mmol, 1 eq.) were dissolved in 20 mL dry EtOH under nitrogen and the solution was stirred at room temperature overnight. An excess of saturated aqueous NH$_4$PF$_6$ was then added. The precipitate that formed was collected by centrifugation, and was then washed with water and diethyl ether (3 × 5 mL each). The residue was dissolved in MeCN. The solvent was removed under reduced pressure and [Fe(**3**)$_2$][PF$_6$]$_2$ was isolated as a dark purple powder (47 mg, 0.02 mmol, 70%).

Fig. 2.33 500 MHz ^{1}H-NMR of a CD$_3$CN solution of [Fe(**3**)$_2$)][PF$_6$]$_2$. See Scheme 2.3 for NMR labelling.

^{1}H-NMR (500 MHz, CD$_3$CN) δ/ppm: 9.22 (s, 4H, H^{B3}), 8.88–8.91 (m, 6H, $H^{F3/F4/F3'/F4'+H3}$), 8.86 (s, 4H, H^{I3+I4}), 8.82 (d, J_{HH} = 4.54 Hz, 4H, $H^{F3+F4/F3'+F4'}$), 8.75 (d, J_{HH} = 7.97 Hz, 4H, H^{A3}), 8.32 (m, 4H, H^{G2}), 8.25 (m, 8H, $H^{E2+E2'}$), 8.08 (m, 8H, H^{D2+C2}), 8.01 (t, J_{HH} = 7.4 Hz, 4H, H^{A4}), 7.79–7.87 (m, 18H, $H^{E3+E3'+E4+E4'+G3+G4}$), 7.76 (d, J_{HH} = 7.6 Hz, 4H, H^{C3}), 7.51 (t, J_{HH} = 7.5 Hz, 2H, H^{D4}), 7.43 (t, J_{HH} = 7.4 Hz, 4H, H^{D3}), 7.32 (d, J_{HH} = 5.5 Hz, 4H, H^{A6}), 7.21 (t, J_{HH} = 6.5 Hz, 4H, H^{A5}). ^{13}C NMR (126 MHz, CD$_3$CN) δ/ppm: 161.2 (C^{B2}), 159.1 (C^{A2}), 154.2 (C^{A6}), 151.5 (C^{B4}), 151.8/151.3/151.1/150.9/148.3/147.0 ($C^{F2+F5+F2'+F5'+H2+H4+H5+I2+I5}$), 143.9 ($C^{G1+E1+E1'}$), 143.4 ($C^{C1}$), 143.0 ($C^{D1}$), 139.7 ($C^{A4}$), 137.0 ($C^{D2}$), 135.7 ($C^{H3}$), 135.3 ($C^{G2+E2+E2'}$), 134.3 ($C^{C4}$), 133.4/132.8/132.2 ($C^{F3+F4+F3'+F4'}$), 132.7 ($C^{I3+I4}$), 132.3 ($C^{C3}$), 128.5 ($C^{G3+G4}$), 128.3 ($C^{A5}$), 127.9 ($C^{D4}$), 127.6 ($C^{C2}$), 127.5 ($C^{E3+E3'+E4+E4'}$), 127.1 ($C^{D3}$), 124.9 ($C^{A3}$), 122.9 ($C^{meso-E}$), 122.3 ($C^{B3}$), 121.9 ($C^{meso-D}$); C^{meso-G} not resolved. ESI MS *m/z* 984.7 [**3** + H]$^+$ (calc. 984.3); 1013.4 $[M]^{2+}$ (calc. $[M]^{2+}$ 1012.7). HR-ESI MS 1013.2389 [M – 2PF$_6$]$^{2+}$ (calc. 1013.2408). Satisfactory elemental analysis was not obtained.

2.5.9 Synthesis of [Ru(**3**)$_2$][PF$_6$]$_2$

Compound **3** (57 mg, 0.058 mmol, 1 eq.) and RuCl$_3$·3H$_2$O (15 mg, 0.058 mmol, 1 eq.) were dissolved in 10 mL dry EtOH and heated at reflux for 2.5 h. A precipitate formed and was separated by centrifugation. After washing with ethanol and diethyl ether, brown [Ru(**3**)Cl$_3$] was isolated (46 mg, 0.039 mmol, 67%) and was used for the next step without further characterization.

[Ru(**3**)Cl$_3$] (46 mg, 0.039 mmol), **3** (38 mg, 0.039 mmol) and N-ethylmorpholine (3 drops) were suspended in 3 mL dry EtOH in a vial. The mixture was heated in a microwave reactor at 140 °C for 20 min and then the dark red solution was poured into 50 mL saturated aqueous NH$_4$PF$_6$. After centrifugation, the precipitate was collected and washed with water (3 × 5 mL) and diethyl ether (3 × 5 mL). The residue was dissolved in MeCN and purified by column chromatography (SiO$_2$, MeCN/saturated aq. KNO$_3$/water 38 : 1 : 1 by volume). The first orange fraction was collected, concentrated to 3 mL and poured into 25 mL saturated aqueous NH$_4$PF$_6$ to give a precipitate which was washed with water and ethanol (3 × 5 mL). [Ru(**3**)$_2$][PF$_6$]$_2$ was isolated as a purple powder (9.0 mg, 0.0038 mmol, 9.7%).
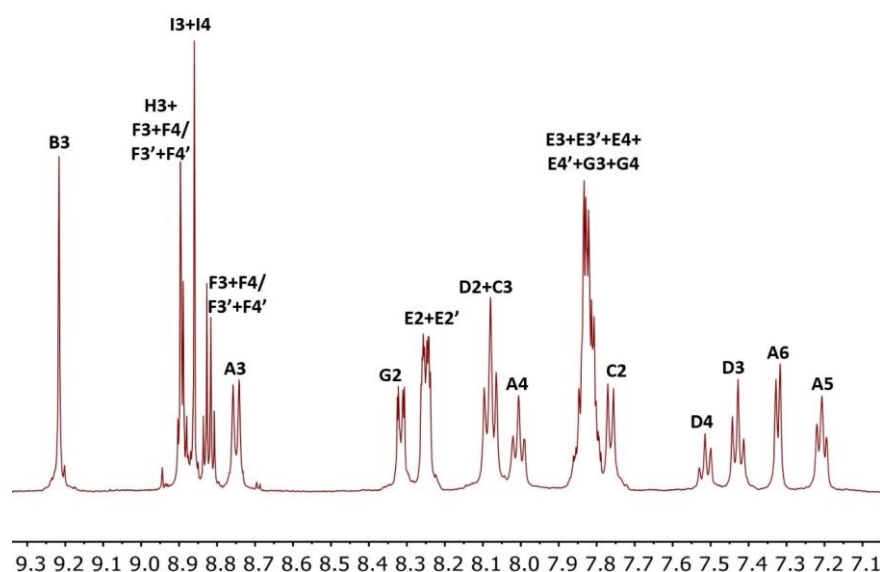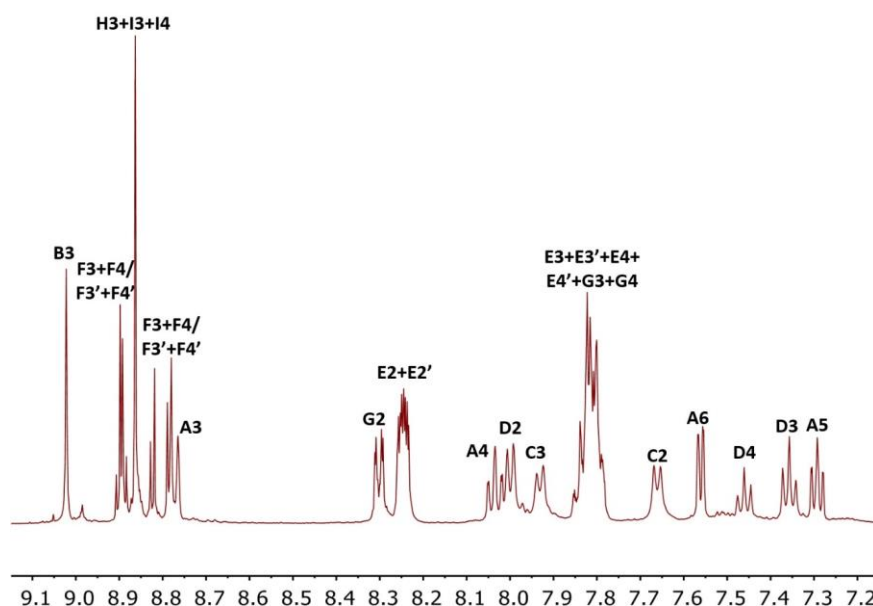

Fig. 2.34 500 MHz ^{1}H-NMR of a CD$_3$CN solution of [Ru(**3**)$_2$)][PF$_6$]$_2$. See Scheme 2.3 for NMR labelling.

^{1}H NMR (500 MHz, CD3CN) δ/ppm: 9.02 (s, 4H, H^{B3}), 8.90 (m, 4H, H$^{F3+F4/F3'+F4'}$), 8.86 (s, 6H, H$^{I3+I4+H3}$), 8.76–8.83 (m, 8H, H$^{F3/F4/F3'/F4'+A3}$), 8.28–8.32 (m, 4H, H^{G2}), 8.25 (m, 8H, H$^{E2+E2'}$), 8.04 (m, 4H, H^{A4}), 8.00 (d, J$_{HH}$ = 7.3 Hz, 4H, H^{D2}), 7.93 (d, J$_{HH}$ = 7.53 Hz, 4H, H^{C2}), 7.70–7.86 (m, 18H, H$^{E3+E4+E3'+E4'+G3+G4}$), 7.67 (d, J$_{HH}$ = 7.53 Hz, 4H, H^{C3}), 7.56 (ddd, J$_{HH}$ = 5.7, 1.5, 0.6 Hz, 4H, H^{A6}), 7.46 (t, J$_{HH}$ = 7.6 Hz, 2H, H^{D4}), 7.36 (t, J$_{HH}$ = 7.5 Hz, 4H, H^{D3}), 7.22 (ddd, J$_{HH}$ = 7.2, 5.7, 1.3 Hz, 4H, H^{A5}). ^{13}C NMR (126 MHz, CD$_3$CN) δ/ppm: 159.3 (C^{A2}), 156.5 (C^{B2}), 153.5 (C^{A6}), 151.9/151.2/151.0/148.2/147.0 (C$^{F2+F5+F2'+F5'+H2+H4+H5+I2+I5}$), 149.4 (C^{B4}), 143.9 (C$^{G1+E1+E1'}$), 143.1 (C^{C1}), 142.9 (C^{D1}), 139.2 (C^{A4}), 137.0 (C^{D2}), 135.4 (C^{H3}), 135.35 (C$^{G2+E2+E2'}$), 135.3, 134.5 (C^{C4}), 133.2/132.9/132.85/132.4 (C$^{F3+F4+F3'+F4'+I3+I4}$), 132.3 (C^{C3}), 128.6 (H^{A5}), 128.0 (C^{D4}), 127.6 (C$^{E3+E3'+E4+E4'+G3+G4}$), 127.5 (C^{C2}), 127.1 (C^{D3}), 125.7 (C^{A3}), 122.9 (C^{meso-D}), 122.2 (C^{B3}), 121.9 (C^{meso-E}), 121.3 (C^{meso-G}). MALDI m/z 984.3 [**3** + H]$^+$ (calc. 984.3). HR-ESI MS 1034.2257 [M − 2PF$_6$]$^{2+}$ (calc. 1034.2243). Satisfactory elemental analysis was not obtained.

2.5.10 General

Microwave reactions were carried out in a Biotage Initiator 8 reactor. ^{1}H, ^{13}C and ^{31}P NMR spectra were recorded at room temperature using a Bruker Avance III-500 NMR spectrometer. ^{1}H and ^{13}C NMR chemical shifts were referenced to residual solvent peaks with respect to δ(TMS) = 0 ppm and ^{31}P NMR chemical shifts with respect to δ(85% aqueous H_3PO_4) = 0 ppm. Solution absorption and emission spectra were measured using an Agilent 8453 spectrophotometer and a Shimadzu RF-5301PC spectrofluorometer, respectively. Spectroelectrochemical and solid-state absorption spectroscopic measurements used a Varian-Cary 5000 spectrophotometer. MALDI TOF were recorded using a Bruker Microflex instrument; electrospray (ESI) mass spectra and high resolution ESI-MS were measured on Bruker Esquire 3000^{plus} and Bruker maXis 4G instruments, respectively.

Nanosecond transient absorption spectra were measured on an LP-920KS spectrometer from Edinburgh Instruments using a frequency-doubled/tripled Quantel Brilliant B laser equipped with an OPO from Optek as a pump source. The pulse duration was ≈10 ns with a typical energy of 15 mJ. UV/Vis transient absorption spectra were recorded with an iCCD camera from Andor. NIR transient absorption spectra were obtained from kinetic decays recorded with an InGaAs photodiode. Transient absorption measurements with picosecond time resolution were performed with the TRASS instrument from Hamamatsu, equipped with a C7701-01 streak camera. Excitation occurred with a picosecond mode-locked Nd:YVO$_4$/YAG laser (PL2251B-20-SH/TH/FH) with PRETRIG option from Ekspla.

Electrochemical measurements were carried out using a CH Instruments 900B potentiostat with [^{n}Bu$_4$N][PF$_6$] (0.1 M) as supporting electrolyte and at a scan rate of 0.1 V s^{-1}. The working electrode was glassy carbon, pseudo-reference electrode silver wire and counter-electrode platinum wire; potentials were referenced with respect to the Fc/Fc+ couple. Spectroelectrochemical measurements were performed using a CH$_2$Cl$_2$ solution of **3** (1 mM) and an MeCN solution of [Ru(**3**)(**4**)][PF$_6$]$_2$ (0.6 mM), [Zn(**3**)$_2$][PF$_6$]$_2$ (0.09 mM), [Fe(**3**)$_2$][PF$_6$]$_2$ (0.21 mM) and [Ru(**3**)$_2$][PF$_6$]$_2$ (0.04 mM) at room temperature with [^{n}Bu$_4$N][PF$_6$] (≈0.1 M) as the supporting electrolyte. A representation of ligands **3** and **4** is given in Scheme 2.1. The solution was added to an optically transparent thin-layer electrochemical (OTTLE) cell with two Pt minigrid electrodes (working and auxiliary), a silver wire pseudoreference electrode, and a path length of ≈0.2 mm. The potential was controlled using a VersaSTAT 3 potentiostat from Princeton Applied Research.

RuCl$_3$•3H$_2$O was purchased from Oxkem, and 5,10,15,20-tetraphenyl-21H,23H-porphyrin (H$_2$TPP), NBS and [Pd(PPh$_3$)$_4$] from Sigma-Aldrich and used as received. 7-Bromo-5,10,15,20-tetraphenyl-21H,23H-porphyrin (BrTPP),[1] **1**,[9] **2**[10] and **4**[2] were prepared as previously reported and spectroscopic data matched those in the literature.

Crystallography

Data were collected on a Bruker Kappa Apex2 diffractometer with data reduction, solution and refinement using APEX[11] and CRYSTALS[12]. The program Mercury v. 3.7[13, 14] was used for structural analysis.

Compound 3•Me₂CO

C₆₈H₄₇N₇OZn, M = 1043.55, red block, monoclinic, space group $P2_1/c$, a = 13.1741(13), b = 20.850(3), c = 19.578(2) Å, β = 102.558(6)°, U = 5249.2(10) Å³, Z = 4, D_c = 1.320 Mg m³, μ(Cu-Kα) = 1.063 mm⁻¹, T = 123 K. Total 66 771 reflections, 9749 unique, R$_{int}$ = 0.078. Refinement of 7565 reflections (694 parameters) with $I > 2\sigma(I)$ converged at final R_1 = 0.0894 (R_1 all data = 0.2457), wR_2 ¼ 0.1059 (wR_2 all data = 0.2583), gof = 1.0000. CCDC 1442417.

DSC fabrication

Solaronix Test Cell Titania Electrodes were heated to 450 °C for 30 min and then cooled to 80 °C, when they were dipped into the dye-baths. N719 (Solaronix) reference electrodes and electrodes with adsorbed [Ru(**3**)(**4**)]²⁺ were made by dipping in an EtOH solution of N719 (0.1 mM) or MeCN solution of [Ru(**3**)(**4**)][PF₆]₂ (0.1 mM), respectively, for 3 days. The electrodes were taken out of the dye-baths, washed with EtOH or MeCN, respectively, and dried using a heatgun (60 °C). Commercial counter electrodes (Solaronix Test Cell Platinum Electrodes) were washed with EtOH, and then heated on a hot plate at 450 °C for 30 min to remove volatile organic impurities.

The working and counter-electrodes were joined using thermoplast hot-melt sealing foil (Solaronix Test Cell Gaskets, 60 µm) by heating while pressing together. The electrolyte (LiI (0.1 M), I₂ (0.05 M), 1-methylbenzimidazole (0.5 M), 1-butyl-3-methylimidazolinium iodide (0.6 M) in 3-methoxypropionitrile) was inserted between the electrodes by vacuum backfilling through a hole in the counter electrode; this was sealed (Solaronix Test Cell Sealings) and capped (Solaronix Test Cell Caps). All DSCs were fully masked for measurements.[15, 16]

Electrodes for solid-state absorption spectroscopy

Dye-functionalized electrodes were assembled as above but using Solaronix Test Cell Titania Electrodes Transparent.

DSC measurements

Masks for the DSCs were made from a black-coloured copper sheet with an aperture of average area 0.06012 cm² (1% standard deviation) placed over the active area of the DSC. The area of the mask hole was less than the surface area of TiO₂ (0.36 cm²). Black tape was used to complete the masking of the cell. Performance measurements were made by irradiating the DSC from behind with a LOT Quantum Design LS0811 instrument (100 mW cm² = 1 sun), and the simulated light power was calibrated with a silicon reference cell.

References

[1] G.-Y. Gao, J. V. Ruppel, D. B. Allen, Y. Chen and X. P. Zhang, *J. Org. Chem.*, 2007, 8, 9060.

[2] V. Spampinato, N. Tuccitto, S. Quici, V. Calabrese, G. Marletta, A. Torrisi, A. Licciardello, *Langmuir,* 2010, 26, 8400.

[3] N. Armaroli, F. Diederich, L. Echegoyen, T. Habicher, L. Flamigni, G. Marconi and J.-F. Nierengarten, *New J. Chem.*, 1999, 77.

[4] E. C. Constable, A. M. W. Cargill Thompson, *New J. Chem.*, 1992, 16, 855.

[5] H. S. Chow, E. C. Constable, C. E. Housecroft, M. Neuburger and S. Schaffner, *Dalton Trans.*, 2006, 2881.

[6] M. Gouterman, *J. Mol. Spectros.* 6, 138, 1961.

[7] A. Harriman, *J. Chem. Soc., Faraday Trans. 1*, 1980, 76, 1978.

[8] E. C. Constable, C. E. Housecroft, A. Cargill Thompson, P. Passaniti, S. Silvi, M. Maestri and A. Credi, *Inorg. Chim. Acta*, 2007, 360, 1102.

[9] S. A. Vail, D. I. Schuster, D. M. Guldi, M. Isosomppi, N. Tkachenko, H. Lemmetyinen, A. Palkar, L. Echegoyen, X. Chen and J. Z. H. Zhang, *J. Phys. Chem. B*, 2006, 110, 14155.

[10] H. S. Mehr, N. C. Romano, R. Altamimi, J. M. Modarelli and D. A. Modarelli, *Dalton Trans.*, 2015, 44, 3176.

[11] *APEX2, version 2 User Manual*, Bruker Analytical X-ray Systems, Inc., M86-E01078, Madison, WI, 2006.

[12] P. W. Betteridge, J. R. Carruthers, R. I. Cooper, K. Prout and D. J. Watkin, *J. Appl. Crystallogr.* , 2003, 36, 1487.

[13] I. J. Bruno, J. C. Cole, P. R. Edgington, M. K. Kessler, C. F. Macrae, P. McCabe, J. Pearson and R. Taylor, *Acta Crystallogr., Sect. B: Struct. Sci.*, 2002, 58, 389.

[14] C. F. Macrae, I. J. Bruno, J. A. Chisholm, P. R. Edgington, P. McCabe, E. Pidcock, L. Rodriguez-Monge, R. Taylor, J. van de Streek and P. A. Wood, *J. Appl. Crystallogr.*, 2008, 41, 466.

[15] H. J. Snaith, *Energy Environ. Sci.*, 2012, 5, 6513.

[16] H. J. Snaith, *Nat. Photonics*, 2012, 6, 337.

3 SPECTROELECTROCHEMISTRY

The spectroelectrochemistry of both H_2TPP and [Zn(TPP)] has been extensively studied[1] and the main processes are summarized in Scheme 3.1 . Over the entire redox range, H_2TPP can exist in five oxidation states, formally described as: H_2TPP^{2-}, H_2TPP^-, H_2TPP, H_2TPP^+ and H_2TPP^{2+}. Single-electron abstraction generates a π-radical cation, which automatically undergoes proton transfer to its tetra-protonated form H_2TPP^{2+}, evidence of which is the not complete back-conversion to H_2TPP once the potential is reverted. As anticipated, the double cation couldn't be isolated and studied, since rapid decomposition occurs (Scheme 3.1, entry a). When Zn^{II} is introduced in the cavity of H_2TPP, the resulting complex [Zn(TPP)] shows similar electrochemical behavior. Being the oxidation state +2 the most favorable for zinc, the metal center is not electroactive and all the processes involving [Zn(TPP)] can be considered as deriving uniquely from the porphyrin. With an ionic radius of 74 ppm[2, 3], the Zn^{2+} ion sits in the cavity and causes no ligand distortion; a factor that contributes to make its presence similar to that of the two protons in H_2TPP and renders the spectroelectrochemical behaviour similar (Scheme 3.1, entry c). For [Zn(TPP)], initial oxidation leads to a π-radical cation, the Soret band of which is blue-shifted and about half the intensity of the original Soret band. At the same time, the Q bands disappear and an absorption band with $\lambda_{max} \approx 650$ nm grows in. Since all of the nitrogen atoms are coordinating, the self-protonation step cannot take place and [Zn(TPP)]$^+$ can be reverted to [Zn(TPP)] without loss. Although [Zn(TPP)]$^+$ is stable on the experimental timescale, the second oxidation to [Zn(TPP)]$^{2+}$ is irreversible and the dication is transformed by further chemical reactions.

Moving our attention to reduction, H_2TPP can be reversibly reduced to its monoanion, while the dianion quickly decomposes (scheme 3.1, entry b). [Zn(TPP)] can be reduced to mono- and dianionic forms, the latter of which is only stable under rigorous experimental conditions (scheme 3.1, entry d). [Zn(TPP)]$^{2-}$ has been obtained by the reduction of [Zn(TPP)] with sodium, and its absorption spectrum has been recorded in THF (Soret band at 437 nm and Q bands at ~550 and ~600 nm)[4]. Spectroscopic changes associated with the reduction of [Zn(TPP)] include a red-shift, a decrease in intensity of the Soret band, and loss of the Q-bands in favor of a new band at ~800 nm (monoanion). Further reduction to the dianion leads to a new set of Q-bands and the disappearance of the absorption at 800 nm[1].
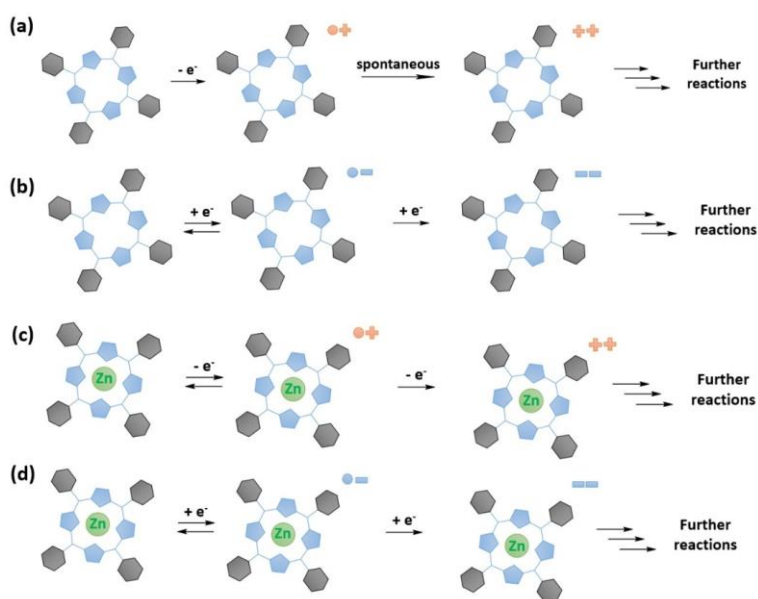
Scheme 3.1. Spectroelectrochemical behaviour of H_2TPP upon (a) oxidation and (b) reduction; [Zn(TPP)] upon (c) oxidation and (d) reduction.

3.1 Anodic Region

We commence the spectroelectrochemical discussion by presenting the results obtained from a study of a CH_2Cl_2 solution of compound **3**. Fig. 3.1 shows a superimposition of the absorption spectra of **3** recorded before and after an oxidative cycle, and the complete set of scans for the oxidative cycle. The irreversible changes are consistent with the literature data for [Zn(TPP)][1]. Initial oxidation leads to a π-radical cation, the Soret band of which is about half as intense as the original band, and the Q bands are replaced with an absorption with $\lambda_{max} \approx 650$ nm. The second oxidation leads to a dication which is unstable on the experimental timescale.
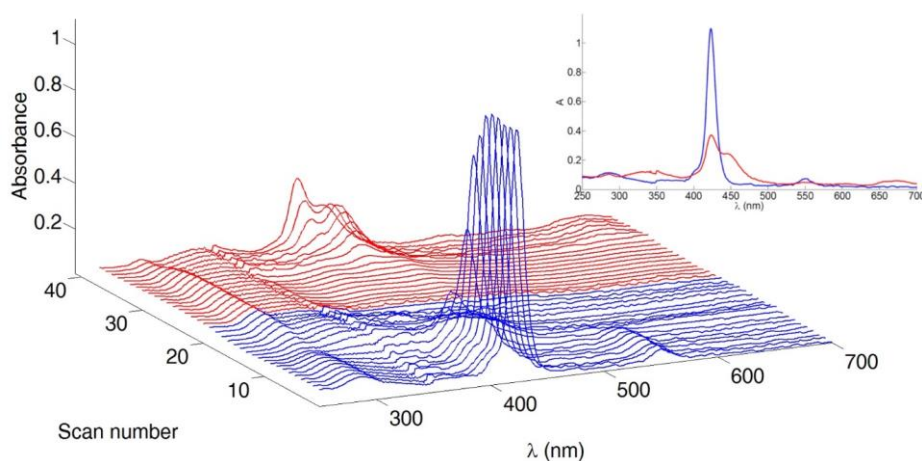
Figure 3.1 Spectroelectrochemical data for the oxidative cycle of **3** (≈ 1 mM in CH_2Cl_2, [$^nBu_4N$][PF_6] supporting electrolyte). A spectrum was recorded every 0.1 V, starting from 0 V (first blue line at the front) to +1.8 V (last blue line) and back to 0 V (last red line). The potential is referenced with respect to the Fc/Fc$^+$ couple with the same cell under the same experimental conditions. (inset) Absorption spectra before (blue line) and after (red line) the oxidative cycle.

For the homoleptic complexes [**M**(**3**)$_2$][PF$_6$]$_2$ with **M** = Zn, Fe or Ru, it was possible to oxidize the porphyrin moiety either reversibly or irreversibly, depending on the potential applied during the experiment. For potentials ≤1.3 V, the redox processes are almost completely reversible, while for peak-potentials >1.6 V it was not possible to return the complex to its initial state. We start by discussing the spectroelectrochemistry for both the irreversible and the reversible cases. Fig. 3.2 shows the absorption spectra of [Zn(**3**)$_2$][PF$_6$]$_2$ recorded before and after an oxidative cycle up to +2.0 V: the Soret band decreases in intensity and red-shifts as the potential is increased to more positive values. The figure depicts the set of 41 scans covering the oxidative cycle and the irreversible oxidation is consistent with that reported for [Zn(TPP)][1]. The Q bands disappear during the oxidation, and a new band develops at 667 nm (Fig. 3.2). The tpy-based absorption band is unchanged during the oxidation cycle. Fig. 3.3 shows the results of the spectroelectrochemistry if the scan is interrupted at +1.3 V and then reversed. The recovery of the absorption bands is almost complete and a partial decrease in the intensity of the Soret band is the only significant difference with respect to the initial spectrum.
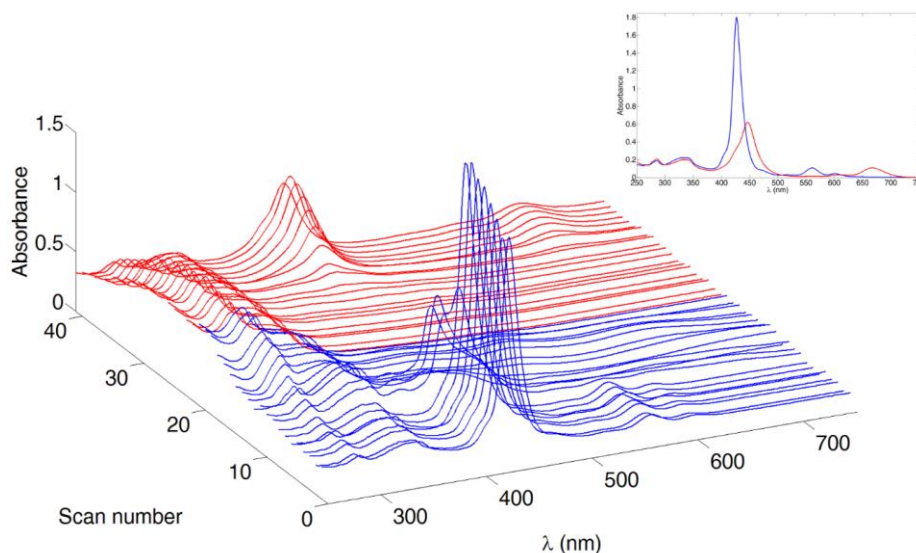
Figure 3.2 Spectroelectrochemical data for the oxidative cycle of [Zn(**3**)$_2$][PF$_6$]$_2$ (≈ 0.3 mM in MeCN, [^{n}Bu$_4$N][PF$_6$] supporting electrolyte). A spectrum was recorded every 0.1 V, starting from 0 V (first blue line at the front) to +2 V (last blue line) and back to 0 V (last red line). See caption to Fig. 3.1 for referencing to Fc/Fc$^+$. (inset) Absorption spectra before (blue line) and after (red line) the oxidative cycle.

Figure 3.3 Spectroelectrochemical data for the oxidative cycle of [Zn(**3**)$_2$][PF$_6$]$_2$ (≈ 0.3 mM in MeCN, [^{n}Bu$_4$N][PF$_6$] supporting electrolyte). A spectrum was recorded every 0.1 V, starting from 0 V (first blue line at the front) to +1.3 V (last blue line) and back to 0 V (last red line). See caption to Fig. 3.1 for referencing to Fc/Fc$^+$. (inset) Absorption spectra before (blue line) and after (red line) the oxidative cycle.

Fig. 3.4 shows the spectroelectrochemical data for the oxidative cycle of [Fe(**3**)$_2$][PF$_6$]$_2$ upon scanning from 0 to +2.0 V and back. The spectroscopic behavior of the [Zn(TPP)] moiety is comparable to that of [Zn(**3**)$_2$][PF$_6$]$_2$ discussed above. Upon oxidation, the Q bands are the first to disappear, followed by the MLCT band at 573 nm. The exact position for the MLCT maximum can only be found by analyzing one of the spectra in which the MLCT band is free of the Q band contributions. Reversing the potential, the reappearance of the MLCT band at 573 nm confirms the regeneration of the {Fe(tpy)$_2$}$^{2+}$ core. This is followed by the appearance of a new band at 666 nm. Both absorptions are present at the end of the experiment, indicating the generation of new stable chemical species. As for [Zn(**3**)$_2$][PF$_6$]$_2$, if the scan is interrupted at +1.3 V and then reversed, the redox processes involving the [Zn(TPP)] domain are reversible (Fig. 3.5).
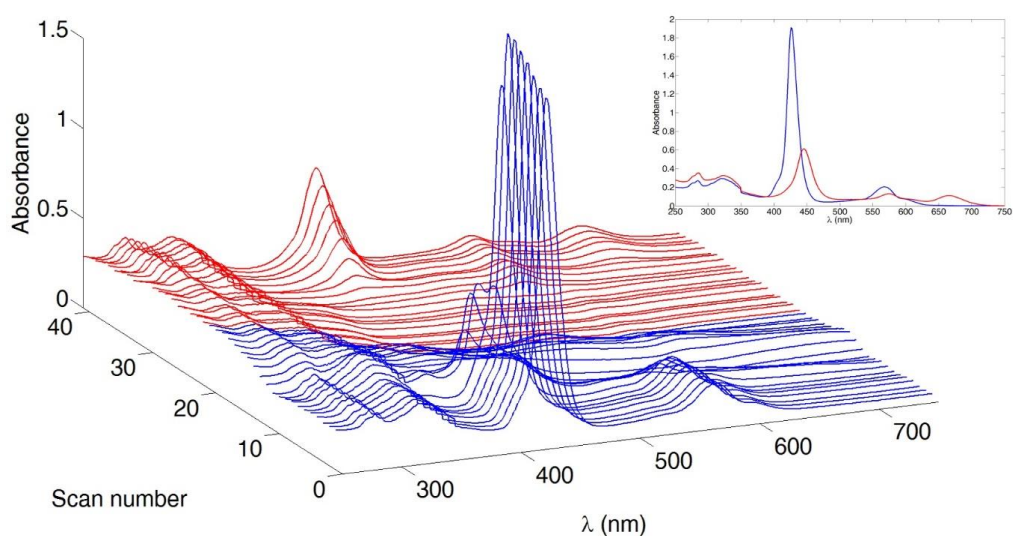
Figure 3.4 Spectroelectrochemical data for the oxidative cycle of [Fe(**3**)$_2$][PF$_6$]$_2$ (≈ 0.6 mM in MeCN, [^{n}Bu$_4$N][PF$_6$] supporting electrolyte). A spectrum was recorded every 0.1 V, starting from 0 V (first blue line at the front) to +2.0 V (last blue line) and back to 0 V (last red line). See caption to Fig. 3.1 for referencing to Fc/Fc$^+$. (inset) Absorption spectra before (blue line) and after (red line) the oxidative cycle.
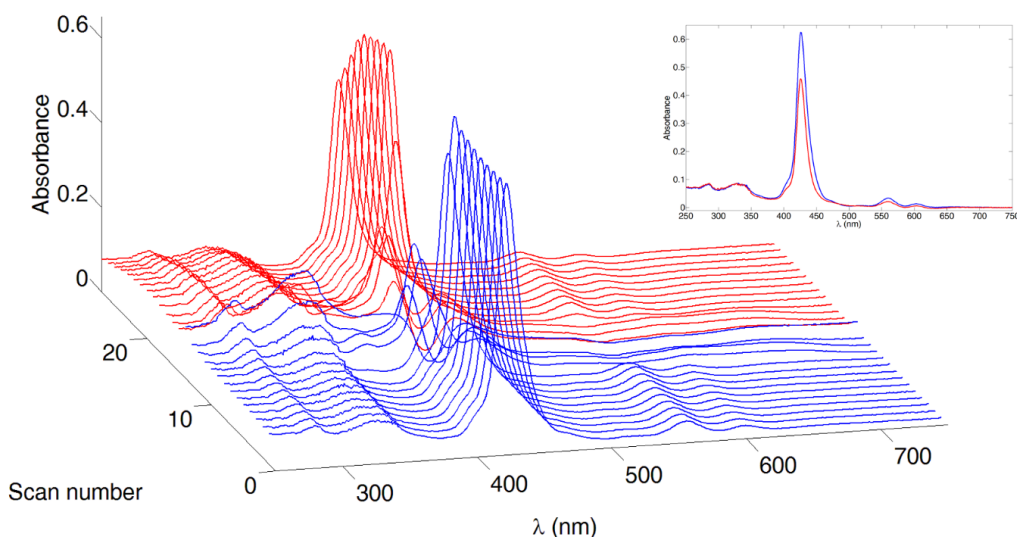
Figure 3.5 Spectroelectrochemical data for the oxidative cycle of [Fe(**3**)$_2$][PF$_6$]$_2$ (≈ 0.6 mM in MeCN, [^{n}Bu$_4$N][PF$_6$] supporting electrolyte). A spectrum was recorded every 0.1 V, starting from 0 V (first blue line at the front) to +1.3 V (last blue line) and back to 0 V (last red line). See caption to Fig. 3.1 for referencing to Fc/Fc$^+$. (inset) Absorption spectra before (blue line) and after (red line) the oxidative cycle.

The irreversible spectroelectrochemical oxidative cycle for [Ru(**3**)$_2$][PF$_6$]$_2$ is presented in Fig. 3.6. Reducing the potential window and reversing the scan at +1.3 V result in the changes presented in Fig. 3.7. The spectroscopic changes associated with the first oxidation involve the porphyrin, with the loss of Q bands, and a blue-shift (to 410 nm) and loss in intensity of the Soret band; the MLCT band at 495 nm is unchanged. In the second oxidation step both the Soret and the MLCT band are lost. Reversing the scan regenerates the MLCT band, with the Soret band appearing in its blue-shifted form. Bringing the potential back to the initial 0 V recovers the original Soret and Q bands, with intensities that compare well with those of the original spectrum (Fig. 3.7).
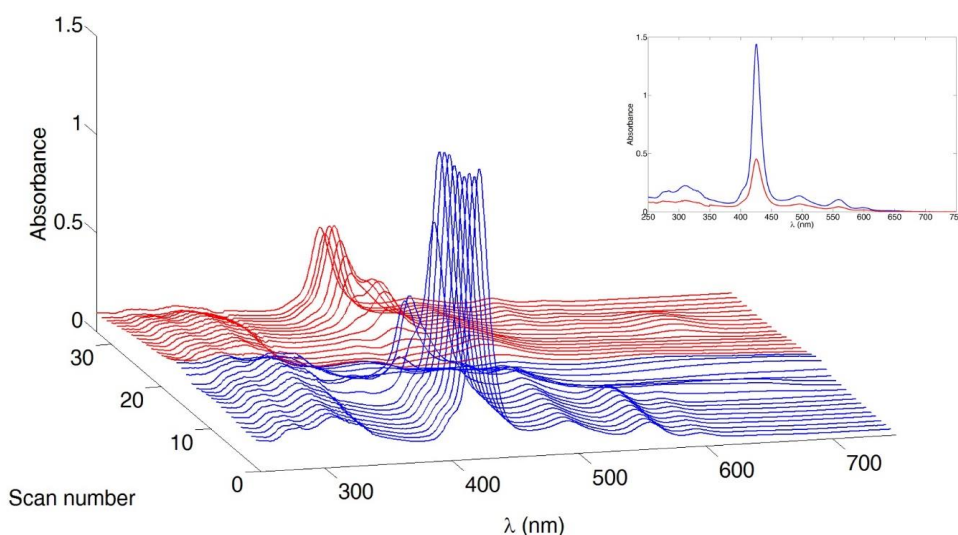
Figure 3.6 Spectroelectrochemical data for the oxidative cycle of [Ru(**3**)$_2$][PF$_6$]$_2$ (≈ 0.5 mM in MeCN, [^{n}Bu$_4$N][PF$_6$] supporting electrolyte). A spectrum was recorded every 0.1 V, starting from 0 V (first blue line at the front) to +1.6 V (last blue line) and back to 0 V (last red line). See caption to Fig. 3.1 for referencing to Fc/Fc$^+$. (inset) Absorption spectra before (blue line) and after (red line) the oxidative cycle.
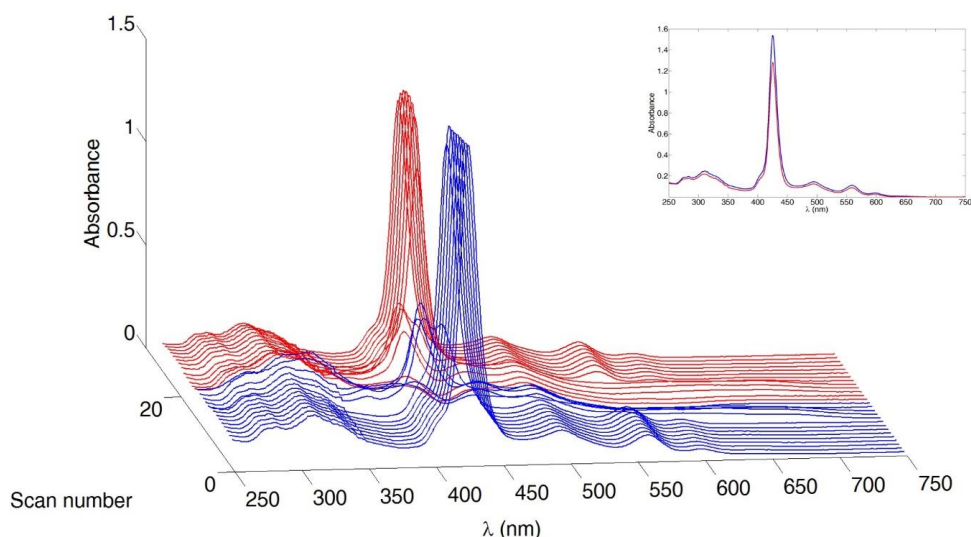
Figure 3.7 Spectroelectrochemical data for the oxidative cycle of [Ru(**3**)$_2$][PF$_6$]$_2$ ($\approx$ 0.5 mM in MeCN, [^{n}Bu$_4$N][PF$_6$] supporting electrolyte). A spectrum was recorded every 0.1 V, starting from 0 V (first blue line at the front) to +1.3 V (last blue line) and back to 0 V (last red line). See caption to Fig. 3.1 for referencing to Fc/Fc$^+$. (inset) Absorption spectra before (blue line) and after (red line) the oxidative cycle.
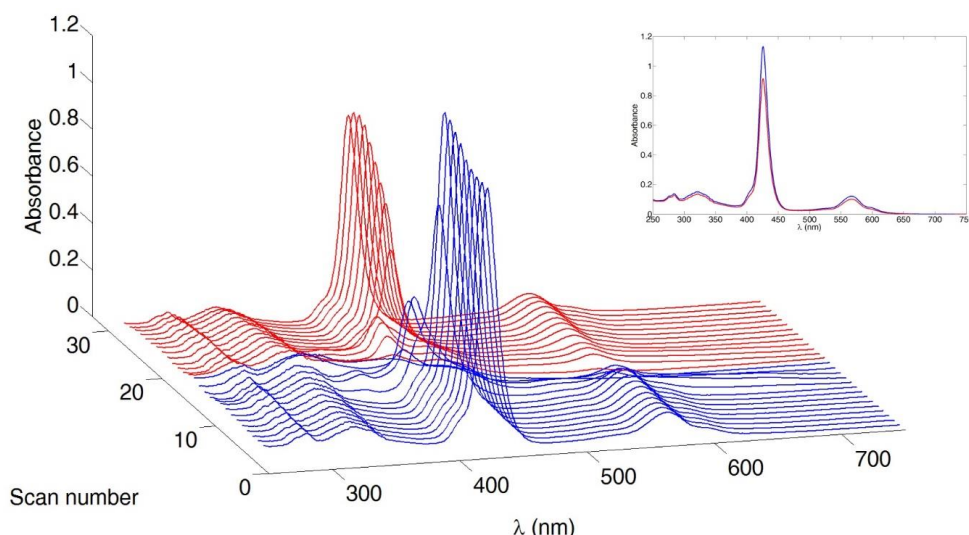
The oxidative cycle of the spectroelectrochemical measurements carried out on an MeCN solution of [Ru(**3**)(**4**)][PF$_6$]$_2$ are shown in Fig. 3.8. At the end of the oxidative cycle, the regeneration of the absorptions associated with the {Ru(tpy)$_2$}$^{2+}$ domain (the MLCT band at 492 nm, and the bands at 284 and 310 arising from the phenyltpy $\pi^* \leftarrow \pi$ transitions) confirms the reversibility of these processes. In contrast, the oxidation of the [Zn(TPP)] moiety within the complex is irreversible, the processes mimicking those of compound **3** with the exception that the band at 650 nm is now transient. This may be due to over-oxidation of the porphyrin core.
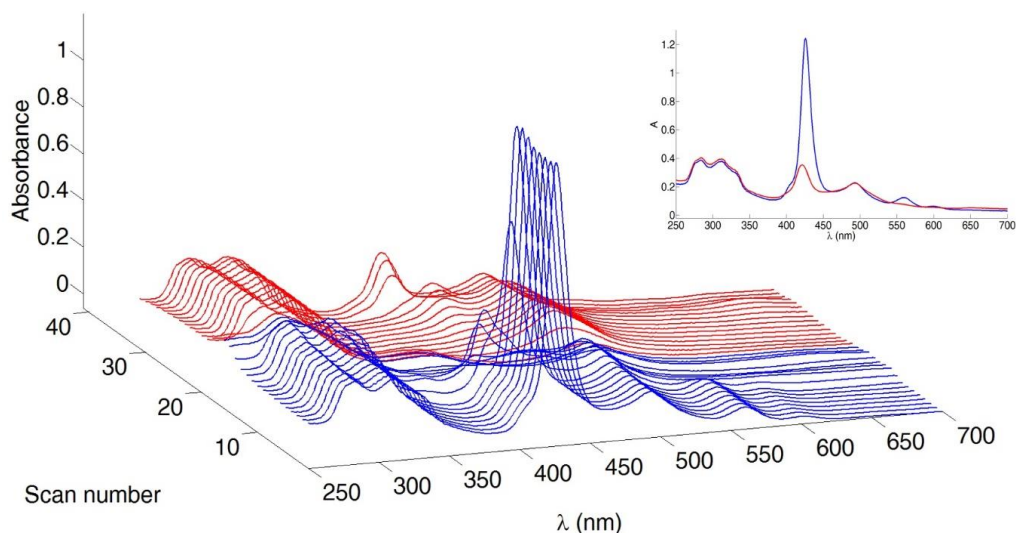
Figure 3.8 Spectroelectrochemical data for the oxidative cycle of [Ru(**3**)(**4**)][PF$_6$]$_2$ ($\approx$ 1 mM in MeCN, [^{n}Bu$_4$N][PF$_6$] supporting electrolyte). A spectrum was recorded every 0.1 V, starting from 0 V (first blue line at the front) to +1.5 V (last blue line) and back to 0 V (last red line). See caption to Fig. 3.1 for referencing to Fc/Fc$^+$. (inset) Absorption spectra before (blue line) and after (red line) the oxidative cycle.

3.2 Cathodic Region

In this section, we focus on the reduction processes, involving the porphyrin and the terpyridine unit. The results of the spectroelectrochemical reductive cycle for **3** are depicted in Fig. 3.9 and are again consistent with the literature data for [Zn(TPP)]. Fig. 3.10 shows the spectroelectrochemical measurement for [Zn(**3**)$_2$][PF$_6$]$_2$ during a reductive cycle from 0 to −2 V and back. The main electronic structural changes occur at the porphyrin unit and are consistent with the spectroscopic changes detailed above, with each [Zn(TPP)] domain in [Zn(**3**)$_2$][PF$_6$]$_2$ undergoing two reductions (Fig. 3.11). The doubly-reduced species is characterized by two broad bands centred at 562 and 613 nm (green spectrum in Fig. 3.11). A similar situation is observed for [Fe(**3**)$_2$][PF$_6$]$_2$ in a reductive cycle from 0 to −1.8 V (scans 1 to 19 in Fig. 3.12). Although the absorptions at 562 and 613 nm are at similar wavelengths and have similar relative intensities to those observed for a chlorin[5], the lack of a Soret band (Fig. 3.11) rules out the latter as a possible product of the reductive process. The spectral response upon reversing the potential from −2 to 0 V is different for [Zn(**3**)$_2$][PF$_6$]$_2$ and [Fe(**3**)$_2$][PF$_6$]$_2$. In the case of [Fe(**3**)$_2$][PF$_6$]$_2$, Fig. 3.12 shows that all absorptions are essentially lost confirming that the reduction is chemically irreversible. For [Zn(**3**)$_2$][PF$_6$]$_2$, the Q bands at 560 and 613 nm which are present at the limit of the reductive cycle disappear during the sweep from −1.8 to −2 V, whilst the absorption in the UV region undergoes a series of changes, but remains a dominant component in the spectrum (Fig. 3.13).
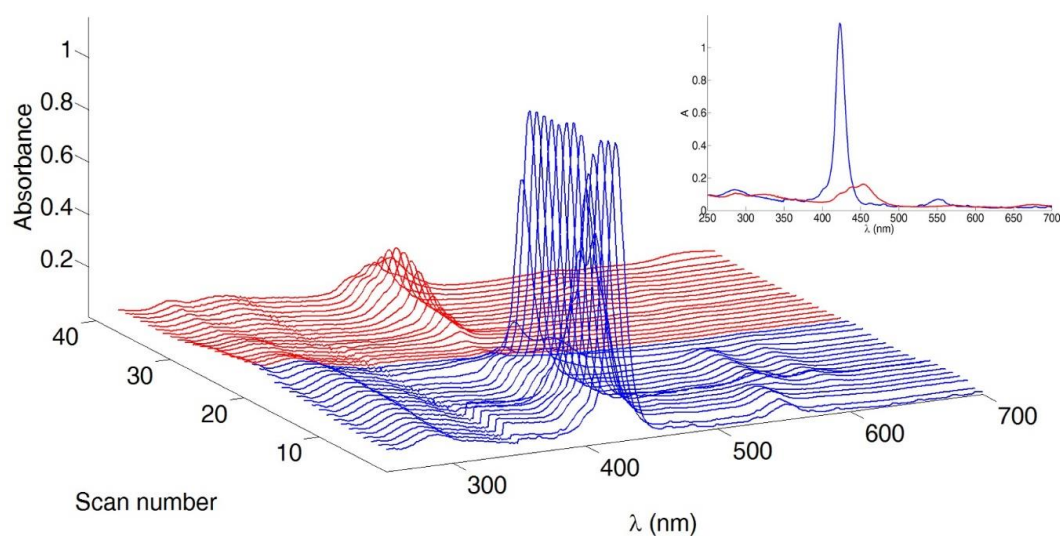
Figure 3.9 Spectroelectrochemical data for the reductive cycle of **3** (≈1 mM in CH$_2$Cl$_2$, [^{n}Bu$_4$N][PF$_6$] supporting electrolyte). A spectrum was recorded every 0.1 V, starting from 0 V (first blue line at the front) to -1.8 V (last blue line) and back to 0 V (last red line). See caption to Fig. 3.1 for referencing to Fc/Fc$^+$. (inset) Absorption spectra before (blue line) and after (red line) the reductive cycle.
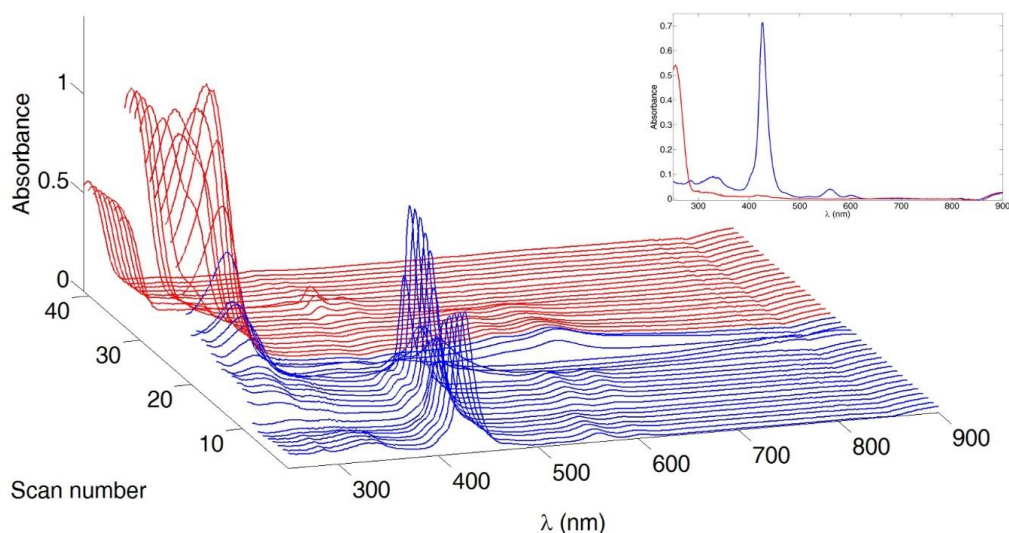
Figure 3.10 Spectroelectrochemical data for the reductive cycle of [Zn(**3**)$_2$][PF$_6$]$_2$ ($\approx$ 1 mM in MeCN, [^{n}Bu$_4$N][PF$_6$] supporting electrolyte). A spectrum was recorded every 0.1 V, starting from 0 V (first blue line at the front) to -2.0 V (last blue line) and back to 0 V (last red line). See caption to Fig. 3.1 for referencing to Fc/Fc$^+$. (inset) Absorption spectra before (blue line) and after (red line) the reductive cycle.

Figure 3.11 Absorption spectra of neutral [Zn(**3**)$_2$][PF$_6$]$_2$ (blue), its monoanion (red corresponding to scan number 18 (-1.7 V) in Fig. 3.10) and its dianion (green corresponding to scan number 21 (-2.0 V) in Fig. 3.10) in MeCN.
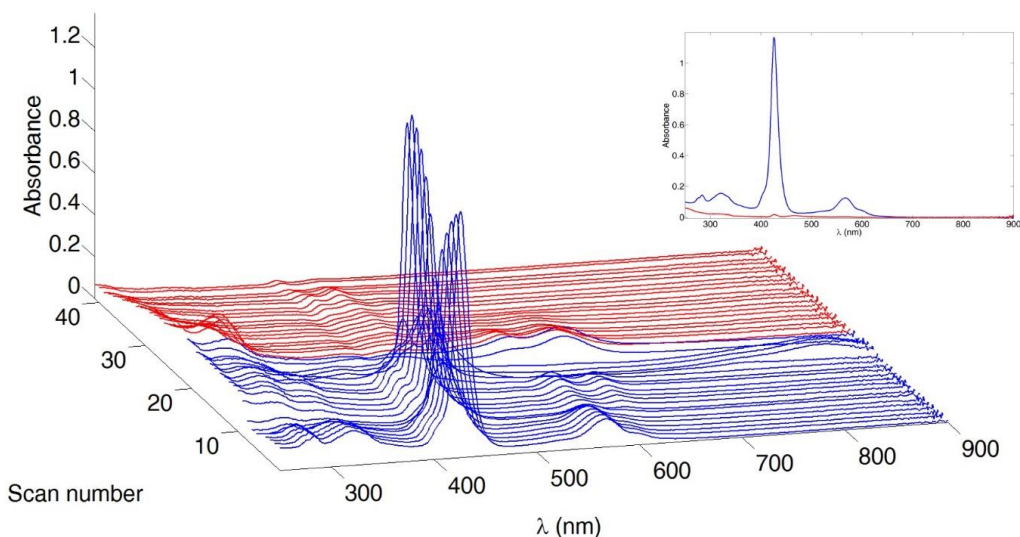
Figure 3.12 Spectroelectrochemical data for the reductive cycle of [Fe(**3**)$_2$][PF$_6$]$_2$ (≈ 1 mM in MeCN, [^{n}Bu$_4$N][PF$_6$] supporting electrolyte). A spectrum was recorded every 0.1 V, starting from 0 V (first blue line at the front) to -2.0 V (last blue line) and back to 0 V (last red line). See caption to Fig. 3.1 for referencing to Fc/Fc$^+$. (inset) Absorption spectra before (blue line) and after (red line) the reductive cycle.
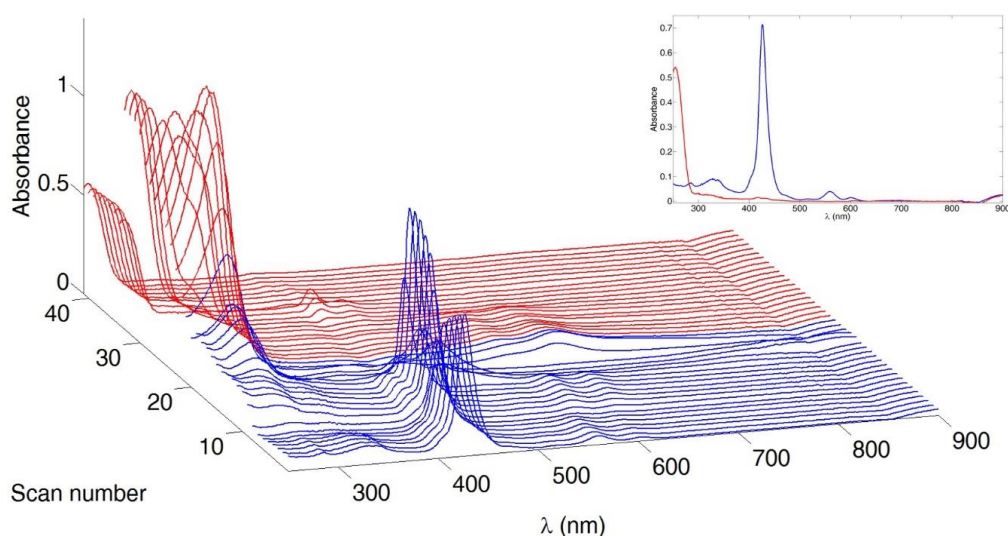
Figure 3.13 Spectroelectrochemical data for the reductive cycle of [Zn(**3**)$_2$][PF$_6$]$_2$ (≈ 1 mM in MeCN, [^{n}Bu$_4$N][PF$_6$] supporting electrolyte). A spectrum was recorded every 0.1 V, starting from 0 V (first blue line at the front) to -2.0 V (last blue line) and back to 0 V (last red line). See caption to Fig. 3.1 for referencing to Fc/Fc$^+$. (inset) Absorption spectra before (blue line) and after (red line) the reductive cycle.

The reductive processes for [Zn(**3**)$_2$][PF$_6$]$_2$ and [Fe(**3**)$_2$][PF$_6$]$_2$ are reversible if the potential cycle is reversed at −1.6 V (Fig. 3.14 and 3.15). The [Zn(TPP)] domains are reduced to their monoanionic forms and re-oxidized in a reversible manner. The original spectrum is recovered (albeit at a lower intensity, Fig. 3.14) for [Zn(**3**)$_2$][PF$_6$]$_2$ at the end of the cycle. In contrast, for [Fe(**3**)$_2$][PF$_6$]$_2$, the porphyrin-based absorption bands are redshifted (the Soret band shifts from 426 to 437 nm) and the shoulder of the Soret band at 405 nm becomes more distinct (Fig. 3.15) after the reduction cycle. The tpy-centred absorptions and the MLCT band at ~573 nm of [Fe(**3**)$_2$][PF$_6$]$_2$ are not regenerated after the reductive cycle. The MLCT band is completely lost at the end of the experiment, leaving only Q bands at 577 and 617 nm indicating that the ligand is irreversibly chemically modified.
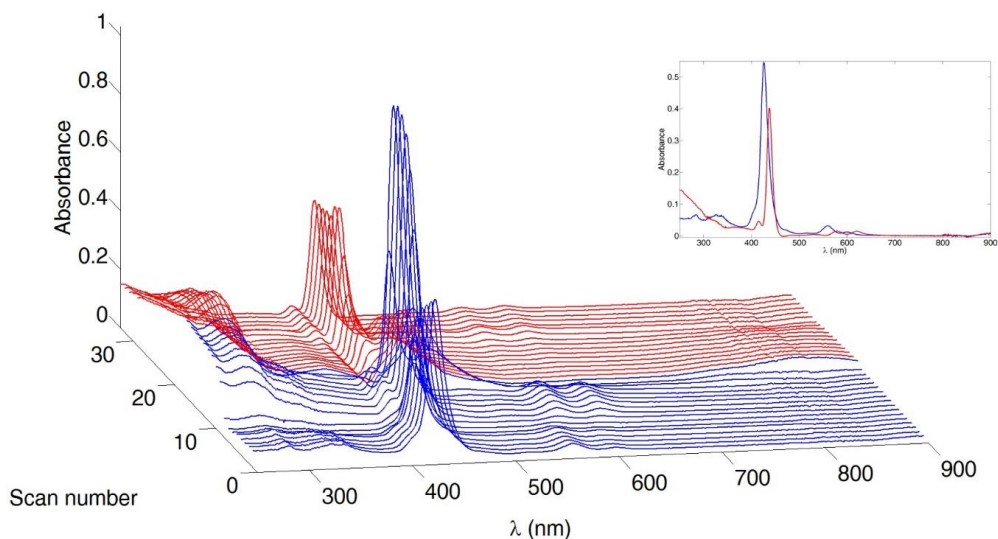
Figure 3.14 Spectroelectrochemical data for the reductive cycle of [Zn(**3**)$_2$][PF$_6$]$_2$ (≈ 1 mM in MeCN, [^{n}Bu$_4$N][PF$_6$] supporting electrolyte). A spectrum was recorded every 0.1 V, starting from 0 V (first blue line at the front) to - 1.6 V (last blue line) and back to 0 V (last red line). See caption to Fig. 3.1 for referencing to Fc/Fc$^+$. (inset) Absorption spectra before (blue line) and after (red line) the reductive cycle.
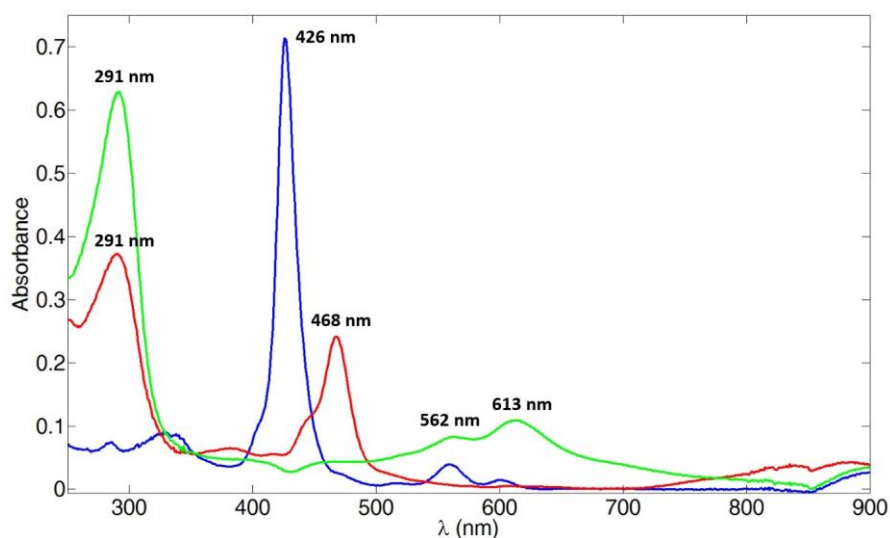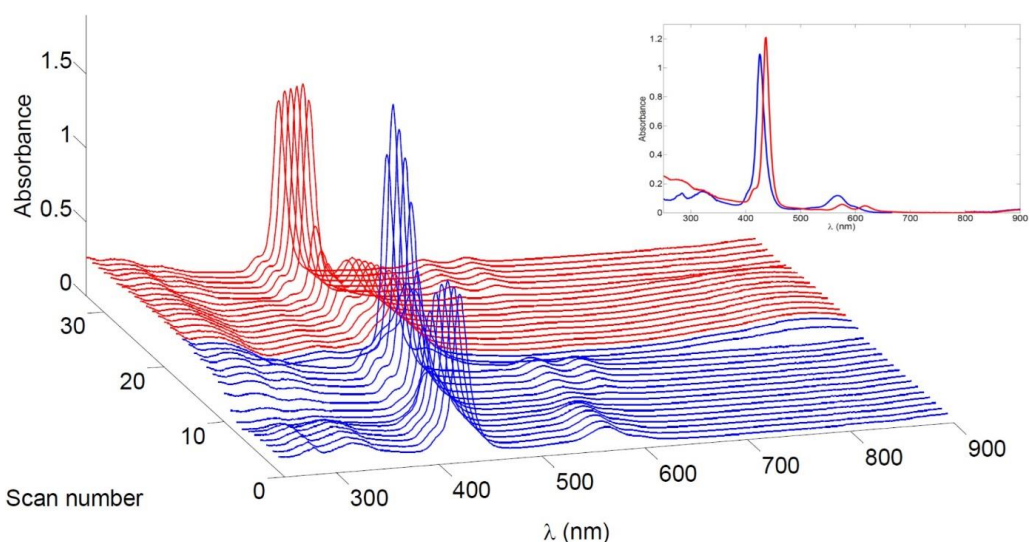

Figure 3.15 Spectroelectrochemical data for the reductive cycle of [Fe(**3**)$_2$][PF$_6$]$_2$ (≈ 1 mM in MeCN, [^{n}Bu$_4$N][PF$_6$] supporting electrolyte). A spectrum was recorded every 0.1 V, starting from 0 V (first blue line at the front) to - 1.6 V (last blue line) and back to 0 V (last red line). See caption to Fig. 3.1 for referencing to Fc/Fc$^+$. (inset) Absorption spectra before (blue line) and after (red line) the reductive cycle.

Fig. 3.16 shows the spectroelectrochemical response of [Ru(**3**)$_2$][PF$_6$]$_2$ during the reductive cycle when the potential is taken to −2 V. The irreversible changes are reminiscent of those for [Zn(**3**)$_2$][PF$_6$]$_2$, with an additional loss of the MLCT band at 495 nm. Fig. 3.17 displays the redox behaviour of [Ru(**3**)$_2$][PF$_6$]$_2$ in the cathodic region if the reduction cycle is reversed at −1.6 V. Between 0 and −0.6 V, the Soret band loses intensity and shifts towards the red (434 nm). In addition, there is a complete loss of tpy-based absorptions, as well as the MLCT and Q bands. Reduction between −0.6 and −1.3 V results in an enhancement of the Soret band (437 nm) and recovery of the Q bands. After reversing the scan, the Soret band again diminishes but is regenerated at ∼−0.6 V. The MLCT band is regenerated just before the scan is completed (Fig. 3.17). A comparison of Fig. 3.15 and 3.17 reveals a similar

relationship between the starting complex ([Fe(**3**)$_2$][PF$_6$]$_2$ or [Ru(**3**)$_2$][PF$_6$]$_2$) and the final product of the reductive cycle, with the exception of the different positions of the MLCT bands associated with the {Fe(tpy)$_2$}$^{2+}$ and {Ru(tpy)$_2$}$^{2+}$ domains.
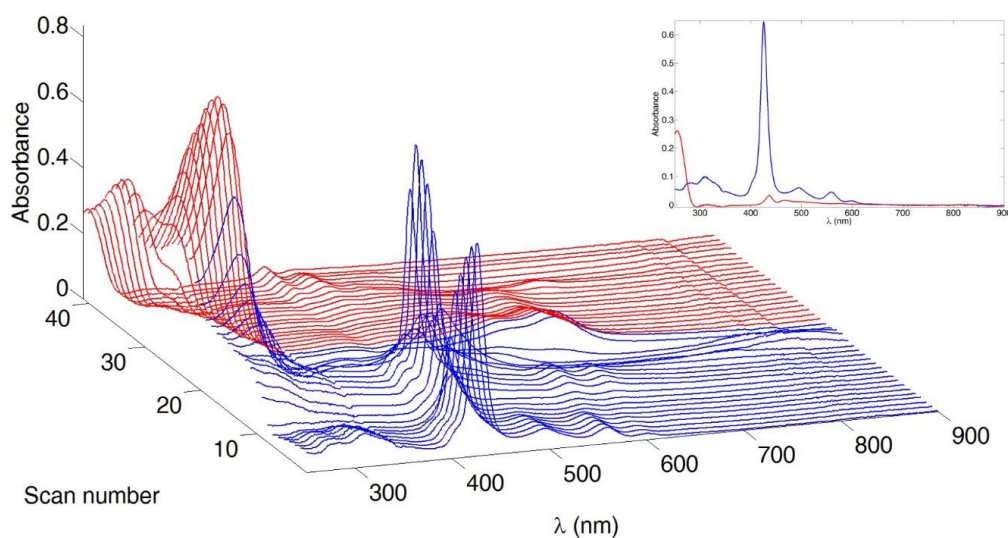
Figure 3.16 Spectroelectrochemical data for the reductive cycle of [Ru(**3**)$_2$][PF$_6$]$_2$ (≈ 1 mM in MeCN, [^{n}Bu$_4$N][PF$_6$] supporting electrolyte). A spectrum was recorded every 0.1 V, starting from 0 V (first blue line at the front) to -2.0 V (last blue line) and back to 0 V (last red line). See caption to Fig. 3.1 for referencing to Fc/Fc$^+$. (inset) Absorption spectra before (blue line) and after (red line) the reductive cycle.
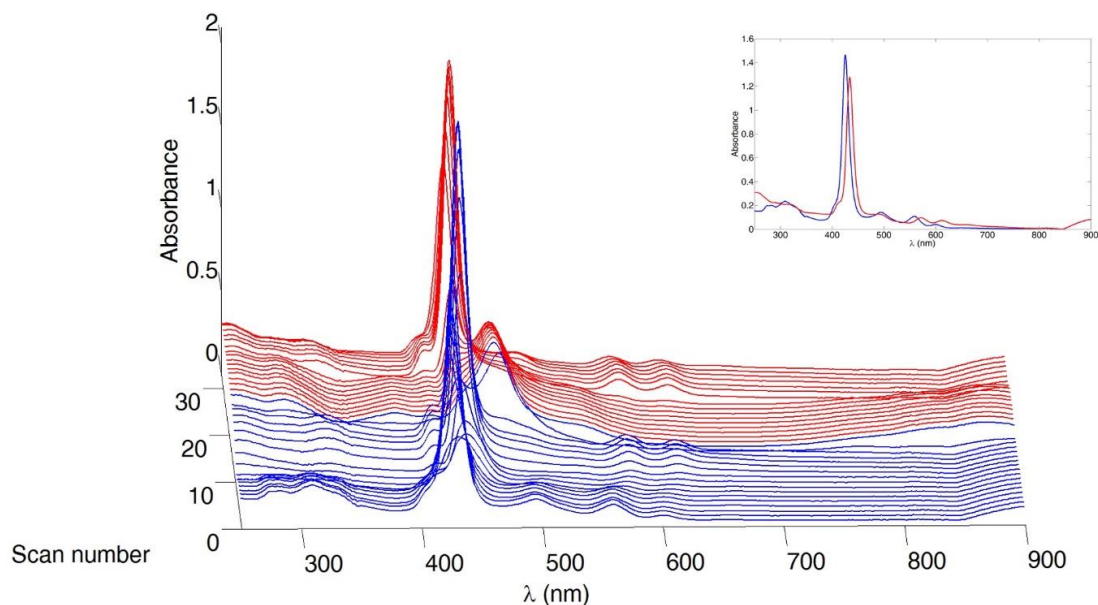
Figure 3.17 Spectroelectrochemical data for the reductive cycle of [Ru(**3**)$_2$][PF$_6$]$_2$ (≈ 1 mM in MeCN, [^{n}Bu$_4$N][PF$_6$] supporting electrolyte). A spectrum was recorded every 0.1 V, starting from 0 V (first blue line at the front) to -1.6 V (last blue line) and back to 0 V (last red line). See caption to Fig. 3.1 for referencing to Fc/Fc$^+$. (inset) Absorption spectra before (blue line) and after (red line) the reductive cycle.

During the reductive cycle of [Ru(**3**)(**4**)][PF$_6$]$_2$ (Fig. 3.18), the absorptions arising from both the porphyrin and {Ru(tpy)$_2$}$^{2+}$ domains are irreversibly transformed. The irreversible changes to the Soret and Q bands are consistent with those observed for **3** and [Zn(TPP)][1] while irreversible reduction processes centred on the phenyltpy units are responsible for the loss of the bands associated with the π*←π and MLCT transitions. Fig. 3.18 provides

evidence for a transient band between 800 and 900 nm, which can be assigned to the [3]$^{\bullet-}$ radical anion[6].
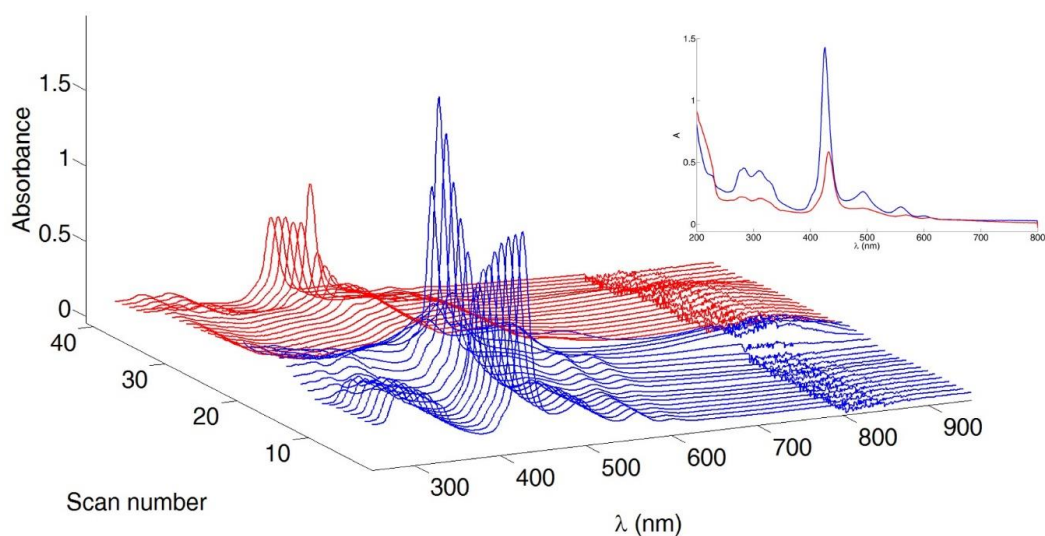
Figure 3.18 Spectroelectrochemical data for the reductive cycle of **3** ($\approx$ 1 mM in MeCN, [^{n}Bu$_4$N][PF$_6$] supporting electrolyte). A spectrum was recorded every 0.1 V, starting from 0 V (first blue line at the front) to -1.8 V (last blue line) and back to 0 V (last red line). See caption to Fig. 3.1 for referencing to Fc/Fc$^+$. (inset) Absorption spectra before (blue line) and after (red line) the reductive cycle.

References

[1] A. Klein, in *Spectroelectrochemistry*, ed. W. Kaim and A. Klein, Royal Society of Chemistry, Cambridge, 2008, ch. 4, p. 91.

[2] R. D. Shannon and C. T. Prewitt, *Acta Crystallogr.*, 1969, B25, 925-946.

[3] R. D. Shannon, *Acta Crystallogr.*, 1976, A32, 751-767.

[4] G. L. Closs and L. E. Closs, *J. Am. Chem. Soc.*, 1963, 85, 818.

[5] G. D. Dorough and F. M. Huennekens, *J. Am. Chem. Soc.*, 1952, 74, 3974.

[6] J. Pawlik, L. Gherghel, S. Karabunarliev and M. Baumgarten, *Chem. Phys.*, 1997, 221, 121.

4 DSCs parameters and transient absorption

Firstly, we focus our attention on the heteroleptic complex [Ru(**3**)(**4**)][PF$_6$]$_2$ and its possible application as a sensitizer in DSCs. Secondly, we discuss energy-transfer processes for the compounds **1**, **3** and [Ru(**3**)(**4**)][PF$_6$]$_2$ by means of emission spectroscopy. Finally, a more detailed investigation of energy-transfer is carried out by means of transient absorption spectroscopy (TA), both on [Ru(**3**)(**4**)][PF$_6$]$_2$ and homoleptic [Zn(**3**)$_2$][PF$_6$]$_2$, [Fe(**3**)$_2$][PF$_6$]$_2$ and [Ru(**3**)$_2$][PF$_6$]$_2$ complexes.

4.1 [Ru(3)(4)]$^{2+}$ as sensitizers in DSCs

Phosphonic acids are known to bind to nanoparticulate titania, and phosphonate esters as well proved to anchor through an esterification mechanism[1, 2]. According to the mechanism, hydroxyl groups, exposed on the titania surface, hydrolyze the ester at the connection P-OEt resulting in covalent links of the type P-O-Ti[3]. Confident that our dye [Ru(**3**)(**4**)]$^{2+}$ would anchor, we used solid state absorption spectroscopy to check whether or not a TiO$_2$ transparent electrode soaked in a solution of the dye had incorporated it. A first indication that the anchoring was successful came from the development of an intense orange color on the electrode surface, similar to that of an electrode soaked in a reference dye (N719) solution (Fig. 4.1). Anchoring imparts a redshift to the absorption bands of [Ru(**3**)(**4**)]$^{2+}$ with the absorption maxima shifting from 425, 492, 560 and 600 nm to 432, 500, 564 and 641 nm.
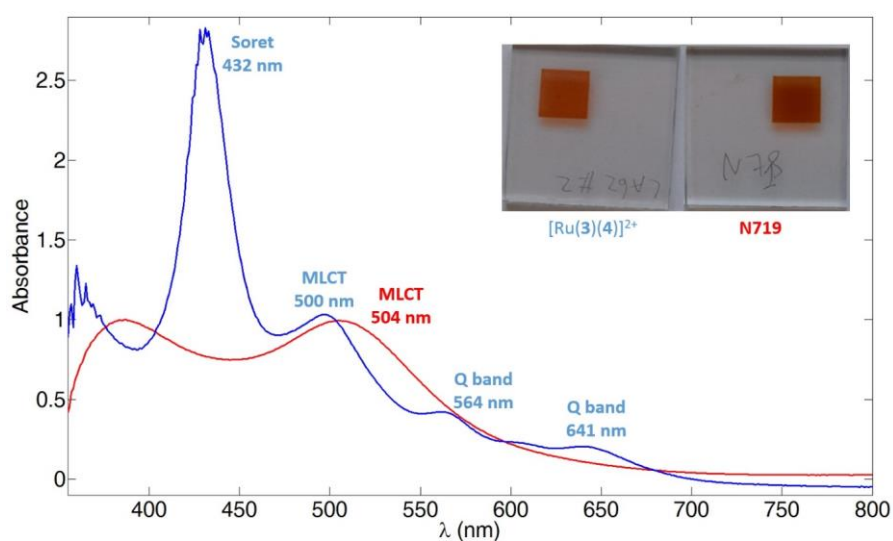
Figure 4.1 Solid-state absorption spectra of transparent TiO2 electrodes with dyes N719 (red) and [Ru(**3**)(**4**)]$^{2+}$ (blue). (inset) Photograph of the electrodes used for the measurement.

Encouraged by this positive result, and from the fact that absorption of [Ru(**3**)(**4**)]$^{2+}$ spans over a wider range than that of N719, we decided to build a solar cell based on [Ru(**3**)(**4**)]$^{2+}$. Photoanodes for n-type DSCs were made by immersion of FTO/TiO$_2$ electrodes in an MeCN solution of [Ru(**3**)(**4**)][PF$_6$]$_2$ for 3 days, and reference electrodes were made similarly using an EtOH solution of N719. DSCs were fabricated using an I$^-$/I$_3^-$ electrolyte (see Experimental section at the beginning) and were fully masked during measurements[4, 5]. Cells were built in duplicate to check for the reproducibility of performance parameters (summarized in Table 4.1). Despite the fact that the electrodes prepared with two different

dyes look the same by eye and one possesses an enhanced absorption, the photoconversion efficiency for $[Ru(\mathbf{3})(\mathbf{4})]^{2+}$ η is too low to be of any use. This disappointing result triggered our interest in gaining a deeper understanding of the energy-transfer processes that dissipate the energy gained through excitation.

Table 4.1 Performance parameters of duplicate DSCs with $[Ru(\mathbf{3})(\mathbf{4})]^{2+}$ and N719. Measurements were made on the day of DSCs fabrication. Isc short-circuit current, Voc open circuit voltage, ff filling factor, η conversion efficiency.

Dye	J_{SC}/mA cm^{-2}	V_{OC}/mV	ff/%	η/%
N719 (cell 1)	12.29	657	67	5.37
N719 (cell 2)	11.21	655	65	4.74
$[Ru(\mathbf{3})(\mathbf{4})]^{2+}$ (cell1)	0.10	333	52	0.02
$[Ru(\mathbf{3})(\mathbf{4})]^{2+}$ (cell1)	0.11	334	53	0.02

4.2 Emission spectroscopy as a probe for energy transfer

We start describing how energy flows in the model compound **1**. Its absorption and emission spectra are shown in Fig. 4.2, with the absorption displaying bands arising from $S_2 \leftarrow S_0$ and $S_1 \leftarrow S_0$ transitions and emission displaying the usual $S_1 \rightarrow S_0$ fluorescence and, interestingly, the rare $S_2 \rightarrow S_0$ transition. Normally, for an organic molecule, population of the S_2 excited state is followed by fast internal conversion to S_1[6], and the emission spectrum can be related to the radiative decay of the lowest excited state of same multiplicity (a principle generally known as Kasha's rule). [Zn(TPP)] is emissive from both the S_2 and S_1 states, although the fluorescence originating from the S_2 state has a much lower quantum yield and only a picosecond lifetime[7].

[Zn(TPP)] is one of very few molecule to disobey Kasha's rule, other exceptions being azulene and thiophosgene. In the case of azulene, the transition $S_1 \rightarrow S_0$ is so unfavorable that its quantum yield is of the order of 10^{-4}[8]. Thiophosgene, and in general thioketones, fluoresce from S_2 with high quantum yield in the gas phase, but poorly in solution[8]. For a review of the possible mechanism by which a molecule fluoresces from the S_2 state we suggest reference[9]. Excitation of **1** at 400 nm (into the Soret shoulder) results in the emission spectrum shown in Fig. 4.2 with fluorescence from both the S_2 (431 and 453 nm) and S_1 (607 and 659 nm) excited states. The assignments were confirmed from the excitation spectra (Fig. 4.3). Note that λ_{max} of the Soret band (425 nm) is too close to the emission λ_{max} of 431 and 453 nm from the S_2 fluorescence to observe these emissions using λ_{exc} = 425 nm. Excitation into the Q bands of **1** leads to the S_1 emissions at 607 and 659 nm; the excitation spectrum relative to this transition was recorded at 660 nm is displayed in Fig. 4.4.
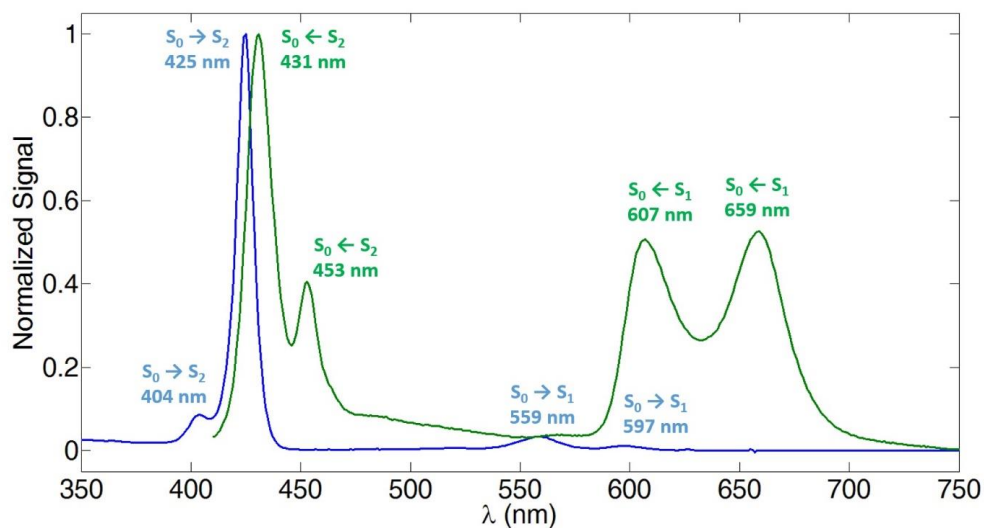
Figure 4.2 Normalized solution absorption (blue) and emission spectrum (green) of **1** (EtOH, 1 μM, λ_{exc}= 400 nm).
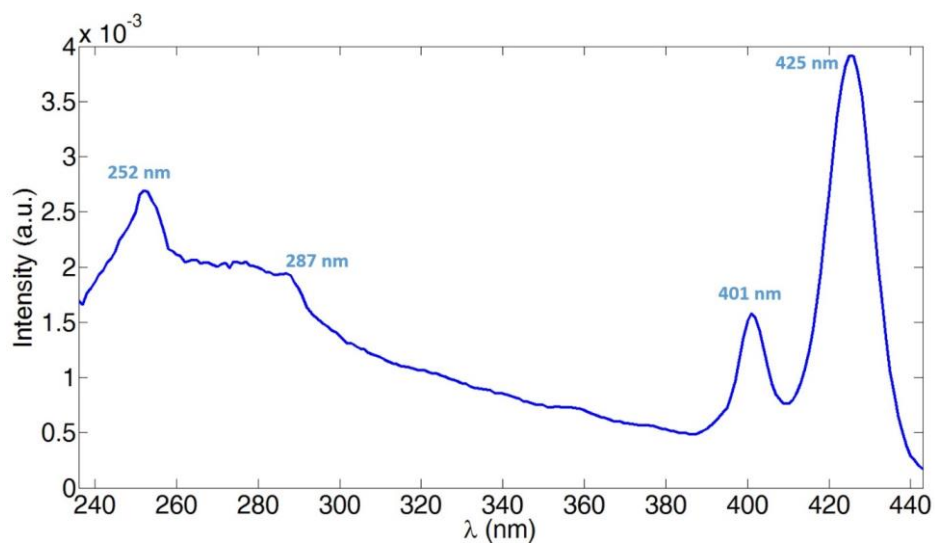
Figure 4.3 Excitation spectrum of **1** (EtOH, 1 μM) monitored at λ_{emi} = 453 nm ($S_2 \rightarrow S_0$ transition).
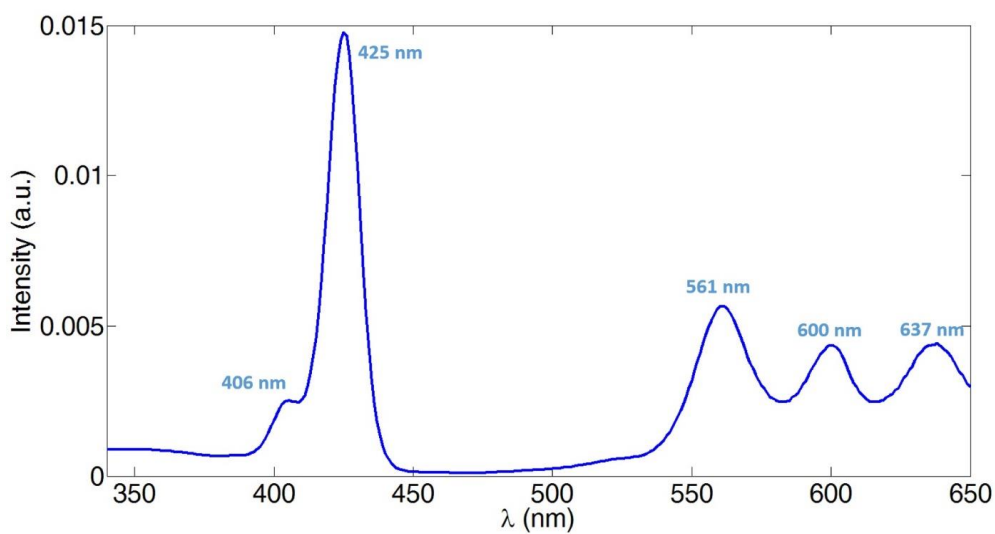
Figure 4.4 Excitation spectrum of **1** (EtOH, 1 μM) monitored at λ_{emi} = 660 nm ($S_1 \rightarrow S_0$ transition).

The emission spectrum of compound **3** does not display an S_2 fluorescence. Excitation into either the Soret or Q bands leads to emission at 613 and 660 nm. Interestingly it is possible to detect porphyrin fluorescence even upon exciting into the tpy bands (λ_{exc} = 285 and 320 nm) (Fig. 4.5). Since the tpy absorption is well separated from the porphyrin absorption bands, this is a clear indication of intramolecular energy transfer. The energetics of the system are favourable for an energy transfer from the (π– π *) tpy excited states (upper lying levels) to the S_2 state (lower level), followed by internal conversion to S_1 and radiative decay. Excitation spectra monitored at 560 and 600 nm confirm the presence of a broad peak centred at 285 nm, in agreement with the involvement of a tpy absorption in the population of the S_1 state (Fig. 4.6).
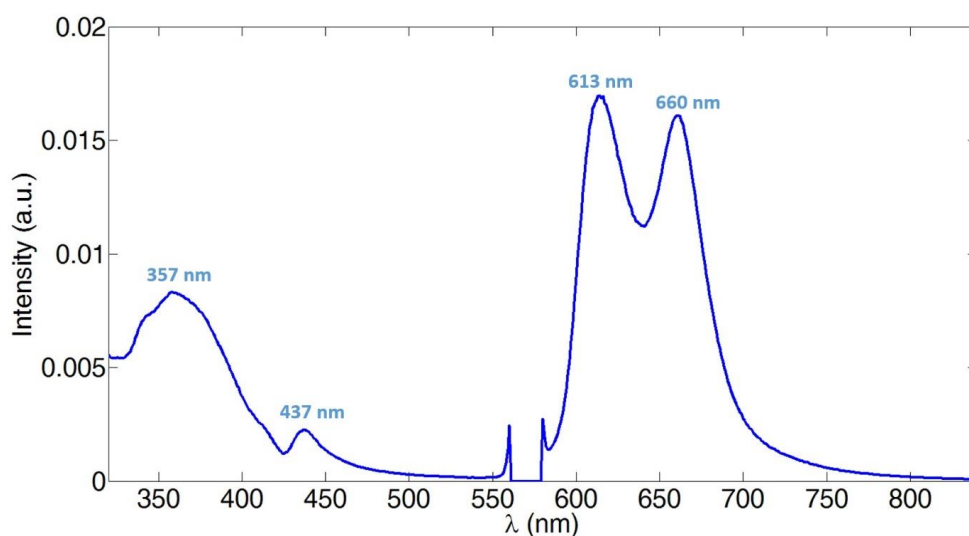
Figure 4.5 Emission spectrum of **3** (EtOH, 1 μM, λ_{exc}= 400 nm, tpy $\pi^* \leftarrow \pi$ transition). First harmonic at 570 nm has been removed
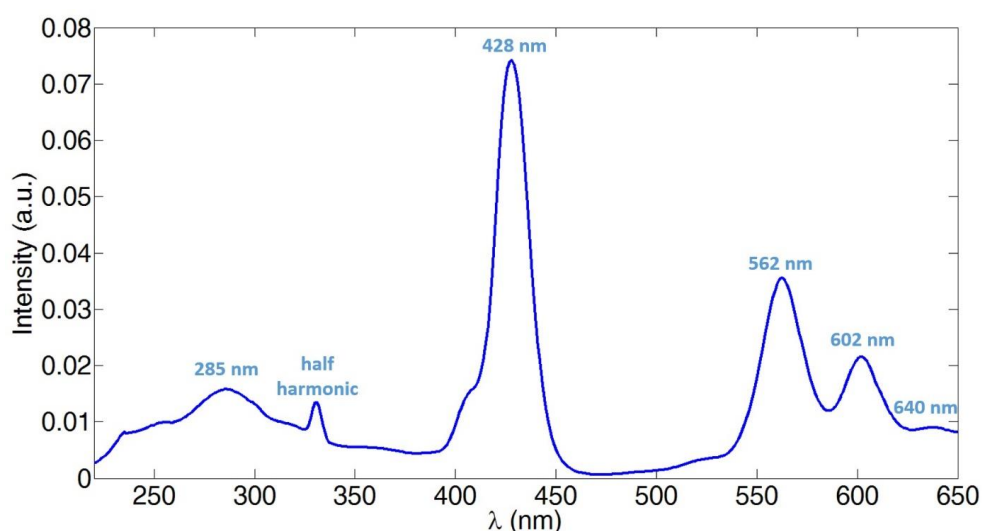
Figure 4.6 Excitation spectrum of **3** (EtOH, 1 μM) monitored at λ_{emi} = 660 nm ($S_1 \rightarrow S_0$ transition).

[Ru(**3**)(**4**)][PF$_6$]$_2$ exhibits an emission behaviour similar to that of **3**. Excitation into the tpy absorption bands (λ_{exc} = 284 and 310 nm) results in porphyrin fluorescence (emission λ_{max} = 613 and 661 nm, not shown). Moreover Fig. 4.7 shows that if the excitation is in the

MLCT band (λ_{exc} = 492 nm), emission is again observed from the S_1 state of the porphyrin. It was not possible to detect S_2 fluorescence by exciting into the shoulder of the Soret band.
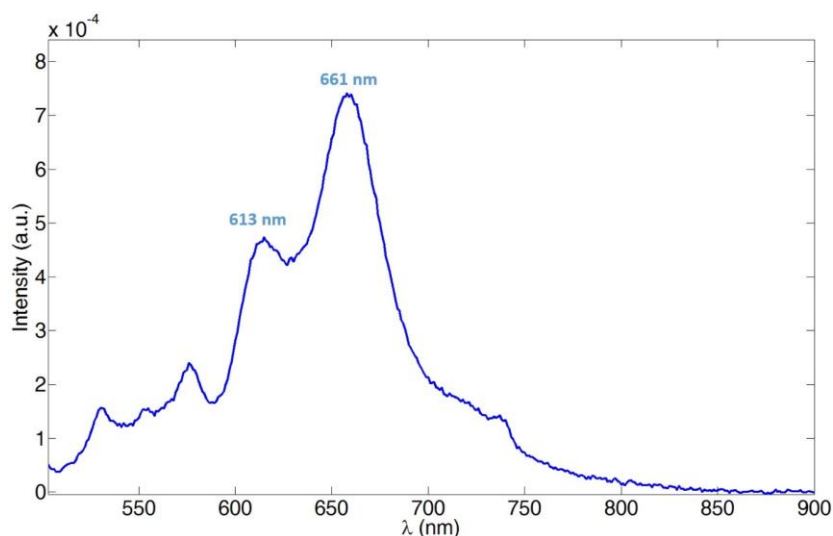
Figure 4.7 Solution emission spectrum of [Ru(**3**)(**4**)][PF$_6$]$_2$ (MeCN, 1 µM, λ_{exc} = 492 nm, ^{1}MLCT $\leftarrow$ S_0 transition).

4.3 Transient absorption spectroscopy

In order to further probe the emission behavior of [Ru(**3**)(**4**)][PF$_6$]$_2$, the transient absorption spectrum of the complex was recorded at room temperature. Upon excitation in the MLCT band (λ_{exc} = 532 nm), the transient absorption spectrum obtained resembles the characteristic triplet–triplet spectrum of [Zn(TPP)], first predicted by Gouterman[10] and later reported by Holten and coworkers[11]. Gouterman predicted two possible transitions from the porphyrin T_1 state: an intense allowed transition that would result in a doubly excited configuration and consists of two absorption peaks to lower energy of the Soret band, and a weak, forbidden transition in the near infrared (IR) leading to a highly excited singlet configuration (Scheme 4.1).
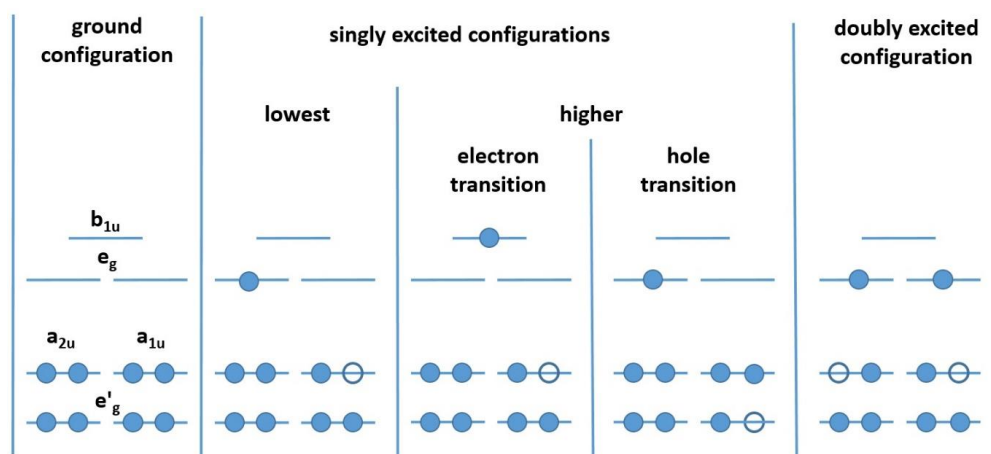
Scheme 4.1 Electron configurations for the circular box model of porphyrin. The solid circles are electrons; the empty circles are holes. In the first panel the symmetries of the molecular orbital are indicated.

The transient absorption spectrum of [Ru(**3**)(**4**)][PF$_6$]$_2$ has been recorded both on a nanosecond (Fig. 4.8) and picosecond setup (Fig. 4.9). The loss of the ground state porphyrin is clearly indicated by bleaching of the Soret band (425 nm) and of the Q(0, 1) and Q(0, 0) bands (560 and 600 nm). The broad bands at 470 and 500 nm are associated with absorption of the porphyrin T$_1$ state and creation of the doubly excited configuration. A broad absorption is present at lower energies, extending from 600 nm to the near-infrared region (NIR), in agreement with the literature spectrum [Holten]. The NIR transient absorption spectra of [Ru(**3**)(**4**)][PF$_6$]$_2$ are shown in Fig. 4.10. The band at 820 nm is associated with the forbidden, higher energy singlet which appears at 832 nm for [Zn(TPP)][11] in CH$_2$Cl$_2$. For [Ru(**3**)(**4**)][PF$_6$]$_2$, the NIR absorption was detected only in deaerated solution.
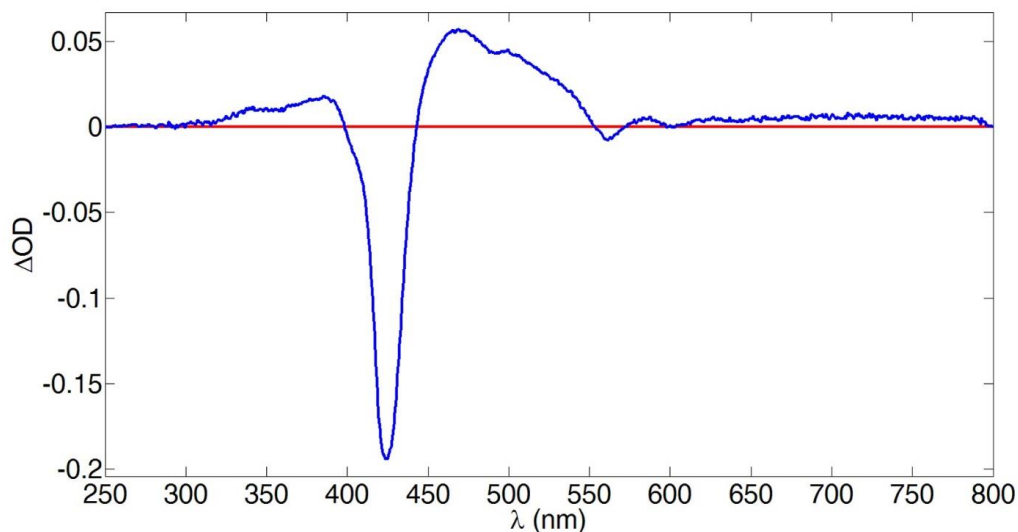
Figure 4.8 Transient absorption spectrum of [Ru(**3**)(**4**)][PF$_6$]$_2$ (MeCN, 2 µM, room temperature). λ_{exc} = 532 nm. Acquisition time 200 ns, 5 acquisitions without time delay. Red line indicates the value considered as baseline.
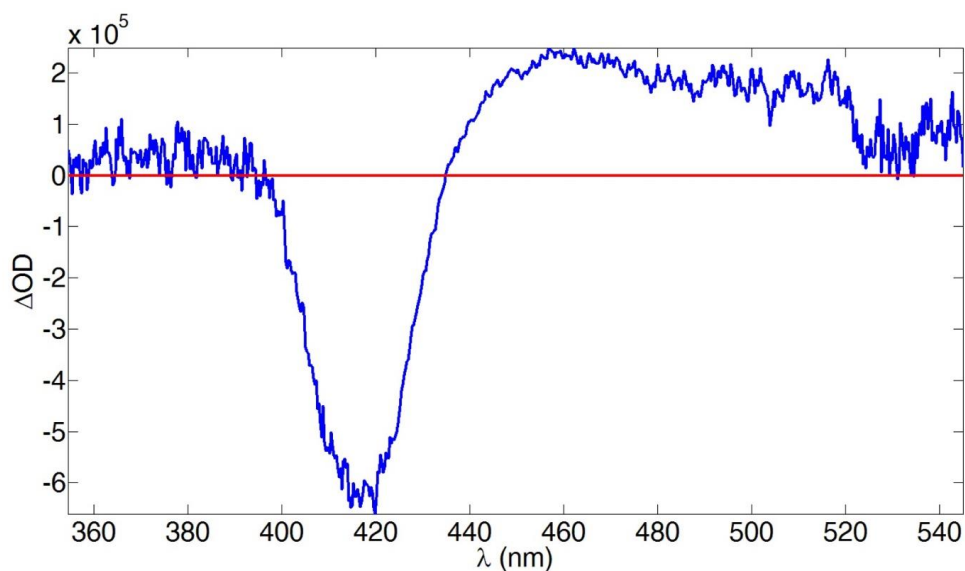
Figure 4.9 Transient absorption spectrum of [Ru(**3**)(**4**)][PF$_6$]$_2$ (MeCN, 2 µM, room temperature). λ_{exc} = 532 nm. Red line indicates the value considered as baseline.
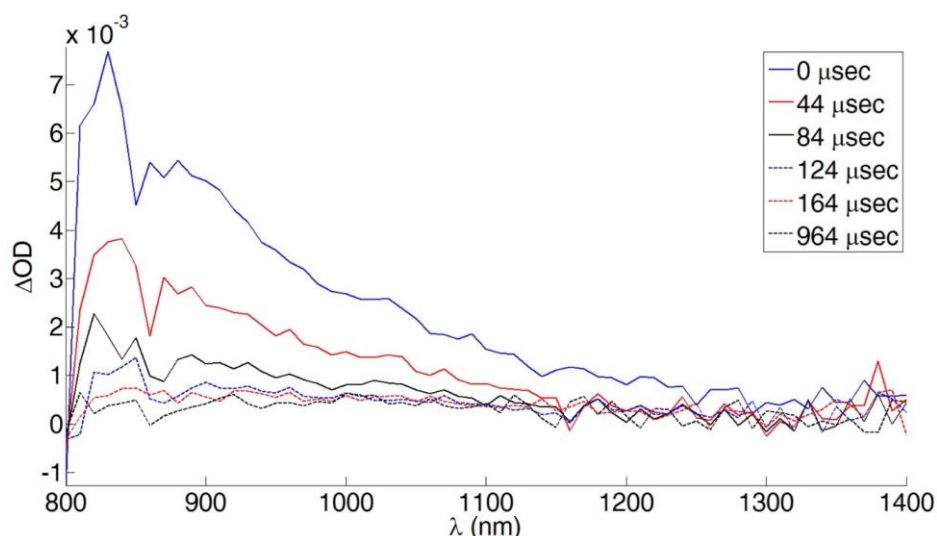
Figure 4.10 NIR transient absorption spectrum of [Ru(**3**)(**4**)][PF$_6$]$_2$ (MeCN, 2 µM, room temperature). λ_{exc} = 532 nm. The spectra were reconstructed from decay curves recorded every 10 nm.

The recovery of the ground state was monitored at 385, 425 and 470 nm for the aerated solution and at 385, 425, 470 and 820 nm for the deaerated one. As expected for a triplet state, the lifetimes ranged from hundreds of nanoseconds for the aerated solution to tens of microseconds for the deaerated one, due to the exclusion of a non-radiative deactivation pathway through reaction with triplet O$_2$. The decay curves (not shown) are consistent with a mono-exponential decay in all cases; the lifetimes for ground state recovery are: τ_{385} = 440 ± 40 ns and 59 ± 6 ms, τ_{425} = 420 ± 40 ns and 52 ± 5 ms, τ_{470} = 440 ± 40 ns and 48 ± 5 ms, τ_{820} = 49 ± 5 ms. Since all the lifetimes are consistent within experimental error, it is reasonable to assume that all observed transitions originate from a single chemical species which we propose to be the porphyrin T$_1$ state. Furthermore, we conclude that upon MLCT excitation, a triplet-to-triplet energy transfer occurs from the ^{3}MLCT level to T$_1$, the latter being the lowest accessible level for [Ru(**3**)(**4**)][PF$_6$]$_2$.

To precisely assess the triplet-to-triplet energy transfer rate constant (k$_{TTET}$) for [Ru(**3**)(**4**)][PF$_6$]$_2$, the compound was sent to Professor Evan Moore at Queensland University who has recorded its femtosecond transient absorption spectrum (data not shown). His analysis shows that the fitting of the kinetic traces require a three-exponential model. A lifetime of 1.86 ± 0.03 ps is associated with vibrational cooling and/or solvent reorganisation of the ^{3}MLCT state, after which the porphyrin T$_1$ state quenches the ^{3}MLCT state with a rate constant of 3.2 x 10^{10} s^{-1}, equivalent to a lifetime of 30.2 ± 0.1 ps. Finally, a lifetime of 422 ns refers to T$_1$ relaxation to the ground state.

The literature contains a number of molecular triads and dyads related to [Ru(**3**)(**4**)][PF$_6$]$_2$ (Scheme 4.2)[12]. When the triad (Scheme 4.2a) reported by Benniston et al.[13] is excited in the MLCT band, the ^{3}MLCT emission is quenched in favour of a triplet-to-triplet energy transfer to the porphyrin T$_1$ state. The lifetime of T$_1$ was determined to be 65 ± 5 ms with a triplet-to-triplet energy transfer rate constant of 8 x 10^{10} s^{-1}. A Dexter type mechanism of energy transfer[14] was proposed, and it is significant that excitation into the Q band resulted in a decreased S1 fluorescence. Benniston et al.[15] rationalize this in terms of singlet (S$_1$) to triplet (^{3}MLCT) energy transfer (k = 4 x 10^8 s^{-1}), involving an endergonic Dexter type mechanism (a process that is spin-forbidden). In the osmium-containing dyad in Scheme 4.2b, excitation in the Soret band leads to direct transfer to the ^{3}MLCT state[14, 16]

followed by triplet-to-triplet energy transfer to T_1. A high rate constant for porphyrin fluorescence quenching again accounts for complete energy transfer. In oligopyridine complexes, the excited MLCT state is localized on one of the ligands[17], and Benniston et al. argue that the energy flows from S_1 to the tpy domain directly connected to the porphyrin. In addition, if the second tpy in the complex lacks an extended π-system in the 4-position of the central pyridine ring, the electronic energy can be considered to reside on the porphyrin-bearing tpy because the intra-ligand energy transfer would not be as fast as that of energy transfer to the porphyrin triplet state. The overall effect is an intersystem crossing involving the porphyrin unit, involving the {Ru(tpy)$_2$}$^{2+}$ domain. For the triad reported by Flamigni et al. (Scheme 4.2c)[18], the energy transfer rate constant for the triplet-to-triplet transfer is >5 x 10^{10} s^{-1} consistent with a fast and quantitative quenching of the ruthenium-containing manifold. Once again the fluorescence originating from S_1 in quenched in favour of population of the ^{3}MLCT.
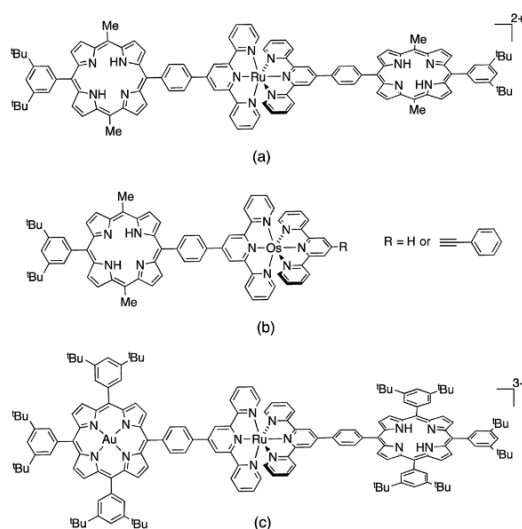
Scheme 4.2 Triads and dyads related to [Ru(**3**)(**4**)][PF$_6$]$_2$ and reported by (a) and (b) Benniston et al.[14, 15] and (c) Flamigni et al.[18].

Scheme 4.3a shows the relative energies of the tpy, MLCT and {Zn(TPP)} singlet and triplet states of [Ru(**3**)(**4**)]$^{2+}$. The energy of the tpy domain was obtained by plotting the normalized absorption and emission spectra (λ_{exc} = 284 and 310 nm) of [Ru(**3**)(**4**)][PF$_6$]$_2$, expressed in wavenumbers and searching for a crossing point which corresponds to the (0, 0) transition. The values obtained were 345 and 353 nm, corresponding to 3.59 and 3.51 eV. An average value of 3.55 eV has been adopted for the tpy level. The {Zn(TPP)} S_2 level was obtained with the aforementioned procedure using spectra of **1**. A value of 427 nm (2.90 eV) was obtained. The {Zn(TPP)} S_1 level was calculated from spectra of [Ru(**3**)(**4**)][PF$_6$]$_2$, and searching for the crossing point between the Q(0, 0) bands. This gave a value of 596 nm (2.08 eV). The ^{1}MLCT energy level was derived from the UV-Vis maximum of [Ru(**3**)(**4**)][PF$_6$]$_2$, and the ^{3}MLCT level from the emission maximum of the analogous [Ru(pytpy)$_2$][PF$_6$]$_2$ (pytpy = 4'-(4-pyridyl)-2,2':6',2''-terpyridine) in MeCN (655 nm[19], 1.89 eV) since the ^{3}MLCT state of [Ru(**3**)(**4**)][PF$_6$]$_2$ is not emissive at room temperature in solution. Contrary to other [Ru(4'-Xtpy)$_2$]$^{2+}$ complexes, the emission of which are weak but detectable[20], [Ru(**3**)(**4**)][PF$_6$]$_2$ exhibits emission behavior centered on the porphyrin moiety when irradiating at 532 nm due to energy transfer to [Zn(TPP)] S_1 once the ^{3}MLCT state is populated. Finally, the {Zn(TPP)} T_1 energy (770 nm[21] corresponding to 1.61 eV) was obtained from the literature

data. The relative energies of the states allow us to propose the energy transfer process shown in Scheme 4.3b. Upon ^{1}MLCT excitation, fast intersystem crossing to ^{3}MLCT occurs. Triplet-to-triplet energy transfer takes place with a rate constant $>2 \times 10^{10}$ s^{-1} (Scheme 4.3b), leading to the {Zn(TPP)} T_1 state. By deactivation of this state the ground state is recovered.
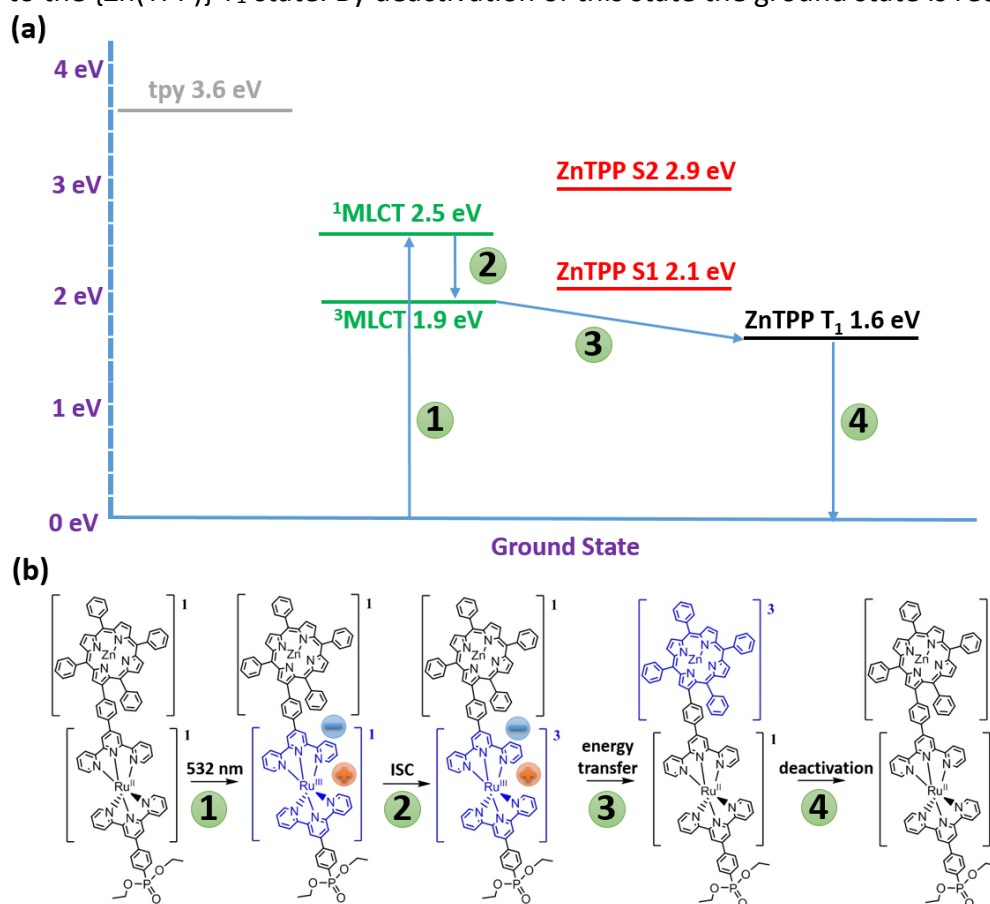
Scheme 4.3 (a) Energetic level diagram for [Ru(**3**)(**4**)][PF$_6$]$_2$ (b) energy-transfer scheme upon ^{1}MLCT excitation at 532 nm in [Ru(**3**)(**4**)][PF$_6$]$_2$. For the middle species in the scheme, the negative charge could be on either tpy domain. ISC = intersystem crossing.

Acetonitrile solutions of [Zn(**3**)$_2$][PF$_6$]$_2$ and [Fe(**3**)$_2$][PF$_6$]$_2$ were excited at 550 nm (corresponding to the Q(1,0) transition), while [Ru(**3**)$_2$][PF$_6$]$_2$ was excited at 532 nm. The transient absorption spectrum of [Zn(**3**)$_2$][PF$_6$]$_2$ is presented in Fig. 4.11. This correlates well with the triplet–triplet spectrum of [Zn(TPP)][10, 11]. A broad absorption is present at low energy, extending from 600 to 800 nm, in agreement with the literature spectrum[11]. Another fingerprint of the T_1 state is a weak forbidden transition in the near infra-red (832 nm) region. It was not possible to record such a signal in the transient absorption spectra of either [Zn(**3**)$_2$][PF$_6$]$_2$ or [Fe(**3**)$_2$][PF$_6$]$_2$, but it is visible in the spectrum of a deaerated solution of [Ru(**3**)$_2$][PF$_6$]$_2$ (Fig. 4.12). The transient absorption spectrum for [Fe(**3**)$_2$][PF$_6$]$_2$ (Fig. 4.13) was similar to that of [Zn(**3**)$_2$][PF$_6$]$_2$. Excitation was performed at 550 nm, where both Fe(II)-MLCT and Q(0,1) bands absorb. The iron(II) ^{3}MLCT state is known to rapidly deactivate through ^{3}MC d-states[22, 23]. Hence, it is reasonable to assume that the resulting triplet–triplet spectrum is solely due to absorption by the Q-band.

The transient absorption spectrum of an MeCN solution of [Ru(**3**)$_2$][PF$_6$]$_2$ is shown in Fig. 4.14. Excitation at 532 nm resulted in an excited state species arising from absorption in the MLCT band of the complex. As for the other complexes, the triplet–triplet spectrum of a [Zn(TPP)] species results. In the case of [Ru(**3**)$_2$][PF$_6$]$_2$, the final T_1 state is populated through

a triplet-to-triplet energy transfer from the Ru(II)-^{3}MLCT state. A rate constant for the transfer could not be determined, since it was faster than the instrumental time resolution. A comparison can, however, be made with the transient absorption spectrum of [Ru(**3**)(**4**)][PF$_6$]$_2$; this complex also contains a [Zn(TPP)] moiety conjugated to a {Ru(tpy)$_2$}$^{2+}$ unit. For [Ru(**3**)(**4**)][PF$_6$]$_2$, the energy transfer is faster than the resolution of a picosecond setup, i.e. <50 ps[24]. This precludes more detailed mechanistic investigations.
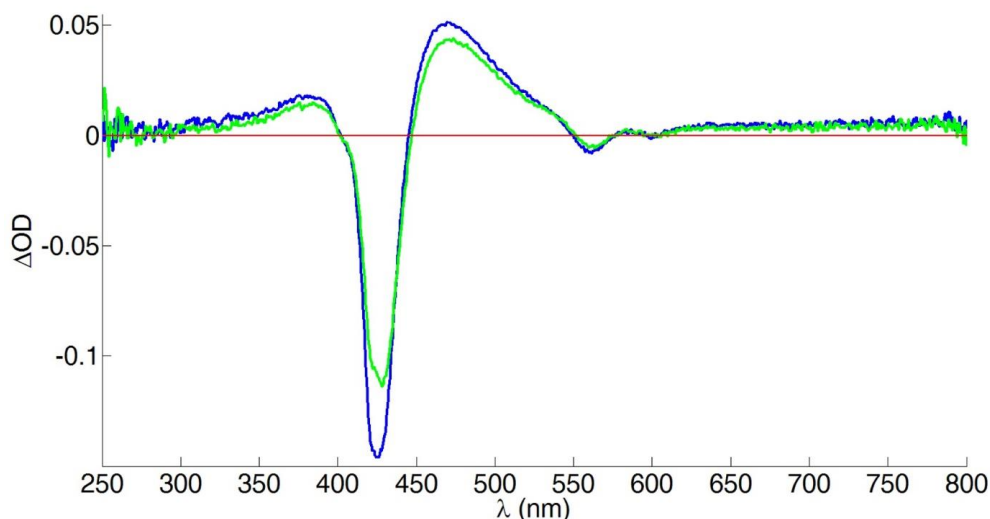
Figure 4.11 Transient absorption spectrum of [Zn(**3**)$_2$][PF$_6$]$_2$ (MeCN, ≈2 μM, room temperature). λ_{exc} = 550 nm. Acquisition time 200 ns, 5 acquisitions. Red line indicates the value considered as baseline. Blue line, deaerated solution; green line, air-equilibrated solution.
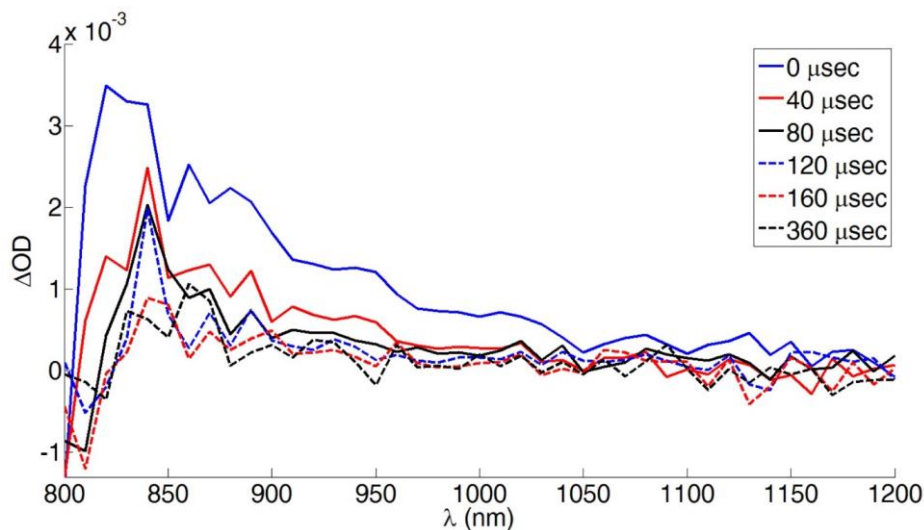
Figure 4.12 NIR transient absorption spectrum of [Ru(**3**)$_2$][PF$_6$]$_2$ (MeCN, ≈2 μM, room temperature). λ_{exc} = 532 nm. The spectra were reconstructed from decay curves recorded every 10 nm.
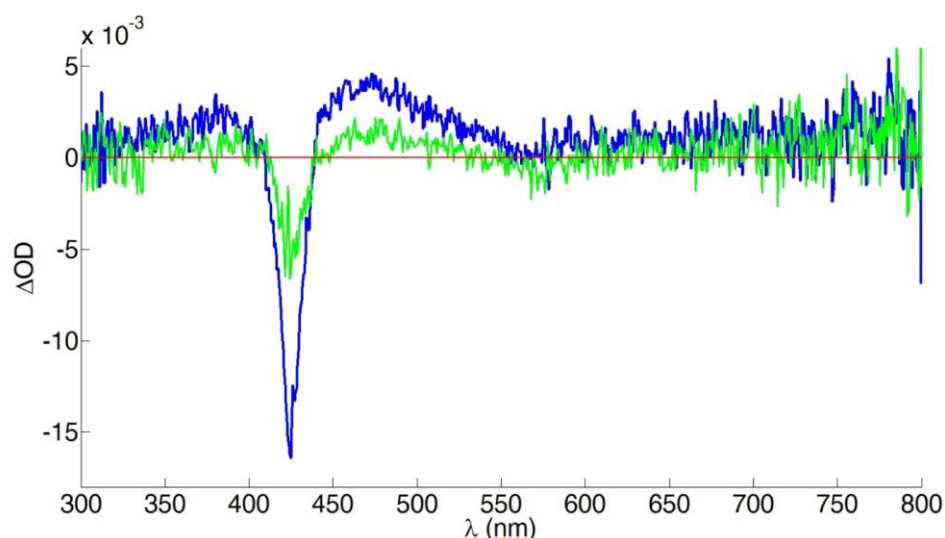
Figure 4.13 Transient absorption spectrum of [Fe(**3**)₂][PF₆]₂ (MeCN, ≈2 μM, room temperature). λ_{exc} = 550 nm. Acquisition time 200 ns, 5 acquisitions. Red line indicates the value considered as baseline. Blue line, deaerated solution; green line, air-equilibrated solution.
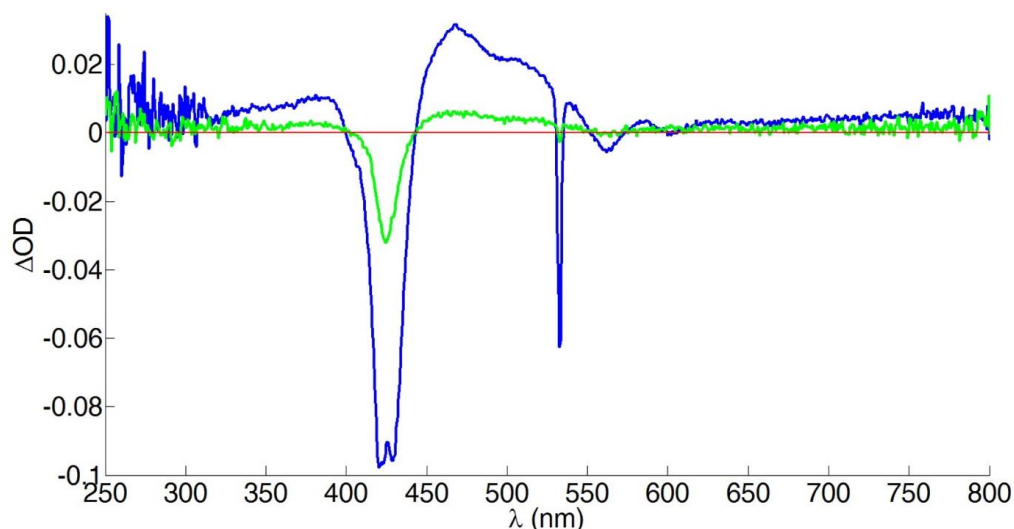
Figure 4.14 Transient absorption spectrum of [Ru(**3**)₂][PF₆]₂ (MeCN, ≈2 μM, room temperature). λ_{exc} = 532 nm. Acquisition time 200 ns, 5 acquisitions. Red line indicates the value considered as baseline. Blue line, deaerated solution (the Soret band is doubled due to a slightly over-concentrated solution); green line, air-equilibrated solution. Different intensities are due to different concentration of the samples. Sharp peak at 532 nm in the figure is due to stray laser light.

Scheme 4.4a shows the relative energies for [Zn(**3**)₂][PF₆]₂ and [Fe(**3**)₂][PF₆]₂, while the energetic diagram for [Ru(**3**)₂][PF₆]₂ is equivalent to that of [Ru(**3**)(**4**)][PF₆]₂, and will be discussed no further. The [Zn(TPP)] S_1 level in [Zn(**3**)₂][PF₆]₂ matches that of [Ru(**3**)(**4**)][PF₆]₂, and we have previously described how to obtain energies for [Zn(TPP)] S_2 and T_1 levels. The ¹MLCT energy level was derived from the absorption maximum of [Fe(**3**)₂][PF₆]₂; unfortunately ³MLCT and ³MC energies were not accessible. The relative energies of the states allow us to draw the energy transfer scheme presented in Scheme 4.4b. For [Zn(**3**)₂][PF₆]₂, upon excitation to S_1, an efficient intersystem crossing to T_1 occurs. For [Fe(**3**)₂][PF₆]₂, excitation at 550 nm triggers both [Zn(TPP)] S_1 and ¹MLCT transitions. While the course of [Zn(TPP)] S_1 is the same than in [Zn(**3**)₂][PF₆]₂, ¹MLCT first interconverts to ³MLCT, followed by fast deactivation into the ³MC state. There is evidence in literature that

after population of ^{3}MC (^{3}T$_2$ and ^{3}T$_1$) states, the fastest deactivation pathway involves spin-crossover to the ^{5}T$_2$ state[22, 23], which then thermally decays to the ground state ^{1}A$_1$.
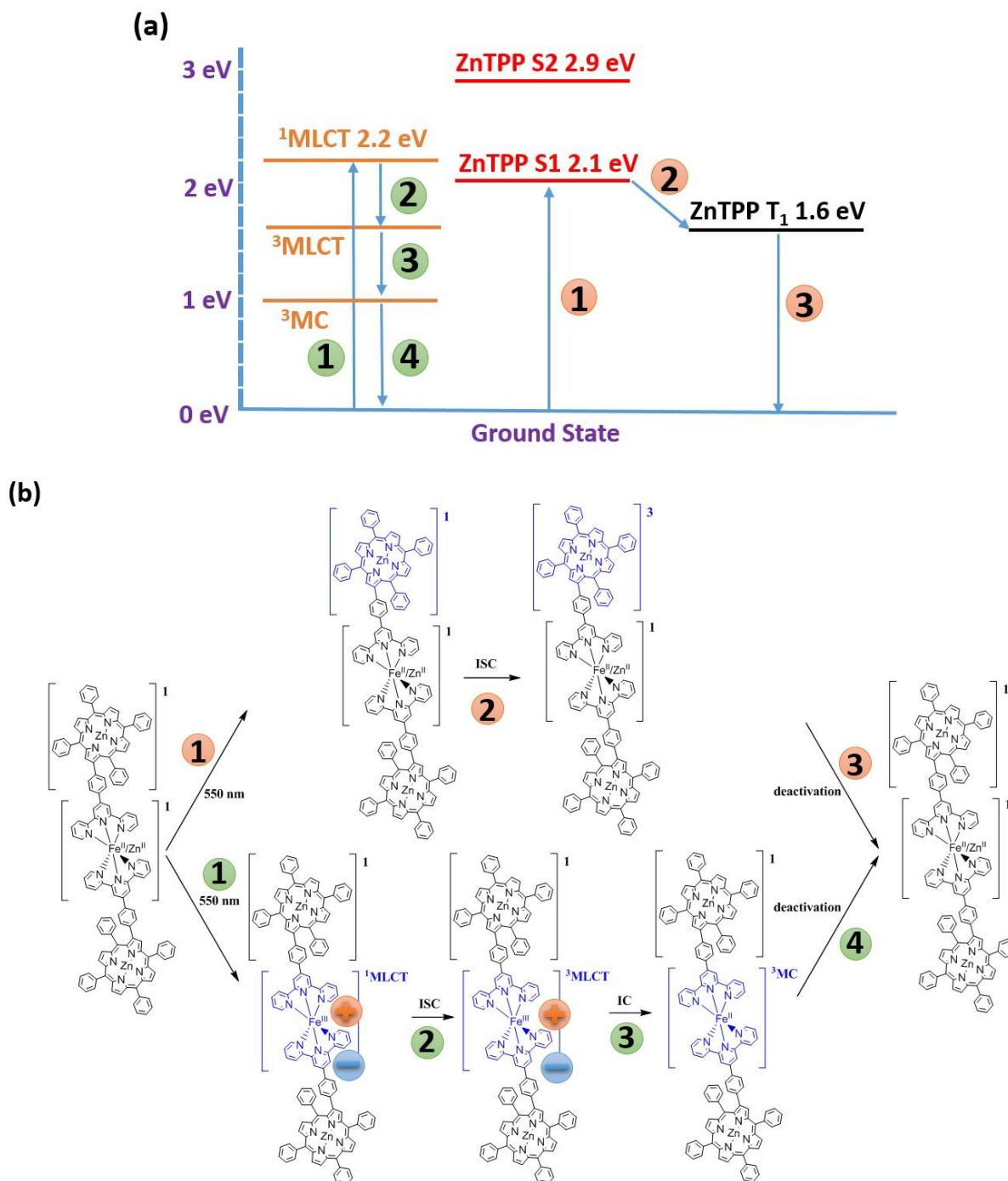
Scheme 4.4 (a) Energetic level diagram for [Zn(**3**)$_2$][PF$_6$]$_2$ and [Fe(**3**)$_2$][PF$_6$]$_2$ (b) energy-transfer scheme upon ^{1}MLCT (for [Fe(**3**)$_2$]$^{2+}$) or Q band (for [Zn(**3**)$_2$]$^{2+}$) excitation at 550 nm. ISC = intersystem crossing, IC = internal conversion. ^{3}MLCT and ^{3}MC [Fe(**3**)$_2$][PF$_6$]$_2$ energies are unknown.

Concluding, we have shown how the dye [Ru(**3**)(**4**)][PF$_6$]$_2$ is characterized by an improved light-absorbance with respect to N719. Surprisingly, its DSC performance is rather low; a result that could be regarded as counterintuitive. In order to assess the pathway responsible for the energy loss, we performed transient absorption experiments. They showed that no matter if the initial excitation energy resides on {Ru(tpy)$_2$} or [Zn(TPP)], eventually energy moves to the porphyrin T$_1$ state within tens of picoseconds. This state represent the lowest

excited state and returns to the ground state by means of thermal deactivation. A similar mechanism has been proven for the homoleptic complexes [Zn(**3**)$_2$][PF$_6$]$_2$, [Fe(**3**)$_2$][PF$_6$]$_2$ and [Ru(**3**)$_2$][PF$_6$]$_2$. A strategy to favour electron injection over energy transfer would be to increase the separation between [Zn(TPP)] and {Ru(tpy)$_2$}. In fact, the introduction of an additional phenylene spacer would increase of 4.5 Å the separation, which in turns translates in a decrease of the quenching constant by a factor of nine. We did not procced along this path and decided to move our attention to other applications of the porphyrin triplet state.

References

[1] G. Guerrero, P. H. Mutin and A. Vioux, *Chem. Mater.*, 2001, 13, 4367.

[2] G. Guerrero, P. H. Mutin, E. Framery and A. Vioux, *New J. Chem.*, 2008, 32, 1519.

[3] A. Vioux, J. Le Bideau, P. H. Mutin and D. Leclercq, *Top. Curr. Chem.*, 2004, 232, 145.

[4] H. J. Snaith, *Energy Environ. Sci.*, 2012, 5, 6513.

[5] H. J. Snaith, *Nat. Photonics*, 2012, 6, 337.

[6] M. Kasha, Discuss. *Faraday Soc.*, 1950, 9, 14.

[7] A. Lukaszewicz, J. Karolczak, D. Kowalska, A. Maciejewski, M. Ziolek and R. P. Steer, *Chem. Phys.*, 2007, 331, 359.

[8] *Modern Molecular Photochemistry*, ed. Nicholas J. Turro, University Science Books, Sausalito 1991, ch. 5, p. 148.

[9] *Reviews in Fluorescence 2015*, ed. Chris D. Geddes, Springer, 2016, ch. 9, p. 236.

[10] M. Gouterman, *J. Chem. Phys.*, 1960, 33, 1523.

[11] J. Rodriguez, C. Kirmaier and D. Holten, *J. Am. Chem. Soc.*, 1989, 111, 6500.

[12] P. K. Poddutoori, P. Poddutoori and B. G. Maya, *J. Porphyrins Phthalocyanines*, 2006, 10, 1049.

[13] A. C. Benniston, A. Harriman, C. Pariani and C. A. Sams, *Phys. Chem. Chem. Phys.*, 2006, 8, 2051.

[14] D. L. Dexter, *J. Chem. Phys.*, 1953, 21, 836.

[15] A. C. Benniston, A. Harriman, C. Pariani and C. A. Sams, *J. Phys. Chem. A*, 2007, 111, 8918.

[16] A. C. Benniston and A. Harriman, *Coord. Chem. Rev.*, 2008, 252, 2528.

[17] P. G. Bradley, N. Kress, B. A. Hornberger, R. F. Dallinger and W. H. Woodruff, *J. Am. Chem. Soc.*, 1981, 103, 7441.

[18] L. Flamigni, F. Barigelletti, N. Armaroli, B. Ventura, J.-P. Collin, J.-P. Sauvage and J. A. G. Williams, *Inorg. Chem.*, 1999, 38, 661.

[19] E. C. Constable, C. E. Housecroft, A. Cargill Thompson, P. Passaniti, S. Silvi, M. Maestri and A. Credi, *Inorg. Chim. Acta*, 2007, 360, 1102.

[20] J.-P. Sauvage, J.-P. Collin, J.-C. Cambron, S. Guillerez, C. Coudret, V. Balzani, F. Barigelletti, L. De Cola and L. Flamigni, *Chem. Rev.*, 1994, 94, 993.

[21] V. A. Waiters, J. C. de Paula, B. Jackson, C. Nutaitis, K. Hall, J. Lind, K. Cardozo, K. Chandran, D. Raible and C. M. Phillips, *J. Phys. Chem.*, 1995, 99, 1166.

[2] J. E. Monat and J. K. McCusker, *J. Am. Chem. Soc.*, 2000, 122, 4092.

[23] A. L. Smeigh, M. Creelman, R. A. Mathies and J. K. McCusker, *J. Am. Chem. Soc.*, 2008, 130, 14105.

[24] A. Lanzilotto, L. A. Büldt, H. C. Schmidt, A. Prescimone, O. S. Wenger, E. C. Constable and C. E. Housecroft, *RSC Adv.*, 2016, 6, 15370.

Part II

Singlet oxygen

5 MOLECULAR OXYGEN SENSITIZATION

In this introductory chapter we will give an overview of singlet oxygen (section 5.1), its molecular properties (section 5.2) and reactivity (section 5.3).

5.1 History of Singlet Oxygen

As of today, involvement of singlet oxygen in photocatalytic oxidation is widely accepted and is one of those theories that seems to have been with us for as long time. Like the assignment of phosphorescence to the radiative deactivation of triplet states[1], singlet oxygen photooxidation faced fiery opponents and gave rise to the story we are about to tell[2]. Most of what we know today derives from the work of a few names. Among them, Christopher S. Foote played a crucial role. . Let us start at the beginning.

The history of singlet oxygen dates back to the 1900s, when biologists observed how the combined action of dyes, oxygen and light is toxic to microorganisms. Toxicity was ascribed to oxidation of biomolecules, but a mechanism was nowhere to be found. At that time, not even the electronic structure of molecular oxygen was known; it is only in 1924 that Lewis proposed that oxygen possesses a triplet diradical ground-state[3]. Later, Mulliken identified the electronic states of molecular oxygen (1932)[4] (Scheme 5.1a) and their contribution to the atmospheric absorption bands (1928)[5].
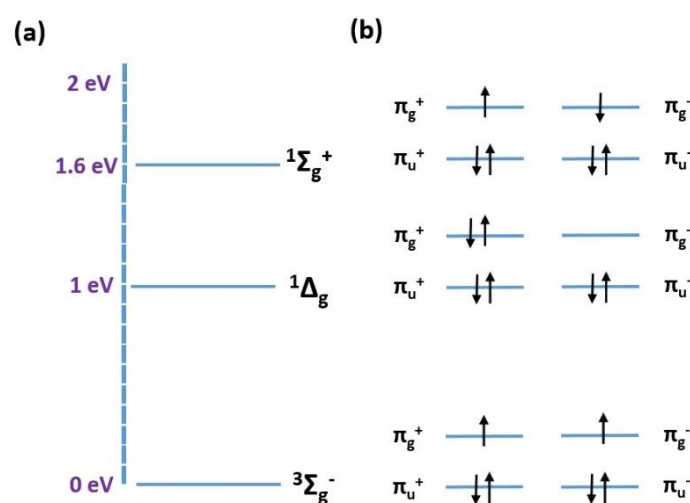
Scheme 5.1 (a) O_2 energetic level diagram and (b) corresponding electronic configuration. Note that in $^1\Delta_g$ the electron pair can be on either of π_g orbitals.

Around the same time, on the other side of the Atlantic Ocean Kautsky and de Bruijn in Germany conducted the experiment that would open the doors to singlet oxygen as a candidate for photooxidation[6]. As depicted in Scheme 5.2, the dyes trypaflavine (**1**) and leucomalachite green (**2**) were adsorbed on separate silica beads (different bead dimensions reflect those of the experiment). **2** is colourless because of the central C-sp^3, which interrupts the conjugation. This peculiarity makes **2** prone to oxidation since its oxidized form (malachite green, **3**) can resonate the positive charge through an extended aromatic system. The intense colour of **3**, visible by eye, can be used as a handle to check whether

oxidation has happened, and that is what the experiment was about. As it was conceived, the experiment saw the beads being mixed and irradiated. **2** was oxidized to **3** and **4**, which opened to **5** and **6** (Scheme 5.2)[7]. Importantly, the chemistry was not due to diffusion of either **1** or **2**, which remained attached to their respective bead and the oxygen source was not water. Because **1** and **2** were not adsorbed on the same bead, the experiment pointed towards the formation of a diffusible species, responsible for the oxidation. Kautsky hypothesized this species to be singlet oxygen in the $^1\Sigma_g^+$ state[8], and was immediately challenged by the scientific community for having done so. For the first time, singlet oxygen was considered to be the key to photocatalytic oxidation.
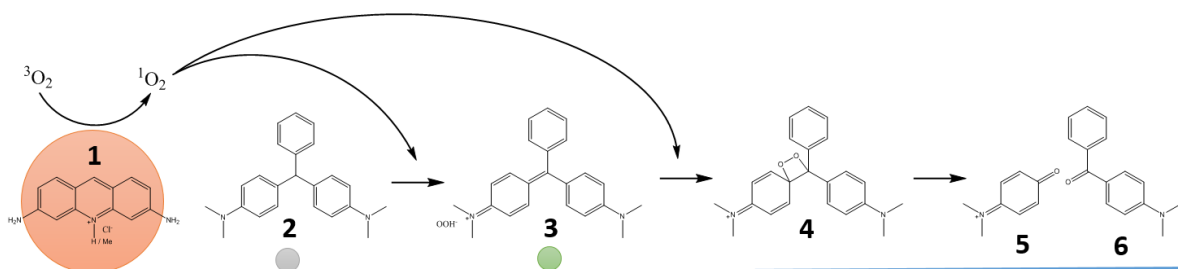
Scheme 5.2 Schematic representation of Kautsky experiment. Trypaflavine (orange) and leucomalachite green (grey) were adsorbed on silica beads. Diffusion of singlet oxygen initiates the reaction, which results in the formation malachite green (green bead).

The argument used against Kautsky was of energetic origin. In 1935 Gaffron conducted an experiment irradiating at 820 nm (≈35 kcal/mol) bacteriochlorophyll or hematoporphyrin in the presence of molecular oxygen. Under these conditions, allylthiourea could successfully be oxidized[9, 10]. But the $^1\Sigma_g^+$ state lies at an energy of 37 kcal/mol, therefore he argued that the energetic requirement was not met. Terenin shared the same idea, believing that infrared excitation would provide too less energy to effectively form oxygen in the $^1\Sigma_g^+$ state[11]. It did not take much for Kautsky to reply; he argued that the state $^1\Delta_g$ was of right multiplicity and would meet the energetic requirements, lying at 22 kcal/mol[12]. If that was true, he pointed out, then chlorophylls in plants were producing singlet oxygen in the $^1\Delta_g$ state, and this species could play a role in biological oxidation[6].

If it is true that at the time little or nothing was known about the mechanism of biological oxidation, the discovery of an enzyme containing flavin adenine dinucleotide by Warburg[13, 14] and of NAD and NADP a few years later can explain why Kautsky's work had been overlooked. With cofactors playing a key role in biological transformations, the need for singlet oxygen to rationalize biological oxidations was no longer necessary. For the next twenty years (1940-1963), singlet oxygen would fall into oblivion and the literature on photooxidation would rely on a mechanism involving the action of a photosensitizer-oxygen adduct[15-17]. As late of 1964, 23 years after Kautsky, Gollnick and Schenk published a mechanism for the hydroperoxylation of alkenes in which a moloxide (adduct between excited sensitizer and oxygen) is the key intermediate (Scheme 5.3)[18, 19].
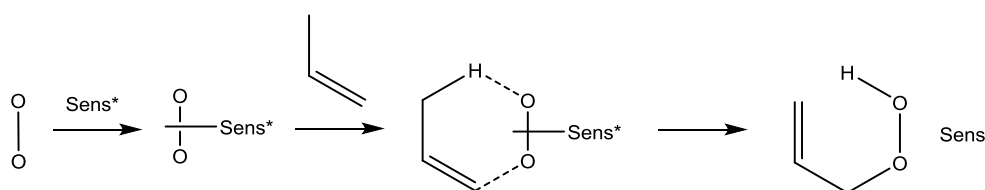
Scheme 5.3 Representation of Schenck's moloxide model for the hydroperoxylation of alkenes.

In the same year, Kasha and independently Ogryzlo, moved the discussion back to singlet oxygen. Specifically, Kasha and Khan undoubtedly confirmed that mixing NaOCl and H_2O_2 does form singlet oxygen. To do so, they recorded (for the first time) the emission spectrum of the red chemiluminescence resulting from mixing. They attributed the emission to pairs of singlet oxygen molecules, effectively weakening the distinction between photosensitized and chemical generation of singlet oxygen[20-22]. On the other hand, Ogryzlo and co-workers excited molecular oxygen via an electric discharge and successfully generated singlet oxygen dimers[23-25]. At this point, singlet oxygen was ubiquitous: it could be generated by sensitization, chemical reaction or electrical discharge, and in all cases, it could be shown that the spectroscopic trace belonged to oxygen in the singlet state. In addition, singlet oxygen luminescence was established in the gas and condensed phase, and the emission spectrum was assigned to the deactivation pathways: 1268 nm $^1\Delta_g$ $^1O_2 \rightarrow$ $^3O_2$, 634 and 701 nm $^1\Delta_g$ $^1O_2 \bullet$ $^1\Delta_g$ $^1O_2 \rightarrow 2$ $^3O_2$[26-32].

At this point of the story, Foote became an important player. We have seen how 1964 had been an important year for research on singlet oxygen. Another reason is that in the same year Foote and Wexler reported that the oxidation of organic molecules by the mixture NaOCl/H_2O_2 or by photosensitization yielded almost identical product distributions[33, 34]. At that time, no one yet believed that oxidation was due to the action of singlet oxygen and, in fact, Foote concludes in his paper: "*the weight of evidence favors the intermediacy of singlet oxygen. Further experiments are in progress*"[33]. Since it was known from the work from Kasha that the reaction NaOCl/H_2O_2 yielded singlet oxygen, the fact that sensitization yielded the same product distributions became Foote's strongest argument in favour of drawing a parallel between the two. Foote claimed an energy transfer mechanism was responsible for the change of spin in oxygen, with the dye in the triplet state transferring its energy to ground state oxygen[35]. Finally, near the end of his life, the Kautsky hypothesis was confirmed, even though it is not clear whether he was aware of Foote's work. A direct influence of Kautsky on Foote's research can be seen in the experiment performed by Wolf, Foote and Rebeck, in which they repeated the beads experiments. The dye Rose Bengal was attached to a polymer-bead, and 6-methyl-5-heptenoate to another. Again, upon irradiation, singlet oxygen generated on the first bead would diffuse and attack the acceptor located on a different one[36-38].

In response to Foote's work, other researchers started investigating the parallelism between the different ways of generating singlet oxygen. Corey and Taylor managed to produce singlet oxygen in an electric discharge and oxidize 9,10-disubstituted anthracenes, obtaining the same product resulting from reaction with NaOCl and H_2O_2[39]. In 1956 Foner and Hudson passed molecular oxygen through an electric discharge and then bubbled it in a solution of the acceptor. Again, the product distribution was similar to that obtained under chemical (NaOCl/H_2O_2) and photochemical (dye-sensitization) oxidation[40].

With the amount of evidence growing by the day, Schenk remained unmoved and, as late of 1970, continued to advocate for the moloxide (sensitizer-oxygen adduct) mechanism: "*The complexolytic mechanism of $^1O_2$ formation appears to be internally consistent and free of contradiction to the presently known experimental facts*"[41]. The last nails to the moloxide's coffin were put by Kopecky and Reich with the discovery that reaction rates were independent on the sensitizer used[42] and Foote, Ando and Wexler who showed that sensitizers exert no steric influence on oxygen reactivity[43] and that radical scavengers do

not alter the reaction[43]. Once the argument of the nature of the reactive intermediate was settled, chemists went on exploring the reactivity of this peculiar reactant.

5.2 Singlet oxygen properties

Molecular oxygen represents an exception among homonuclear diatomic molecules. Its ground state is a triplet, due to the presence of two unpaired electrons in two degenerate π^* orbitals. According to the nomenclature developed for the spectroscopy of diatomic molecules, this state is denoted as $^1\Sigma_g^+$. The lowest excited states are singlets and can be generated by moving one π^*-electron either onto an upper level or by pairing it to its counterpart (Scheme 5.1).

Spectroscopically, a free molecule in the gas phase (conditions typical of the upper atmosphere) is characterized by two electronic transitions, both in absorption and emission: $^1\Delta_g \leftarrow {}^3\Sigma_g^-$ (7882 cm^{-1}) and $^1\Sigma_g^+ \leftarrow {}^3\Sigma_g^-$ (13 121 cm^{-1}). The radiative lifetime was estimated from the absorption coefficients to be 45 min for $^1\Delta_g$[44, 45] and 7-12 s for $^1\Sigma_g^+$[46, 47], while the observed lifetimes are shorter, due to collisional deactivation ($\approx$1 ns for $^1\Sigma_g^+$ and $\approx$1 ms for $^1\Delta_g$). Absorption bands are detected at lower altitudes in the atmosphere or in liquid oxygen[48,49], where collisions become important. Therefore, the bands result from simultaneous transitions, i.e. a photon is able to excite two molecules at the time[50, 51]. These bands are assigned as follows: 634 nm 2($^1\Delta_g$) $\leftarrow$ 2($^3\Sigma_g^-$), 476 nm $^1\Sigma_g^+$ + $^1\Delta_g$ $\leftarrow$ 2($^3\Sigma_g^-$) and 381 nm 2($^1\Sigma_g^+$) $\leftarrow$ 2($^3\Sigma_g^-$) (Fig. 5.1).
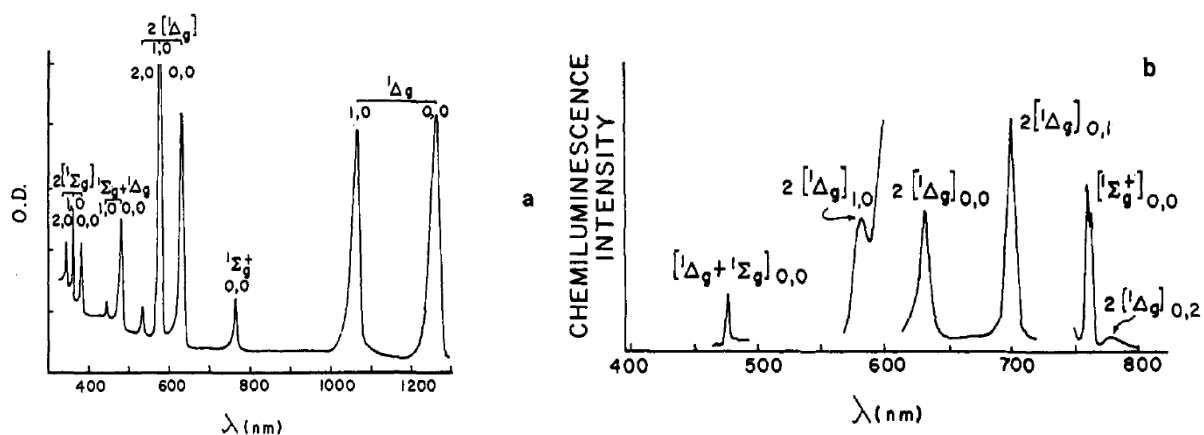
Fig. 5.1 Absorption spectrum of liquid oxygen (a) and chemiluminescence spectrum of the reaction NaOCl/H$_2$O$_2$ (b). Adapted with permission from D. R. Kearns, *Physical and chemical properties of singlet molecular oxygen*, Chemical Reviews, 1971[52]. Copyright 1971 American Chemical Society.

Molecular oxygen is a good quencher of both singlet and triplet states. To rationalize singlet quenching, Kearns examines the possible states arising from the interaction with an organic molecule in the excited state $^1M_1$[52] (Scheme 5.4). From the states, it is possible to extract the pathways that are most likely to happen.

(a)

$$^1M_1 + {}^3O_2 \rightarrow M^+ + O_2^- \qquad \text{(I)}$$
$$\rightarrow {}^3M_2 + {}^3O_2(^3\Sigma_g^-) \text{ (II)}$$
$$\rightarrow {}^3M_1 + {}^1O_2(^1\Delta_g) \text{ (III)}$$
$$\rightarrow {}^3M_1 + {}^3O_2(^3\Sigma_g^-) \text{ (IV)}$$
$$\rightarrow {}^1M_0 + {}^3O_2(^3\Sigma_g^-) \text{ (V)}$$

(b)

$$^3M_1 + {}^3O_2 \rightarrow {}^1M_0 + {}^1O_2(^1\Sigma_g^+) \text{ (VI)}$$
$$\rightarrow {}^1M_0 + {}^1O_2(^1\Delta_g) \text{ (VII)}$$
$$\rightarrow {}^1M_0 + {}^3O_2(^3\Sigma_g^-) \text{ (VIII)}$$

(c) ${}^1M_1$; ${}^3M_2$; ${}^3M_1$; ${}^1M_0$ (left). Encounter complex states (middle): ${}^3(^3\Sigma_g^- + {}^1M_1)$ (I); $^{1,3,5}(^3\Sigma_g^- + {}^3M_2)$; $^{1,3}(O_2^- + M^+)$ (III); ${}^3(^1\Delta_g + {}^3M_1)$ (IV); $^{1,3,5}(^3\Sigma_g^- + {}^3M_1)$ (VI); ${}^3(^1\Sigma_g^+ + {}^1M_0)$ (VII); $(^1\Delta_g + {}^1M_0)$; ${}^3(^3\Sigma_g^- + {}^1M_0)$ (VIII). Molecular oxygen states (right): ${}^1\Sigma_g^+$; ${}^1\Delta_g$; ${}^3\Sigma_g^-$.
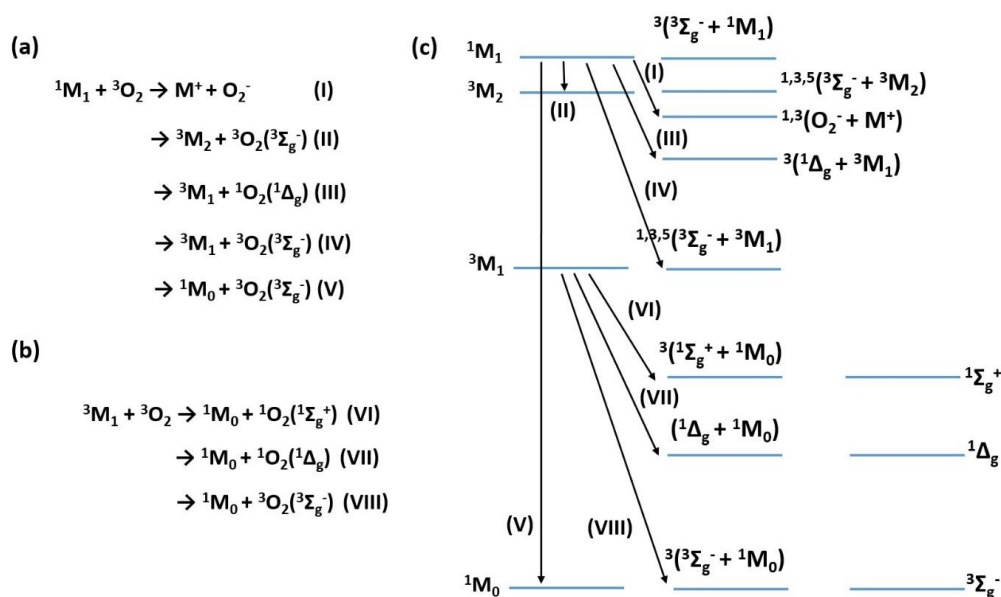
Scheme 5.4 Energetically feasible quenching mechanisms for M in a (a) singlet and (b) triplet state; (c) electronic states of an encounter complex [M - - - O_2] (middle) between a molecule M (left) and molecular oxygen (right).

Experimental observations are consistent with quenching of aromatic hydrocarbon fluorescence appearing to be virtually diffusion controlled[53-61]. Parmenter and Rau showed how the quenching rate constant is independent of the energy gap between the aromatic's S_1 and the T_1 states and from the position of T_2 with respect to S_1[60]. This evidence goes against mechanism III (direct formation of $^1\Delta_g$), which was discarded. By studying benzene sensitization of molecular oxygen, Snelling provided direct evidence against mechanism V (direct quenching to S_1)[62]. He monitored the phosphorescence $^1\Delta_g \rightarrow {}^3\Sigma_g^-$ as a function of oxygen pressure. As expected, at low pressure $^1\Delta_g$ is produced via energy transfer from benzene triplet states (quenching of the short-lived excited singlet is unlikely at this pressure). As the pressure increases, singlet benzene is quenched as well, but the concentration of $^1\Delta_g$ reaches a plateau. At high pressures, only 4% of the fluorescence is quenched with respect to the oxygen-free case. Other studies showed how oxygen quenching is due mostly to enhanced intersystem crossing (mechanism II or IV)[63-67].

Scheme 5.4 can also be used to predict the quenching pathways of M in a triplet state. Mechanisms VI and VII are basically those suggested by Kautsky to account for singlet oxygen production in his bead-experiment, while mechanism VIII is an enhanced intersystem crossing due to the interaction of M with paramagnetic oxygen. Although the magnetic field generated from a radical could promote such crossing[68], Tsumobura and Mulliken demonstrated that the effective field does not possess the necessary intensity to account for experimental observations[69]. Another proof in this sense is the report from Porter and Wright that the quenching efficiency of triplet states by paramagnetic ions does not depend on the magnitude of the magnetic moment[70]. Weiss included electron transfer as a possible source of quenching; while this is true for triplet states with very low oxidation potentials (amines in polar solvents), in general the energetics are against this mechanism accounting for the majority of cases[71].

Apart from energy transfer, molecular oxygen could be directly excited to its singlet state; in fact, we have seen how the absorption spectrum of liquid oxygen possesses absorption bands in the visible. An attempt in this sense has been performed by means of a

He-Ne laser (623.8 nm), almost coincident with the wavelength required to promote the transition $2(^1\Delta_g) \leftarrow 2(^3\Sigma_g^-)$ (634 nm)[72]. With this setup, Evans was able to perform photooxidation of 9,10-dimethylanthracene under high oxygen pressure; most importantly, he showed that photooxidation occurs only when excitation is performed at wavelengths known to correspond to oxygen absorption. What Evans could not expect is that the photooxidation efficiency was proportional to the extinction coefficient for the generation of the states $^1\Delta_g$ and $^1\Sigma_g^+$. He concluded that either the two states react with the acceptor with the same efficiency (but this would have to hold regardless of the chemical nature of the acceptor) or that population of the $^1\Sigma_g^+$ state is followed by deactivation to the $^1\Delta_g$ state prior to reaction. Additional evidence came from Gollnick[73], who used a wide range of photosensitizers to vary the energy of the triplet state responsible for oxygen sensitization. He decided to work on substrates that lead to more than one product when oxygenated, in the hope that he would see a different distribution as he moved the energy of the triplet state. Disappointingly, he detected no variation whether the triplet state lied above or below the energy of $^1\Sigma_g^+$ state, and had to conclude that evidence supported a mechanism in which $^1\Sigma_g^+$ oxygen does play an active role.

The lifetime of the $^1\Delta_g$ state does not depend upon temperature. In 1968, Koch reported that in methanol singlet oxygen lifetime changed negligibly passing from -120 to +20 °C[74]. Foote reported a similar effect in acetone ranging from -80 °C (50 µs) to +21 °C (47 µs)[75]. The most pronounced effect in this sense was observed with solvent deuteration: the lifetime sharply increases in deuterated solvent and it is proportional to the degree of deuteration[29, 75, 76].

5.3 The reactivity of singlet oxygen

With the discovery that chemically generated singlet oxygen leads to the same product as that generated photochemically, synthetic chemists had a powerful new tool to play with. Over the last 50 years, extensive research has been conducted in organic chemistry to pin down singlet oxygen reactivity and explore the plethora of substrates that act as acceptors. For the sake of this dissertation, we assign a short section to each class of substrates. Section 5.3.1 deals with hydroperoxylation, also known as "ene"-reaction, Section 5.3.2 discusses the reactivity of enamines, Section 5.3.3 is about sulfoxides, Section 5.3.4 describes [2+2] and [4+2] cycloadditions, Section 5.3.5 discusses 1,3-dipolar additions and Section 5.3.6 oxidation of phenols.

5.3.1 The "ene"-reaction

Singlet oxygen adds to alkenes which possess allylic hydrogens to yield allylic hydroperoxides; the proposed mechanisms are collected in Scheme 5.5. For many decades, the reaction mechanism was thought to be with all probability a concerted oxygen insertion-hydrogen abstraction-double bond shifts[43], but in 2003, isotopic substitution studies (H/D and $^{12}C/^{13}C$) elucidated perepoxide as the only mechanism able to explain the product distribution[77]. Kearns reviewed the literature and collected 13 experimental evidences regarding the "ene"-reaction[52]: i) oxygen is always introduced on the same face from which

hydrogen is abstracted and the double bond always shifts[18, 43, 73, 78-80], ii) reaction is not quenched by the presence of radical traps,[43] iii) with substituted alkenes, secondary and tertiary hydroperoxides are produced in same amounts,[18, 73, 78-81] iv) oxygen addition is prevented in sterically hindered alkenes,[82] v) optical activity is conserved during the reaction,[43, 83] and no cis-trans conversion is observed,[81] vi) reactivity increases with alkyl substitution by a factor of ten per methyl group introduced,[42] vii) solvent plays a minor role towards rate of reaction and product distribution,[18, 73, 78-80] viii) isotope effects are small,[84] ix) for trimethylstyrenes, product distribution is unaffected by phenyl substitution,[85] x) a specific dioxetane is stable at room temperature, but decomposes to carbonyl compounds upon heating,[86, 87] xi) the rates of reaction between olefins and peracids correlates excellently with those of singlet oxygen,[42] xii) poor correlation exists between rates of reaction for olefins with radicals and with singlet oxygen,[42] xiii) addition of azide lead to *trans*-azido hydroperoxides[88].

concerted   radical   perepoxide
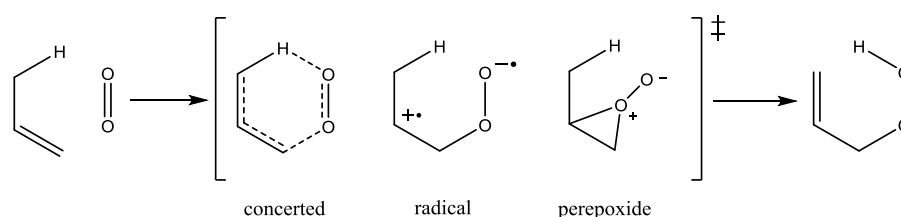
Scheme 5.5 Suggested hydroperoxylation mechanisms.

Among others, Foote noted how the structure of the alkene dictates the reactivity. Mono- and dialkylated alkenes show poor conversion, while trialkylated alkenes are around 100 times less reactive than tetraalkylated ones[35, 43, 85]. It is significant the case of (+)-limonene, which contains a di- and a trisubstituted double bond: only the trisubstituted is reactive (Scheme 5.6); the same follows for α-pinene, in which case the reaction is slower than for 1-methylcyclohexene. This evidence points towards steric effects being important. Oxygen addition does not follow the Markonikov rule: asymmetric alkenes undergo addition by nearly the same amount at both ends.
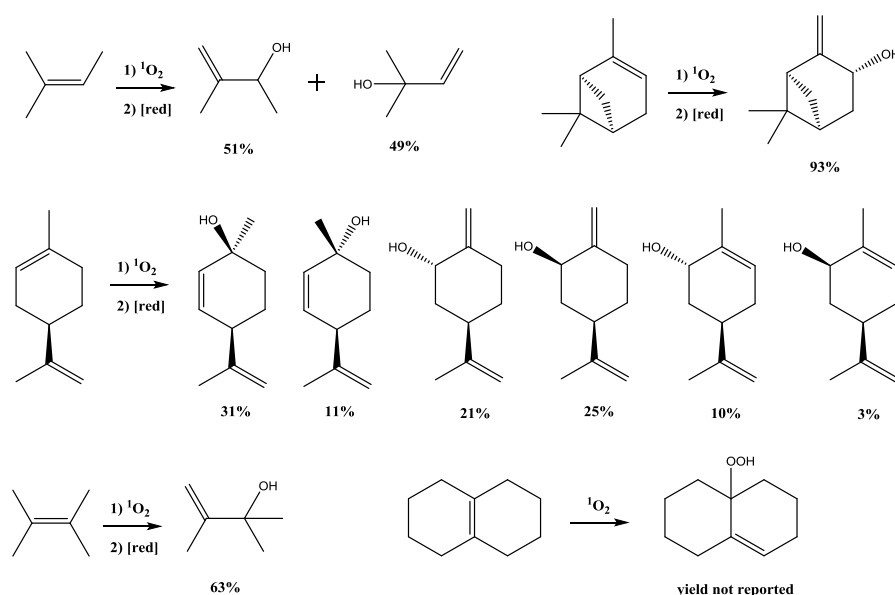
Scheme 5.6 Experimental product distribution for photocatalytic oxidation of substituted olefins: (+)-limonene, α-pinene and 2-methyl-2-butene[43], Δ[9,10]-octalin and 2,3-dimethyl-2-butene[35].

5.3.2 Enamine cleavage

In 1968, Huber discovered that enamines readily react with singlet oxygen and published "*Photooxygenation of enamines - a partial synthesis of progesterone*". He shared his results with Foote prior to publication[89], allowing Foote to publish his mechanistic investigation of the reaction in the same year, and in the same journal as Huber[90]. Scheme 5.7 shows the compounds investigated by Foote. He wrote that enamines **Ia**, **Ib** and **Ic** react with singlet oxygen yielding high yields of the corresponding ketone and amide. It was evident that the role of singlet oxygen is to cleave the C-C double bond, substituting an oxygen atom onto the position previously occupied by carbon. The electronic nature of the substituent plays an important role; no conversion could be obtained for enamine **II**. In order to understand whether oxygen adds to the carbon atom in alpha or beta with respect to the nitrogen atom, Foote conducted the photooxygenation of **Ic** at low temperature. In this way, he trapped the hydroperoxyl species, which then was reduced to an alcohol, confirming that the position of attack is beta. If a triple bond replaces the double bond at the site of cleavage (compound **III**), then the product retains a single C-C bond and a dicarbonyl structure results. Foote interpreted this as the final stage of an initial 1,2-cycloaddition.
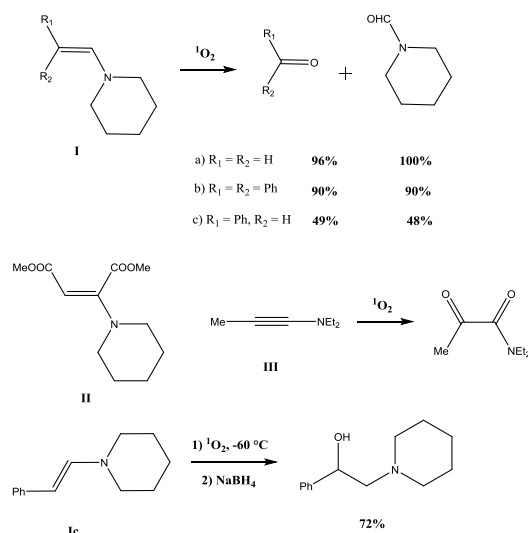
Scheme 5.7 Experimental product distribution for photocatalytic oxidation of substituted enamines[90].

In 1964, Hoffman and Häuser showed that 1,1,2,2-tetramethoxyethylene undergoes 1,2-cycloaddition[91]. This prompted Foote's idea that this chemical could trap the dioxetane state and, in 1970, Foote managed to obtain this result[92] (Scheme 5.8). Evidence for the successful trapping of the dioxetane was the sharp resonance at 3.45 ppm in the ^{1}H-NMR (100 MHz, Freon 12, -118 °C). Additionally, Foote resorted to a peculiar way to confirm the structure. He noted how the structure of the dioxetane resembles that of 1,2-dioxetanedione, an intermediate in chemiluminescent reaction of oxalyl esters and hydrogen peroxide (still employed nowadays in glowing sticks) (Scheme 5.9)[93, 94]. He therefore heated his dioxetane in a solution containing fluorescent hydrocarbons; heating would promote decomposition and release of the strain energy stored in the 4-member ring, energy transferred as excitation energy to the electronic excited states of the hydrocarbons. Foote detected peculiar fluorescence for each of the hydrocarbon used and concluded that dioxetane was indeed the product of photooxygenation.
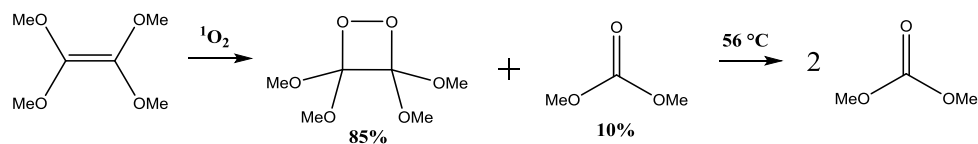
Scheme 5.8 Foote's synthesis of the first room-temperature stable dioxetane[92].
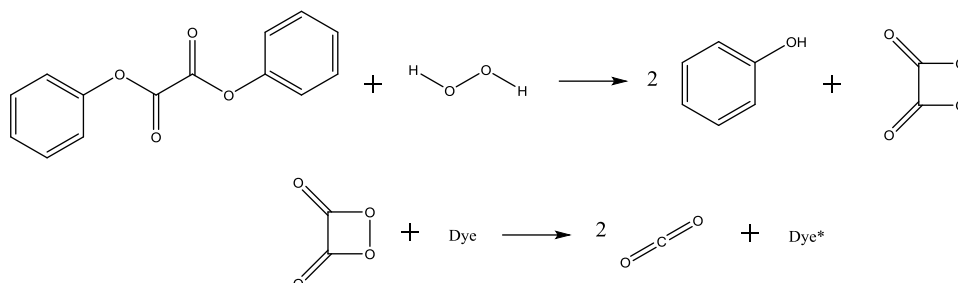
Scheme 5.9 Mechanism of chemiluminescent decomposition of oxalyl esters in presence of hydrogen peroxide.

Once the role of steric factors has been established, Foote went on to investigate the influence of electronic factors[85]. He prepared a series of *meta*- and *para*-derivatives of α,β,β-trimethylstyrene (**IV**). Hydroperoxylation is expected to generate two products (after reduction): a tertiary alcohol (**V**) or a benzylic alcohol (**VI**), illustrated in Scheme 5.10. Experimentally the ratio **V/VI** is the same for *meta*- and *para*-substituted rings, regardless if the source of singlet oxygen is sensitization or NaOCl/H_2O_2 decomposition. The electronic nature of the substituent, represented by its Hammet parameter, correlates weakly with the ratio **V/VI**, which ranges between an upper limit of 2.86 for *p*-CN (σ = +0.66) and a lower limit of 2.44 for *m*-OMe (σ = +0.12).
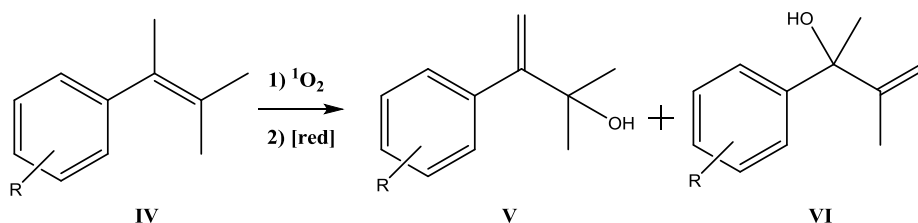
Scheme 5.10 hydroperoxylation of styrene derivatives[85].

5.3.3 Sulfoxides

In 1970, during a quest for singlet oxygen quenchers, Foote reported that diethylsulfide was a good quencher. What he later realized is that quenching occurred through a chemical reaction, which lead to the sulfoxide and of which we will make extensive use in this doctoral dissertation[95]. Foote adds that singlet oxygen would add to sulfur in methanol, but not in benzene. In his second paper on sulfide oxidation,[96] Foote claimed to have experimentally detected an unstable intermediate, which he assigned as the persulfoxide (Scheme 5.11).
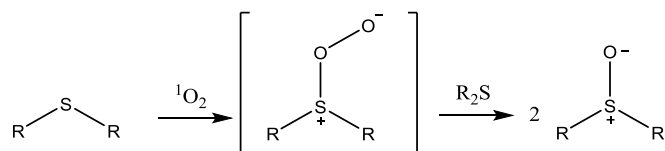
Scheme 5.11 Foote's mechanistic model for sulfide oxidation.

He gave three experimental observations to support the persulfoxide model. First, he trapped the transition state by reacting it with a sulfide which is inert to singlet oxygen, namely diphenylsulfide Ph_2S. Aromatic sulfides, in fact, cannot be oxidized by direct sensitization of molecular oxygen. In the presence of singlet oxygen, a mixture Et_2S/Ph_2S 20 mM : 100 mM was transformed to Et_2SO/Ph_2SO 3.6 mM : 1.4 mM after 75 s of irradiation. Foote claimed that the persulfoxide Et_2SOO acted as atom transfer reagent, effectively passing to the inert sulfide one of the two oxygen atoms acquired from singlet oxygen addition (Scheme 5.11).

Secondly, Foote made good use of the cyclic disulfide 1.4-dithiane (Scheme 5.12). Employing a concentration such that encounters between molecules becomes rare, he generated the persulfoxide intermediate. Since the molecule cannot deactivate via the usual pathway, (that is oxygen transfer to a second disulfide molecule), both oxygen atoms stay on the same ring, namely in an intramolecular atom transfer which ultimately leads selectively to the *cis*-disulfoxide. The general mechanism presented in Scheme 5.11 remains valid at high concentration of 1,4-thiane. When a sulfide is reacted at very low concentrations with singlet oxygen, then sulfone is created along with sulfoxide[96]. Foote pointed out that sulfone does not derive from further oxidation of the sulfoxide, but most likely from the fact that the persulfoxide cannot transfer one of the two oxygen atoms and so retains both on them on the same sulfur atom.
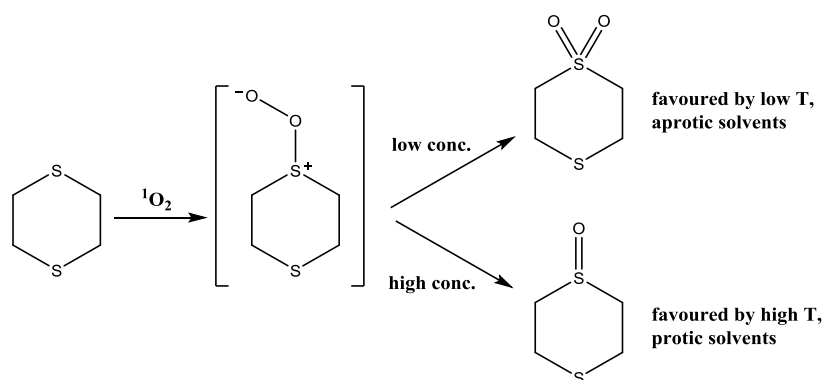
Scheme 5.12 Foote's experiments on 1,4-dithiane.

The third piece of evidence relies solvent effect. Both Et_2S and 1,4-dithiane were oxidized slowly in dry solvents; the rate increases as more and more water is added. Water concentration in acetonitrile as high as 10 mM induced a four-fold increase in the reaction rate. Foote interprets this behaviour as a stabilization by hydrogen bonding of the charged persulfoxide intermediate.

5.3.4 [2+2] and [4+2] cycloadditions

Under normal conditions indene undergoes [2+2] cycloaddition followed by ring opening to homophtalaldehyde[80]; new products could be isolated when working in methanol[97] (Scheme 5.13). The product distribution observed by Radlick and coworkers made them rethink about the nature of the intermediate: a hydroperoxide could not explain the result, but a concerted [2+2] cycloaddition followed by nucleophilic ring opening could (Scheme 5.14).
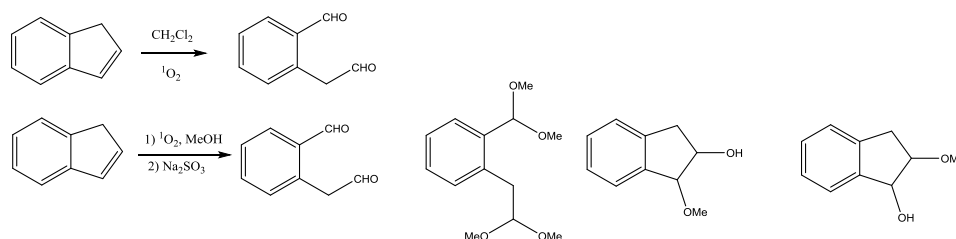
Scheme 5.13 Indene photooxygenation product distribution.
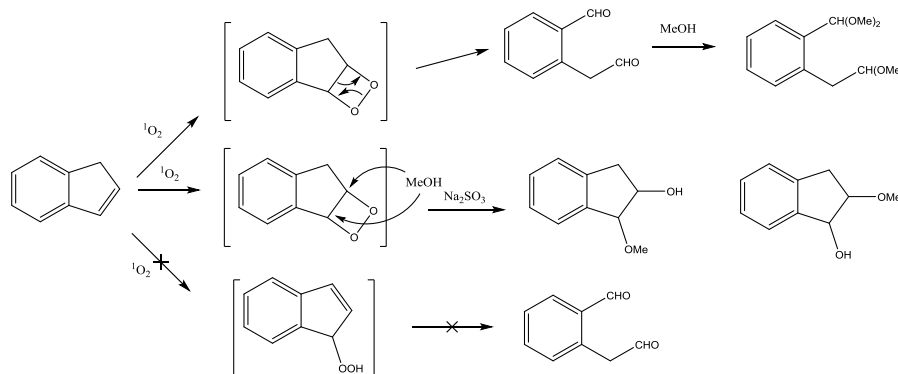
Scheme 5.14 Radlick's mechanism for indene photooxygenation.

In a JACS paper of 1973, Foote reported a new reaction pathway for indene[98]. Reacting 1-methyl-2-phenyl-1H-indene (**VII**) in acetone at -78 °C resulted in a compound the elemental analysis of which showed the uptake of two oxygen molecules; IR showed no carbonyl or hydroxyl stretching modes, but rather epoxide bands; finally, the product freed I_2 from an acidified KI solution. Foote proposed structure **IX** as a possible candidate (Scheme 5.15). For this hypothesis to hold, Foote invoked first a [4+2] cycloaddition; he then drew a parallel between the rearrangement of ascaridole endoperoxide[99, 100] and that of the highly strained peroxide **VIII**, yielding **IX**. Addition of a second molecule converts **IX** to **X**, the product that was effectively isolated. Searching for more evidence, Foote heated compound **X** and observed the isomerization to a product which does not possess carbonyl or hydroxyl and the NMR spectrum of which showed no aromatic protons (except phenyl ones). Structure **XI** seemed the most likely; if that were true, Foote would be the first to have ever prepared what he called 'benzene trioxide'.
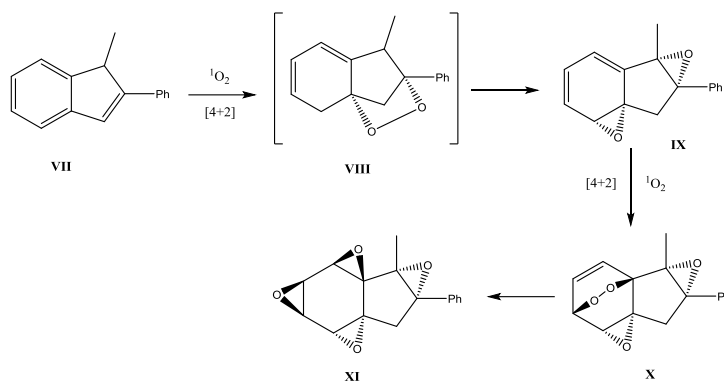
Scheme 5.15 Foote's transformation of indene.

In 1979 Foote was interested in a possible [4+2] cycloaddition between imidazole and singlet oxygen[101]. There had been reports on singlet oxygen-related loss of activity in proteins containing histidine [102-108]. Mechanistic studies revealed that the target was specifically the imidazole ring of this residue[52, 109-114]. When histidine was photooxygenated outside a protein environment, aspartic acid and urea were the major products[112]. Up to 17 different products were isolated, showing how sensible the intermediates were to nucleophilic attack [113]. What was missing was the direct evidence of the first intermediate, and Foote succeeded in providing it. To elucidate the mechanism, he worked on N-methyl and N-unsubstituted imidazole (Scheme 5.16). By performing the reaction at low temperature and recording low-temperature NMR spectra, he could prove the existence of an endoperoxide intermediate both for alkylated or plain imidazole. For 4-methyl-N-methylimidazole, proton NMR spectroscopy revealed the presence of an iminomethyl group in position 4 and a tertiary carbon in position 2. If singlet oxygen performed [2+2] cycloaddition on just one of the two double bonds, no such signals would be observed. Likewise is what happens to N-unsubstituted 4-methyl-imidazole. At room temperature the two tautomers[115, 116] give raise to an averaged NMR spectrum[117], but at -100 °C the two could be distinguished. More interestingly, the two tautomers react with singlet oxygen yielding two products, always according to a [4+2] cycloaddition. Upon heating, all of the imidazolyl endoperoxides reacts in a way that is not understood to form complex reaction mixtures.
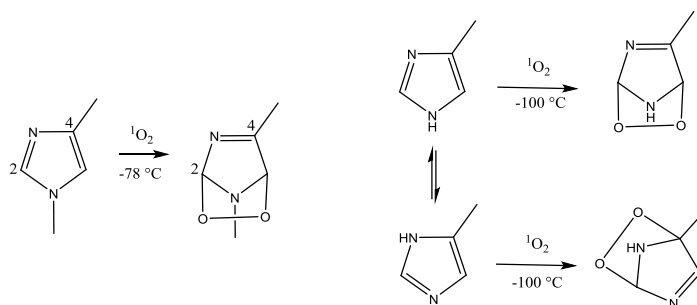
Scheme 5.16 Reaction of singlet oxygen and imidazole.

5.3.5 1,3-Dipolar addition

A report from Highley and Murray in 1974 brought attention to the reaction between singlet oxygen and diazo-compounds[38]. They found that an ozonide was the final product of the reaction involving an aldehyde, its diazo-compound and singlet oxygen. Next to the ozonide, a carbonyl derivative of the original diazo was observed. To explain the experimental evidence, the authors proposed the mechanism in Scheme 5.17. For R = Ph, benzophenone was obtained in 67% yield and triphenylethylene ozonide in 26% yield. Mass spectrometry detection of N_2O provided evidence for a mechanism according to which two different pathways lead to the two products as shown in Scheme 5.17.
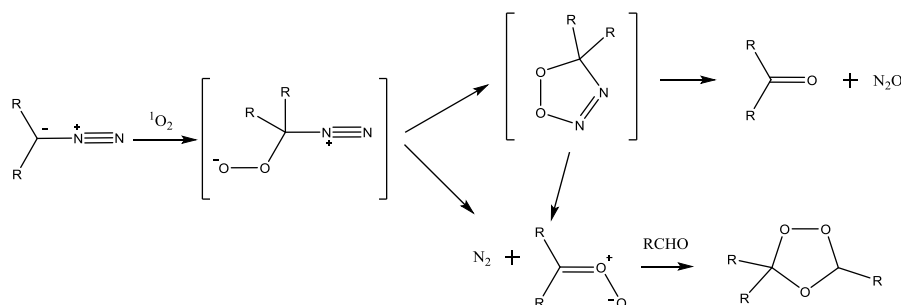
Scheme 5.17 Singlet oxygen addition to diazo-compounds followed by reaction with aldehyde to yield the ozonide.

Aware of this result, Foote tried out a reaction on another dipolar system: nitrone[118]. 2,4,4-trimethyl-Δ^1-pyrroline-N-oxide (**XII** in Scheme 5.18) was photooxygenated and quantitatively converted to **XIII**. **XIII** reacts violently on warming to room temperature or in presence of silica, is quantitatively reduced to **XII** on treatment with $NaBH_4$ and does not oxidize olefins. In order to establish a mechanism, Foote reacted the analogue **XIV** with singlet oxygen, but no reaction took place. This made Foote repeal the dipolar addition hypothesis and go for an "ene"-like reaction.
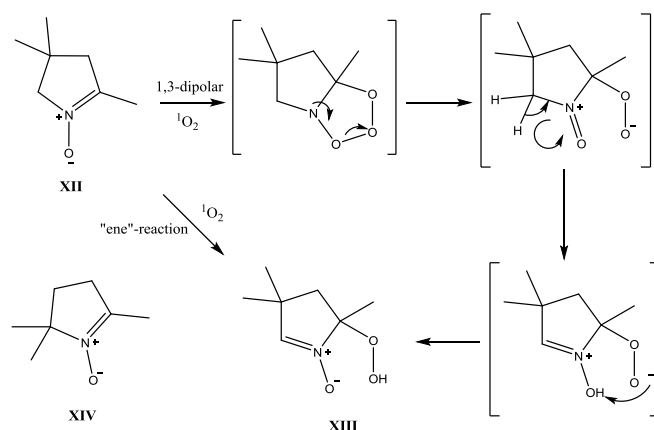
Scheme 5.18 Reaction of singlet oxygen with 2,4,4-trimethyl-Δ^1-pyrroline-N-oxide.

5.3.6 Oxidation of phenols

In 1978 Foote looked at the effect of singlet oxygen on phenols. His interest was prompted by the work of Matsuura and Saito[114, 119, 120-122] and Tamir and Pospišil[123]. These authors saw an effect when reacting *o,p*-substituted phenols with singlet oxygen and proposed two intermediates: a formal [4+2] cycloaddition leading to an endoperoxide or a charge transfer state (superoxide/phenol radical cation); both intermediates then reacted to give the same phenol hydroperoxide (Scheme 5.19).
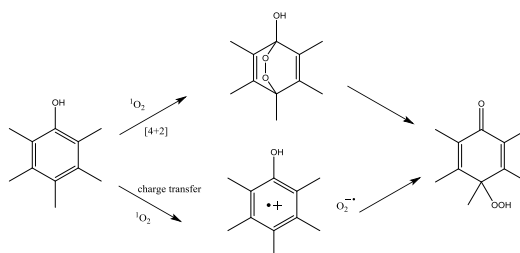
Scheme 5.19 Mechanism of the reaction between singlet oxygen and a monohydric phenol.

The products from dye-sensitized photo-oxidation are similar to those obtained from radical oxidations[124-127]. Foote aimed to show that electron-rich phenols would prefer the charge transfer pathway to the product, therefore he conducted experiments on the phenols represented in Scheme 5.20 (and others). Combining kinetic experiments and transient absorption techniques for the detection of the absorption of phenol radical cation, Foote came to the conclusion that charge transfer plays a major role in phenolic quenching of singlet oxygen[128]. Experimental evidence of electron transfer came from the plot of quenching constant *versus* phenolic halfpeak potential, which was shown to be linear. Furthermore, Hammett plot (k_R/k_H vs. σ) showed that most of the substituents fit on a straight line, confirming a direct correlation between quenching and electronic nature of the quencher. Last, quenching constants were significantly larger in methanol than in benzene, supporting a charge-separated transition state. Since the plot regarding phenolic halfpeak potential was similar to that of alkylamine plotted *versus* peak potential and of methoxybenzene *versus* halfwave potential, all compounds interact with singlet oxygen according to the same mechanism. Methoxybenzenes do not possess an alcoholic hydrogen, therefore direct hydrogen abstraction by singlet oxygen is not required. Still, these was ambiguity as to whether deprotonation precedes product formation or not.
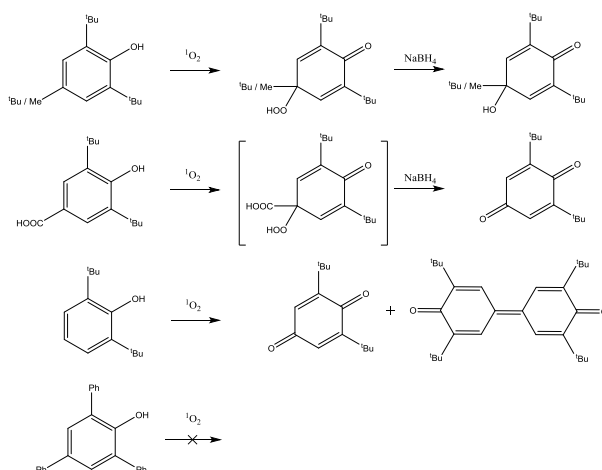
Scheme 5.20 Product distribution for the reaction between singlet oxygen and different monohydric phenols.

References

[1] G. L. Lewis, M. Kasha, *J. Amer. Chem. Soc.*, 66, 2100, 1944.

[2] A. Greer, *Acc. Chem. Res.,* 39, 797, 2006.

[3] G. N. Lewis, *Chem. Rev.*, 1924, 1, 231.

[4] R. S. Mulliken, *Rev. Mod. Phys.,* 1932, 4, 54.

[5] R. S. Mulliken, *Nature*, 1928, 122, 505.

[6] H. Kautsky, *Trans. Faraday Soc.*, 1939, 35, 216.

[7] H. Kautsky, H. de Bruijn, R. Neuwirth and W. Baumeister, *Ber.*, 1933, 66B, 1588.

[8] H. Kautsky, A. Hirsch and W. Flesch, *Ber.*, 1935, 68B, 152.

[9] H. Gaffron, *Ber.*, 1935, 68B, 1409.

[10] H. Gaffron, *Biochem. Z.*, 1936, 287, 130.

[11] A. N. Terenin, *Akad. Nauk S.S.S.R.*, 1955, 85.

[12] H. Kautsky, *Biochem. Z.*, 1937, 291, 271.

[13] O. Warburg and W. Christian, *Biochem. Z.*, 1933, 258, 496.

[14] O. Warburg and W. Christian, *Biochem. Z.*, 1936, 287, 291.

[15] v. A. Schönberg, *Liebigs Ann. Chem.*, 1935, 518, 299.

[16] G. O. Schenck, *Naturwissenschaften*, 1948, 35, 28.

[17] J. L. Rosenberg and D. J. Shombert, *J. Am. Chem. Soc.*, 1960, 82, 3257.

[18] K. Gollnick and G. O. Schenk, *Pure Appl. Chem.,* 1964, 9:4, 507.

[19] A. Nickon and J. F. Bagli, *J. Am. Chem. Soc.*, 1959, 81, 6330.

[20] A. U. Khan and M. Kasha, *J. Chem. Phys.*, 1963, 39, 2105.

[21] A. U. Khan and M. Kasha, *Nature*, 1964, 204, 241.

[22] A. U. Khan and M. Kasha, *J. Am. Chem. Soc.*, 1970, 92, 3293.

[23] S. J. Arnold, E. A. Ogryzlo and H. Witzke, *J. Chem. Phys.*, 1964, 40, 1769.

[24] L. W. Bader, E. A. Ogryzlo, *Discuss. Faraday Soc.*, 1964, 46.

[25] J. S. Arnold, R. J. Browne and E. A. Ogryzlo, *Photochem. Photobiol.*, 965, 4, 963.

[26] A. A. Krasnovskii, *Biofizika*, 1976, 21, 748.

[27] A. U. Khan and M. Kasha, *Proc. Nat. Acad. Sci. U.S.A.*, 1979, 76, 6047.

[28] J. R. Hurst, J. D. McDonald and G. B. Schuster, *J. Am. Chem. Soc.*, 1982, 104, 2065.

[29] P. R. Ogilby and C. S. Foote, *J. Am. Chem. Soc.*, 1982, 104, 2069.

[30] E. Wasserman, R. W. Murray, H. L. Kaplan and Y. A. Yager, *J. Am. Chem. Soc.*, 1968, 90, 4160.

[31] D. R. Kearns, A. U. Khan, C. K. Duncan and A. H. Maki, *J. Am. Chem. Soc.*, 1969, 91, 1039.

[32] E. Wasserman, V. J. Kuck, W. M. Delavan and Y. A. Yager, *J. Am. Chem. Soc.*, 1969, 91, 1040.

[33] C. S. Foote and S. Wexler, *J. Am. Chem. Soc.*, 1964, 86, 3879.

[34] C. S. Foote and S. Wexler, *J. Am. Chem. Soc.*, 1964, 86, 3880.

[35] C. S. Foote, S. Wexler, W. Ando and R. Higgins, *J. Am. Chem. Soc.*, 1968, 90, 975.

[36] S. Wolf, C. S. Foote and J. Rebek, *J. Am. Chem. Soc.*, 1978, 100, 7770.

[37] W. R. Midden and S. Y. Wang, *J. Am. Chem. Soc.*, 1983, 105, 4129.

[38] W. C. Eisenberg, K. Taylor and R. W. Murray, *J. Phys. Chem.*, 1986, 90, 1945.

[39] E. J. Corey and W. C. Taylor, *J. Am. Chem. Soc.*, 1964, 86, 3881.

[40] S. N. Foner and R. L. Hudson, *J. Chem. Phys.*, 1956, 25, 601.

[41] G. O. Schenck, *Ann. N. Y. Acad. Sci.*, 1970, 171, 67.

[42] K. R. Kopecky and H. J. Reich, *Can. J. Chem.*, 1965, 43, 2265.

[43] C. S. Foote, S. Wexler and W. Ando, *Tetrahedron Lett.*, 1965, 46, 4111.

[44] R. M. Badger, A. C. Wright, and R. F. Whitlock, *J. Chem. Phys.,* 43, 4345, 1965.

[45] R. W. Nicholls, *Can. J. Chem.*, 47, 1847, 1969.

[46] W. H. J. Childs and R. Mecke, *Z. Physik*, 68, 344, 1931.

[47] L. Wallace and D. M. Hunten, *J. Geophys. Res.*, 73, 4813, 1968.

[48] C. W. Cho, E. J. Allin, and H. L. Welsh, *Can. J. Phys.*, 41, 1991, 1963.

[49] W. Finkelnburg and W. Steiner, *Z. Physik*, 79, 69, 1932.

[50] J. W. Ellis and H. O. Kneser, *Z. Physik.*, 86, 583, 1933.

[51] V. I. Dianov-Klokov, *Opt. Spectrosc. (USSR)*, 6, 290, 1959.

[52] D. R. Kearns, *Chem. Rev.*, 1971, 71, 395.

[53] W. R. Ware, *J. Phys. Chem.*, 66, 455, 1962.

[54] W. R. Ware and S. K. Lee, *J. Chem. Phys.*, 49, 217, 1968.

[55] J. T. Dubois, *J. Chem. Phys.*, 25, 178, 1956.

[56] B. Stevens, *Trans. Faraday Soc.*, 51, 610, 1955.

[57] H. Ishikawa and W. A. Noyes, *J., Chem. Phys.*, 37, 583, 1962.

[58] A. Schmillen and R. Legler in "Luminescence of Organic Compounds," Vol. 3, Landolt-Bornstein (N.S.), Springer Verlag, Berlin-Wilmersdorf, 1967.

[59] E. K. C. Lee, M. W. Schmidt, R. G. Shortridge, and G. A. H. Haninger, *J. Phys. Chem.*, 73, 1805, 1969.

[60] C. S. Parmenter and J. D. Rau, *J. Chem. Phys.*, 51, 2242, 1969.

[61] A. Morikawa and R. T. Cvetanovic, *J. Chem. Phys.,* 52, 3237, 1970.

[62] D. R. Snelling, *Chem. Phys. Lett.*, 2, 346, 1968.

[63] B. Stevens and M. F. Tomaz, *Chem. Phys. Lett.*, 1, 549, 1968.

[64] B. Stevens and B. E. Algar, *J. Phys. Chem.*, 72, 2582, 1968.

[65] B. Stevens and B. E. Algar, *J. Phys. Chem*., 72, 3468, 1968.

[66] B. Stevens and B. E. Algar, *J. Phys. Chem*., 72, 3794, 1968.

[67] B. Stevens and B. E. Algar, *J. Phys. Chem*., 73, 1711, 1968.

[68] D. Evans, *J. Chem. Soc.*, 1351, 3885, 1957.

[69] H. Tsubomura and R. S. Mulliken, *J. Amer. Chem. Soc.*, 82, 5966, 1960.

[70] G. Porter and M. R. Wright, *Discuss. Faraday Soc.,* 27, 18, 1959.

[71] J. Weiss, *Trans. Faraday Soc.*, 35, 48, 1939.

[72] D. Evans, *Chem. Commum.*, 367-368, 1969.

[73] K. Gollnick, *Advan. Chem. Ser*., 77, 1968.

[74] Koch, E. *Tetrahedron* 1968, *24,* 6295.

[75] P.R. Ogilby and C. S. Foote, *J. Am. Chem. Soc.*, 1983, 105, 3423.

[76] P.R. Ogilby and C. S. Foote, *J. Am. Chem. Soc.*, 1981, 103, 1219.

[77] D. A. Singleton, C. Hang, M. J. Szymanski, M. P. Meyer, A. G. Leach, K. T. Kuwata, J. S. Chen, A. Greer, C. S. Foote and K. N. Houk, *J. Am. Chem. Soc*., 125, 1319.

[78] C. S. Foote, *Science,* 1968, 162, 3857, 963.

[79] C. S. Foote, *Acc. Chem. Res.*, 1968, 1, 104.

[80] K. Gollnick, *Advan. Photochem*., 6,1, 1968.

[81] F. A. Litt and A. Nickon, "*Oxidation of Organic Compounds III*", Advances in Chemistry Series, 77, American Chemical Society, Washington D. C., 1968, 118.

[82] K. Gollnick, S. Schroeter, G. Ohloff, G. Schade, and G. O. Schenck, *Justus Liebigs Ann. Chem*., 687, 14, 1965.

[83] G. O. Schenck, K. Gollnick, G. Buchwald, S. Schroeter, and G. Ohloff, *Justus Liebigs Ann. Chem*., 674, 93, 1964.

[84] C. S. Foote, *Pure and Applied Chemistry*, 27, 635, 1971.

[85] C. S. Foote and R. W. Denny, *J. Am. Chem. Soc.*, 93, 5162, 1971.

[86] K. R. Kopecky, J. H. Van de Sande, and C. Mumford, *Can. J. Chem.*, 46, 25, 1968.

[87] K. R. Kopecky and C. Mumford, *Can. J. Chem*., 47, 709, 1969.

[88] W. Fenical, D. R. Kearns, and P. Radlick, *J. Amer. Chem. Soc.,* 91, 7771, 1969.

[89] J. Huber, T*etrahedron Letters*, 29, 3271, 1968.

[90] C. S. Foote, J. W.-P. Lin, *Tetrahedron Lett.* 29, 3267-3270, 1968.

[91] R. W. Hoffman and H. Häuser, *Angew. Chem. Int. Ed. Engl.*, 3, 380, 1964.

[92] S. Mazur, C. S: Foote, *J. Am. Chem. Soc.*, 92, 3225, 1970.

[93] M. M .Rauhut, *Accounts Chem. Res*., 2, 80, 1969.

[94] H. F. Cordes, H. P. Richter and C. A. Heller, *J. Am. Chem. Soc.*, 91, 7209, 1969.

[95] C. S. Foote, R. W. Denny, L. Weaver, *Y.* Chang, and J. Peters, A*nn. N. Y. Acad. Sei.,* 171, 139, 1970.

[96] C. S. Foote, J. W. Peters, *J. Am. Chem. Soc.*, 93:15, 1971, 3795.

[97] W. Fenical, D. R. Kearns, and P. Radlick, J. *Am. Chem.* Soc., 91,

[98] C. S. Foote, S. Mazur, P. A. Burns, D. Lerdal*, J. Am. Chem. Soc*., 95, 1973, 586.

[99] J. Boche and 0. A. Rundquist, *J. Org. Chem.,* 33, 4285, 1968.

[100] J.-P. LeRoux and J.-J. Basselier, *C.* R. *Acad. Sci. Paris,* 271, 461, 1970.

[101] H.-S. Ryang and C. S. Foote, *J. Am. Chem. Soc.*, 101, 1979, 6683.

[102] J. D. Spikes and R. Straight, *Annu. Rev. Phys. Chem.*, 18, 409, 1967.

[103] J. D. Spikes and M. McKnight, *Ann. N. Y. Acad. Sci.*, 171, 149, 1970.

[104] G. Jori, *Photochem. Photobiol.,* 21, 463, 1975.

[105] L. Weil, T. S. Seibles, and T. T. Herskovits, *Arch. Biochem. Biophys.,* 11, 308, 1965.

[106] L. Weil, W. G. Gordon, and A. R. Buchert, *Arch. Biochem. Biophys*., 46, 266, 19.

[107] E. W. Westhead, *Biochemistry*, 4, 2139, 1965.

[108] M. Martinez-Carrion, *J. Biol. Chem*., 242, 1426, 1967.

[109] A. Lukton, R. Weisbrod, and J. S. Schlesinger, *Photochem. Photobiol.,* 4, 277, 1965.

[110] J. R. Fisher, G. R. Julian, and S. J. Rogers, *Physiol. Chem*. *Phys.,* 6, 179, 1974.

[111] R. Straight and J. D. Spikes, *Photochem*. *Photobiol.,* 27, 565, 1978.

[112] H. H. Wasserman, K. Stiller, and M. B. Floyd., *Tetrahedron Lett*., 9:29, 3277, 1968.

[113] M. Tomita., M. Ire, and T. Ukita, *Biochemistry*, 8, 5149, 1969.

[114] Matsuura, T., A. Nishinaga, N. Yoshimura, T. Arai, K. Omura, H. Matsushima, S. Kato and I. Saito, 1969, *Tetrahedron Lett.* 1673.

[115] M. Charton, *J. Org. Chem.,* 30, 3346, 1965.

[116] W. F. Reynolds, I. R. Peat, M. H. Freedman, and J. R. Lyerla, *J. Am.* Chem. Soc., 95, 328, 1973.

[117] R. M. S. R. Nandi and H. B. Benusan, *J. Org. Chem.,* 33, 1307, 1966.

[118] T.-Y. Ching, C. S. Foote, *Tetrahedron Lett.*, 44, 3771-3774, 1985.

[119] Matsuura, T., K. Omura and R. Nakashima, 1965, *Bull. Chem. Soc. Jpn 38,* 1358.

[120] Saito, I., S. Kato and T. Matsuura, 1970, *Tetrahedron Lett.* 239.

[121] Matsuura, T., N. Yoshimura, A. Nishinaga and I. Saito, 1969, *Tetrahedron Lett.,* 1669.

[122] Matsuura, T., N. Yoshimura, A. Nishinaga and I. Saito, 1972, *Tetrahedron, 28,* 4933.

[123] Taimr, L. and J. PospiSil, *Macromol. Mater. Eng.*, 39, 1974, 189.

[124] Kharasch, M. S. and B. S. Joshi, 1957, *J. Org. Chem.*, 22, 1439.

[125] Gersmann, H. R. and A. F. Bickel, 1959, *J. Chem. Soc.,* 2711.

[126] Coppinger, C. M., 1964, *J. Am. Chem. Soc.,* 86, 4385.

[127] Howard, J. A. and K. U. Ingold, 1967, *Can. J. Chem.,* 45, 785.

[128] M. J. Thomas, C. S. Foote, *Photochem. and Photobiol*., 27, 683, 1978.

6 ANTIMICROBIAL ACTIVITY OF SINGLET OXYGEN

As we pointed out in Section 5.1, oxygen sensitization was known to microbiologists at the beginning of the last century. The term *oxidative stress* has been coined to indicate the action of reactive oxygen species (ROS) on living organisms. Singlet oxygen belongs to this group, next to peroxides, superoxides, hypochlorite and hydroxyl radicals. Defence mechanisms against ROS developed over the course of evolution, from bacteria to cells, and examples are the enzymes superoxide dismutase and catalase. The first catalyses the transformation of two superoxide ions to molecular oxygen and hydrogen peroxide; the second breaks two molecules of hydrogen peroxide down to water and molecular oxygen. The only defence mechanism against singlet oxygen seems to appear in plants. In biology, light-harvesting complexes and photosystems I and II represent the very engine of plant metabolism. These systems are rich in chlorophylls, whose triplet state well suits the energetic demand for oxygen sensitization. Packed in the supramolecular assembly, molecules of β-carotene puzzled scientists who did not see an immediate need for their present in close proximity to the chlorophylls. Today, we know that β-carotene offers a protection against singlet oxygen; in fact, its triplet state lies lower than that of $^1\Delta_g$ O_2 and inverse energy transfer brings it back to its triplet ground state[1-3].

Since singlet oxygen can be formed by light-independent pathways[4, 5], all kind of organisms have developed diverse mechanisms of response[6, 7]. No matter what the mechanism is, as the amount of ROS increases, more and more damage accumulates, until the point at which the organism undergoes the so-called programmed death or apoptosis. The fact that an organism would program its own death if properly stimulated has opened the way to the use of singlet oxygen as a therapeutic tool. The benefit of singlet oxygen over conventional drugs is that it may be generated locally and its lifetime is limited, allowing both spatial and temporal control of the process. A whole new field has developed, and nowadays photodynamic therapy (PDT) has medical applications to treat pathologies for which sensitizer and light can be easily conveyed to the site of interest[8-12]. If you ever tried to pass white light through one of your fingers, you will know that as it comes out, light has become red. This is a filter effect: according to Rayleigh's law, photon scattering cross-section is inversely proportional to the fourth power of the wavelength[13]. Therefore, blue photons are more likely to be scattered than red ones as they travel through a medium. An important consequence is that tissue penetration is wavelength specific, and only a few centimetres of tissue is sufficient to cut out most of the visible spectrum. For a successful PDT-dye, the strictest requirement is operating at long wavelength. This means having an absorption that extends into the red-NIR part of the spectrum. Such dyes are rare; if on one hand dyes can be modified by increasing the conjugation over extensive aromatic structures and giving raise to NIR absorption, the energy of the excited state could be too little to ensure oxygen sensitization. A variety of photocatalysts generate singlet oxygen upon irradiation in the presence of triplet oxygen. Among them, the most widely used are UV-absorbing compounds including fullerenes[14, 15] naphthalene and anthracene derivatives[16-18] and quinones[19], blue-absorbing flavins[20, 21] and coumarins[22], green-absorbing xanthene derivatives eosin[23, 24], erythrosine[25, 26], fluorescein[26, 27], phloxine[28], Rose Bengal [26] and red-absorbing porphyrins[29-31], phthalocyanines[32] and methylene blue[33, 34]. The D_2O solution absorption spectrum of Rose Bengal (Scheme 9.1) has an absorption maximum at 559 nm and acts as a photosensitizer when irradiated with green light. In contrast, porphyrin-based photosensitizers can be triggered by irradiation in the red region of the

visible spectrum, despite the dominance in the absorption spectrum of the Soret band at higher energy.

Apart from naturally occurring riboflavins and protoporphyrins, the major part of the dyes used in oxygen sensitization is of synthetic origin; light-independent side effects cannot be excluded *a priori*, creating the need for the dye confinement from cytoplasmic media. The use of carriers based on nanostructures (micelles, nanoparticles, polymersomes) seemed appealing because their chemistry can be tuned to meet the optimal requirements for cellular uptake[35, 36]. For our own contribution to this area, we chose to explore the use of so-called 'nanoreactors' through which we could deliver singlet oxygen on demand. The use of nanoassemblies, based both on natural and synthetic polymers, provides an efficient approach to photodynamic therapy[37, 38] and to the generation of surfaces with antimicrobial properties[39]. Polymer vesicles, referred to as polymersomes, are excellent candidates since they are mechanically more stable than the lipid counterpart (liposomes). The chemical nature of the amphiphilic copolymer renders polymersomes biocompatible and stimuli-responsive, with their water cavity which permits the encapsulation of hydrophilic compounds and their lipophilic membrane allows the insertion of hydrophobic compounds[40, 41]. An elegant solution to improve the control of the photosensitizers is not to release them at the desired bio-region[42, 43], but to ensure that they remain encapsulated in polymersomes allowing one to produce reactive species "on demand" upon irradiation[44, 45].

6.1 Photosensitizer

The choice of the sensitizer was a porphyrin-based one. Two reasons can be given to support the choice: first, we had accumulated considerable synthetic experience and spectroscopic data on porphyrins and porphyrin-conjugates, and secondly, porphyrin-derivatives can be easily made water-soluble. This latter point is critical because a catalyst which works in a homogeneous phase is a strict requirement in biology. Commercially, there are three types of water-soluble porphyrins: those obtained through functionalization of the phenyl groups of H_2TPP with carboxylic acid or sulfonate groups and those obtained by *N*-alkylation of 5,10,15,20-tetra(pyridin-4-yl)porphyrin (TPyP). The first two options strictly require that the added groups are not modified if solubility is to be preserved, therefore we discarded them in favour of *N*-alkylation which allows significant variation in structure and structure-related properties. Symmetric alkylation of TPyP introduces a positive charge on each of the four peripheral nitrogen atoms (sharply increasing solubility in water) and, at the same time, allows the introduction of a variety of functionalities at the termini of the alkyl chain. In the present investigation, an ester functionality was chosen, giving the potential for further derivatization at a later stage. The compound TPyCP (Scheme 6.1) was prepared by treatment of TPyP with an excess ethyl 6-bromohexanoate in boiling DMF according to the previously reported method[46].
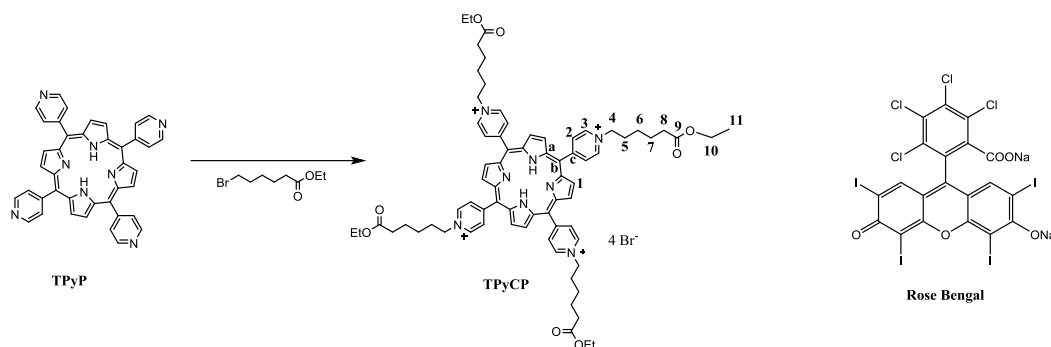
Scheme 6.1 (left) synthesis of TPyCP. Numbering is for NMR spectroscopic assignment (section 7.6). (right) structure of Rose Bengal.

Fig. 6.1 shows the solution absorption spectrum of TPyCP in D_2O with all the hallmarks of a free-base porphyrin: an intense Soret band with λ_{max} = 424 nm (ε_{max} = 48,500 L cm^{-1} mol^{-1}) and four Q bands at lower energy (λ_{max} = 519, 555, 586 and 640 nm, ε_{max} = 3400, 1400, 1400 and 300 L cm^{-1} mol^{-1}, respectively). The absorptions at higher energy (<400 nm) arise from the alkylpyridinium units. Since the absorption extends over a wide portion of the visible spectrum, we could activate the photocatalyst TPyCP by operating a three-wavelength LED: 470, 505 and 660 nm. To be noted that LED-light is not monochromatic and a quantitative measure of the size of the bands can be given by the full width at half maximum: 40 nm for 470 nm, 30 nm for 505 nm and 20 nm for 660 nm[47]. Fig. 6.1 highlights the overlap of these excitation bands with the absorption spectrum of TPyCP and Scheme 6.2 summarizes the relevant energy levels of TPyCP compared to the ground and low-lying excited states of O_2[48]. The energy of the TPyCP T_1 state is taken from the literature data for the model compound 5,10,15,20-tetra(*N*-methylpyridin-4-yl)-21*H*,23*H*-porphyrin tetrachloride[49].
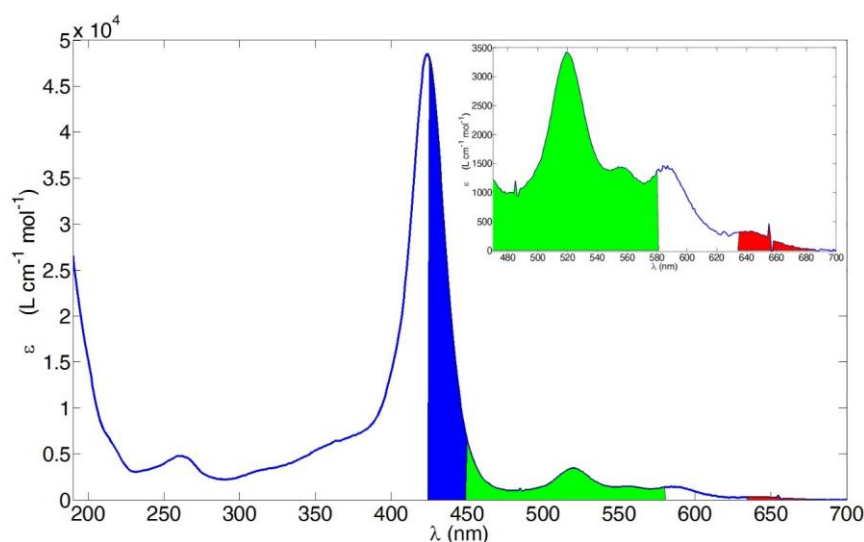
Fig. 6.1 Absorption spectrum of TPyCP (4 µM in D_2O). The coloured areas show the overlap of the absorption with the emission bands of the LED used for the irradiation. (inset) Expansion of the green-red part of the spectrum.

Scheme 6.2 provides a visual aid to visualize how energy flows in the system: irradiation at 470 nm populates the S_2 state of TPyCP, whilst irradiation at 505 or 660 nm populates the S_1 state. After deactivation to the lowest vibrational S_1 state, an intersystem crossing leads to TPyCP in the T_1 state. In fluid solution, T_1 is non-emissive and lives long

enough (lifetime = 170 μs) to be quenched by molecular oxygen[49]. Energy transfer from the T_1 state of TPyCP to molecular O_2 can occur to either of the $^1\Sigma_g$ or $^1\Delta_g$ excited states since both are of appropriate energy (Scheme 6.2).Whichever it is, $^1\Sigma_g$ quickly deactivates to $^1\Delta_g$ and singlet oxygen reactivity uniquely derives from this state[50]. Thus, further reference to singlet oxygen refers exclusively to $^1\Delta_g$ O_2.
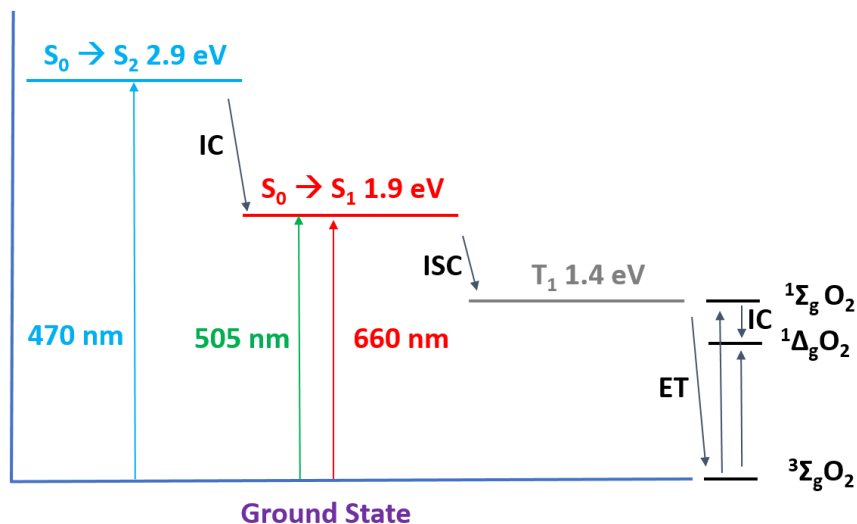
Scheme 6.2 Energetic level diagram for TPyCP. IC = internal conversion, ISC = intersystem crossing, ET = energy transfer. The arrows represent LED excitation wavelengths. Due to its vibrational structure, S_1 level can be populated by both green and red irradiation.

Even though absorption properties and position of the T_1 state are the most important parameters, we recorded emission and excitation spectra for TPyCP to have a complete characterization. Interestingly, excitation at 260 nm (alkylpyridinium unit) induces emission from both pyridinium ion and porphyrin (Fig. 6.2). While energy transfer accounts for porphyrin emission, fluorescence at 320 nm deserves a deeper look.

Pyridine is not emissive at room temperature in fluid solution. This is easily understood in the light of its electronic levels: the lowest energy transition, involves the excitation of one electron located in a nonbonding orbital (n→π*); the second is of π→π* nature. Absorption spectrum of pyridine displays an intense band with regard to π→π* and a much weaker n→π*. n→π* transitions are characterized by much smaller absorption cross sections than those of π→π* ones. The primary reason is the poor overlap between nonbonding and π*orbitals. As a result, lifetime of nπ* states is 100-fold longer than that of ππ* and non-radiative decays become dominant[51]. Another property of nπ* states is the increased rate of intersystem crossing, up to three times higher when the compound possesses a ππ* state lying below the nπ* one[52]. Another way to phrase this principle is according to IUPAC definition: "*the rate of intersystem crossing is relatively large if the radiationless transition involves a change in orbital type*"[53]. Therefore, $^1(\pi,\pi^*)$→$^3(n,\pi^*)$ is faster than $^1(\pi,\pi^*)$→$^3(\pi,\pi^*)$ and $^1(n,\pi^*)$→$^3(\pi,\pi^*)$ is faster than $^1(n,\pi^*)$→$^3(n,\pi^*)$, one to the latter being pyridine case. A look at the extinction coefficients indicates that direct population of the $^1(\pi,\pi^*)$ state is strongly favoured and the only happening under normal conditions. This state is not emissive, with all of the electronic energy ultimately being dissipated by means of internal conversion to $^1(n,\pi^*)$, intersystem crossing to $^3(\pi,\pi^*)$ and internal conversion to the ground state (Scheme 6.3).
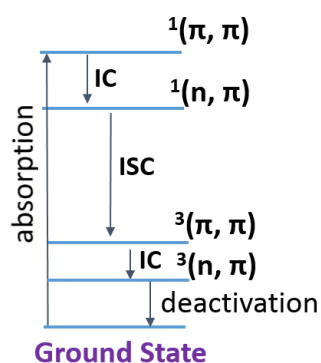
Scheme 6.3 Energetic level diagram for pyridine. IC = internal conversion, ISC = intersystem crossing. Levels are not in scale.

Fluorescence was first detected in the vapour phase at low pressures from $^1(n,\pi^*)$[54] and only recently pyridine has been made emissive by pressure-induced fluorescence from $^1(\pi,\pi^*)$[55]. A diamond anvil cell compressed the liquid to the point that if formed solid domains, resulting in the first detection of fluorescence for solid pyridine. The authors interpret this as a swapping of the level order from $^1(\pi,\pi^*) > ^1(n,\pi^*)$ in pyridine to $^1(\pi,\pi^*) < ^1(n,\pi^*)$ in crystalline pyridine[55]. The situation is radically different for protonated/alkylated pyridines. Placing a positive charge on the nitrogen rearranges the level to the point that $^1(\pi,\pi^*)$ becomes the lowest excited state and fluorescence becomes a feasible deactivation pathway[56].
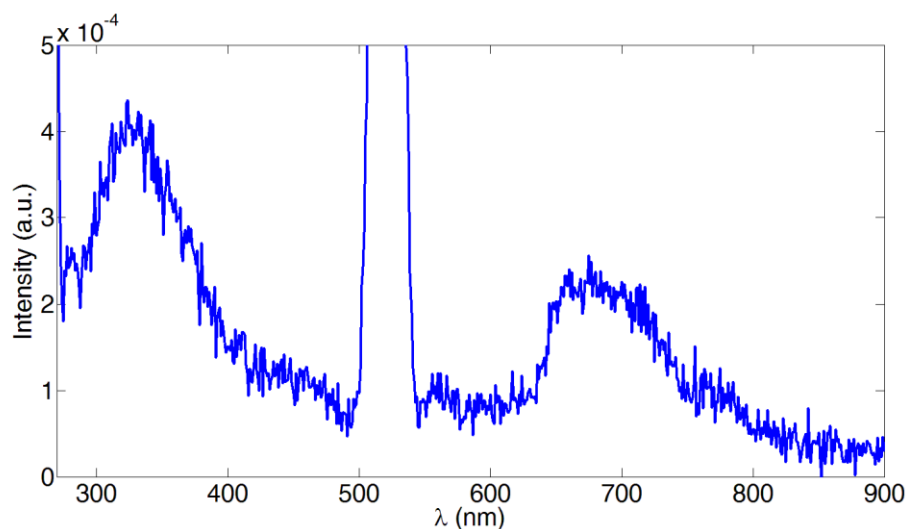
Fig. 6.2 Solution emission spectrum of TPyCP (D$_2$O, 2 µM, λ_{exc}= 260 nm). The peak at 520 nm corresponds to the first harmonic and its intensity has therefore been cut.

Exciting TPyCP in the Soret or Q bands results in the emission from the porphyrin core Fig. 6.3. Emission occurs as a broad band, which extends from 660 to 720 nm, centred at 690 nm. It should be noted that the detector is not saturated and reabsorption of emitted light does not occur under the experimental conditions employed; the plateau shape of the emission band is not an artefact. Last, in Fig. 6.4 we report the excitation spectrum for the TPyCP monitored at 710 nm (porphyrin fluorescence). Interestingly, no bands appear to be present around 260 nm (pyridinium absorption), but this can be easily explained bearing in mind that excitation of the pyridinium unit leads to very little fluorescence as already shown in Fig. 6.2.
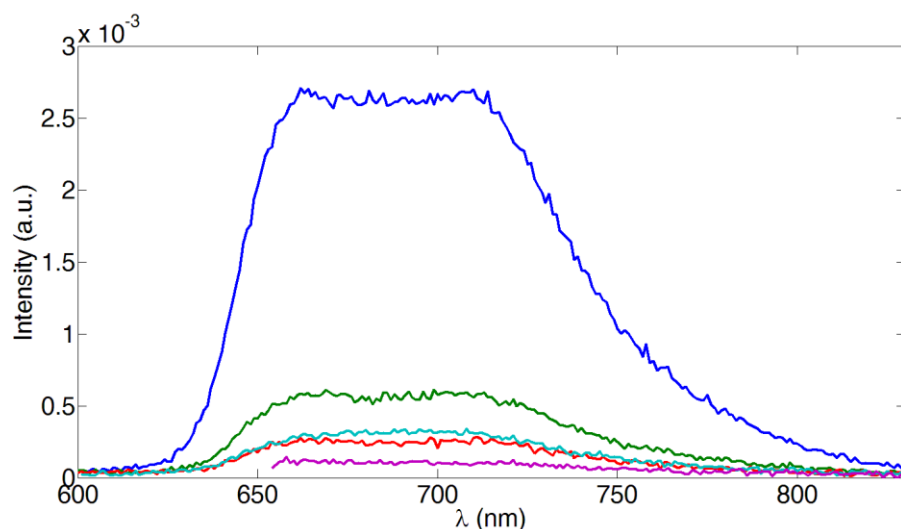
Fig. 6.3 Solution emission spectrum of TPyCP (D$_2$O, 2 µM): (blue) λ_{exc} = 424 nm, (dark green) λ_{exc} = 520 nm, (red) λ_{exc} = 560 nm, (turquoise) λ_{exc} = 580 nm and (violet) λ_{exc} = 640 nm.
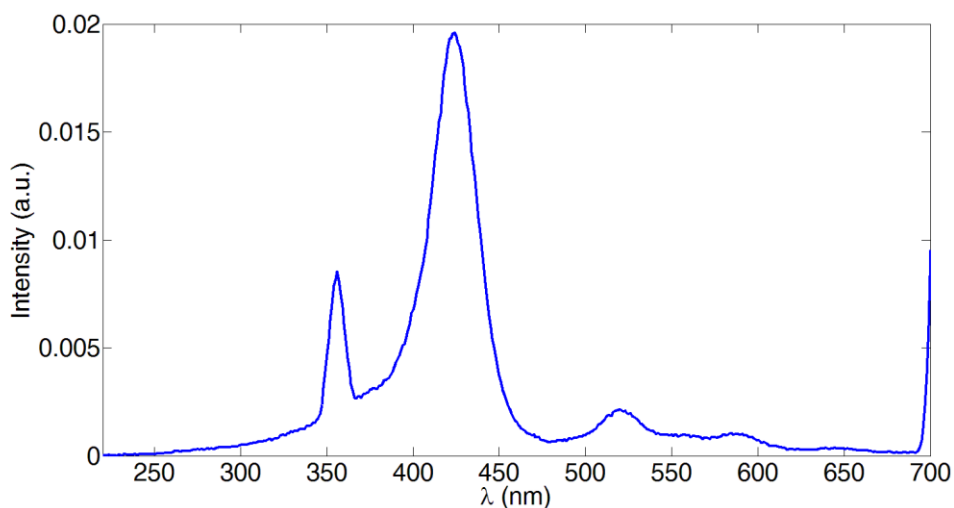
Fig. 6.4 Solution excitation spectrum of TPyCP (D$_2$O, 2 µM, λ_{emi}= 710 nm). The peak at 355 nm corresponds to an artefact created at half of the detection wavelength.

6.2 Preliminary studies

Having the photocatalyst in our hands, we needed to prove that it is able to work as a molecular oxygen sensitizer. As substrate, we chose the amino acid L-methionine[57]; its selective photocatalytic oxidation to the sulfoxide represents a model for the oxidation of methionine residues in proteins[58-61]. An aqueous solution of L-methionine containing 0.06 mol% of TPyCP was irradiated with red light (λ_{exc} = 660 nm) and the reaction mixture was monitored by ^{1}H NMR spectroscopy. Complete and selective conversion of L-methionine to L-methionine sulfoxide (IUPAC name (S)-2-amino-4-(methylsulfinyl)butanoic acid) (Scheme 6.4) was achieved in 61 h. The ^{1}H and ^{13}C NMR spectra of the product (Fig. 6.5 and 6.6) were consistent with those of pristine L-methionine sulfoxide[62]. A comparison of the spectra of L-methionine and L-methionine sulfoxide confirmed the generation of a second stereogenic

centre (Fig. 6.5 and 6.6) with ^{13}C NMR resonances for atoms C^2 and C^5 (see labelling in Scheme 6.4) each showing the presence of the expected two diastereoisomers.
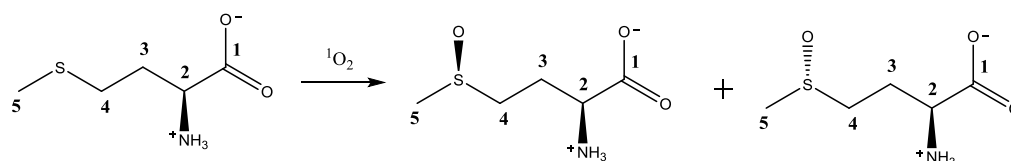
Scheme 6.4 Conversion of L-methionine to the diastereoisomeric pair of L-methionine sulfoxides. Atom labels are for NMR spectroscopic assignments.
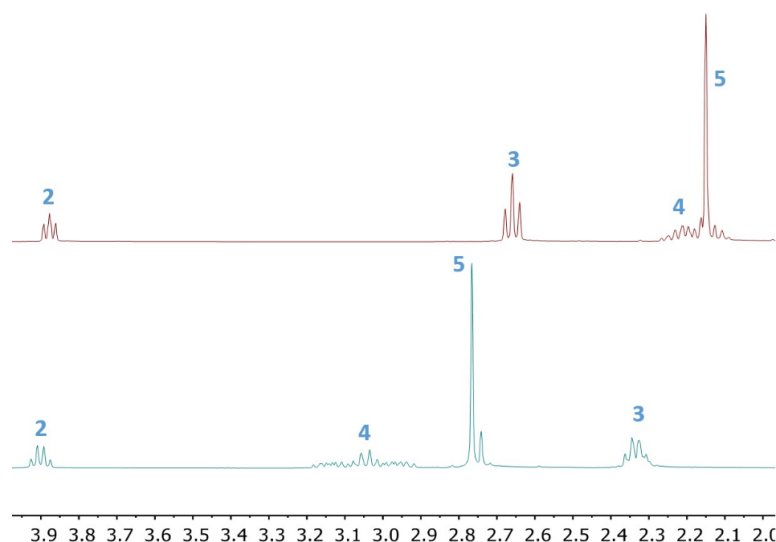
Fig. 6.5 400 MHz ^{1}H NMR spectra of a D$_2$O solution of L-methionine (top) and L-methionine sulfoxide (bottom). Numbering refers to Scheme 6.1.
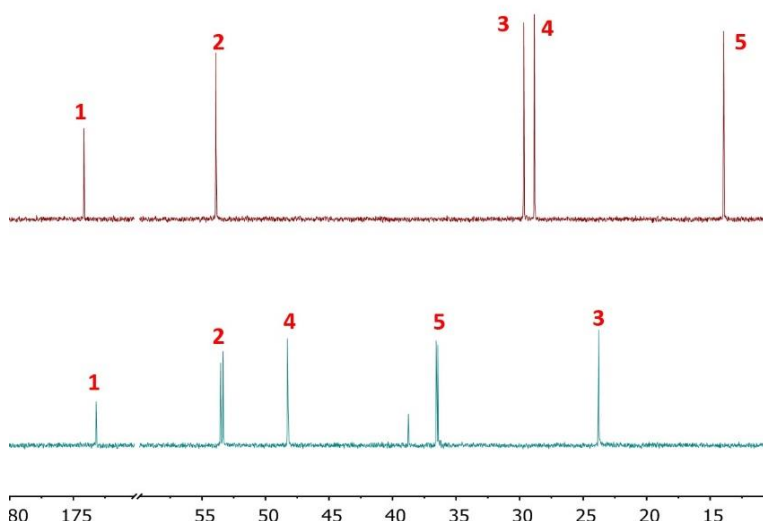
Fig. 6.6 400 MHz ^{13}C NMR spectra of a D$_2$O solution of L-methionine (top) and L-methionine sulfoxide (bottom). Numbering refers to Scheme 6.1.

The ESI-MS of the product showed a peak at m/z = 165.94 corresponding to [M+H]$^+$, M being L-methionine sulfoxide (Fig. 6.7 left). Isolation in the quadrupole trap and fragmentation of the ion at m/z = 166 lead to the pattern shown in Fig. 6.7 right. This preliminary study confirmed that even though light absorption by TPyCP at 660 nm is low

88

(300 at this wavelength L cm^{-1} mol^{-1}, Fig. 6.1), a 0.06 mol% catalytic loading is sufficient to realize complete selective oxidation within 61 h.
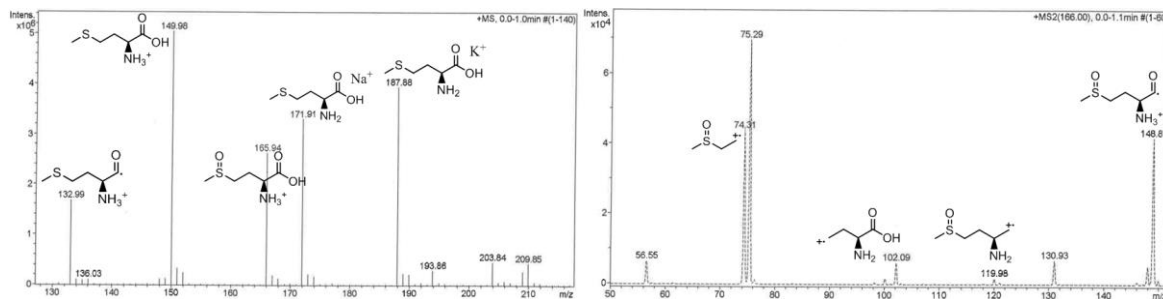
Fig. 6.7 (left) ESI-MS of the reaction mixture containing both L-methionine and L-methionine sulfoxide. (right) MS-MS of the ion with *m/z* = 166.00. Fragmentation pattern is displayed on top.

TPyCP is characterized by several absorption bands, of which the one in the red part of the spectrum is the weakest. If it is true that excitation in the red is a specific requirement for the photocatalyst we are designing, one could think that excitation in a region where the absorption coefficient is higher would result in a faster conversion or diverse reactivity. In order to confirm that the rate of reaction was not affected by irradiating the sample with higher energy light, the reaction was repeated using λ_{exc} = 470, 505 and 660 nm. For each reaction, 0.35 mmol of L-methionine in 5 mL D$_2$O containing 0.06 mol% of TPyCP was used, and the reaction was followed by ^{1}H NMR spectroscopy. Despite the differences in overlap of the absorption spectrum of TPyCP with the LED excitation bands shown in Fig. 6.1, there was no difference in the rate of the reaction (Fig. 6.8). This can be rationalized in terms of the energy level diagram shown in Scheme 6.2. Recall that irradiation at 470 nm populates the S$_2$ state of TPyCP, while with λ_{exc} = 505 or 660 nm, the S$_1$ state is directly populated. The first process after excitation, regardless of the excitation wavelength, is the fast (according to Kasha's rule) relaxation to lower lying excited states and ultimately to T$_1$. From T$_1$, oxygen sensitization occurs independent of the wavelength of the excitation light, and so the photocatalysis yields at any given time will be the same.

Fig. 6.8 L-Methionine conversion (given as % on the ordinate) to the diastereoisomeric L-methionine sulfoxides in the presence of 0.06 mol% TPyCP. λ_{exc} = 470 nm (blue), λ_{exc} = 505 nm (green), λ_{exc} = 660 nm (red).

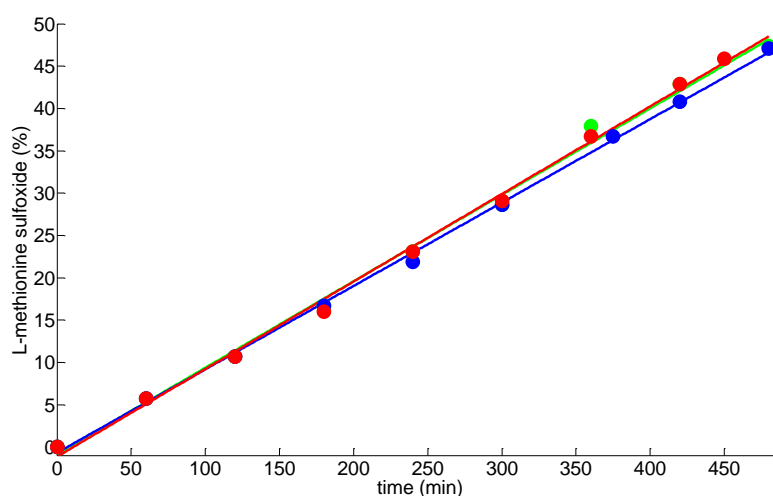We next carried out a comparative investigation of the kinetics of the selective oxidation of L-methionine using TPyCP or the commercially available Rose Bengal as photosensitizer. Rose Bengal has been and still is extensively used in photooxygenation (many of the reactions in Section 5.3 made use of it), and it was of interest to determine whether use of the TPyCP could be advantageous over that of Rose Bengal. An important point to make is that the data in Fig. 6.8 confirmed that TPyCP acts with equal efficiency upon irradiation at 505 or 660 nm. In contrast, Rose Bengal possesses no absorption at 660 nm[63] and, as expected, no conversion of L-methionine to its sulfoxides was observed upon irradiating at this wavelength (data not shown).

For the kinetic experiments, a D_2O solution of L-methionine (0.42 mmol) was irradiated in the presence of TPyCP (0.2 mol%) or Rose Bengal (1 mol%) with λ_{exc} = 660 or 505 nm, respectively. The reaction was monitored by ^1H NMR spectroscopy and the results are shown in Fig. 6.9. Both photocatalysts lead to complete conversion of L-methionine to a 1:1 ratio of both diastereoisomers of L-methionine sulfoxide, and although Fig. 6.9 might suggest that the reaction with Rose Bengal is faster, it is significant that TPyCP is present at 0.2 mol% compared to 1 mol% of Rose Bengal. The difference in the concentration of the two dyes derives from the fact that TPyCP would convert the substrate too quickly at a concentration of 1 mol%. Our last statement could be confusing: classical kinetic theory requires photocatalytic rate constants to be independent on catalyst concentration and obey a zero-order kinetic equation. While the kinetic profile is clearly of zero-order (Fig. 6.8 and 6.9), catalyst concentration does play a role (Fig. 6.10). We will come back to this issue later in this chapter, specifically when we discuss in detail the kinetic treatment of L-methionine conversion (Section 6.3).
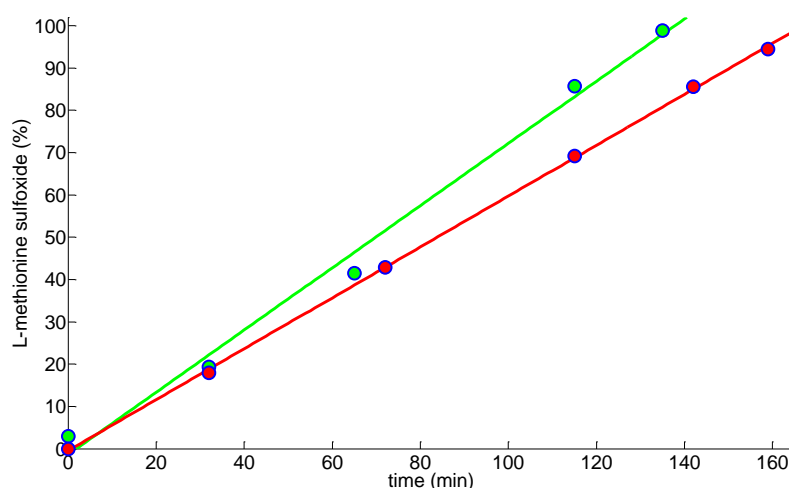
Fig. 6.9 Conversion of a 0.42 mmol L-methionine solution in D_2O in presence of 0.2 mol% TPyCP (red) or 1 mol% Rose Bengal (green). Irradiation was performed at 505 nm for Rose Bengal or at 660 nm for TPyCP. Data points (circles) and linear best fit (straight lines), r^2 = 0.9915 for Rose Bengal and 0.9872 for TPyCP.
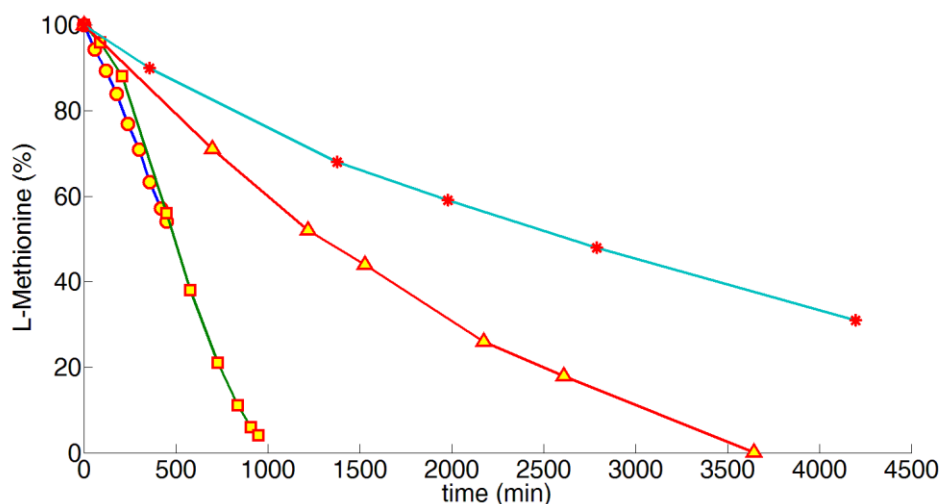
Fig. 6.10 L-methionine (270 mM in D$_2$O) conversion for a TPyCP concentration of 150 μM (0.055 mol%) (circles), 67 μM (0.024 mol%) (squares), 34 μM (0.013 mol%) (triangles) and 17 μM (0.006 mol%) (stars) (λ$_{exc}$ = 660 nm).

We next varied the catalyst loading and depending on the photocatalyst concentration, either an exponential or linear regime was observed (Fig. 6.10). Keeping the methionine concentration at 270 mM, for a porphyrin concentration of 150 and 67 μM, a near-linear correlation of conversion to reaction time is observed. If the photocatalyst concentration is either of 34 or 17 μM, an exponential decay is observed.

6.3 Kinetic treatment

The addition of oxygen to L-methionine and subsequent formation of diastereoisomeric L-methionine sulfoxides has been studied in the past[57, 64] and the mechanism shown in Scheme 6.5 has been proposed.
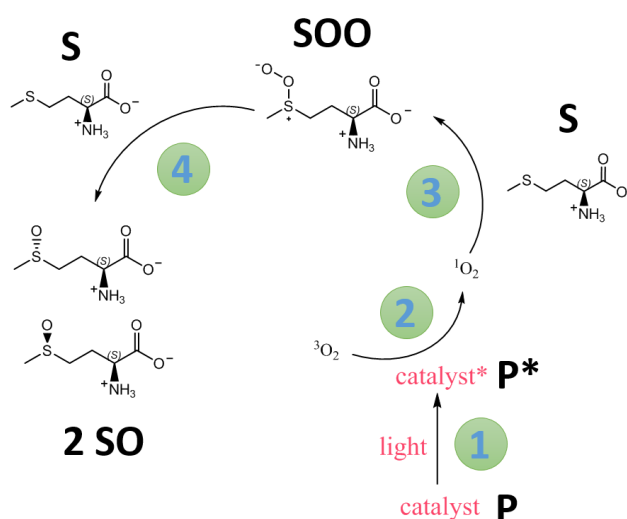
Scheme 6.5 Proposed mechanism for the photocatalytic oxidation of L-methionine [based on scheme in ref. [57].

The scheme can be summarized, and made more general, by writing equations 1–4 in which **P** and **P*** are the porphyrin catalyst in its ground and excited state, respectively, $^3O_2$ and $^1O_2$ are molecular oxygen in its triplet ground and singlet excited state, respectively; **S** is the sulfide, **SOO** the persulfoxide intermediate and **SO** the final sulfoxide (see Scheme 6.5).

$$P + h\nu \xrightarrow{k_1} P^* \qquad (1)$$

$$P^* + {}^3O_2 \xrightarrow{k_2} {}^1O_2 \qquad (2)$$

$$S + {}^1O_2 \xrightarrow{k_3} SOO \qquad (3)$$

$$SOO + S \xrightarrow{k_4} 2\,SO \qquad (4)$$
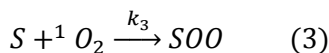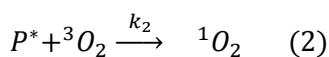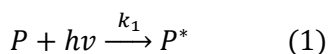
From eqns. 1–4, we can derive eqns. 5–9 for species in the catalytic cycle.

$$\frac{d[P^*]}{dt} = k_1 - k_2[{}^3O_2][P^*] \qquad (5)$$

$$\frac{d[{}^1O_2]}{dt} = k_2[{}^3O_2][P^*] - k_3[S][{}^1O_2] \qquad (6)$$

$$\frac{d[S]}{dt} = -k_3[S][{}^1O_2] - k_4[SOO][S] \qquad (7)$$

$$\frac{d[SOO]}{dt} = k_3[{}^1O_2][S] - k_4[SOO][S] \qquad (8)$$

$$\frac{d[SO]}{dt} = 2k_4[SOO][S] \qquad (9)$$

Experimentally, it is not possible to detect **SOO**. It does not accumulate over the course of the reaction and we may therefore apply the steady state approximation for this intermediate (eqn. 10 and 11).

$$\frac{d[SOO]}{dt} = k_3[{}^1O_2][S] - k_4[SOO][S] = 0 \qquad (10)$$
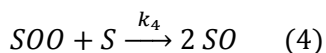
$$[SOO] = \frac{k_3[{}^1O_2]}{k_4} \qquad (11)$$

Equation 11 requires that **SOO** does not accumulate if $k_4 \gg k_3$. Substituting eqn. 11 into eqn. 7 leads to eqn. 12, and hence, eqn. 13.

$$\frac{d[S]}{dt} = -2k_3[S][{}^1O_2] \qquad (12)$$

$$[S] = e^{-2k_3[{}^1O_2]t} \qquad (13)$$

From eqn. 13, it follows that the consumption of L-methionine depends exponentially on the supply of oxygen (represented by k_3) and the concentration of singlet oxygen. The latter dependency can be eliminated if we consider the experimental setup. Triplet oxygen, $^3O_2$, is introduced into the reaction vessel by means of a pump, which keeps the concentration of $^3O_2$ constant at the saturation level of the solvent. In addition, the concentration of the catalyst in the excited state (**P***) is also constant. This is due to the fact that the

concentration used is such that the absorbance of the reaction mixture at the LED λ_{exc} = 660 nm is 0.09 ([catalyst] = 150 µM, path length = 2.5 cm, ε = 200 L mol^{-1} cm^{-1}) which converts to 19% of the excitation light being absorbed as it travels through the reaction flask. It is true that, once excited, **P** is in the lowest singlet excited state, whereas it is the lowest triplet excited state that is able to transfer energy to molecular oxygen. Due to inter-system crossing (ISC) which is a unimolecular process, **P*** relaxes to this state, which constitutes the active state of the catalyst. We have no reason to assume that any of those processes (light absorption in non-saturated conditions and ISC) are time dependent. Furthermore, the extent of the energy transfer to ground state molecular oxygen is a property of a given couple of molecules, and therefore time independent as well. The latter two considerations allow us to simplify eqn. 12 by applying the steady-state approximation to $^1O_2$ (eqn. 14-15). This species is the product of the reaction between **P*** and $^3O_2$, concentrations of which are constant over time.

$$\frac{d[^1O_2]}{dt} = k_2[^3O_2][P^*] - k_3[S][^1O_2] = 0 \quad (14)$$

$$[^1O_2] = \frac{k_2[^3O_2][P^*]}{k_3[S]} \quad (15)$$

Substituting eqn. (15) into eqn. (12) gives eqn. 17 in which $[S]_0$ is the initial concentration of L-methionine. Eqn 17 shows a linear relationship between [S] and t. All of the other dependencies are eliminated.

$$\frac{d[S]}{dt} = -2k_2[^3O_2][P^*] \quad (16)$$

$$[S] = [S]_0 - 2k_2[^3O_2][P^*]t \quad (17)$$

6.4 Biological application

The following section results from the work of MSc Myrto Kyropoulou with whom the author collaborated as part of an NCCR project and with whom he worked closely during the polymersome applications. Myrto Kyropoulou studied the formation of PMOXA6-PDMS34-PMOXA6 polymersomes (Section 6.4.1), she performed the encapsulation of TPyCP into them (Section 6.4.2), assessed their catalytic activity against L-methionine (Section 6.4.3), conducted bacterial essays in their presence both by mean of counting the colonies (section 6.4.4) and staining (Section 6.4.5). Finally, Section 6.4.6 deals with the experimental details.

6.4.1 Polymersome formation

The 3D-structures resulting from the self-assembly of PMOXA$_6$-PDMS$_{34}$-PMOXA$_6$ copolymer, with and without porphyrin, were characterized by a combination of TEM and light scattering. TEM micrographs (data not shown) indicate that, in both cases, a major population of spherical assemblies is formed, with radii of $\approx$100 nm. To confirm that the morphology corresponds to a hollow sphere (morphology expected for a polymersome), we used static light scattering (SLS) and dynamic light scattering (DLS) to determine the radius of

gyration (R_g) and the hydrodynamic radius (R_h), respectively. R_g is defined as "a distance such that if all the mass of a rotating body were at this distance from the axis of rotation, the moment of inertia of the body would be the same"[65], and R_h as the radius of an hard sphere that diffuses at the same rate as the molecule we approximate with it; R_h includes both solvent and shape effects. A perfectly spherical hollow object will possess R_g/R_h = 1[66]. Copolymers in both the presence and absence of TPyCP self-assembled in spherical supramolecular assemblies with R_g ≈100 nm, and R_g/R_h values ranging from 0.91 up to 1.08.

6.4.2 Encapsulation of TPyCP into polymersome

The encapsulation strategy relies on the presence of TPyCP in the rehydration buffer used to trigger the self-assembly of block-copolymers. Upon closure, the polymeric bilayer will segregate a portion of the buffer, which will constitute its inner volume, in turn encapsulating the dye. The process is conceived in such a way that a fraction of the photosensitizer is not encapsulated. This portion was removed by size-exclusion chromatography, passing the polymersome solution on a Sephadex column. Fluorescence spectroscopy was performed on the purified polymersomes to check whether TPyCP had successfully been encapsulated (data not shown). As expected, the lower the porphyrin concentration in the buffer, the lower the polymersome fluorescence signal. We focused on the TPyCP emission and not on absorption because fluorescence is far more sensitive and TPyCP is present at micromolar concentration.

6.4.3 Photocatalytic activity

The key point in our strategy is the embedding of the catalyst in a confined space, from which only the reactive species generated by irradiation can escape and react with molecules present in the outer volume. We relied on singlet oxygen being able to cross the membrane[44] and to the fact that its lifetime is ten times larger in heavy water than in water. These considerations lead us to perform all the experiments in deuterated water and to choose L-methionine as a benchmark for our system.

To a solution of L-methionine (270 mM in D_2O) was added a suspension of TPyCP-containing polymersomes; all in a flask open to air. The mixture was irradiated and conversion was assessed via ^1H NMR taken at different times (Fig. 6.11). To confirm that the purification process removed excess TPyCP, we tested a suspension which contained empty polymersomes mixed with 200 µM TPyCP for 48h and then purified under the same conditions. In addition, a 150 µM L-methionine solution in D2O was exposed to molecular oxygen to confirm that self-oxidation of L-methionine does not occur. Only the system comprising TPyCP-loaded polymersomes (Fig. 6.11) was efficient in terms of singlet oxygen generation and conversion of L-methionine. Porphyrin-loaded polymersomes successfully converted L-methionine to L-methionine sulfoxides in an exponential manner that reached complete conversion after 26 hours of irradiation. As expected, no oxidation of L-methionine was observed in the presence of empty polymersomes.
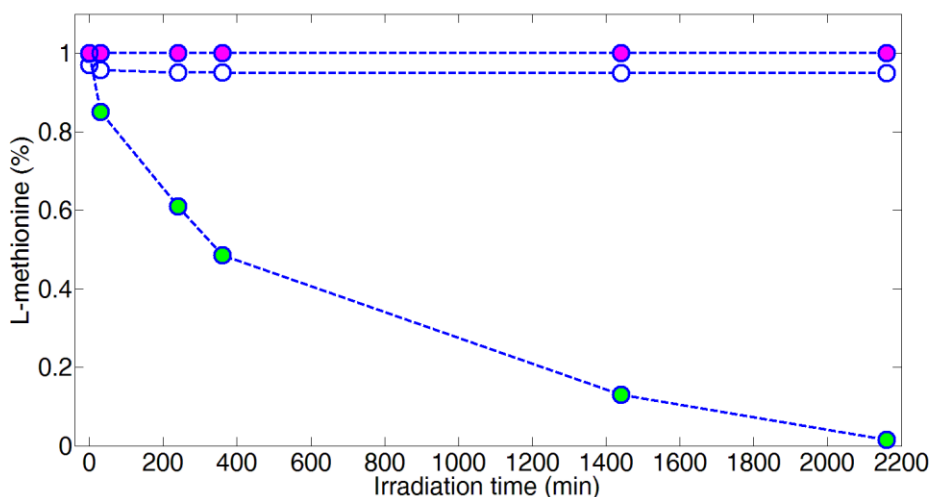
Fig. 6.11 L-Methionine conversion to (*R*)/(*S*)-sulfoxide by TPyCP-loaded polymersomes (initial TPyCP concentration = 200 µM) (green circles), L-methionine only (magenta circles) and empty polymersomes incubated with 200 µM TPyCP and then purified (empty circles); λ_{exc} = 660 nm.

6.4.4 Bacterial assay: colony-forming units (CFU)

With all the data pointing towards a retained photocatalytic activity in polymersomes, we went on and tested TPyCP-loaded polymersomes with respect to their ability to inhibit or prevent the growth of bacteria, using a previously established protocol[67]. We determined the correlation between the colony-forming units (CFU) of *E. coli* in presence of TPyCP (200 µM in D_2O) or TPyCP-loaded polymersomes (pre-encapsulation TPyCP concentration = 200 µM in D_2O), upon irradiation and in dark conditions (Figs. 6.12 and 6.13). CFU is a key-parameter defined as the number of bacteria in a sample that is able to multiply under experimental conditions. Singlet oxygen generation induces oxidative stress, which ultimately leads to the degradation of a plethora of biomolecules and, eventually, to death of the microorganism.

Irradiation at 660 nm of the culture containing TPyCP caused a CFU reduction of 31% after 30 min, and up to 94% after 360 min (Fig. 6.12). Under the same irradiation, cultures in the absence of TPyCP or TPyCP-loaded polymersomes were unharmed (Fig. 6.12). Controls experiment showed that bacterial population remained constant over a period of at least 360 min at room temperature under same irradiation. The logical conclusion is that viability of *E. coli* was not affected either by sole irradiation or by addition of substrates (when added singularly), but from the combination of light and sensitizer.
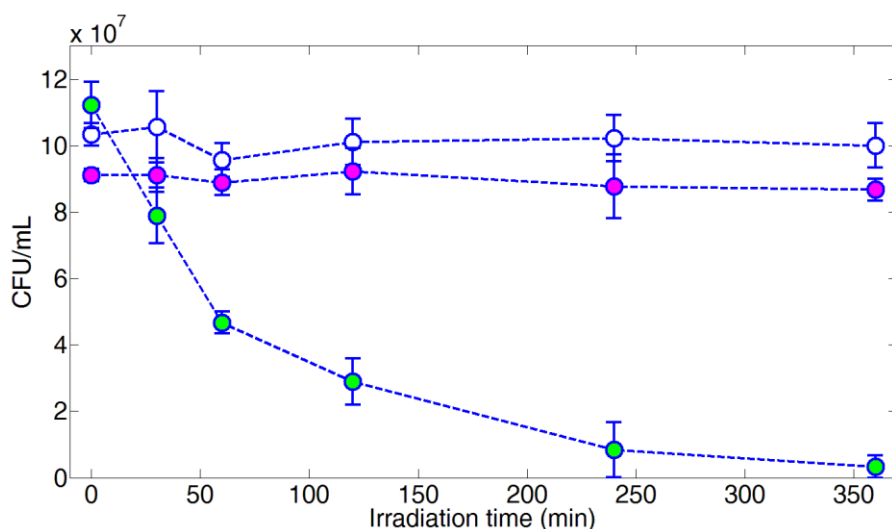
Fig. 6.12 CFU for *E. coli* culture upon addition of 200 μM TPyCP and irradiation with a LED red source (λ$_{max}$ = 660 nm) (green circles), no irradiation nor addition of external factors (empty circles), no irradiation but addition of 200 μM TPyCP (magenta circles).

Similar behaviour was observed for bacterial cultures treated with porphyrin-loaded polymersomes: CFU values were drastically reduced only under the combined action of irradiation and sensitizer (Fig. 6.13). As expected, exposure to empty polymersomes did not influence bacterial growth upon irradiation. Furthermore, porphyrin-loaded polymersomes had no effect on CFU in the dark.
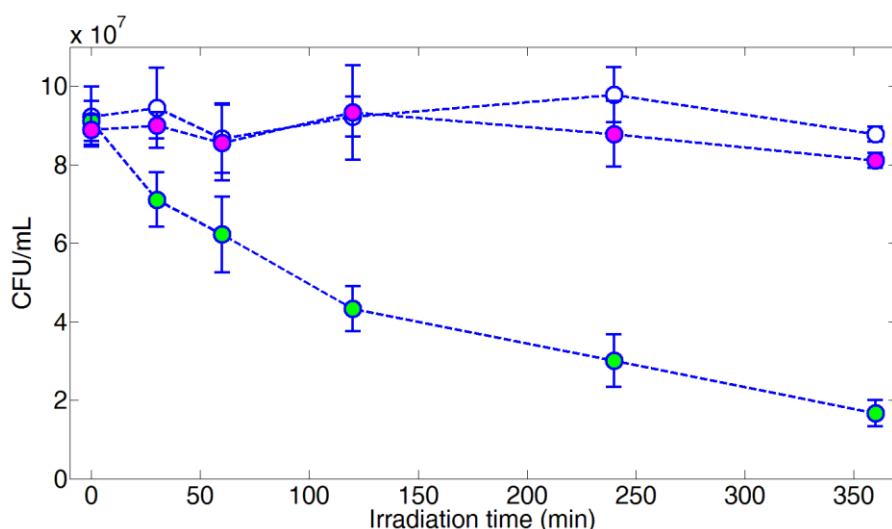
Fig. 6.13 CFU for *E. coli* culture upon addition of TPyCP-loaded polymersomes and irradiation with a LED red source (λ$_{max}$ = 660 nm) (green circles), no irradiation nor addition of external factors (empty circles), no irradiation but addition of TPyCP-loaded polymersomes (magenta circles).

6.4.5 Bacterial assay: live/dead® staining

CFU values constitute a quantitative approach; a qualitative one derives from staining *E. coli* cultures with the commercial kit "live/dead BacLight"[68]. The kit consists of a 1:1 mixture of green-fluorescent nucleic acid stain (SYTO 9) and red-fluorescent nucleic acid stain (propidium iodide). The principle behind the kit is that the two stains differ both in

their spectral characteristics and in their ability to penetrate bacterial membranes. When used alone, SYTO 9 generally penetrates in the whole bacterial population, i.e. in bacteria with intact membranes and in those with damaged ones. In contrast, propidium iodide crosses only damaged membranes. Most importantly, propidium iodide causes a reduction in SYTO 9's fluorescence if both are present. Fig 6.14 rationalises why the energy transfer takes place[69]. A good overlap exists between the absorption spectrum of propidium iodide (red solid line) and the emission spectrum of SYTO 9 (dashed green line). Förster energy transfer accounts for the quenching of SYTO 9 in presence of suitable amounts of propidium iodide.
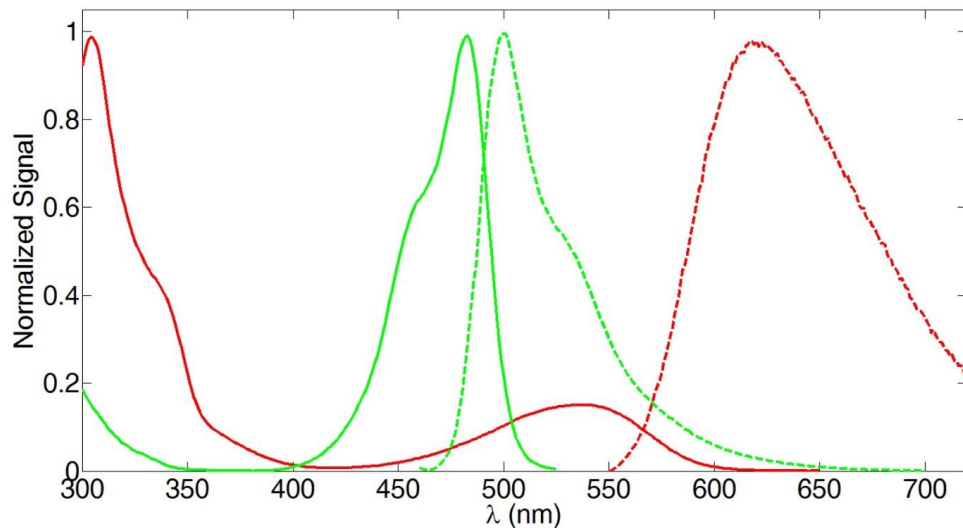
Fig. 6.14 Solution absorption (solid) and emission (dashed) spectrum of propidium iodide (red) and SYTO 9 (green) in water[69].

Liquid cultures of *E. coli* were exposed to the oxidizing conditions described earlier, with the only difference being the staining step. Therefore, bacteria with intact cell membranes (considered alive) will fluoresce green, whereas apoptotic ones will fluoresce red. Fig. 6.15 shows how *E. coli* cultures treated with 200 µM TPyCP initially contained mainly alive bacteria (green dots in the confocal picture). After 30 min of irradiation, the number of green bacteria had reduced, and after 240 min (Fig. 6.15d) most of the bacteria stain red. Within 360 min of irradiation, the population turns red (Fig. 15e). Of greater significance to us is what happens when TPyCP is enclosed in polymersomes (Fig. 6.16). Again, at the beginning the bacteria stain green, while as the irradiation time goes, the population shifts towards red. After 360 min of irradiation (Fig. 6.16e), almost all of the bacteria are apoptotic. Once more, the hypothesis of a retention of function upon encapsulation is confirmed by an independent technique.
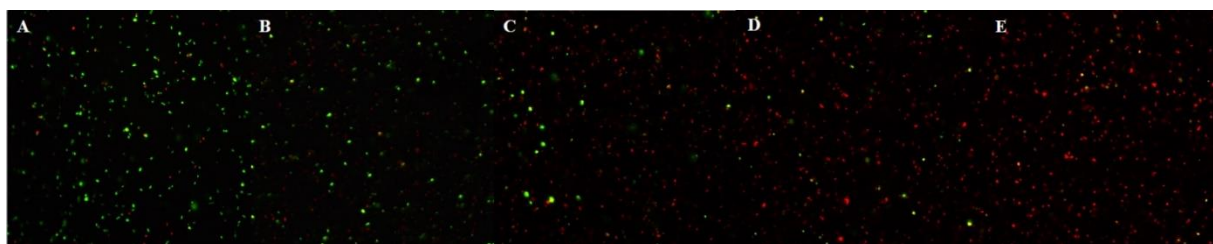
Fig. 6.15 *E. coli* stained with SYTO 9 ("alive", green) and propidium iodide ("dead", red) incubated in presence of 200 µM free TPyCP after (a) 0 min, (b) 30 min, (c) 120 min, (d) 240 min and (e) 360 min of illumination under red LED light (λmax= 660 nm).
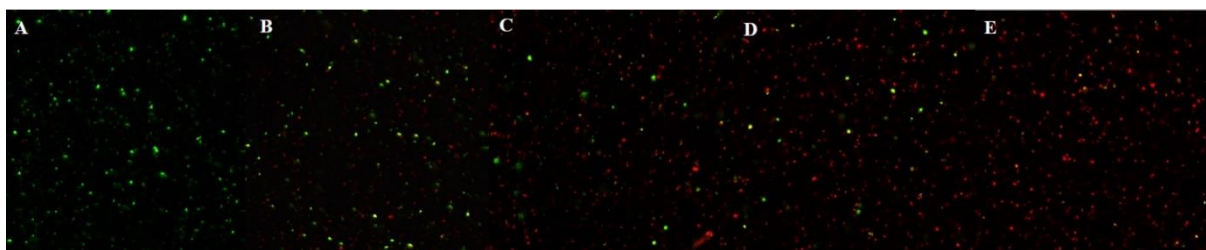
Fig. 6.16 *E. coli* stained with SYTO 9 ("alive", green) and propidium iodide ("dead", red) incubated in presence of TPyCP-loaded polymersomes after (a) 0 min, (b) 30 min, (c) 120 min, (d) 240 min and (e) 360 min of illumination under red LED light (λmax= 660 nm).

Concluding, a water-soluble porphyrin dye has been prepared and tested against photosensitized conversion of triplet to singlet oxygen. The presence of many absorption bands allows the compound to be excited all over the visible range, with the deep red region being of interest because of high tissue penetration. The compound acts as a photocatalyst for the oxidation of L-methionine and, more importantly, its activity is not diminished by encapsulation in polymersomes. Although TPyCP does not diffuse outside of the polymersomes, diffusible, long-lived and reactive singlet oxygen does diffuse and react with external substrate. Encapsulation allows incubating the compound with a bacterial culture, without the drawback of the photosensitizer diffusing in the media. As expected, live bacteria decrease significantly when TPyCP is added to their medium and exposed to irradiation. Of greater interest is the observation that the same happens when bacteria are treated with TPyCP-loaded polymersomes and are irradiated with red light. These promising results prove the antimicrobial activity of TPyCP-polymersome system and make us consider expanding the biological evaluation towards in vitro studies on human cells.

6.4.6 Experimental

LED: the LED light source used to activate the photocatalyst was a THORLABS 4-Wavelength High-Power LED Source LED4D067[47].

TPyCP: the compound TPyCP was prepared according to literature[46]. The compounds TPyP, ethyl 6-bromohexanoate and L-methionine were purchased from Sigma-Aldrich and used without further purification.

Photocatalysis: L-Methionine (200 mg, 1.34 mmol) and TPyCP (0.25 mg, 0.165 μmol, 0.013 mol%) were dissolved in D_2O (5 mL) in a 5 mL round bottomed flask. The reaction was repeated using 0.006 mol% catalyst loading: L-methionine (200 mg, 1.34 mmol) and TPyCP (0.12 mg, 0.79 μmol, 0.006 mol%). In each case, the flask was closed with a rubber septum and two needles were inserted through the septum. A pump was connected to one needle to bubble air into the solution, the other was used as an exhaust. The LED lamp was placed so that the light source was perpendicular to the flask ensuring that the whole of the solution was irradiated. Conversion was monitored using ^{1}H NMR spectroscopy.

Kinetics: L-methionine (63 mg, 0.42 mmol) was dissolved in D_2O (5 mL) in a 5 mL round-bottomed flask. Either TPyCP (1.3 mg, 0.84 μmol, 0.2 mol%) or Rose Bengal (4.3 mg,

4.2 µmol, 1 mol%) were added to the solution and the flask was capped with a rubber septum and two needles were inserted through the septum. The flask was connected to a pump to force air in through one needle and the second needle was the outlet. The mixture containing Rose Bengal was irradiated at 505 nm and that with TPyCP at 660 nm. Conversion of L-methionine to L-methionine sulfoxide was monitored using ^{1}H NMR spectroscopy. Reactions were repeated with different catalyst loadings as detailed in the text. Kinetic studies were also performed with the TPyCP loaded polymersomes in three different initial concentrations.

Polymersome preparation: the amphiphilic triblock copolymer PMOXA$_{34}$-PDMS$_6$-PMOXA$_{34}$ was prepared as previously described[70]. Polymersomes formed by the film rehydration method[71]. The aforementioned polymer (5 mg) was dissolved in MeOH (1 mL) and dried under vacuum to form a polymer film on the inner bottom surface of a 5 mL glass flask. The polymer film was rehydrated with Tris-buffer (50 mM, pH 7.6) at room temperature for 48 h in the dark in the presence or absence of a 200 µM TPyCP D$_2$O solution, respectively. The suspension was then sequentially extruded through 0.2 µm and 0.1 µm Nucleopore Track-Etch membranes from Whatman using an Avanti Extruder (Avanti Polar Lipids, USA). Any TPyCP left in solution was separated from the polymersomes containing TPyCP by passage through a HiTrap desalting column (Sephadex G-25 Superfine, GE Healthcare, UK) or a 20 cm^3 in-house prepacked column (Sepharose 2B, Sigma Aldrich). The polymersomes obtained were characterized by light scattering measurements (LS) and transmission electron microscopy (TEM).

Transmission Electron Microscopy: For visualization, 10 µL of a polymersome solution was negatively stained with 2% aqueous uranyl acetate solution, deposited on a carbon-coated copper grid, and then examined with a transmission electron microscope (Philips Morgani 268 D) operating at 80 kV.

Light scattering: dynamic (DLS) and static (SLS) light-scattering experiments were performed on an ALV (Langen, Germany) goniometer equipped with an ALV He–Ne laser (JDS Uniphase, wavelength λ = 632.8 nm). Polymersome emulsions were serially diluted to polymer concentrations ranging from 5 to 0.325 mg/mL, and measured in 10 mm cylindrical quartz cells at angles of 30–150° and a temperature of 293 K ± 0.5 K. The photon intensity autocorrelation function $g^2(t)$ was determined with an ALV-5000E correlator (scattering angles between 30° and 150°). A non-linear decay-time analysis supported by regularized inverse Laplace transform of $g^2(t)$ (CONTIN algorithm) was used to analyse DLS data. The angle-dependent apparent diffusion coefficient was extrapolated to zero momentum transfer (q^2) using the ALV/Static and dynamic FIT and PLOT 4.31 software. Angle and concentration-dependent SLS data were analysed using Guinier plots. Errors were calculated from the deviation of the fit parameters using the ALV/Static&Dynamic FIT and PLOT software.

Confocal laser-scanning microscopy (CLSM): CLSM experiments were performed on a confocal laser-scanning microscope (Zeiss LSM 880, Carl Zeiss, Jena, Germany) with an Argon/2 laser (λ = 488 nm, 30 mW, 10% power output, 0.5% transmission) as the excitation source. A main dichromatic beam splitter (HFT 488/543), and a band pass filter (BP 505-530) were used in all experiments. The images were recorded with a water immersion objective (C-Apochromat 40x/1.2W).

Bacterial assays: aliquots of 5 µL taken from a stock *E. coli* colony were dispersed into 15 mL of lysogenic broth (LB) in a 50 mL falcon tube. The suspension was shaken at 180 rpm in an incubator overnight at 37 °C, with the cup not entirely closed to allow molecular oxygen to diffuse and reach the bacteria. The culture was then concentrated by centrifugation at 10^4 g for 10–15 minutes. The supernatant was removed and the culture was suspended in 15 mL of phosphate buffered saline solution (PBS), centrifuged again to remove the remaining media and suspended for the last time in 15 mL of PBS containing 1% tryptic soy broth (TSB). The bacterial culture was serially diluted (10^{-1} to 10^{-5} CFU/10 µL, CFU being colony forming units) in a 24-well plate. In the last liquid culture, which corresponds to the desired dilution, 200 µL of an aqueous TPyCP solution or a solution with polymersomes containing TPyCP were added. The 24-well plate was kept in the dark until the exposure to LED irradiation started. Liquid cultures were taken and placed into LB-Agar plates after 0, 30, 120, 240 and 360 min of irradiation. The plated cultures were incubated overnight at 37 °C and the colonies formed counted. As a control, the same series of experiment were performed in the absence of TPyCP. Furthermore, a dark control was performed: an *E. coli* culture in the presence of TPyCP was kept in the dark by means of aluminum foil wrapping. Three independent experiments were run, and for each three replicates were plated. Both controls were carried out during each experiment. All the *E. coli* essays were carried out in a sterile environment.

Live/Dead® staining for microscopy: for this assay, the Live/Dead® BacLight[68] bacterial Viability Kit for microscopy has been used. Briefly, the *E. coli* bacteria liquid cultures were grown as described previously, with the difference that instead of PBS, aqueous 0.85% NaCl (0.85 g per 100 mL) was used as the suspension buffer. After illumination with a red LED light at 660 nm, the cultures were stained with a 1:1 mixture of SYTO 9[72], which belongs to the family of SYTO dyes and is a cell-permeant nucleic acid stain, and propidium iodide dyes using 3 µL of 72 nM stain per 1 ml of sample, and then incubated for 10 min at room temperature. Bacteria with intact cell membranes (considered alive) stained fluorescent green, whereas bacteria with damaged membranes (considered dead) stained fluorescent red. The excitation/emission maxima for these dyes are in the range 480-500 nm for SYTO 9 and 490-635 nm for propidium iodide. The background remains virtually non-fluorescent. The results were analysed by CLSM.

References

[1] C. S. Foote, R. W. Denny, *J. Am. Chem. Soc.*, 90:22, 1968, 6233.

[2] C. S. Foote, Y. W. Chang, R. W: Denny, *J. Am. Chem. Soc.*, 92:17, 1970, 5216.

[3] C. S. Foote, Y. W. Chang, R. W: Denny, *J. Am. Chem. Soc.*, 92:17, 1970, 5218.

[4] S. Miyamoto, G. R. Martinez, M. H. G. Medeiros, P. Di Mascio, *J. Photochem. Photobiol. B*: Biology 139, 2014, 24.

[5] H. Wefers, *Bioelectrochem. Bioenerg.*, 18, 1987, 91.

[6] E. C. Ziegelhoffer, T. J. Donohue, *Nat. Rev. Microbiol.*, 2009, 7, 856.

[7] C. Triantaphylid_s, M. Havaux, *Trends Plant Sci.,* 2009, 14, 219.

[8] T. J. Dougherty, C. J. Gomer, B. W. Henderson, G. Jori, D. Kessel, M, Korbelik, J. Moan and Q. Peng, *J. Natl. Cancer. Inst.*, 1998, 90, 889.

[9] E. F. Gudgin Dickson, R. L. Goyan, R. H. Pottier, *Cell. Mol. Bio.,* 2002; 48, 939.

[10] B. C. Wilson, *Can. J. Gastroenterol.,* 2002; 16, 393.

[11] D. E. Dolmans, D. Fukumura and R. K. Jain, *Nat. Rev. Cancer,* 2003; 3, 380.

[12] M. B. Vrouenraets, G. W. Visser, G. B. Snow and G. A. van Dongen, *Anticancer Res.,* 2003; 23, 505.

[13] John Strutt (1871) "On the light from the sky, its polarization and colour," *Philosophical Magazine*, series 4, vol.41, pages 107–120, 274–279. (b) John Strutt (1871) "On the scattering of light by small particles," *Philosophical Magazine*, series 4, vol. 41, pages 447–454. (c) John Strutt (1881) "On the electromagnetic theory of light," *Philosophical Magazine*, series 5, vol. 12, pages 81–101. (d) John Strutt (1899) "On the transmission of light through an atmosphere containing small particles in suspension, and on the origin of the blue of the sky," *Philosophical Magazine*, series 5, vol. 47, pages 375–394.

[14] M. Orfanopoulos, S. Kambourakis, 1995, *Tetrahedron. Lett.*, 36, 435.

[15] N. Tagmatarchis, H. Kato and H. Shinohara, 2001, *Phys. Chem. Chem. Phys.*, 3, 3200.

[16] D. J. McGarvey, P. G. Szekeres and F. Wilkinson, 1992, *Chem. Phys. Lett.*, 199, 314.

[17] A. F. Olea and F. Wilkinson, *J. Phys. Chem.*, 1995, 99, 4518.

[18] E. Baciocchi, C. Crescenzi and O. Lanzalunga, 1997, *Tetrahedron,* 53, 4469.

[19] I. Gutierrez, S. G. Bertolotti, M. A. Biasutti, A. T. Soltermann and N. A. García, 1997, *Can. J. Chem.*, 75, 423.

[20] J. Dad'ová, E. Svobodová, M. Sikorski, B. König and R. Cibulka, 2012, *ChemCatChem*, 4, 620.

[21] A. Yoshimura and T. Ohno, 1988, *Photochem. Photobiol.*, 48, 561.

[22] J. J. Inbaraj, R. Gandhidasan, S. Subramanian and R. Murugesan R, 1998, *J. Photochem. Photobiol. A*, 117, 21.

[23] E. Gandin, Y. Lion, A. van de Vorst, 1983, *Photochem. Photobiol.*, 37, 271.

[24] P. Bilski, L. J. Martinez, E. B. Koker, C. F. Chignell, 1998, *Photochem. Photobiol.*, 68, 20.

[25] J. N. Chacon, J. McLearie, R. S. Sinclair, 1988, *Photochem. Photobiol.*, 47, 647.

[26] D. C. Neckers, 1989, *J. Photochem. Photobiol. A*, 47, 1.

[27] N. Miyoshi, G. Tomita, 1980, *Z. Naturforsch.,* 35b, 731.

[28] K. Arakane, A. Ryu, K. Takarada, T. Masunaga, K. Shinmoto, R. Kobayashi, S. Mashiko, T. Nagano and M. Hirobe, 1996, *Chem. Pharm. Bull.,* 44, 1.

[29] S. M. Bonesi, M. Mella, N. D'Alessandro, G. G. Aloisi, M. Vanossi and A. Albini, 1998, *J. Org. Chem.,* 63, 9946.

[30] Y. Liu, A. J. Howarth, J. T. Hupp and O. K. Farha, 2015, *Angew. Chem. Int. Ed.,* 54, 9001.

[31] M.-H. Xie, X.-L. Yang, C. Zou, C.-D. Wu, 2011, *Inorg. Chem.,* 50, 5318.

[32] S. Kimel, B. J. Tromberg, W. G. Roberts, M. W. Berns, 1989, *Photochem. Photobiol.,* 50, 175.

[33] M. Wainwright, D. A. Phoenix, L. Rice, S. M. Burrow, J. Waring, 1997, *J. Photochem. Photobiol. B,* 40, 233.

[34] S. J. Wagner, A. Skripchenko, D. Robinette, J. W. Foley, L. Cincotta, 1998, *Photochem. Photobiol.,* 67, 343.

[35] R. R. Allison, H. C. Mota, V. S. Bagnato, C. H. Sibata, 2008, *Photodiag. Photodyn. Therapy*, 5, 19.

[36] M. G. Walker, P. J. Jarman, M. R. Gill, X. Tian, H. Ahmad, P. A. N. Reddy, L. McKenzie, J. A. Weinstein, A. J. H. M. Meijer, G. Battaglia, C. G. W. Smythe, J. A. Thomas, 2016, *Chem. Eur. J.,* 22, 5996.

[37] D. Bechet, P. Couleaud, C. Frochot, M.-L. Viriot, F. Guillemin, M. Barberi-Heyob, 2008, *Trends Biotechnol.*, 26, 612.

[38] X. Li, M. Gao, K. Xin, L. Zhang, D. Ding, D. Kong, Z. Wang, Y. Shi, K. Kiessling, T. Lammers, J. Cheng, Y. Zhao, 2017, *J. Contolled Release*, 260, 12.

[39] K. Langowska, J. Kowal, C. G. Palivan, W. Meier, 2014, *J. Mater. Chem. B*, 2, 4684.

[40] C. G. Palivan, R. Goers, A. Najer, X. Zhang, A. Car, W. Meier, 2016, *Chem. Soc. Rev.*, 45, 377.

[41] L. Guan, L. Rizzello, G. Battaglia, 2015, *Nanomedicine,* 10:2757–2780.

[42] A. Najer, D. Wu, D. Vasquez, C. G. Palivan, W. Meier, 2013, *Nanomedicine*, 8, 28.

[43] G. Gunkel-Grabole, S. Sigg, M. Lomora, S. Lörcher, C. G. Palivan, W. P. Meier, 2015, *Biomater. Sci.,* 3, 25.

[44] P. Baumann, V. Balasubramanian, O. Onaca-Fischer, A. Sienkiewicz, C. G. Palivan, 2013, *Nanoscale*, 5, 217.

[45] P. Baumann, M. Spulber, I. A. Dinu, C. G. Palivan, 2014, *J. Chem. Phys. B*, 118, 9361.

[46] K.-P. S. Dancil, L. F. Hilario, R. G. Khoury, K. U. Mai, C. K. Nguyen, K. S. Weddle, A. M. Shachter, 1997, *J. Heterocyclic Chem.*, 34, 749.

[47] THORLABS LED Source. https://www.thorlabs.de/newgrouppage9.cfm?objectgroup_id=3836.

[48] M. C. De Rosa, R. J. Crutchley, 2002, *Coord. Chem. Rev.,* 233, 351.

[49] M. Montalti, A. Credi, L. Prodi, M. T. Gandolfi, 2006, *Handbook of Photochemistry*, 3rd edn, CRC Press, Boca Raton., page 137.

[50] M. Kasha, A. U. Khan, 1970, *Ann. New York Acad. Sci.,* 171, 5.

[51] B. Valeur, *Molecular Fluorescence: principles and applications*; Wiley-VCH: Weinheim, 2002.

[52] M. A. El-Sayed, *Acc. Chem. Res*., 1968, 1, 8.

[53] https://goldbook.iupac.org/html/E/ET07369.html. Last access on 11th October 2017.

[54] I. Yamazaki, H. Baba, *J. Chem. Phys*., 1977, 66, 5826–5827.

[55] S. Fanetti, M. Citroni and R. Bini, *J. Phys. Chem. B*, 2011, 115, 12051.

[56] T. Handa, Y. Utena, H. Yajima, T. Ishii and H. Morita, *J. Phys. Chem.*, 1986, 90, 2589.

[57] M. J. Davies, 2004, *Photochem. Photobiol. Sci.*, 3, 17.

[58] E. Folzer, K. Diepold, K. Bomans, C. Finkler, R. Schmidt, P. Bulau, J. Huwyler, H.-C. Mahler, A. V. Koulov, 2015, *J. Pharmaceutical. Sci.*, 104, 2824.

[59] R. Petitdemange, E. Garanger, L. Bataille, W. Dieryck, K. Bathany, B. Garbay, T. J. Deming, S. Lecommandoux , 2017, *Biomacromolecules*, 18, 544.

[60] F. Mulinacci, S. E. J. Bell, M. A .H Capelle, R. Gurny, T. Arvinte, 2011, *J. Pharmaceutical Sci.*, 100, 110.

[61] R. Saletti, S. Reina, M. G. G. Pittala, R. Belfiore, V. Cunsolo, A. Messina, V. De Pinto, S. Foti, 2017, *Biochim. Biophys. Acta*, 1859, 301.

[62] www.hmdb.ca/metabolites/HMDB02005. Accessed 02 July 2017.

[63] http://omlc.org/spectra/PhotochemCAD/html/084.html. Last access on 11th October 2017.

[64] P. K Sysak, C. S. Foote, T.-Y. Ching, 1977, *Photochem. Photobiol.*, 26, 19.

[65] https://en.oxforddictionaries.com/definition/radius_of_gyration. Last access on 11th October 2017.

[66] O. Stauch, R. Schubert, G. Savin, W. Burchard, 2002, *Biomacromolecules,* 3, 565.

[67] N. M. M. Moura, C. I V. Ramos, I. Linhares, S. M. Santos, M. A. F. Faustino, A. Almeida, J. A. S. Cavaleiro, F. M. L. Amado, C. Lodeirobc, M. G. P. M. S. Neves, 2016, *RSC Adv.*, 6, 110674.

[68] https://assets.thermofisher.com/TFS-Assets/LSG/manuals/mp07007.pdf. Last access on 11th October 2017.

[69] https://www.chroma.com/spectra-viewer?fluorochromes=10406,10448. Last access on 11th October 2017.

[70] S. Lörcher, W. Meier, 2017, *Eur. Polymer J.*, 88, 575.

[71] M. Lomora, M. Garni, F. Itel, P. Tanner, M. Spulber, C. G. Palivan, 2015, *Biomaterials*, 53, 406.

[72] https://assets.thermofisher.com/TFSAssets/ LSG/manuals/mp07572.pdf. Last access on 11th October 2017.

7 SINGLET OXYGEN ON ALIPHATIC SULFIDES

In this chapter we exploit our photocatalyst (TPyCP) to explore the oxidation of a wide range of aliphatic sulfides. Given the number of substrates, we divided them into families: Section 7.1 deals with sulfur-containing aminoacids, Section 7.2 with heterocycles containing one sulfur atom, Section 7.3 with heterocycles containing two sulfur atoms, Section 7.4 with heterocycles containing three sulfur atoms and Section 7.5 with heterocyclic aliphatic sulfides. Section 7.6 contains all the NMR spectroscopic data.

A well-established reaction in organic chemistry is the oxidation of sulfides. Depending on the oxidant, both the sulfoxide and the sulfone can be easily obtained in high yields. The reaction proceeds stoichiometrically and, if no stereoselectivity is required, simple addition of $NaIO_4$ will form the sulfoxide[1] whilst addition of H_2O_2 gives both the sulfoxide and the sulfone[2, 3]. Under particular conditions (decomposition of hydrogen peroxide in the presence of catalytic amounts of Na_2WO_4 tungsten oxide), selectively the sulfoxide can be obtained[4]. Homogeneous catalytic oxidation at sulfur is also well-established, and, being sulfur a prochiral centre in R_1SR_2, oxidation in presence of a chiral catalyst yields a specific enantiomer. Catalysts are based on aluminium[5], titanium[6], vanadium[7], manganese[8], iron[9], copper[10], tungsten[11] or osmium[12]. At room temperature, inversion at sulfur is generally slow and sulfoxides retain their stereogenic centre[13]. Sulfoxides find application as solvents, as ligands[14-17], as pharmaceuticals[18-21] and as chiral auxiliaries[22-25]. Synthetic procedures which utilize dioxygen rather than a high-valent oxidizing agent have an added value, especially if the oxidation reaction can be made photocatalytic[26-30]. We will show how, in addition to making use of O_2, photocatalysis with lower energy light has the advantage of modulating the degree of oxidation with substrates containing more than one reactive site.

Experimentally, 1 mmol of the investigated compounds has been dissolved in 4 mL of deuterated solvent (D_2O, DMSO-d_6 or MeOD). TPyCP was added in catalytic amounts (0.25 mol%); only for the compounds lamivudine and emtricitabine it was present as 1 mol%, to accelerate the reaction. The reaction mixture was placed in a 5 mL round bottomed flask, which was closed with a rubber septum and two needles were inserted through the septum. A pump was connected to one needle to bubble air into the solution, air that previously passed through protiated solvent to pre-saturate it; the other was used as an exhaust. The LED red lamp was placed so that the light source was perpendicular to the flask ensuring that the whole of the solution was irradiated at 660 nm. In the following sections, we will show both proton and carbon NMR spectra of starting materials and products; complete conversion was achieved for all the substrates that reacted with singlet oxygen. The spectra are presented as figures in the chapter, with the peaks numbered to facilitate the assignment. The signals are fully listed and assigned in Section 7.6 and references to literature data are given for already known compounds.

7.1 Sulfur containing amino acids

Of all the natural occurring amino acids, the only ones that are reactive towards singlet oxygen constitute a small subgroup, due to the presence in their structure of a reactive functional group. Singlet oxygen reacts preferably with aromatics and sulfur-containing molecules and reaction with tryptophan, histidine, tyrosine, methionine and cysteine have been reported to be major targets[31]. Of these five substrates, clean and complete conversion to products is only observed for methionine and cystine. Another three derivatives exist, namely homocysteine, S-phenyl-L-cysteine and 4-thiazolidine carboxylic acid, and these are presented in Scheme 7.1.
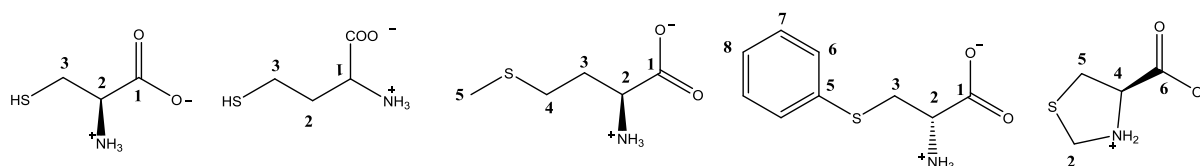
Scheme 7.1 Structures of L-cysteine (**1**), DL-homocysteine (**2**), L-methionine (**3**), S-phenyl-L-cysteine (**4**), 4-thiazolidine carboxylic acid (**5**). Positions are numbered for NMR assignment.

Singlet oxygen has proved to react differently with sulfur, depending on its oxidation state[31]. When present as a thiol, oxidation leads to the disulfide as is known for cysteine and homocysteine, while sulfides are oxidized to the sulfoxide (methionine and S-phenyl-L-cysteine). Further exposure of the products to the photocatalyst, once the conversion is completed, does not result in a transformation to the sulfone or related compounds; an evidence that supports singlet oxygen selectivity.

L-cysteine and DL-homocysteine are fully soluble in D_2O, but once the photocatalyst transforms them into their disulfide forms, they precipitate as they form. Even though the low solubility of cystine and homocystine , it was still possible to detect their presence in solution by ^1H NMR spectroscopy (Fig. 7.1 left for L-cysteine and Fig. 7.1 right for DL-homocysteine). Recording a ^{13}C NMR spectrum proved to be more difficult. A significant increase in the acquisition time did not result in a better signal to noise ratio. HMBC and HMQC experiments run on cystine and homocystine gave well resolved 2D spectra only for homocystine (Fig. 7.2), while carbon data could not be collected for cysteine.
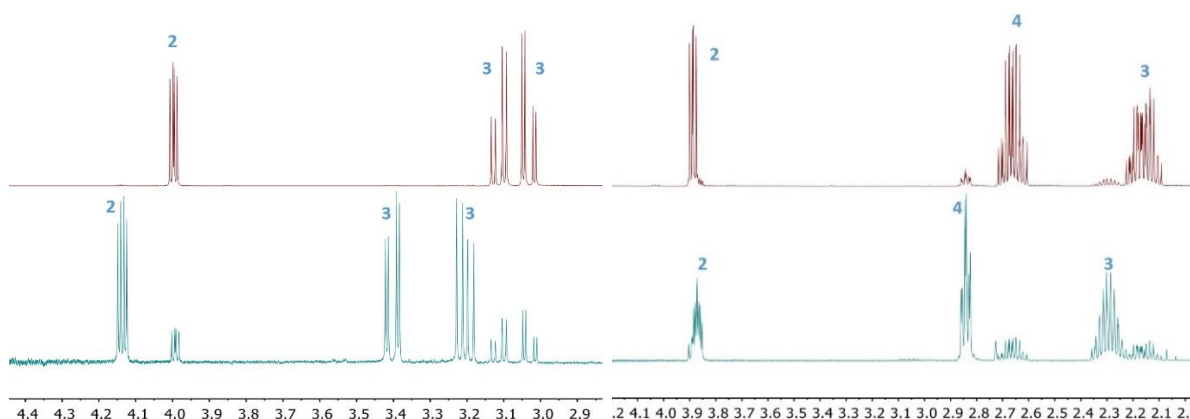

Fig. 7.1 400 MHz ^1H NMR spectrum of a D_2O solution of (left) L-cysteine (top) and L-cystine (bottom), (right) DL-homocysteine (top) and DL-homocystine (bottom). See Scheme 7.1 for atom labelling.
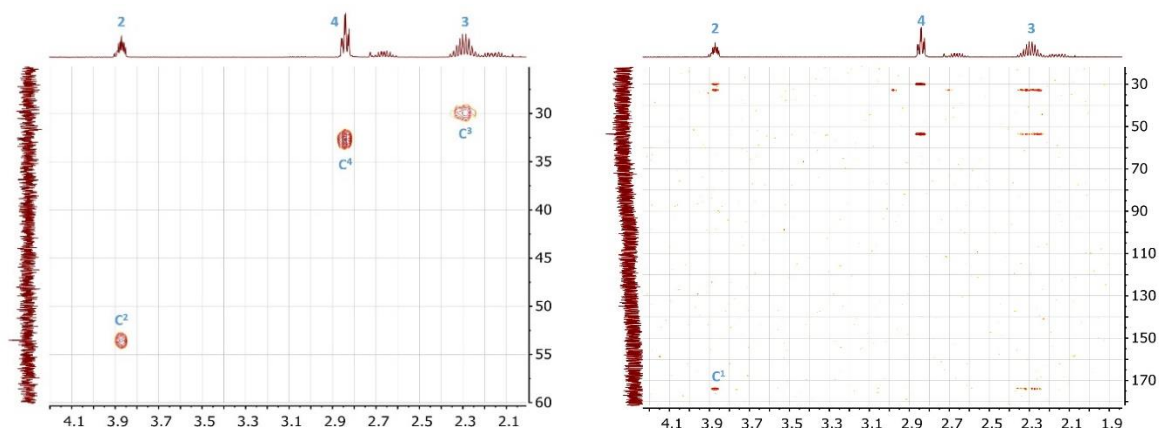
Fig. 7.2 HMBC (left) and HMQC (right) spectra (^{1}H, 500 MHz; ^{13}C, 126 MHz) of a D_2O solution of DL-homocystine (395 K). See Scheme 7.1 for atom labelling.

Considering the case of S-phenyl-L-cysteine, the major changes in the ^{1}H NMR spectrum involve the shift downfield of the protons, with the aromatic signals merging together (Fig. 7.3 left). In the ^{13}C NMR spectrum, it is prominent the shift of the carbon atoms next to the sulfur, namely positions 3 and 5. Moreover the ^{13}C NMR signals relative to positions 2 and 3 are split, sign of a mixture of diastereoisomers (Fig. 7.3 right). Position 2 has, in fact, a fixed chirality (the starting material being enantiomerically pure), but while oxidation of the sulfur creates equal amounts of the R and S-enantiomers at the sulfoxide S atom. The situation is similar to that of methionine (Figs. 6.5 and 6.6). All the protons move downfield and C^3 and C^5 are the most shifted on going to the sulfoxide (Figure 7.3).
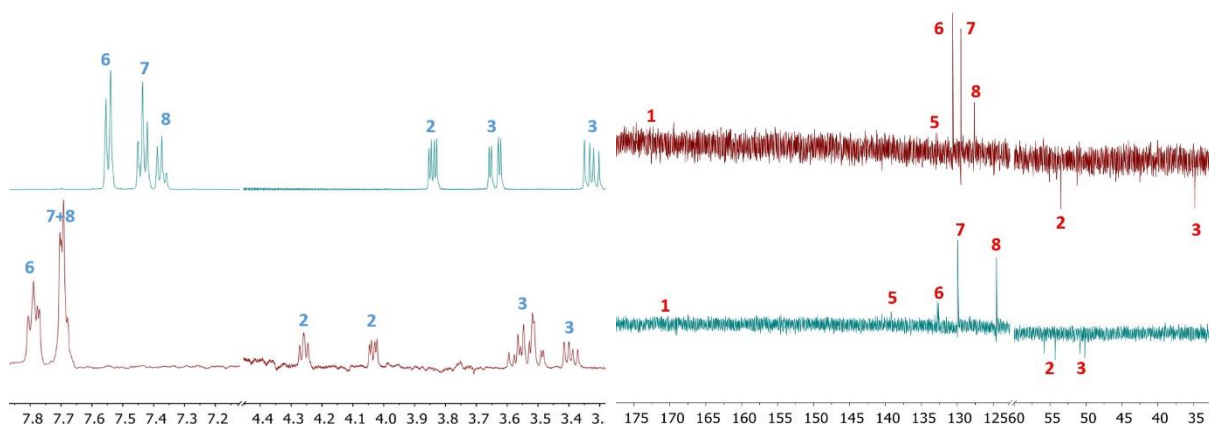

Fig. 7.3 (left) 500 MHz ^{1}H NMR spectrum and (right) 126 MHz ^{13}C NMR spectrum of a D_2O solution of S-Phenyl-L-cysteine (top) and 3-(phenylsulfoxide)-L-alanine (bottom). Position of C^1 is derived from the HMBC spectrum. See Scheme 7.1 for atom labelling.

A fifth, non-natural amino acid derivative was tested: 4-thiazolidine carboxylic acid, which is related to proline by substitution of one of the carbon atoms in the five-membered ring with sulfur. Surprisingly, this compound shows no reactivity when exposed to singlet oxygen. However, the corresponding unsubstituted ring (thiazolidine), readily reacts (Fig. 7.4).
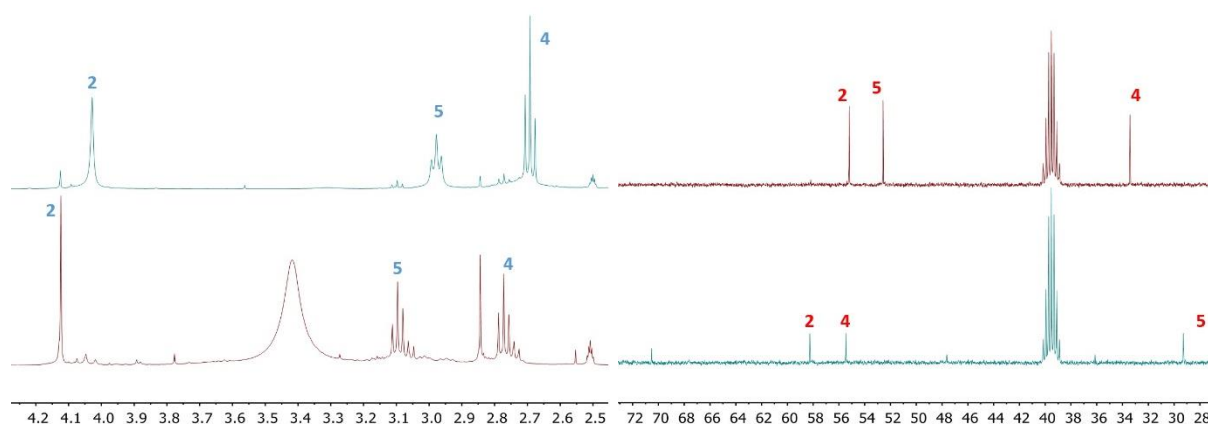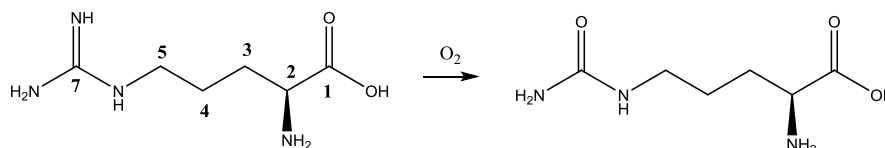
Fig. 7.4 (left) 400 MHz ^{1}H NMR spectrum and (right) 100 MHz ^{13}C NMR spectrum of a DMSO-d_6 solution of thiazolidine (top) and thiazolidine-3-oxide (bottom). See Scheme 7.1 for atom labelling.

L-Arginine was found convert to L-citrulline in the presence of molecular oxygen (Scheme 7.2). The mechanism includes a nitrogen monoxide releasing step, which is of biological significance, since it constitutes a source of NO in living organisms. For this to happen, the guanidinium group is transformed into a ureic one. We observed that the reaction is promoted by oxygen under normal conditions, so that generation of singlet oxygen is not required. A sealed D$_2$O solution of L-arginine did not show conversion after three days, but it was readily transformed when oxygen was bubbled through (data not shown). This evidence rules out a hydrolysis mechanism and points at molecular oxygen as the principal reactant. For the sake of completion, we report both the ^{1}H- and ^{13}C NMR spectra of L- arginine and L-citrulline (Fig. 7.5).

Scheme 7.2 Conversion of L-arginine to L-citrulline. Numbering is for NMR assignment.
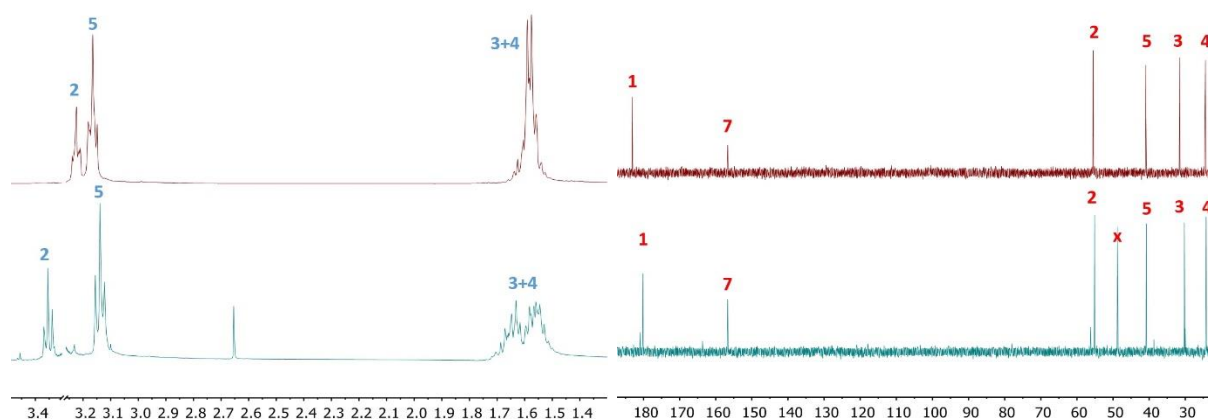

Fig. 7.5 (left) 400 MHz ^{1}H NMR spectrum and (right) 100 MHz ^{13}C NMR spectrum of a D$_2$O solution of L-Arginine (top) and L-Citrulline (bottom). The signal indicated with a cross in the ^{13}C NMR spectrum belongs to a solvent used in a previous run and remained in the pumping system. See Scheme 7.2 for atom labelling.

106

7.2 Heterocycles containing one sulfur atom

We move our attention to a series of cyclic organic sulfides, starting from the simplest, which are cycles of different sizes containing one sulfur atom each (Scheme 7.3). To this group belong thiirane, thietane, thiolane, thiinane and isothiocineole. Interestingly, the corresponding sulfoxide is known for the first four members, while a literature search showed a positive match for isothiocineole sulfone[32]. This compound is of interest because it is used by the perfume industry as grapefruit scent[33].
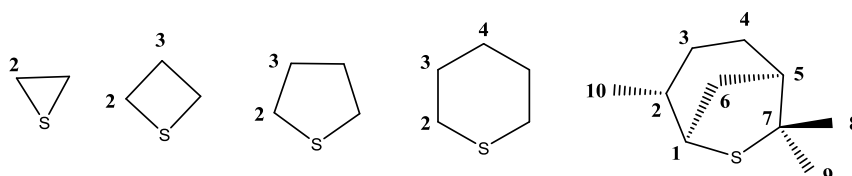
Scheme 7.3 Structures of thiirane, thietane, thiolane, thiinane and isothiocineole Positions are numbered for NMR assignment.

Photooxidation of thiirane was performed in MeOD or DMSO-d_6 solutions. Despite literature reports of conversion to the sulfoxide or ring opening to the sulfinic acid[34], the main process we detected was the evaporation of the compound from the reaction mixture. For MeOD, all of the compound was gone in less than one hour, while $d6$-DMSO solution retains the compound for four hours nevertheless showing no conversion. A rationale for this behaviour cannot be given, especially considering that all the other sulfides in Scheme 7.3 converted selectively to the sulfoxide.

Four, five and six-membered ring sulfides show similar NMR spectroscopic features upon oxidation (Fig. 7.6 to 7.8). Axial and equatorial protons at each of positions 2 and 3 are isochronous in the sulfide, whereas they split in the sulfoxide. This is interpreted as the consequence of the oxidation of the sulfur prochiral centre, with H_{ax} and H_{eq} finding themselves in diastereotopic environments. H^4 (present only in thiinane) does not split, indicating that the effect does not extend to position 4 of the ring. This is a result that is to be expected if we consider that, in a chair conformation, oxygen and C^4 point in opposite directions (Scheme 7.4). Moving to the carbon spectra of the sulfoxides, C^2, the closest carbon atom to sulfur, moves downfield, significantly shifting with respect to the pristine sulfide. C^3 and C^4 instead move highfield, to a chemical shift lesser than that of the sulfide.
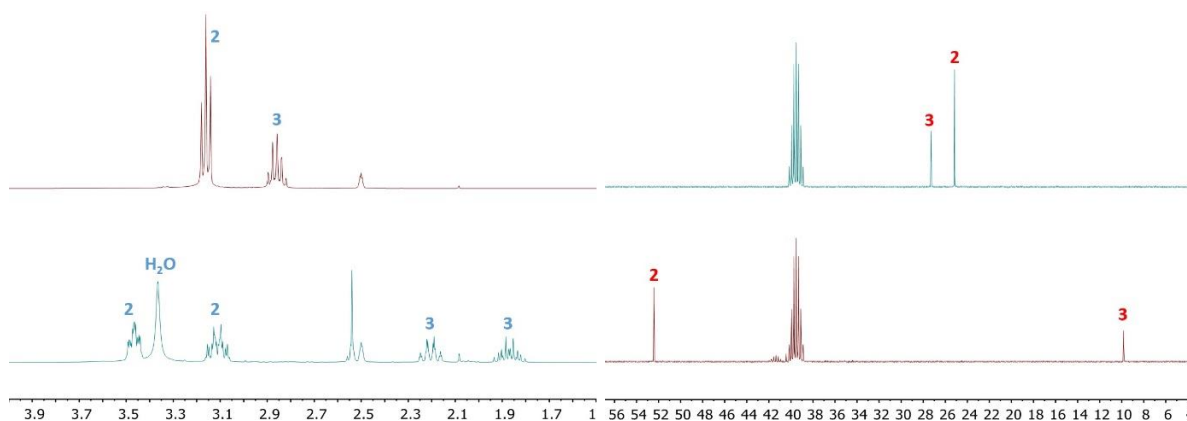

Fig. 7.6 (left) 400 MHz ^{1}H NMR spectrum and (right) 100 MHz ^{13}C NMR spectrum of a DMSO-d_6 solution of thietane (top) and thietane sulfoxide (bottom). See Scheme 7.3 for atom labelling.

Fig. 7.7 (left) 400 MHz ^{1}H NMR spectrum and (right) 100 MHz ^{13}C NMR spectrum of a DMSO-d_6 solution of thiolane (top) and thiolane sulfoxide (bottom). See Scheme 7.3 for atom labelling.
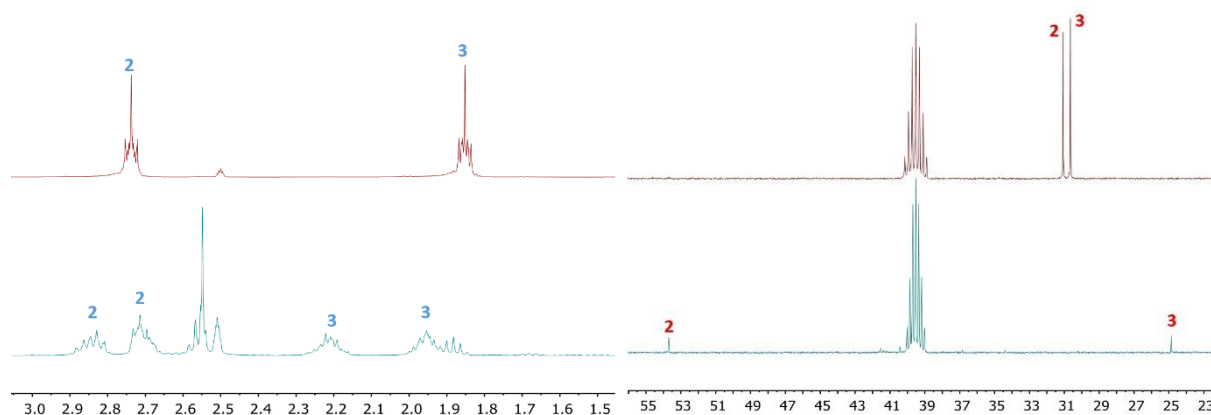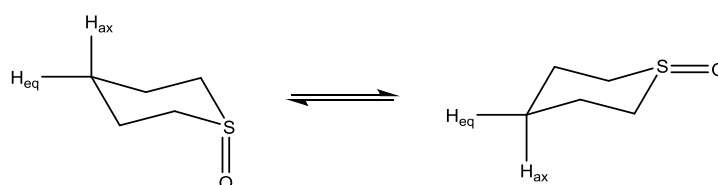

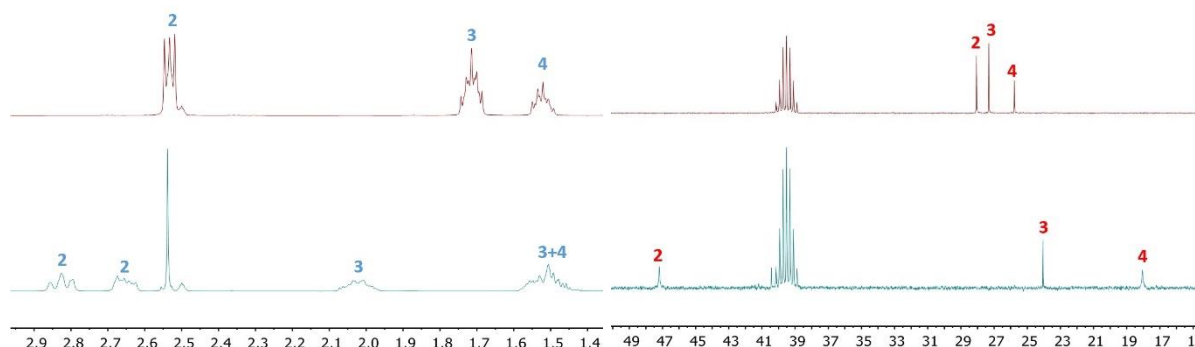Scheme 7.4 Chair conformation for thiinane sulfoxide.

Fig. 7.8 (left) 400 MHz ^{1}H NMR spectrum and (right) 100 MHz ^{13}C NMR spectrum of a DMSO-d_6 solution of thiinane (top) and thiinane sulfoxide (bottom). See Scheme 7.3 for atom labelling.

It is interesting discussing isothiocineole on its own because of the stereogenic centres that are present. Singlet oxygen can approach the sulfur centre either from the top or bottom face of the seven-membered ring, therefore no enantioselectivity is expected when performing photooxidation. For isothiocineole, ^{1}H and ^{13}C NMR support the hypothesis that only one diastereoisomer was obtained (Fig. 7.9). The reason for that has to originate in the transition state, illustrated in Scheme 7.5, which, upon opening of the four-membered ring, forms two molecules in the same configuration: in our hypothesis with the oxygen atom pointing down the plane described by the seven-membered ring containing the sulfur atom. A closer look at the ^{1}H NMR spectrum reveals that H^1 moves to higher field even though it is the closest to the newly generated sulfoxide. An evidence that, while H^1 is pointing above the plane, the oxygen that has been added points in the other direction, i.e. below the plane. The most prominent feature in the ^{13}C NMR spectrum (Fig. 7.9) is the downfield shift of C^1 and C^7 following sulfoxide generation.
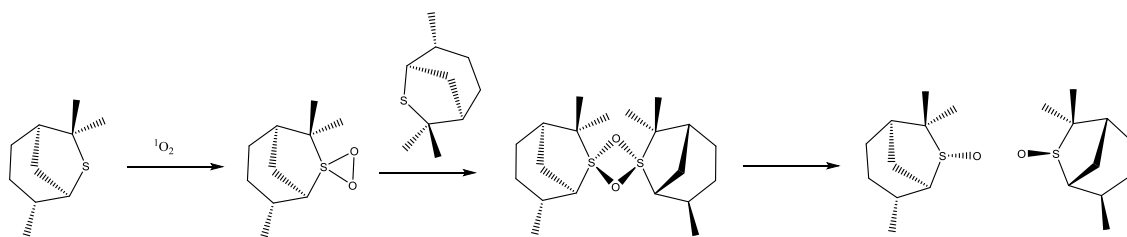
Scheme 7.5 Proposed mechanism for the diastereospecificity of the oxidation of isothiocineole.
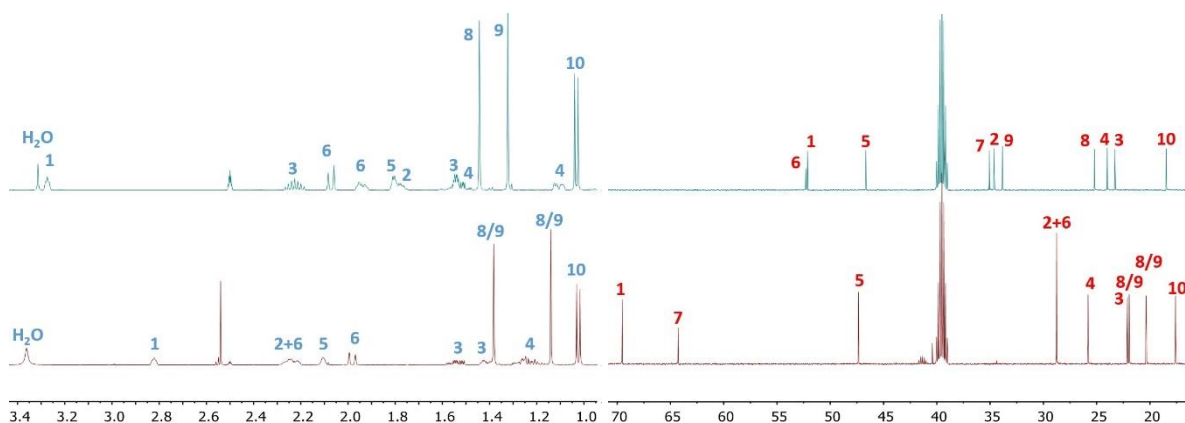

Fig. 7.9 (left) 500 MHz ^{1}H NMR spectrum and (right) 126 MHz ^{13}C NMR spectrum of a DMSO-d_6 solution of isothiocineole (top) and isothiocineole sulfoxide (bottom). See Scheme 7.3 for atom labelling.

7.3 Heterocycles containing two sulfur atoms

The choice of cyclic substrates containing more than one heteroatom allows multiple substitution patterns, as shown in Scheme 7.6 for the 5- and 6-membered rings which were investigated.
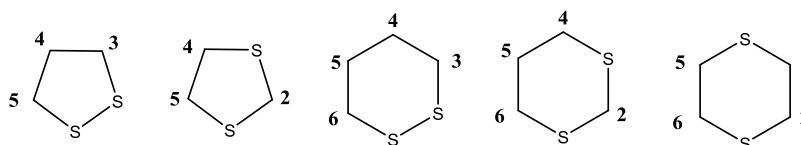
Scheme 7.6 Structures of 1,2-dithiolane, 1,3-dithiolane, 1,2-dithiinane, 1,3-dithiinane and 1,4-dithiinane. Positions are numbered for NMR assignment.

1,2-Dithiolane and 1,2-dithiane possess a disulfide bond, which, as already discussed for cystine and homocystine, does not undergo oxidation in the presence of singlet oxygen. DL-Lipoic acid (Scheme 7.7, top) was investigated as representative of 1,2-dithiolane and trans-4,5-dihydroxy-1,2-dithiane (Scheme 7.7, bottom) as a model for 1,2-dithiane (Scheme 7.7); both compounds did not react with singlet oxygen generated by irradiation of the reaction mixture in presence of TPyCP (data not shown).
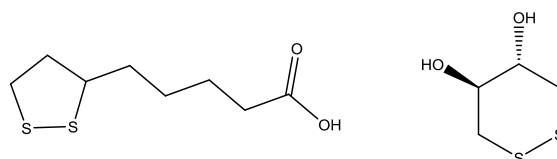
Scheme 7.7 Structures of DL-lipoic acid and *trans*-4,5-dihydroxy-1,2-dithiinane.

More interesting is what happens to the other compounds of the series illustrated in Scheme 7.6. Even though they contain more than one sulfur atom per cycle, and even though the sulfur atoms are not in electronic communication with each other, oxidation of the first sulfur slows down the reaction rate, so that it is possible to stop the reaction at the point where only the mono-sulfoxide is produced. The oxidation was performed in MeOD for 1,3-dithiolane since one of the signals of its sulfoxide lies underneath the water peak present in DMSO-d_6. 1,3-Dithiolane and 1,3-dithiinane can be regarded as thioacetals, with position 2 being interposed in between two sulfur atoms. Their NMR spectra are reported in Fig. 7.10 and 7.11. While H^2 displays a single resonance in the starting material, it splits in two doublets in the mono-sulfoxide. This is due to the fact that the sulfoxide will exist in equal proportion as both enantiomers. Axial and equatorial hydrogens in position 2 are in different chemical environments according to their orientation in space with respect to the S=O bond. It is worth noting that the introduction of one oxygen atom breaks the ring symmetry. The carbon atoms next to sulfur (C^4 and C^5 in 1,3-dithiolane and C^4 and C^6 in 1,3-dithiinane) have identical chemical shifts in the starting material by symmetry. In the sulfoxides, they split since one of the two carbons now sits next to a sulfoxide unit.

Fig. 7.10 (left) 400 MHz ^{1}H NMR spectrum and (right) 100 MHz ^{13}C NMR spectrum of a DMSO-d_6 solution of 1,3-dithiolane (top) and 1,3-dithiolane-1-oxide (bottom). See Scheme 7.6 for atom labelling.

Fig. 7.11 (left) 400 MHz ^{1}H NMR spectrum and (right) 100 MHz ^{13}C NMR spectrum of a DMSO-d_6 solution of 1,3-dithiinane (top) and 1,3-dithiinane-1-oxide (bottom). See Scheme 7.6 for atom labelling.

Upon oxidation, 1,4-dithiinane is lowered in symmetry, with positions 2 and 3 being non-equivalent in the sulfoxide. H^2 and H^3 split into two signals, whose multiplicity is more complex than the initial singlet (Fig. 7.12). The situation becomes clearer by looking at the

^{13}C NMR spectrum. C^{2+3} splits in C^2 and C^3, both move downfield, with C^2 moving the furthest.
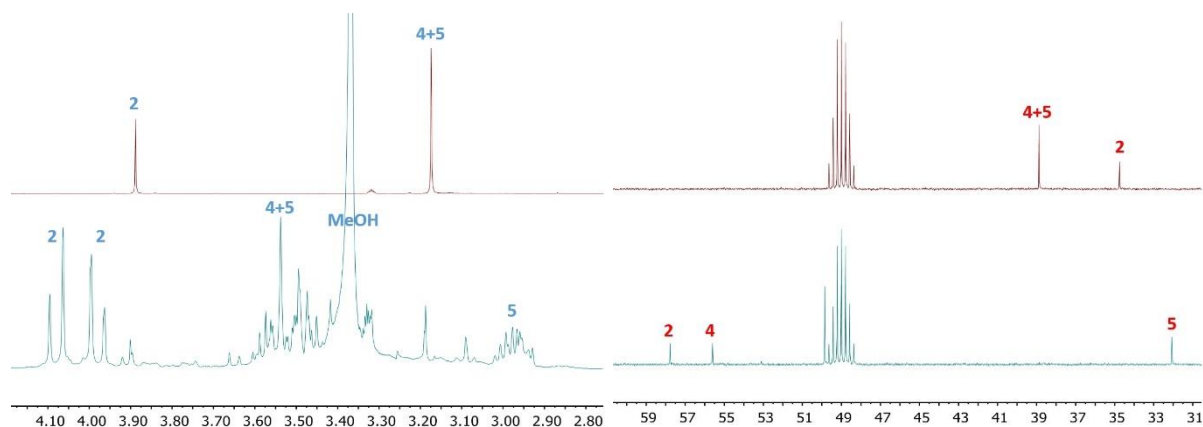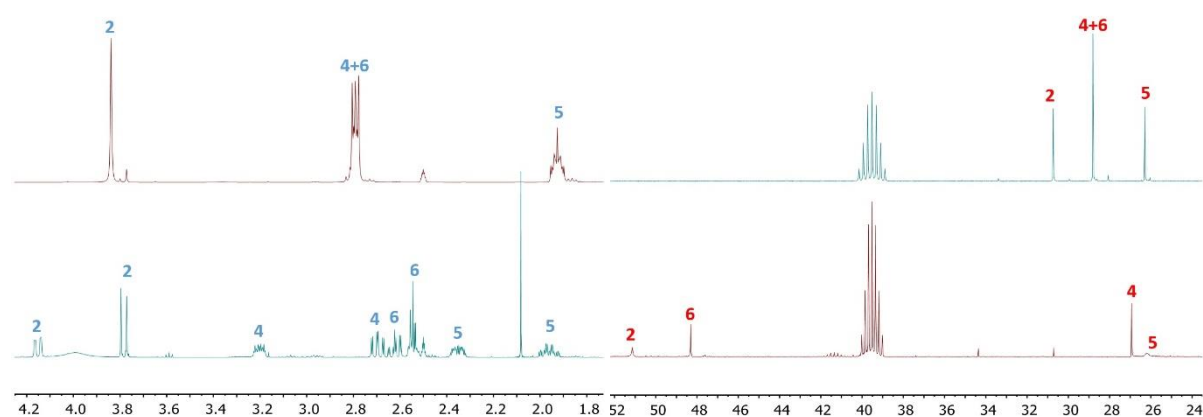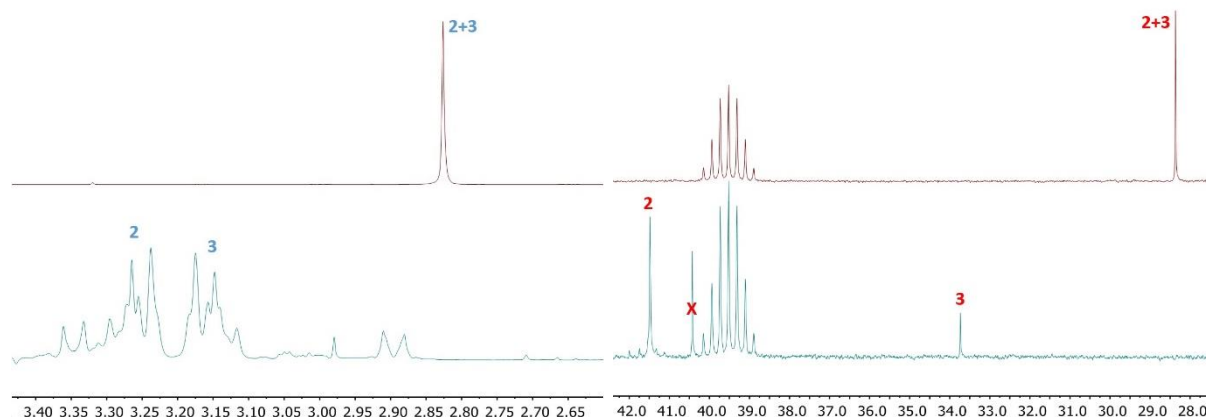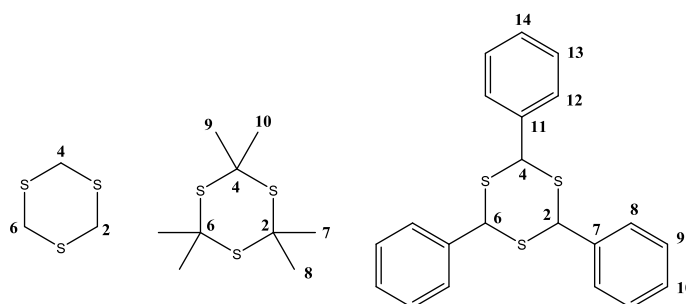

Fig. 7.12 (left) 400 MHz ^1H NMR spectrum and (right) 100 MHz ^{13}C NMR spectrum of a DMSO-d_6 solution of 1,4-dithiinane (top) and 1,4-dithiinane-1-oxide (bottom). See Scheme 7.6 for atom labelling.

7.4 Heterocycles containing three sulfur atoms

1,3,5-Trithiinane is a 6-membered heterocycle in which the S atoms are non-adjacent. The derivatives shown in Scheme 7.8 have been studied:

Scheme 7.8 Structures of 1,3,5-trithiinane, 2,2,4,4,6,6-hexamethyl-1,3,5-trithiinane, 2,4,6-triphenyl-1,3,5-trithiinane. Positions are numbered for NMR assignment.

The oxidation has been conducted in DMSO-d_6, with TPyCP as photocatalyst. The solutions have been irradiated with red LED light, whose emission band is centred at 660nm. Molecular oxygen was provided to the reaction mixture by means of a peristaltic pump which would pump atmospheric oxygen into the flask. Oxidation of 1,3,5-trithiinane afforded the mono-sulfoxide as confirmed by NMR spectroscopy, with H^2 and H^6 being in a different chemical environment to that of H^4 (Fig. 7.13). This observation would hold true for the disulfoxide as well, but the ^{13}C NMR spectrum indicates that the most shifted peak belongs to two carbons, while the less shifted peak accounts for one and its chemical shift is at higher field than that of the starting material (Fig. 7.13). Reasoning in terms of chemical shift, we can rule out that the highest field signal belongs to a carbon atom placed in between two sulfoxide groups. Therefore, it is concluded that the product is a mono-sulfoxide derivative.
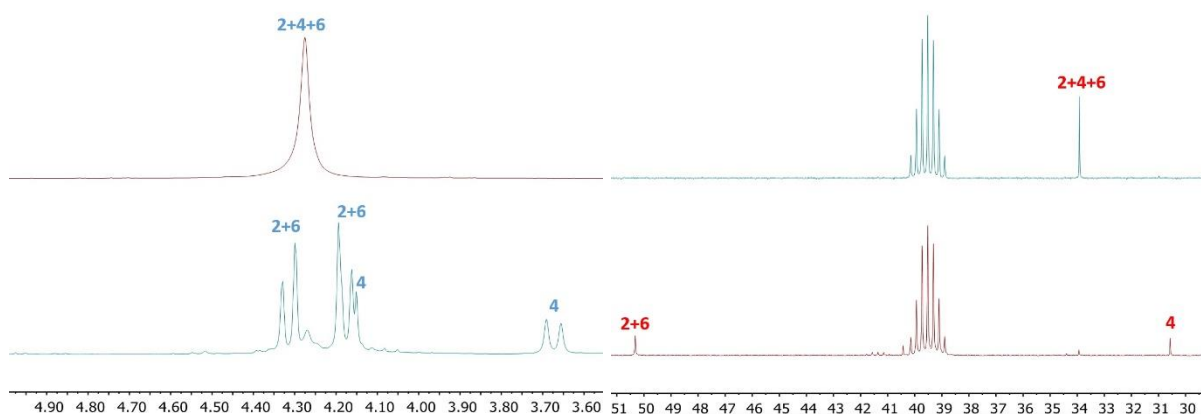
Fig. 7.13 (left) 400 MHz ^{1}H NMR spectrum and (right) 100 MHz ^{13}C NMR spectrum of a DMSO-d_6 solution of 1,3,5-trithiinane (top) and 1,3,5-trithiinane-1-oxide (bottom). See Scheme 7.8 for atom labelling.

The situation becomes more complex when considering the hexamethyl derivative. The conditions for photocatalysis were the same as those used for oxidation of 1,3,5-trithiiane. However, no oxidation of 2,2,4,4,6,6-hexamethyl-1,3,5-trithiinane was observed on a short timescale, whilst prolonged irradiation (approximatively 62 hours) led to the formation of white crystals on the walls of the flask in which the reaction was taking place. In Fig. 7.14 we report the ^{1}H NMR spectrum for the starting material and a solution made used dissolved crystals. The starting methyl signal (one singlet) splits into four singlets. Specifically, two of the four singlets integrate for six protons each, and the remaining two singlets integrate for three. This is again in accordance with the presence of oxygen on only one sulfur atom in the product. In the mono-sulfoxide, the methyl groups at C^2 and C^6 give raise to two singlets, depending on the relative orientation with respect to the oxygen atom; the methyl groups at C^4 splits in two signals, each accounting for three protons. ^{13}C NMR supports this assignment. Due to a low signal-to-noise ratio, ^{13}C chemical shifts for the dissolved crystals were determined from HMQC and HMBC experiments (Fig. 7.15). C^9 and C^{10} have virtually the same chemical shift, while C^7 and C^8 are well separated. It is evident from the HMBC cross-peaks that two types of quaternary carbons exist: C^{2+6} (shifted downfield) and C^4.
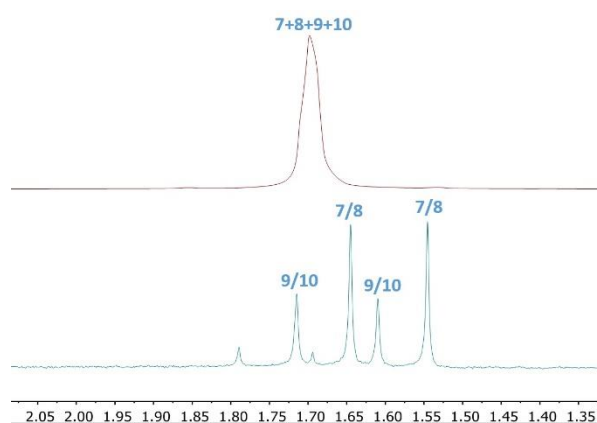

Fig. 7.14 500 MHz ^{1}H NMR spectrum of a DMSO-d_6 solution of 2,2,4,4,6,6-hexamethyl-1,3,5-trithiinane (top) and 2,2,4,4,6,6-hexamethyl-1,3,5-trithiinane-1-oxide (bottom). See Scheme 7.8 for atom labelling.
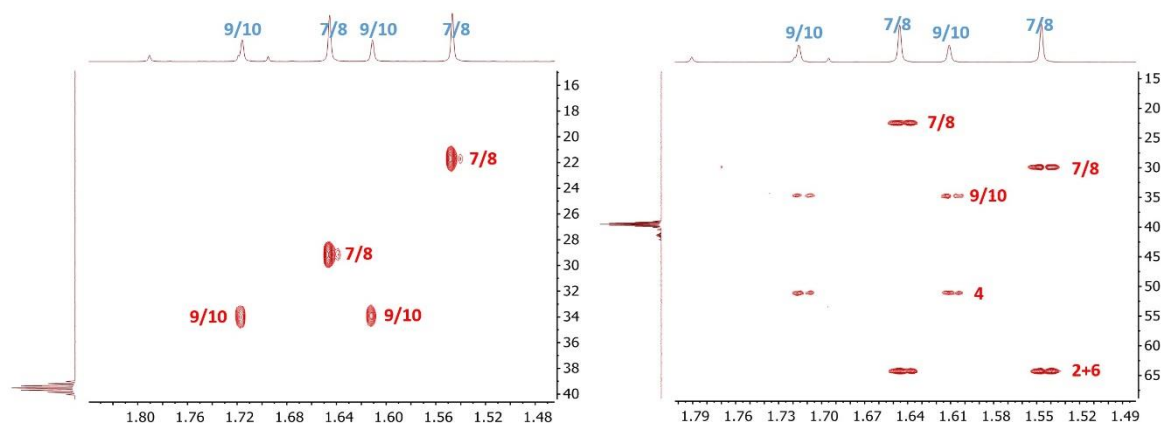
Fig. 7.15 HMQC (left) and HMBC (right) spectra (^{1}H, 500 MHz; ^{13}C, 126 MHz) of a DMSO-d_6 solution of 2,2,4,4,6,6-hexamethyl-1,3,5-trithiinane-1-oxide (395 K). See Scheme 7.8 for atom labelling.

2,4,6-Triphenyl-1,3,5-trithniane represents the most sterically hindered compound of the series. Nevertheless, it reacted when exposed to singlet oxygen in the presence of the porphyrin photocatalyst. No information is available on the starting material stereochemistry, so that we assume it is sold as a mixture of all possible stereoisomers and no stereochemical descriptors are required. It possesses a C$_{3v}$ axis, which makes equivalent the three aliphatic protons H^2, H^4 and H^6; the aromatic part is of more complex interpretation, with all of the resonances clustering together. Moving to the product, the symmetry decreases and the aliphatic protons split in H^{2+6} and H^4 (Fig. 7.16). Surprisingly the most shifted is H^4 and not the one at the vicinal position to the sulfoxide. It could be argued that a 1,3-disulfoxide would have same symmetry as the 1-sulfoxide and would retain the same integral ratio in the proton spectrum (Scheme 7.9). However, if we follow the temporal evolution of the reaction, we notice that the ratio H^{2+6}:H^4 2:1 arises from the very beginning and is maintained throughout the reaction. We are convinced that the mono-sulfoxide is the first product of the catalytic cycle and therefore we would only expect to see the disulfoxide emerging after formation of the mono-sulfoxide. There is little change in the aromatic region of the spectrum. Signals arising from the phenyl protons overlap in the precursor (Fig 7.16, top), while, in the product, the signal for H^{10} (accounting for 2 protons) is clearly distinguished from the remaining phenyl proton signals (Fig 7.16, bottom). The ^{13}C NMR spectra are shown in Fig. 7.16. The trend discussed for positions 2, 4 and 6 is conserved. The quaternary *ipso*-carbon of the phenyl ring splits in two signals, one for the phenyl rings to the left and to the right of the sulfoxide (C^7) and one for the further one (C^{11}).
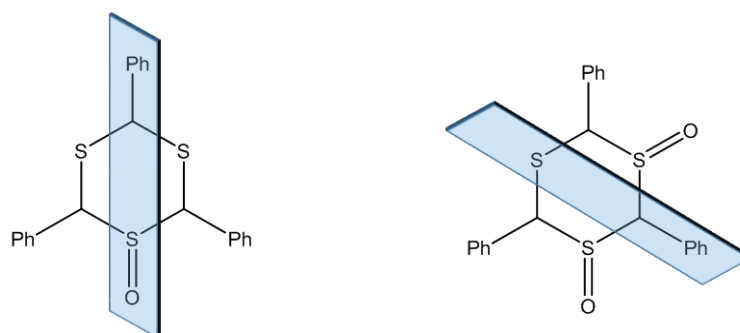
Scheme 7.9 Symmetry element (mirror plane) for 2,4,6-triphenyl-1,3,5-trithiianane-1-sulfoxide and for 2,4,6-triphenyl-1,3,5-trithiianane-1,3-disulfoxide.
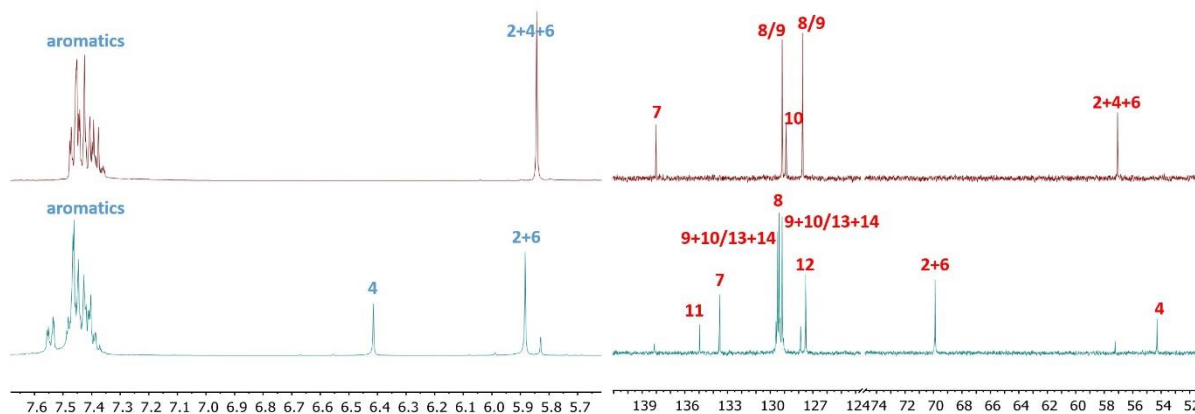
Fig. 7.16 (left) 400 MHz ^{1}H NMR spectrum and (right) 100 MHz ^{13}C NMR spectrum of a DMSO-d_6 solution of 2,4,6-triphenyl-1,3,5-trithiiane (top) and 2,4,6-triphenyl-1,3,5-trithiiane-1-oxide (bottom). See Scheme 7.8 for atom labelling.

7.5 Heterocycles containing S and O or NH units

We now move to heterocycles that contain both S and O or NH units. Those reported in Scheme 7.10 cover all the possible substitution patterns by addition of oxygen and nitrogen atoms. For some of the compounds, the unsubstituted ring is not commercially available. Thus, in Scheme 7.11 we present the structures of substituted compounds that were available for the investigation.
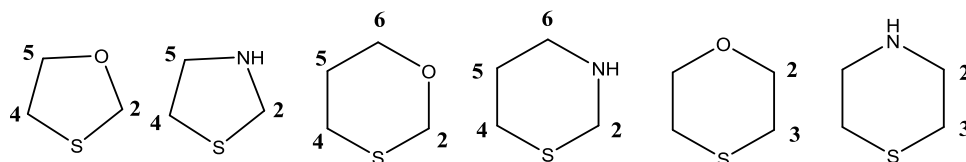
Scheme 7.10 1,3-Oxathiolane, 1,3-thiazolane, 1,3-oxathiinane, 1,3-thiazinane, 1,4-oxathiinane and 1,4-thiazinane (thiomorpholine). Positions are numbered for NMR assignment.
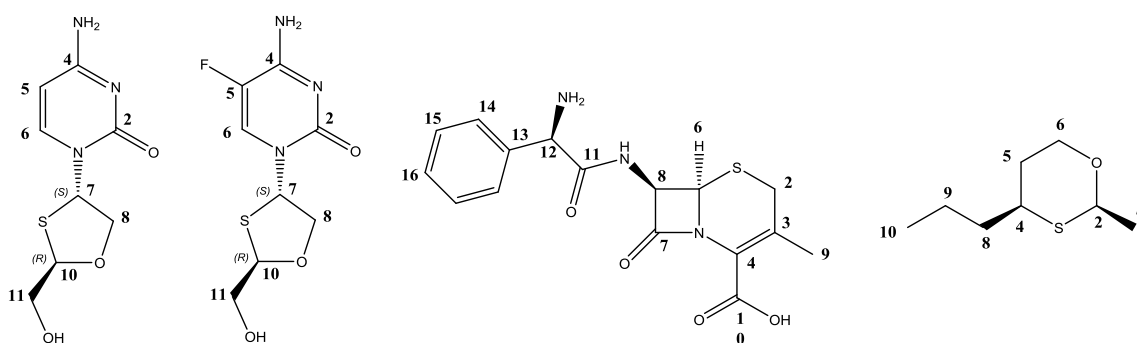
Scheme 7.11 Structures of lamivudine, emtricitabine, cephalexin and 2-methyl-4-propyl-1,3-oxathiinane. Positions are numbered for NMR assignment.

1,3-Oxathiolane is not commercially available and the heterocyclic unit was represented by the compounds lamivudine (2'-deoxy-3'-thiacytidine) and emtricitabine (2'-deoxy-5-fluoro-3'-thiacytidine), shown in Scheme 7.11. These two compounds are of interest for the pharmaceutical industry since they are nucleoside reverse transcriptase inhibitors, active against HIV infection. The sulfur atom makes the compound susceptible to

114

photocatalytic oxidation, and, in fact, the combined action of TPyCP and red light results in conversion to the sulfoxide. Interestingly, the sulfur atom in both active ingredients is located in between two chiral centres. This conformation induces, upon introduction of an oxygen atom, the creation of an ulterior chiral centre in enantiomeric excess (70 % of one diastereoisomer and 30% of the other) as shown by the splitting of H^6 in the ^1H NMR (Fig. 7.17 and 7.18). The stereochemistry of the products is assigned as (S) and it was deduced by the effect the introduction of oxygen has on the shift of the neighbouring protons. For a mixture 70% (S) and 30% (R), an enantiomeric excess ee = (S-R)/(R+S) of 0.4 is calculated. In our opinion the oxygen belonging to the sulfoxide is pointing up with respect to the plane described by the five-membered ring (Scheme 7.12). If so, H^7, which is also pointing up, should shift downfield (experimental downfield shifts of 0.40 ppm for lamivudine and 0.42 ppm for emtricitabine in n). H^{10} points downwards, and it is expected to shift highfield (experimentally it shifts highfield by 0.4 ppm in both cases). Finally H^{11} would find itself parallel to the oxygen atom and therefore should shift downfield (0.25 ppm and 0.20 ppm). The presence of a fluorine atom in emtricitabine constitutes a useful NMR-handle. Upon complete conversion, the ^{19}F signal at δ −165.8 ppm is replaced by to two ^{19}F signals at δ -164.0 and -164.5 ppm, and the relative intensity of the signals reflects that of the ratio 7:3, indicating the presence of two diastereoisomers (Fig. 7.19).
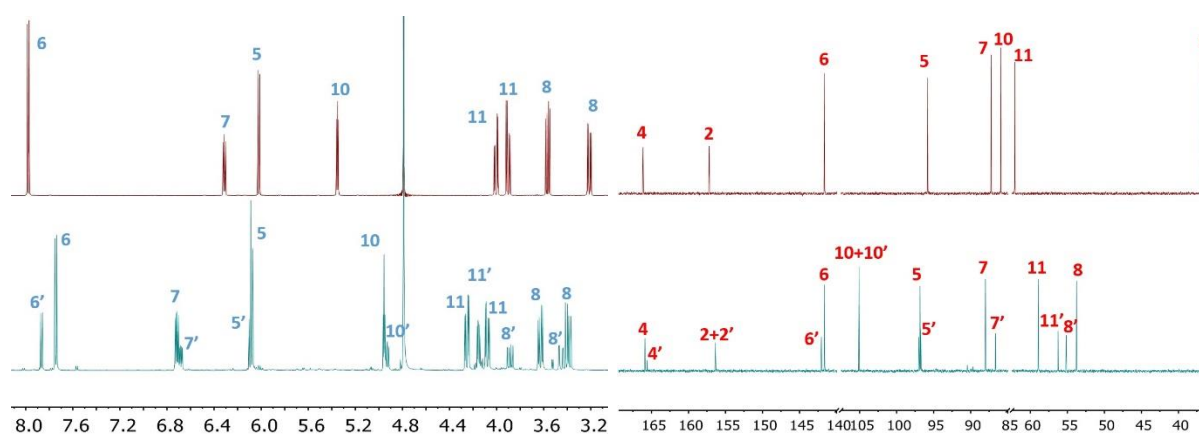
Fig. 7.17 (left) 500 MHz ^1H NMR spectrum and (right) 126 MHz ^{13}C NMR spectrum of a D_2O solution of lamivudine (top) and lamivudine-3'-oxide (bottom). See Scheme 7.12 for atom labelling.
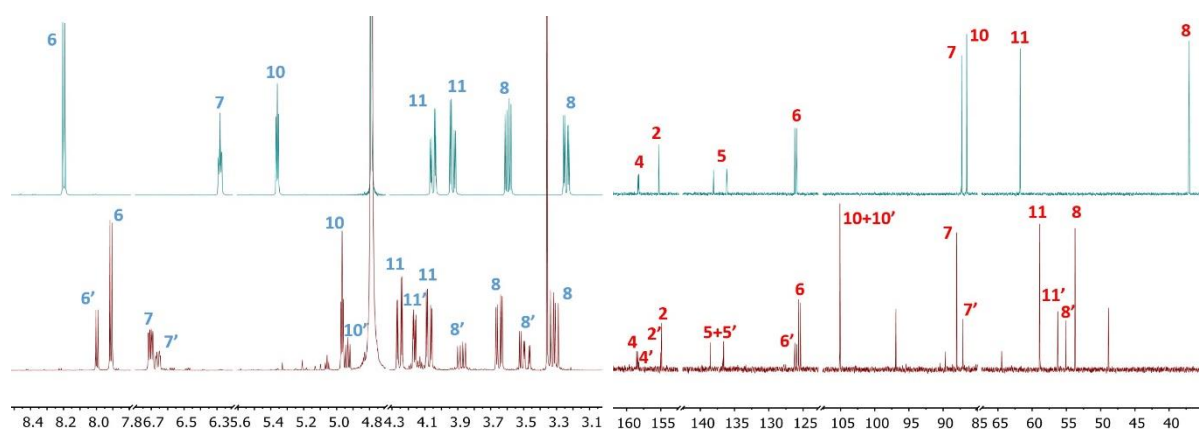
Fig. 7.18 (left) 500 MHz ^1H NMR spectrum and (right) 126 MHz ^{13}C NMR spectrum of a D_2O solution of emtricitabine (top) and emtricitabine-3'-oxide (bottom). See Scheme 7.12 for atom labelling.
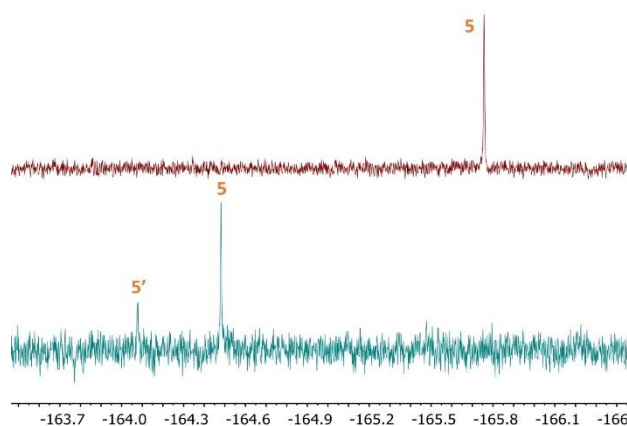
Fig. 7.19 470 MHz ^{19}F NMR spectrum of a D_2O solution of emtricitabine (top) and emtricitabine-3'-oxide (bottom). See Scheme 7.12 for atom labelling.
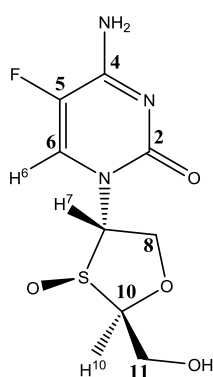
Scheme 7.12 Proposed structure for lamivudine-3'-oxide. Protons in positions 6, 7 and 10 are highlighted in the structure to compare their position to that of oxygen.

1,3-Thiazolane reacts with TPyCP-photocatalytically generated singlet oxygen to give the corresponding sulfoxide and this has already been discussed in section 7.1 when it was compared to the amino acid 4-thiazolidine carboxylic acid. 1,3-Oxathiinane is not commercially available, with 2-methyl-4-propyl-1,3-oxathiinane (Scheme 7.11) being chosen to represent the family. Commercially, it is an important compound for the flavouring industry, constituting passion fruit scent. It is sold as a mixture of cis- and trans-isomers, whose proportions are not known, for a total of four possible diastereoisomers (Scheme 7.13). However, of the four, only two species are not NMR-equivalent, and, in fact, this is observed in the proton spectrum (Fig. 7.20, top-left). Just by looking at H^2, it appears evident that two sets of signals are present, with a ratio of 6 to 1. It is not possible, however to estimate which, between *trans* and *cis*, is the major component.
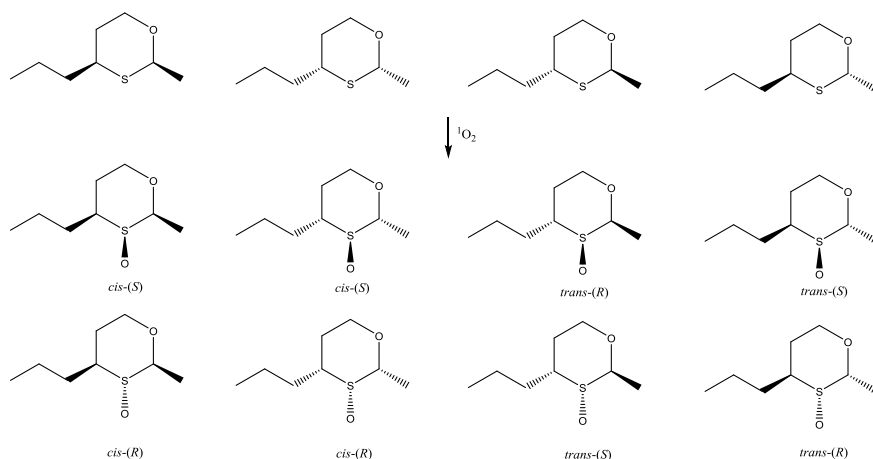
Scheme 7.13 Structures of the single components present in commercial 2-methyl-4-propyl-1,3-oxathiinane. Each can generate two diastereoisomers upon oxidation of the sulfur atom. (*R*) and (*S*) refer to the stereochemistry at the sulfur centre.

Once the compound enters the photocatalytically oxidative cycle and singlet oxygen oxidizes it, a new chiral centre is introduced and a total of eight diastereoisomers are expected (2^n, with n number of chiral centres). Again the number of species, whose NMR spectrum is different is lower: four for the specific case (*trans*-(*S*), *trans*-(*R*), *cis*-(*S*) and *cis*-(*R*)) (Scheme 7.13). By looking at Fig. 7.20 bottom-left, it appears evident how only the major component undergoes photocatalytic oxidation upon exposure to singlet oxygen. In fact, the signal H^2 at around δ 5 ppm (and the sub-spectrum correlated to it), assigned to the minor component, does not shift at all between precursor and product. Another feature visible in the spectrum of the product includes the highfield shifting of position 2 and 4. This can be rationalized only by considering a stereospecific oxidation of position 3, in which oxygen addition is directed by the presence of two pre-existing neighbouring chiral centres (Scheme 7.14). Furthermore, to explain the highshift we need to hypothesize that the oxygen atom points in a direction opposite to position 2 and 4, and that positions 2 and 4 are in a *cis* configuration, since they both move in a direction opposite to the one expected on the basis of increased electronegativity of position 1. If the *cis* assignment is correct, then the oxygen atom points towards the methyl group at position 7 and the methylene group at position 8. Me^7 does shift downfield, but the situation for CH_2^8 is more difficult to interpret, since its chemical shift strongly resembles that of H^9. Moving to the carbon spectrum (Fig. 7.20 right), the most affected positions by the oxidation are C^2 and C^4 regarding downshift and C^7 and C^8 regarding highshift. The presence of a sub-spectrum both in the starting material's and in the product's spectrum is consistent with the *trans* component being simply withstanding.

117
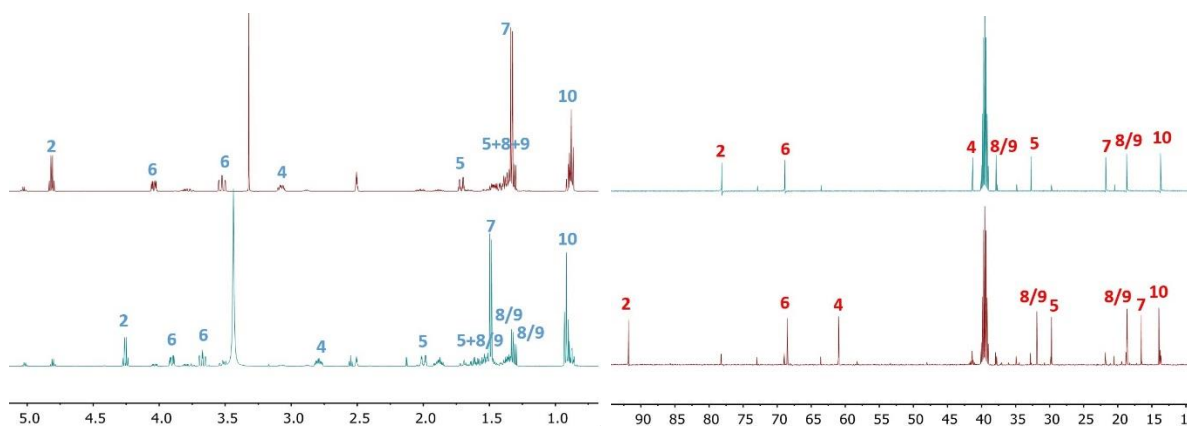
Fig. 7.20 (left) 500 MHz ^{1}H NMR spectrum and (right) 126 MHz ^{13}C NMR spectrum of a DMSO-d_6 solution of 2-methyl-4-propyl-1,3-oxathiinane (top) and 2-methyl-4-propyl-1,3-oxathiinane-3-oxide (bottom). See Scheme 7.14 for atom labelling.
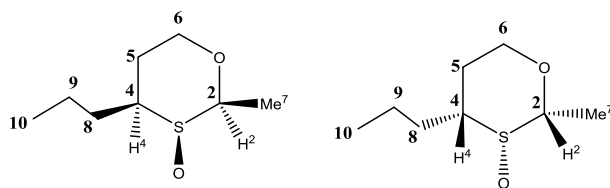
Scheme 7.14 Proposed structures for the two diastereoisomers of 2-methyl-4-propyl-1,3-oxathiinane-3-oxide.

Tetrahydro-2H-1,3-thiazine is also not commercially available. Therefore, the antibiotic cephalexin (Scheme 7.11), belonging to the more general family of cephalosporins, was employed. Fig. 7.21 reproduces the NMR experiments performed on the starting material and on the product. After photocatalytic oxidation, only one of two possible diastereoisomers was formed. According to our assignment, the oxygen atom connected to sulfur points upwards with respect to the six-membered cycle (Scheme 7.15). A rationale for the proposed assignment is the highshift of H^6, which ultimately points in a different direction with respect to the direction towards which oxygen points. In addition, only one of the two methylene protons H^2 is shifted, while the other retains its original chemical shift. The other proton resonances do not move significantly upon oxidation, and will not be discussed. Coming to the ^{13}C NMR spectrum (Fig. 7.21 right), the most pronounced shifts involve C^2 and C^6, as expected. Both move downfield, in accordance with the change from S to S=O.

Fig. 7.21 (left) 500 MHz ^{1}H NMR spectrum and (right) 126 MHz ^{13}C NMR spectrum of a D$_2$O solution of cephalexin (top) and cephalexin oxide (bottom). See Scheme 7.15 for atom labelling.
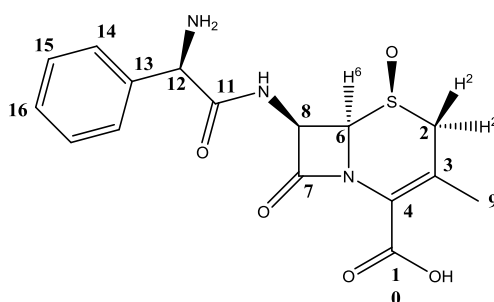
Scheme 7.15 Proposed structures for cephalexin oxide.

Both 1,4-oxathiinane and 1,4-thiazinane readily react with singlet oxygen to form the corresponding sulfoxide. Figs. 7.22 and 7.23 contain the respective ^{1}H and ^{13}C spectra. The main feature is the splitting of H_{ax} and H_{eq} at positions 2 and 3, each of them showing a ddd multiplicity. Between axial and equatorial positions, one shifts from the parent signal, while the other resonance stays almost at the same chemical shift. The carbon spectrum shows the shift highfield of position 3 and the shift downfield of position 2, a characteristic already observed for other six-membered systems as thiinane.
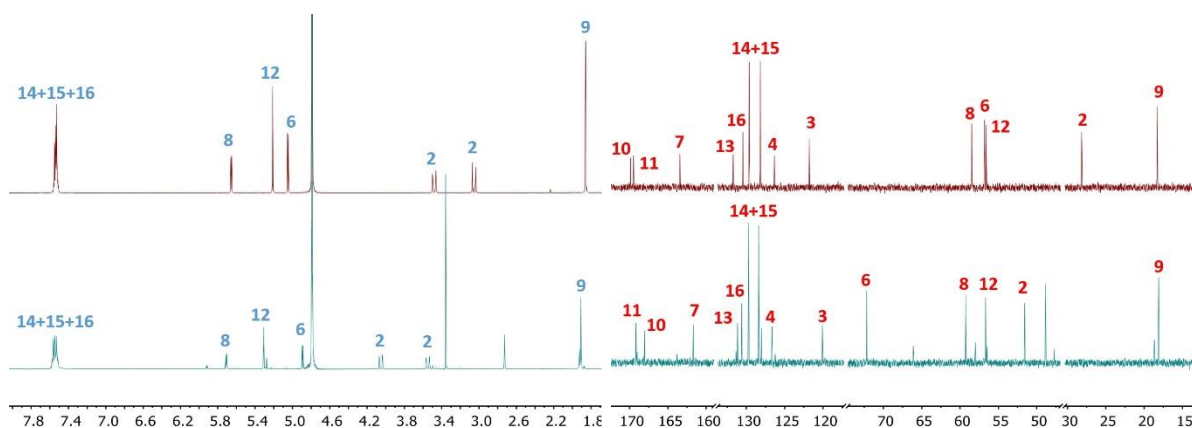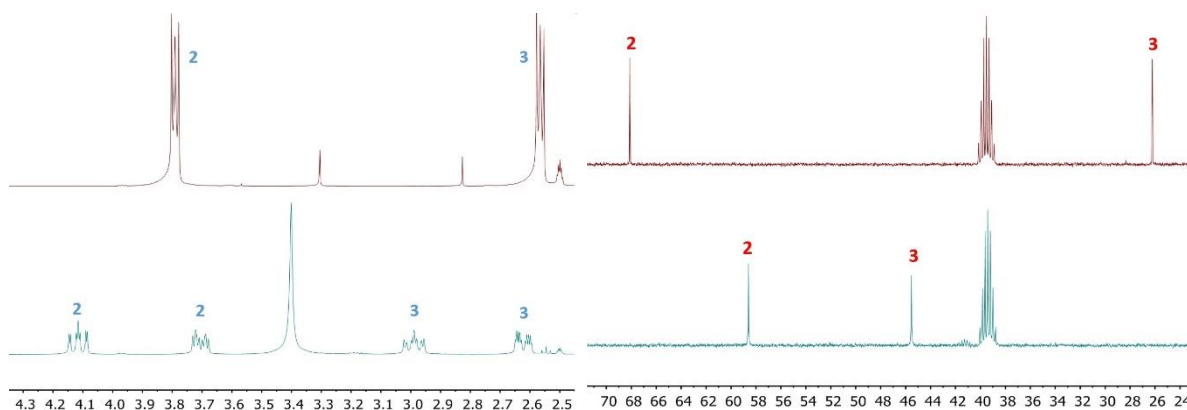

Fig. 7.22 (left) 400 MHz ^{1}H NMR spectrum and (right) 100 MHz ^{13}C NMR spectrum of a DMSO-d_6 solution of 1,4-oxathiinane (top) and 1,4-oxathiinane-4-oxide (bottom). See Scheme 7.10 for atom labelling.
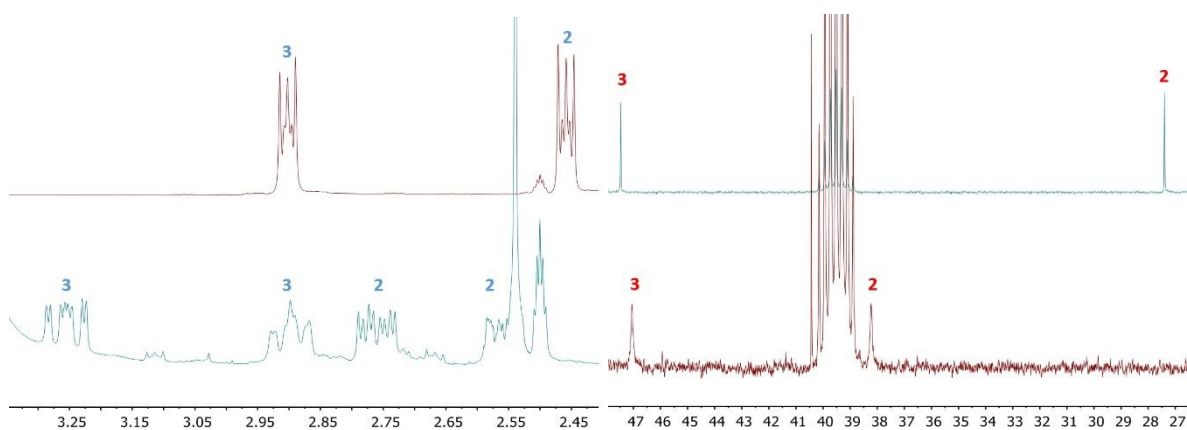
Fig. 7.23 (left) 400 MHz ^{1}H NMR spectrum and (right) 100 MHz ^{13}C NMR spectrum of a DMSO-d_6 solution of 1,4-thiazinane (top) and 1,4-thiazinane-4-oxide (bottom). See Scheme 7.10 for atom labelling.

In this chapter we have shown how singlet oxygen can be a versatile reactive species, which is easy to produce *in situ* and whose reactivity is site-specific. Photooxygenation brings together the added value of catalysis and the use of inexpensive reactants such as light and molecular oxygen. Investigation of a wide class of substrates has been performed, ranging from sulfurated aminoacids to aliphatic sulfides. Next to simple, unsubstituted molecules, more complex compounds that find use in the pharmaceutical and flavour industries were made react with singlet oxygen. Again, generation of their sulfoxides showed us the tolerance of singlet oxygen for a variety of functional groups; a few examples are amino-, carbonyl-, adenyl-, hydroxyl-, phenyl-, amido- and carboxyl- groups present in cephalexin and lamivudine. If it is true that conversion of sulfide to sulfoxide is industrially performed with hydrogen peroxide, we think singlet oxygen should not be overlooked as candidate for oxidations, especially when the substrate is expensive or sensitive to hydrogen peroxide.

7.6 NMR spectroscopic data

TPyCP. ^{1}H (D$_2$O, 500 MHz): 9.41 (d, 8H, J$_{HH}$ = 6.64 Hz, H^3), 9.25 (m, 8H, H^1), 9.05 (d, 8H, J$_{HH}$ = 6.62 Hz, H^2), 5.05 (t, 8H, J$_{HH}$ = 7.30 Hz, H^4), 4.22 (q, 8H, J$_{HH}$ = 7.12 Hz, H^{10}), 2.56 (t, 8H, J$_{HH}$ = 7.29 Hz, H^8), 2.41 (p, 8H, J$_{HH}$ = 7.47 Hz, H^5), 1.87 (p, 8H, J$_{HH}$ = 7.41 Hz, H^7), 1.69 (m, 8H, H^6), 1.28 (d, 12H, J$_{HH}$ = 7.15 Hz, H^{11}). ^{13}**C (D$_2$O, 126 MHz)**: 176.8 C^9, 157.6 C^c, 143.0 C^3, 133.4 C^2, 115.8 C^b, 61.7 C^{4+10}, 33.7 C^8, 30.5 C^5, 24.9 C^7, 23.7 C^6, 13.4 C^{11}. C^1 and C^a were not resolved.

L-Cysteine. ^{1}H (D$_2$O, 400 MHz): 3.98 (dd, 1H, J$_{HH}$ = 5.64, 4.11 Hz, H^2), 3.10 (dd, 1H, J$_{HH}$ = 14.93, 5.65 Hz, H^3), 3.01 (dd, 1H, J$_{HH}$ = 14.97, 4.11 Hz, H^3). ^{13}**C (D$_2$O, 100 MHz)**: 172.4 C^1, 55.8 C^2, 24.7 C^3.

L-Cystine ^{1}H (D$_2$O, 400 MHz): 4.13 (dd, 1H, J$_{HH}$ = 8.21, 3.81 Hz, H^2), 3.39 (dd, 1H, J$_{HH}$ = 15.02, 3.89 Hz, H^3), 3.19 (dd, 1H, J$_{HH}$ = 15.00, 8.20 Hz, H^3). ^{13}**C (D$_2$O, 100 MHz)**: 172.4 C^1, 55.8 C^2, 24.7 C^3. NMR data match those reported in ref [35].

DL-Homocysteine. ^{1}H (D$_2$O, 400 MHz): 3.90 (t, 1H, J$_{HH}$ = 6.76 Hz, H^2), 2.67 (m, 2H, H^4), 2.18 (m, 2H, H^3). ^{13}**C (D$_2$O, 100 MHz)**: 174.2 C^1, 53.6 C^2, 34.6 C^3, 19.8 C^4.

DL-Homocystine. ^{1}H (D$_2$O, 400 MHz): 3.88 (two t, 1H, J$_{HH}$ = 6.40 and 6.36 Hz for the other enantiomer, H^2), 2.85 (m, 2H, H^4), 2.29 (m, 2H, H^3). ^{13}**C (D$_2$O, 126 MHz)**: 173.9 C^1, 53.5 C^2, 32.7 C^3, 29.9 C^4. NMR data match those reported in ref [36].

L-Methionine. ^{1}H (D$_2$O, 400 MHz): 3.88 (t, 1H, J$_{HH}$ = 6.59, 5.84 Hz, H^2), 2.66 (t, 2H, J$_{HH}$ = 7.63, 7.35 Hz, H^3), 2.20 (m, 2H, H^4), 2.15 (s, 3H, H^5). ^{13}**C (D$_2$O, 100 MHz)**: 174.2 C^1, 53.9 C^2, 29.7 C^3, 28.8 C^4, 13.9 C^5.

(S)-2-Amino-4-(methylsulfinyl)butanoic acid. ^{1}H (D$_2$O, 400 MHz): 3.9 (m, 1H, H^2), 3.05 (m, 2H, H^4), 2.77 (s, 3H, H^5), 2.33 (m, 2H, H^3). ^{13}**C (D$_2$O, 100 MHz)**: 173.2 C^1, 53.5 and 53.3 C^2, 48.3 and 48.2 C^4, 36.6 and 36.4 C^5, 23.8 C^3. NMR data match those reported in ref [37].

S-Phenyl-L-Cysteine. ^{1}H (D$_2$O, 500 MHz): 7.55 (m, 2H, H^6), 7.44 (m, 2H, H^3), 7.38 (m, 2H, H^4), 3.84 (ddd, 1H, J$_{HH}$ = 8.68, 3.89, 0.87 Hz, H^2), 3.64 (dd, 1H, J$_{HH}$ = 14.89, 3.92 Hz, H^3), 3.33 (dd, 1H, J$_{HH}$ = 14.89, 8.67 Hz, H^3). ^{13}**C (D$_2$O, 126 MHz)**: 172.6 C^1, 132.8 C^5, 130.6 C^6, 129.5 C^7, 127.6 C^8, 53.5 C^2, 34.9 C^3.

3-(Phenylsulfoxide)-L-alanine. ^{1}H (D$_2$O, 500 MHz): 7.79 (m, 2H, H^6), 7.70 (m, 3H, H^{7+8}), 4.26 (dd, 0.5 H, J$_{HH}$ = 7.72, 5.81 Hz, H^2), 4.03 (dd, 0.5 H, J$_{HH}$ = 8.81, 3.58 Hz, H^2), 3.53 (m, 1.5 H, H^3), 3.39 (dd, 0.5 H, J$_{HH}$ = 14.08, 7.78 Hz, H^3). ^{13}C (D$_2$O, 126 MHz): 171.2 C^1, 139.2 C^5, 132.8 and 132.6 C^6, 130.0 C^7, 124.5 C^8, 58.8 and 54.3 C^2, 50.9 and 50.2 C^3. Half proton integrals refer to one of the two possible diastereoisomers.

L-Arginine. ^{1}H (D$_2$O, 400 MHz): 3.22 (m, 1H, H^2), 3.17 (m, 2H, H^5), 1.58 (m, 4H, H^{3+4}). ^{13}**C (D$_2$O, 100 MHz)**: 183.1 C^1, 156.7 C^7, 55.5 C^2, 40.9 C^5, 31.5 C^3, 24.4 C^4.

L-Citrulline ^{1}H (D$_2$O, 400 MHz): 3.35 (t, 1H, J$_{HH}$ = 6.10 Hz, H^2), 3.14 (t, 2H, J$_{HH}$ = 6.72 Hz, H^5), 1.61 (m, 4H, H^{3+4}). ^{13}**C (D$_2$O, 100 MHz)**: 180.2 C^1, 156.7 C^7, 55.1 C^2, 40.8 C^5, 30.2 C^3, 24.2 C^4. NMR data match those reported in ref [38].

1,3-Thiazolane. ^{1}H (DMSO-d_6, 400 MHz): 4.03 (s, 2H, H^2), 2.89 (t, 2H, J$_{HH}$ = 6.04 Hz, H^5), 2.69 (t, 2H, J$_{HH}$ = 6.07 Hz, H^4). ^{13}**C (DMSO-d_6, 100 MHz)**: 55.2 C^2, 52.6 C^5, 33.4 C^4.

1,3-Thiazolane. ^{1}H (DMSO-d_6, 400 MHz): 4.12 (s, 2H, H^2), 3.10 (t, 2H, J$_{HH}$ = 6.40 Hz, H^5), 2.77 (t, 2H, J$_{HH}$ = 6.32 Hz, H^4). ^{13}**C (DMSO-d_6, 100 MHz)**: 58.3 C^2, 55.5 C^4, 29.3 C^5.

Thietane. ^{1}H (DMSO-d_6, 400 MHz): 3.16 (t, 4H, J$_{HH}$ = 7.58 Hz, H^2), 2.86 (tt, 2H, J$_{HH}$ = 7.94, 7.25 Hz, H^3). ^{13}**C (DMSO-d_6, 100 MHz)**: 52.4 C^2, 9.8 C^3.

Thietane sulfoxide. ^{1}H (DMSO-d_6, 400 MHz): 3.47 (m, 2H, H^2), 3.1 (m, 2H, H^2), 2.21 (m, 1H, H^3), 1.87 (m, 1H, H^3). ^{13}**C (DMSO-d_6, 100 MHz)**: 27.3 C^3, 25.2 C^2. NMR data match those reported in ref [39].

Thiolane. ^{1}H (DMSO-d_6, 400 MHz): 2.74 (m, 4H, H^2), 1.85 (m, 4H, H^3). ^{13}**C (DMSO-d_6, 100 MHz)**: 31.1 C^2, 31.7 C^3.

Thiolane sulfoxide. ^{1}H (DMSO-d_6, 400 MHz): 2.85 (m, 2H, H^2), 2.71 (m, 2H, H^2), 2.21 (m, 2H, H^3), 1.96 (m, 2H, H^3). ^{13}**C (DMSO-d_6, 126 MHz)**: 53.7 C^2, 24.9 C^3. NMR data match those reported in ref [40].

Thiinane. **¹H (DMSO-d_6, 400 MHz)**: 2.53 (m, 4H, H^2), 1.71 (m, 4H, H^3), 1.53 (m, 2H, H^4). **¹³C (DMSO-d_6O, 100 MHz)**: 28.1 C^2, 27.3 C^3, 25.8 C^4.

Thiinane sulfoxide. **¹H (DMSO-d_6, 400 MHz)**: 2.82 (m, 2H, H^2), 2.65 (m, 2H, H^2), 2.02 (m, 2H, H^3), 1.51 (m, 4H, H^{3+4}). **¹³C (DMSO-d_6, 100 MHz)**: 47.2 C^2, 24.1 C^3, 18.1 C^4. NMR data match those reported in ref [41].

Isothiocineole. **¹H (DMSO-d_6, 500 MHz)**: 3.27 (t, 1H, J_{HH} = 4.32 Hz, H^1), 2.23 (tt, 1H, J_{HH} = 13.23, 6.59 Hz, H^3), 2.07 (dt, 1H, J_{HH} = 12.22, 1.32 Hz, H^6), 1.94 (m, 1H, H^6), 1.81 (m, H1, H^5), 1.77 (m, 1H, H^2), 1.55 (m, 1H, H^3), 1.51 (m, 1H, H^4), 1.44 (s, 3H, H^8), 1.32 (s, 3H, H^9), 1.11 (m, 1H, H^4), 1.03 (d, 3H, J_{HH} = 7.06 Hz, H^{10}). **¹³C (DMSO-d_6, 126 MHz)**: 52.3 C^6, 52.1 C^1, 46.7 C^5, 35.1 C^7, 34.6 C^2, 33.8 C^9, 25.2 C^8, 24.0 C^4, 23.3 C^3, 18.5 C^{10}.

Isothiocineole oxide. **¹H (DMSO-d_6, 500 MHz)**: 2.82 (m, 1H, H^1), 2.23 (m, 2H, H^{2+6}), 2.10 (m, 1H, H^5), 1.98 (dt, 1H, J_{HH} = 12.98, 1.11 Hz, H^6), 1.55 (m, 1H, H^3), 1.42 (m, 1H, H^3), 1.38 (s, 3H, H$^{8/9}$), 1.24 (m, 2H, H^4), 1.14 (s, 3H, H$^{8/9}$), 1.02 (d, 3H, J_{HH} = 7.10 Hz, H^{10}). **¹³C (DMSO-d_6, 126 MHz)**: 69.5 C^1, 64.3 C^7, 47.4 C^5, 28.8 C^{2+6}, 25.8 C^4, 22.1 C^3, 22.0 C$^{8/9}$, 20.4 C$^{8/9}$, 17.6 C^{10}.

1,3-dithiolane. **¹H (MeOD, 400 MHz)**: 3.89 (s, 2H, H^2), 3.17 (s, 4H, H^{4+5}). **¹³C (MeOD, 100 MHz)**: 38.9 C^{4+5}, 34.7 C^2.

1,3-dithiolane-1-oxide. **¹H (MeOD, 400 MHz)**: 4.08 (d, J_{HH} = 12.80 Hz, 1H, H^2), 3.98 (d, J_{HH} = 12.87 Hz, 1H, H^2), 3.52 (m, 3H, H^{4+5}), 2.97 (m, 1H, H^5). **¹³C (MeOD, 100 MHz)**: 57.8 C^2, 55.6 C^5, 32.1 C^4. NMR data match those reported in ref [42].

1,3-dithiinane. **¹H (DMSO-d_6, 500 MHz)**: 3.84 (s, 2H, H^2), 2.79 (m, 4H, H^{4+6}), 1.92 (m, 2H, H^5). **¹³C (DMSO-d_6, 126 MHz)**: 30.7 C^2, 28.8 C^{4+6}, 26.3 C^4.

1,3-dithiinane -1-oxide. **¹H (DMSO-d_6, 500 MHz)**: 4.15 (m, 1H, H^2), 3.78 (d, 1H, J_{HH} = 12.37 Hz, H^2), 3.20 (m, 1H, H^4), 2.70 (ddd, 1H, J_{HH} = 12.57, 11.72 and 2.71 Hz, H^4), 2.62 (ddd, 1H, J_{HH} = 13.50, 10.61 and 2.66, H^6), 2.55 (m, 1H, H^6), 2.35 (m, 1H, H^5), 1.96 (m, 1H, H^5). **¹³C (DMSO-d_6, 126 MHz)**: 51.1 C^2, 48.3 C^6, 26.9 C^4, 26.2 C^5. NMR data match those reported in ref [43].

1,4-dithiinane. **¹H (DMSO-d_6, 400 MHz)**: 2.83 (s, 8H). **¹³C (DMSO-d_6, 100 MHz)**: 28.4.

1,4-dithiinane -1-oxide. **¹H (DMSO-d_6, 400 MHz)**: 3.27 (m, 2H, H^2), 3.16 (m, 2H, H^3). **¹³C (DMSO-d_6, 100 MHz)**: 41.5 C^2, 33.7 C^3. NMR data match those reported in ref [43].

1,3,5-trithiinane. **¹H (DMSO-d_6, 400 MHz)**: 4.28 (s, 6H). **¹³C (DMSO-d_6, 100 MHz)**: 33.9.

1,3,5-trithiinane-1-oxide. **¹H (DMSO-d_6, 400 MHz)**: 4.31 (m, 2H, H^2), 4.18 (m, 3H, H^{2+4+6}), 3.67 (d, J_{HH} = 14.02 Hz, 1H, H^{4+6}). **¹³C (DMSO-d_6, 100 MHz)**: 50.3 C^2, 30.6 C^{4+6}.

2,2,4,4,6,6-hexamethyl-1,3,5-trithiinane. **¹H (DMSO-d_6, 400 MHz)**: 1.70 (s, 18H). **¹³C (DMSO-d_6, 100 MHz)**: 53.1 C^{2+4+6}, 34.4 C$^{7+8+9+10}$.

2,2,4,4,6,6-hexamethyl-1,3,5-trithiinane-1-oxide. **¹H (DMSO-d_6, 400 MHz)**: 1.71 (s, 3H, H$^{9/10}$), 1.65 (s, 6H, H$^{7/8}$), 1.61 (s, 3H, H$^{9/10}$), 1.55 (s, 6H, H$^{7/8}$). **¹³C (DMSO-d_6, 126 MHz)**: 64.3 C^4, 51.0 C^{2+6}, 33.9 C$^{9/10}$, 29.2 C$^{7/8}$, 21.7 C$^{7/8}$.

2,4,6-triphenyl-1,3,5-trithiinane. **¹H (DMSO-d_6, 400 MHz)**: 7.43 (m, 15H, H$^{8+9+10+12+13+14}$), 5.84 (s, 3H, H^{2+4+6}). **¹³C (DMSO-d_6, 100 MHz)**: 138.0 C^7, 129.2 C$^{8/9}$, 128.9 C^{10}, 127.7 C$^{8/9}$, 57.1 C^2.

2,4,6-triphenyl-1,3,5-trithiinane-1-oxide. **¹H (DMSO-d_6, 400 MHz)**: 7.54 (m, 2H, H^{10}), 7.43 (m, 13H, H$^{8+9+12+13+14}$), 6.43 (s, 1H, H^4), 5.90 (s, 2H, H^{2+6}). **¹³C (DMSO-d_6, 100 MHz)**: 135.0 C^{11}, 133.6 C^7, 129.5 C$^{9+10/13+14}$, 129.4 C^8, 129.2 C$^{9+10/13+14}$, 127.5 C^{12}, 69.9 C^{2+6}, 54.3 C^4.

Lamivudine. **¹H (D$_2$O, 500 MHz)**: 7.98 (d, 1H, J_{HH} = 7.56 Hz, H^6), 6.31 (dd, 1H, J_{HH} = 5.62, 4.25 Hz, H^7), 6.02 (d, 1H, J_{HH} = 7.58 Hz, H^5), 5.35 (d, 1H, J_{HH} = 4.54, 3.38 Hz, H^{10}), 4.00 (dd, 1H, J_{HH} = 12.72, 3.39 Hz, H^{11}), 3.90 (dd, 1H, J_{HH} = 12.72, 4.54 Hz, H^{11}), 3.57 (dd 1H, J_{HH} = 12.25, 5.63 Hz, H^8), 3.21 (dd, 1H, J_{HH} = 12.24, 4.27 Hz, H^8). **¹³C (D$_2$O, 126 MHz)**: 166.1 C^4, 157.2 C^2, 141.6 C^6, 95.8 C^5, 87.2 C^7, 85.9 C^{10}, 62.1 C^{11}, 36.7 C^8.

Lamivudine oxide, major component (assigned to the diastereosiomer (*S*)). ¹H (D$_2$O, 500 MHz): 7.75 (d, 1H, J_{HH} = 7.62 Hz, H^6), 6.09 (dd, 1H, J_{HH} = 9.07, 4.80 Hz, H^7), 6.08 (d, 1H, J_{HH} = 7.57 Hz, H^5), 4.96 (t, 1H, J_{HH} = 3.61 Hz, H^{10}), 4.25 (dd, 1H, J_{HH} = 13.08, 3.38 Hz, H^{11}), 4.08 (dd, 1H, J_{HH} = 13.07, 3.83 Hz, H^{11}), 3.63 (dd, 1H, J_{HH} = 14.27,

4.82 Hz, H[8]), 3.39 (dd, 1H, J_{HH} = 14.27, 4.82 Hz, H[8]). **^{13}C (D$_2$O, 126 MHz)**: 165.9 C[4], 156.3 C[2], 141.6 C[6], 105.1 C[10], 96.8 C[5], 880 C[7], 58.9 C[11], 53.7 C[8].

Lamivudine oxide, minor component (assigned to the diastereoisomer (*R*)). **^{1}H (D$_2$O, 500 MHz):** 7.87 (d, 1H, J_{HH} = 7.62 Hz, H[6']), 6.68 (dd, 1H, J_{HH} = 8.25, 3.21 Hz, H[7']), 6.08 (d, 1H, J_{HH} = 7.57 Hz, H[5']), 4.92 (m, 1H, H[10']), 4.15 (dd, 2H, J_{HH} = 6.49, 3.94 Hz, H[11']), 3.89 (dd, 1H, J_{HH} = 15.87, 8.25 Hz, H[8']), 3.45 (dd, 1H, J_{HH} = 15.91, 3.20 Hz, H[8']). **^{13}C (D$_2$O, 126 MHz)**: 165.6 C[4'], 156.4 C[2'], 142.0 C[6'], 105.1 C[10'], 96.8 C[5'], 86.6 C[7'], 56.2 C[11'], 55.2 C[8'].

Emtricitabine. **^{1}H (D$_2$O, 500 MHz):** 8.20 (d, 1H, J_{HF} = 6.55 Hz, H[6]), 6.28 (ddd, 1H, J_{HH} = 5.54, 3.67, 1.80 Hz, H[7]), 5.36 (dd, 1H, J_{HH} = 4.17, 3.23 Hz, H[10]), 4.05 (dd, 1H, J_{HH} = 12.85, 3.27 Hz, H[11]), 3.93 (dd, 1H, J_{HH} = 12.84, 4.16 Hz, H[11]), 3.59 (dd, 1H, J_{HH} = 12.41, 5.60 Hz, H[8]), 3.24 (dd, 1H, J_{HH} = 12.45, 3.69 Hz, H[8]). **^{13}C (D$_2$O, 126 MHz)**: 158.3 (d, J_{CF} = 14.67 Hz, C[4]), 155.3 C[2], 137.1 (d, J_{CF} = 242.27 Hz, C[5]), 126.1 (d, J_{CF} = 33.27 Hz, C[6]), 87.8 C[7], 86.6 C[10], 61.7 C[11], 37.1 C[8]. **^{19}F (D$_2$O, 470 MHz)**: -165.8 F[5].

Emtricitabine oxide, major component (assigned to the diastereoisomer (*S*)). **^{1}H (D$_2$O, 500 MHz):** 7.91 (d, 1H, J_{HF} = 6.24 Hz, H[6]), 6.70 (ddd, 1H, J_{HH} = 1.51, 4.69, 9.29 Hz, H[7]), 4.97 (t, 1H, J_{HH} = 3.50 Hz, H[10]), 4.25 (dd, 1H, J_{HH} = 3.28, 13.11 Hz, H[11]), 4.07 (dd, 1H, J_{HH} = 3.75, 13.07 Hz, H[11]), 3.65 (dd, 1H, J_{HH} = 14.30, 4.69 Hz, H[8]), 3.31 (dd, 1H, J_{HH} = 14.30, 9.25 Hz, H[8]). **^{13}C (D$_2$O, 126 MHz)**: 158.5 (d, J_{CF} = 14.98 Hz, C[4]), 154.9 C[2], 137.6 (d, J_{CF} = 244.48 Hz, C[5]), 125.5 (d, J_{CF} = 33.04 Hz, C[6]), 105.1 C[10], 88.0 C[7], 58.9 C[11], 53.7 C[8]. **^{19}F (D$_2$O, 470 MHz)**: -164.5 F[5].

Emtricitabine oxide, minor component (assigned to the diastereoisomer (R)). **^{1}H (D$_2$O, 500 MHz):** 8.00 (d, 1H, J_{HF} = 6.40 Hz, H[6']), 6.66 (ddd, 1H, J_{HH} = 8.26, 2.92, 1.75 Hz, H[7']), 4.93 (dd, 1H, J_{HH} = 7.04, 5.89 Hz, H[10']), 4.16 (dd, 2H, J_{HH} = 6.48, 2.58 Hz, H[11']), 3.88 (dd, 1H, J_{HH} = 15.91, 8.26 Hz, H[8']), 3.50 (m, 1H, H[8']). **^{13}C (D$_2$O, 126 MHz)**: 158.2 (d, J_{CF} = 15.24 Hz, C[4]), 155.0 C2, 137.7 (d, J_{CF} = 244.19 Hz, C[5]), 126.1 (d, J_{CF} = 33.32 Hz, C[6]), 105.1 C[10], 87.1 C[7], 56.3 C[11], 55.1 C[8]. **^{19}F (D$_2$O, 470 MHz)**: -164.1 F[5'].

2-methyl-4-propyl-1,3-oxathiane. **^{1}H (DMSO-*d$_6$*, 500 MHz)**: 4.81 (q, 1H, J_{HH} = 6.18 Hz, H[2]), 4.04 (ddd, 1H, J_{HH} =11.86, 4.03, 2.30 Hz, H[6]), 3.62 (ddd, 1H, J_{HH} =12.49, 11.85, 2.06 Hz, H[6]), 3.07 (dddd, 1H, J_{HH} =11.41, 7.43, 6.01. 2.71 Hz, H[4]), 1.71 (dq, 1H, J_{HH} =13.66, 2.38 Hz, H[5]), 1.40 (m, 7H, H[5+8+9]), 1.33 (d, 3H, J_{HH} =6.20 Hz, H[7]), 0.88 (t, 3H, J_{HH} = 7.30 Hz, H[10]). **^{13}C (DMSO-*d$_6$*, 126 MHz)**: 78.1 C[2], 68.9 C[6], 41.3 C[4], 37.9 C[8/9], 32.7 C[5], 21.8 C[7], 18.7 C[8/9], 13.7 C[10].

2-methyl-4-propyl-1,3-oxathiane-3-oxide. **^{1}H (DMSO-*d$_6$*, 500 MHz)**: 4.25 (q, 1H, J_{HH} = 6.30 Hz, H[4]), 3.90 (ddd, 1H, J_{HH} = 11.71, 4.43, 1.82 Hz, H[6]), 3.67 (td, 1H, J_{HH} = 12.04, 2.00 Hz, H[6]), 2.79 (dddd, 1H, J_{HH} = 12.55, 8.38, 4.14, 2.96 Hz, H[4]), 1.99 (dq, 1H, J_{HH} = 15.20, 1.95 Hz, H[5]), 1.88 (dddd, 1H, JHH = 14.11, 11.10, 6.24, 4.12 Hz, H[8/9]), 1.57 (m, 3H, H[5+8/9]), 1.48 (d, 3H, J_{HH} = 6.28 Hz, H[7]), 1.36 (m, 1H, H[8/9]), 1.31 (m, 2H, H[8/9]), 0.91 (t, 3H, J_{HH} = 7.28 Hz, H[10]). **^{13}C (DMSO-*d$_6$*, 126 MHz)**: 91.8 C[2], 68.5 C[6], 61.0 C[4], 31.9 C[8/9], 29.7 C[5], 18.6 C[8/9], 16.5 C[7], 14.0 C[10]. NMR data match those reported in ref [44].

Cephalexin. **^{1}H (D$_2$O, 500 MHz)**: 7.54 (m, 5H, H[14+15+16]), 5.66 (d, 1H, J_{HH} = 4.41 Hz, H[8]), 5.21 (s, 1H, H[12]), 5.05 (d, 1H, J_{HH} = 4.45 Hz, H[6]), 3.48 (d, 1H, J_{HH} = 18.08 Hz, H[2]), 3.05 (d, 1H, J_{HH} = 17.91 Hz, H[2]), 1.86 (s, 3H, H[9]). **^{13}C (D$_2$O, 126 MHz)**: 169.9 C[10], 169.5 C[11], 163.4 C[7], 131.7 C[13], 130.5 C[16], 129.6 C[14/15], 128.2 C[14/15], 126.3 C[4], 121.8 C[3], 58.5 C[8], 56.8 C[6], 56.6 C[12], 28.2 C[2], 18.3 C[9].

Cephalexin oxide. **^{1}H (D$_2$O, 500 MHz)**: 7.55 (m, 5H, H[14+15+16]), 5.71 (d, 1H, J_{HH} = 4.15 Hz, H[8]), 5.31 (s, 1H, H[12]), 4.89 (d, 1H, J_{HH} = 4.13 Hz, H[6]), 4.05 (d, 1H, J_{HH} = 16.45 Hz, H[2]), 3.55 (d, 1H, J_{HH} = 16.45 Hz, H[2]), 1.91 (s, 3H, H[9]). **^{13}C (D$_2$O, 126 MHz)**: 169.2 C[11], 168.0 C[10], 161.7 C[7], 131.2 C[13], 130.6 C[16], 129.7 C[14/15], 128.4 C[14/15], 126.7 C[4], 120.1 C[3], 72.2 C[6], 59.3 C[8], 56.7 C[12], 51.6 C[2], 18.1 C[9]. NO R

1,4-oxathiinane. **^{1}H (DMSO-*d$_6$*, 400 MHz)**: 3.79 (m, 4H, H[2]), 2.57 (m, 4H, H[3]). **^{13}C (DMSO-*d$_6$*, 100 MHz)**: 68.1 C[2], 26.2 C[3].

1,4-oxathiinane-4-oxide. **^{1}H (DMSO-*d$_6$*, 400 MHz)**: 4.12 (ddd, 2H, J_{HH} = 12.25, 9.90, 2.15 Hz, H[2]), 3.70 (ddd, 2H, J_{HH} = 12.50, 5.18, 3.66 Hz, H[2]), 2.99 (tdd, 2H, J_{HH} = 9.81, 4.13, 2.93 Hz, H[3]), 2.62(ddt, 2H, J_{HH} = 13.68, 4.16, 1.89 Hz, H[3]). **^{13}C (DMSO-*d$_6$*, 100 MHz)**: 58.6 C[2], 45.5 C[3]. NMR data match those reported in ref [45].

1,4-thiazinane. **^{1}H (DMSO-*d$_6$*, 400 MHz)**: 2.90 (m, 4H, H[3]), 2.46 (m, 4H, H[2]). **^{13}C (DMSO-*d$_6$*, 100 MHz)**: 47.5 C[3], 27.4 C[2].

1,4-thiazinane-1-oxide. **^{1}H (DMSO-*d$_6$*, 400 MHz)**: 3.26 (m, 2H, H[3]), 2.90 (ddd, 2H, J_{HH} = 12.18, 9.05, 2.84 Hz, H[3]), 2.76 (ddd, 2H, J_{HH} = 13.78, 6.66, 3.03 Hz, H[2]), 2.57 (ddd, 2H, J_{HH} = 8.93, 3.47, 2.06 Hz, H[2]). **^{13}C (DMSO-*d$_6$*, 100 MHz)**: 47.0 C[3], 38.2 C[2]. NMR data match those reported in ref [46].

References

[1] F. Ruff, A. Kucsman, *J. Chem. Soc. Perkin Trans. II*, 2, 1985, 683.

[2] K. Sato, M. Hyodo, M. Aoki, X.-Q. Zheng and R. Noyori, T*etrahedron* 57, 2001, 2469.

[3] C. Bolm and F. Bienewald, *Angew. Chem. Int. Ed.*, 1995, 34, 2640.

[4] B. Karimi, M. Ghoreishi-Nezhad, J, H, Clark, Org. Letters., 7, 625, 2005.

[5] K. Matsumoto, T. Yamaguchi, J. Fujisaki, B. Saito and T. Katsuki, *Chem. Asian J.*, 2008, 3, 351.

[6] P. Pitchen, E. Dunach, M. N. Deshmukh, H. B. Kagan, *J. Am. Chem. Soc.*, 1984, 106, 8188.

[7] Y. Wu, J. Liu, X. Li, A. S. C. Chan, *Eur. J. Org. Chem.*, 2009, 16, 2607.

[8] K. Noda, N. Hosoya, K. Yanai, R. Irie, T. Katsuki, *Tetrahedron Lett.*, 1994, 35, 1887.

[9] H. Egami and T. Katsuki, *J. Am. Chem. Soc.*, 2007, 129, 8940.

[10] G. E. O'Mahony, A. Ford and A. R. Maguire, *J. Org. Chem.*, 2012, 77, 3288.

[11] V. V. Thakur, A. Sudalai, *Tetrahedron: Asymmetry,* 2003, 14, 407.

[12] M. L. Kantam, B. V. Prakash, B. Bharathi, C. V. Reddy, *J. Mol. Catal. A: Chem.*, 2005, 226, 119.

[13] D. R. Rayner, A. J. Gordon, K. Mislow, *J. Am. Chem. Soc.*, 90, 4854, 1968.

[14] N. Khiar, Á. Salvador, V. Valdivia, A. Chelouan, A. Alcudia, E. Álvarez and I. Fernández, *J. Org. Chem.*, 2013, 78, 6510.

[15] G. Sipos, E. E. Drinkel and R. Dorta, *Chem. Soc. Rev.*, 2015, 44, 3834.

[16] I. Fernández and N. Khiar, 2008, *Asymmetric Catalysis Using Sulfoxides as Ligands, in Organosulfur Chemistry in Asymmetric Synthesis* (eds T. Toru and C. Bolm), Wiley-VCH Verlag GmbH & Co. KGaA, Weinheim, Germany.

[17] B. M. Trost and M. Rao, *Angew. Chem. Int. Ed.*, 2015, 54, 5026.

[18] S. Caron, R. W. Dugger, S. G. Ruggeri, J. A. Ragan and D. H. B. Ripin, *Chem. Rev.*, 2006, 106, 2943.

[19] E. R. Yera, A. E. Cleves and A. N. Jain, *J. Med. Chem.*, 2011, 54, 6771.

[20] S. Liao, I. Čorič, Q. Wang and B. List, *J. Am. Chem. Soc.*, 2012, 134, 10765.

[21] J. Wang, M. Sánchez-Roselló, J. L. Aceña, C. del Pozo, A. E. Sorochinsky, S. Fustero, V. A. Soloshonok and H. Liu, *Chem. Rev.*, 2014, 114, 2432.

[22] F. Colobert, V. Valdivia, S. Choppin, F. R. Leroux, I. Fernández, E. Álvarez and N. Khiar, *Org. Lett.*, 2009, 11, 5130.

[23] I. Fernández, E. Álvarez and N. Khiar, *Chem. Rev.* 2003, 103, 3651.

[24] M. C. Carreño, G. Hernández-Torres, M. Ribagorda and A. Urbano, *Chem. Commun.*, 2009, 0, 6129.

[25] A. Abramovitch, L. Fensterbank, M. Malacria and I. Marek, *Angew. Chem. Int. Ed.*, 2008, 47, 6865.

[26] D. Chao and M. Zhao, ChemSusChem 2017, 10,n 3358.

[27] S. M. Bonesi, E. Carbonell, H. Garcia, M. Fagnoni and A. Albini, *Applied Catalysis B: Environmental*, 79, 2008, 368.

[28] C. Su, R. Tandiana, B. Tian, A. Sengupta, W. Tang, J. Su and K. P. Loh, *ACS Catal.*, 2016, 6, 3594.

[29] M. C. DeRosa and R. J. Crutchley, *Coord. Chem. Rev.,* 233, 2002, 351.

[30] A. A. Ghogare and A. Greer, *Chem. Rev.* 2016, 116, 9994.

[31] M. J. Davies, *Photochem. Photobiol. Sci.*, 2004, 3, 17.

[32] A. W. Weitkampf, *J. Am. Chem. Soc.*, 1959, 81, 3430.

[33] The Good Scent Company, catalogue of flavours and fragrances.

[34] F. Jensen and C. S. Foote, *J. Am. Chem. Soc.,* 109, 1987, 1478.

[35] The Human Metabolome Database: http://www.hmdb.ca/metabolites/HMDB00192.

[36] The Human Metabolome Database : http://www.hmdb.ca/spectra/nmr_one_d/1427

[37] The Human Metabolome Database: http://www.hmdb.ca/metabolites/HMDB0002005.

[38] The Human Metabolome Database: http://www.hmdb.ca/spectra/nmr_one_d/1596.

[39] C. Cistaro, G. Fronza, R. Mondelli, *Journal of Magnetic Resonance* 15, 367, 1974.

[40] M. H. Ali, W. C. Stevens, *Synthesis* 7, 764, 1977. Entry 2d.

[41] R. J. Abraham, J. B. Byrne, L. Griffiths, *Magnetic Resonance in Chemistry*, 2008, 46, 667.

[42] V. Alphand, N. Gaggero, S. Colonna, P. Pasta, R. Furstoss, T*etrahedron*, 53, 28, 9695, 1997.

[43] E. Juaristi, J. Guzman, V. V. Krane and R. S: Glass, *Tetrahedron*, 40, 1984, 1477.

[44] V. K. Chadha, K. G. Leidal, B. V. Plapp, *J. Med. Chem.* 1983, 26, 916.

[45] G. Singer, G. Heusinger, A. Mosandl and C. Burschka, Liebigs Ann. Chem., 1987, 451.

[46] K. Kamataa, T. Hirano, R. Ishimoto, N. Mizuno, *Dalton Trans.*, 2010, 39, 23, 5509.

8 SINGLET OXYGEN ON AROMATIC/OLEFINIC SULFIDES

The report of Foote *et al.* that diphenylsulfide does not undergo direct singlet oxygen addition brought us to investigate whether this statement holds true for aromatic sulfides in general[1]. Of interest is what happens when sulfides are asymmetrical in the sense that the sulfur atom bears to the one side an aliphatic chain and to the other an sp^2 carbon which is part of an aromatic ring or of a vinyl unit. It is the wish of the author to specify that time limitations limited the investigation to only a few examples, and the reactivity screening is far from being complete.

8.1 Carbon atom hybridization

The series presented in Scheme 8.1 is useful to understand how the degree of reactivity varies from a sulfide attached to unsaturated units (sp^2,sp^2), passing to one of the kind (sp^3,sp^2) equivalent to (sp^2,sp^3), and finally to (sp^3,sp^3).
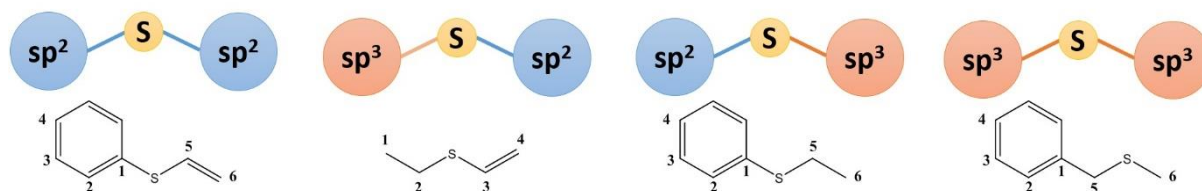
Scheme 8.1 Schematic representation of (left) phenyl vinyl sulfide (sp^2,sp^2), (middle) ethyl vinyl sulfide and phenyl ethyl sulfide (sp^3,sp^2) and (right) benzyl methyl sulfide (sp^3,sp^3). Numbers refer to NMR assignment.

As was the case with Ph_2S[1], a DMSO-d_6 solution of TPyCP (0.25 mol%) and phenyl vinyl sulfide showed no conversion after one day of LED irradiation at 660 nm(data not shown). The inactivity of the sulfur atom in between two sp^2-carbons, both aromatic, seems to be retained between an aromatic sulfide and a vinylic group. Removal of the unsaturation from one of the two arms of the sulfide led to complete conversion to the sulfoxide, indicating that not the phenyl or the vinyl alone are responsible for the inert behaviour of phenyl vinyl sulfide. Fig. 8.1 shows the ^{1}H and ^{13}C NMR spctra for the reaction involving ethyl vinyl sulfide, and Fig. 8.2 refers to the transformation of phenyl ethyl sulfide. Finally, placing an sp^3-carbon at both sides of the sulfur atom leads to the most reactive species of the series, for example, benzyl methyl sulfide, the NMR spectroscopic data of which are presented in Fig. 8.3. Scheme 8.2 shows sulfides that showed no conversion under experimental conditions equivalent to those described above.
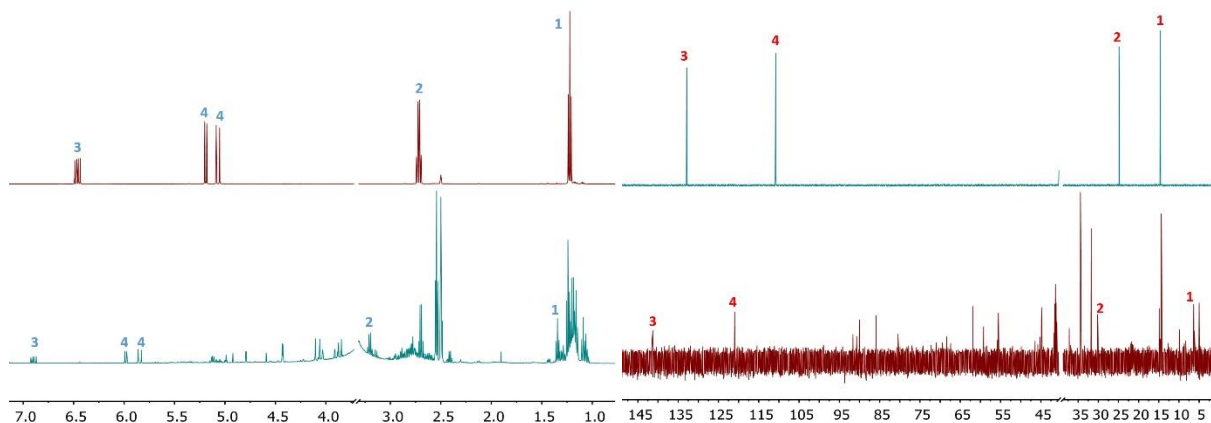
Fig. 7.1 (left) 400 MHz ^{1}H NMR spectrum and (right) 100 MHz ^{13}C NMR spectrum of a DMSO-d_6 solution of ethyl vinyl sulfide (top) and ethyl vinyl sulfoxide (bottom). See Scheme 8.1 for atom labelling.
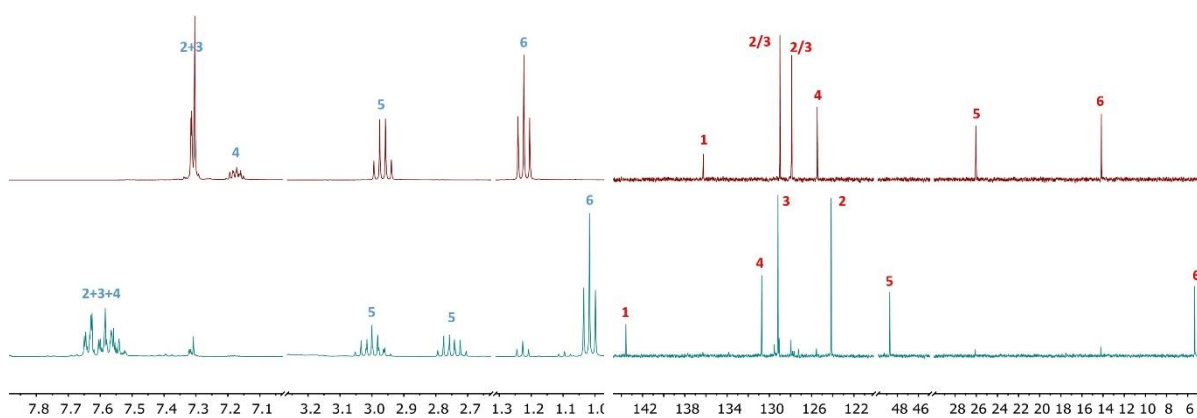

Fig. 8.2 (left) 400 MHz ^{1}H NMR spectrum and (right) 100 MHz ^{13}C NMR spectrum of a DMSO-d_6 solution of phenyl methyl sulfide (top) and phenyl methyl sulfoxide (bottom). See Scheme 8.1 for atom labelling.
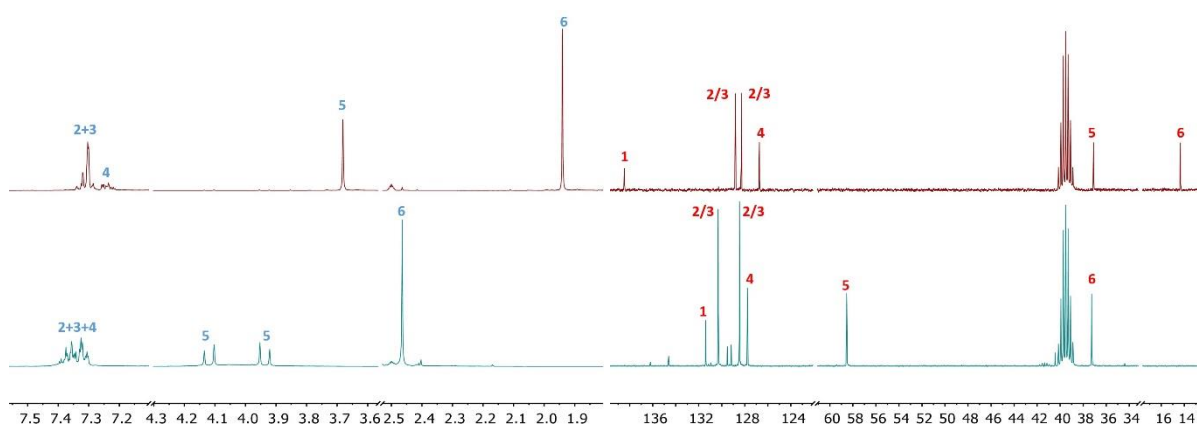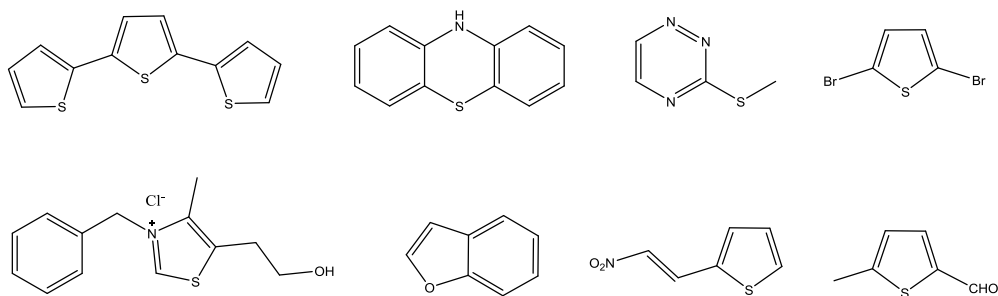

Fig. 8.3 (left) 400 MHz ^{1}H NMR spectrum and (right) 100 MHz ^{13}C NMR spectrum of a DMSO-d_6 solution of benzyl methyl sulfide (top) and benzyl methyl sulfoxide (bottom). See Scheme 8.1 for atom labelling.

125

Scheme 8.2 The structures of sulfur-containing compounds that were not converted to the corresponding sulfoxide upon treatment with singlet oxygen using TPyCP as photocatalyst.

8.2 Singlet oxygen on aromatics

Aromatic five-membered heterocycles possess a *cis*-diene structure, which has been shown previously to to react via a [4+2] cycloaddition with singlet oxygen (Section 5.3). Scheme 8.3 contains the structures of molecules of this kind that we could access. A DMSO-d_6 solution of each in the presence of TPyCP (0.25 mol%) was converted to the sulfoxide after one day of LED irradiation (λ_{ex} = 660nm) .
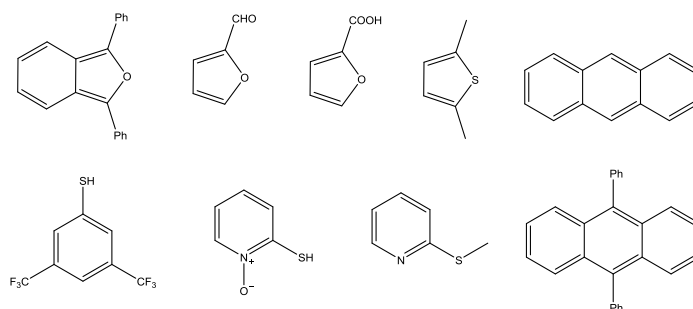
Scheme 8.3 From left to right: 1,3-diphenylisobenzofuran, furfural, furoic acid, 2,5-dimethylthiophene, anthracene, 9,10-diphenylanthracene, 3,5-bis(trifluoromethyl)benzenthiol, 2-mercaptopyridine N-oxide and 2-(methylthio)pyridine.

Each of the compounds in Scheme 8.3 possesses reactivity towards singlet oxygen; importantly, in some cases photooxidation leads to structures otherwise impossible to obtain in a single synthetic step. For 1,3-diphenylisobenzofuran, the reaction rate with singlet oxygen is one the highest ever measured[2]. The reaction proceeds via a [4+2] cycloaddition to form the endoperoxide, which spontaneously opens to give a dicarbonyl compound (Scheme 8.4). The reaction can be followed by means of UV-Vis spectroscopy since the starting material is bright yellow, while the product is white; this procedure is used in the literature to compare the rate of reaction of a specific substrate towards singlet oxygen with respect to 1,3-diphenylisobenzofuran. We preferred to follow the conversion via ^{1}H and ^{13}C NMR spectroscopy (Fig. 8.4).
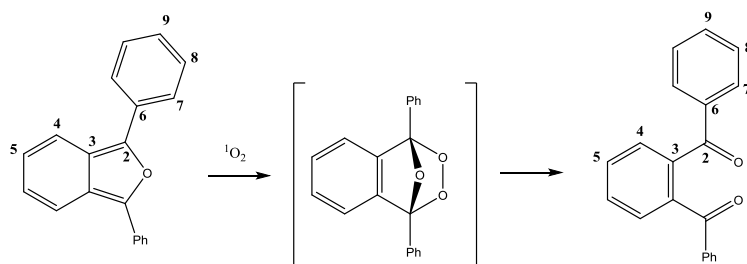
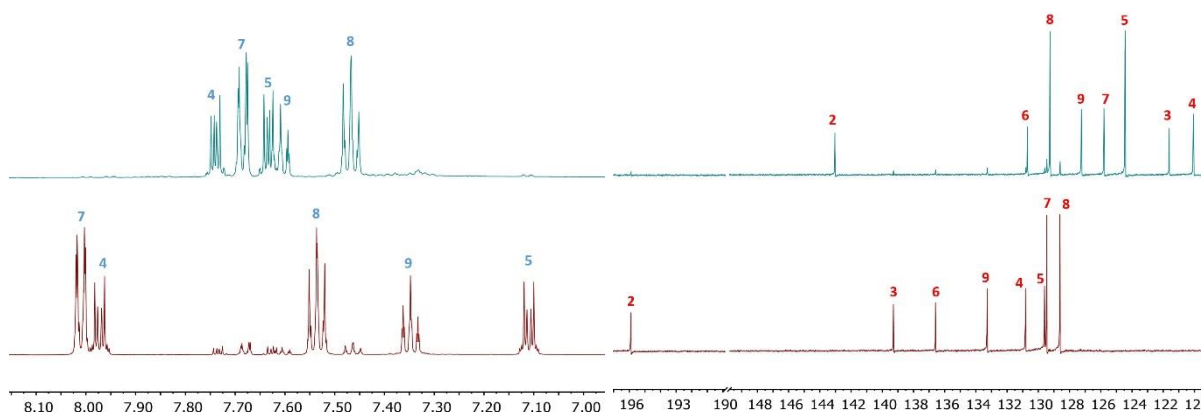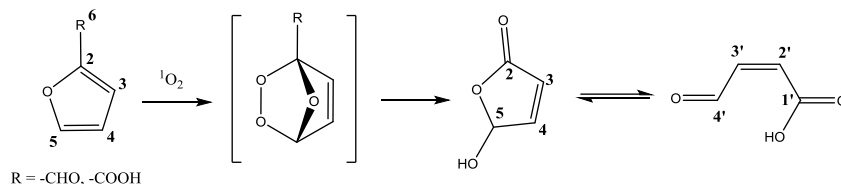Scheme 8.4 Reaction of 1,3-diphenylisobenzofuran and singlet oxygen.

Fig. 8.4 (left) 500 MHz ^{1}H NMR spectrum and (right) 126 MHz ^{13}C NMR spectrum of a DMSO-d_6 solution of 1,3-diphenylisobenzofuran (top) and 1,2-phenylenebis(phenylmethanone)(bottom). See Scheme 8.4 for atom labelling.

To the same family belongs benzo[b]furan, which is not reactive towards singlet oxygen, presumably because of the unfavourable position of the double bonds in the structure. [4+2] addition would lead to loss of aromaticity of the phenyl ring; [2+2] addition to the double bond in the α-position with respect to the oxygen atom would be a viable pathway, but, as Foote has shown for other aromatics, it becomes important only when working at 77 K[3]. Simple furan derivatives have their own reactivity. For both furfural (furan-2-carbaldehyde) and furoic acid (furan-2-carboxylic acid) reaction with singlet oxygen leads to an endoperoxide intermediate, which releases ring tension by elimination of the group in the α-position; rearrangement leads to the five-membered lactone 5-hydroxyfuran(5H)-2-one. In the case of furoic acid, 10% of the lactone undergoes ring opening to fumaraldehydic acid (Scheme 8.5). ^{1}H and ^{13}C NMR spectra of the product obtained reacting either of the two substrates match and are consistent with those reported in the literature[4] (Fig. 8.5 and 8.6).

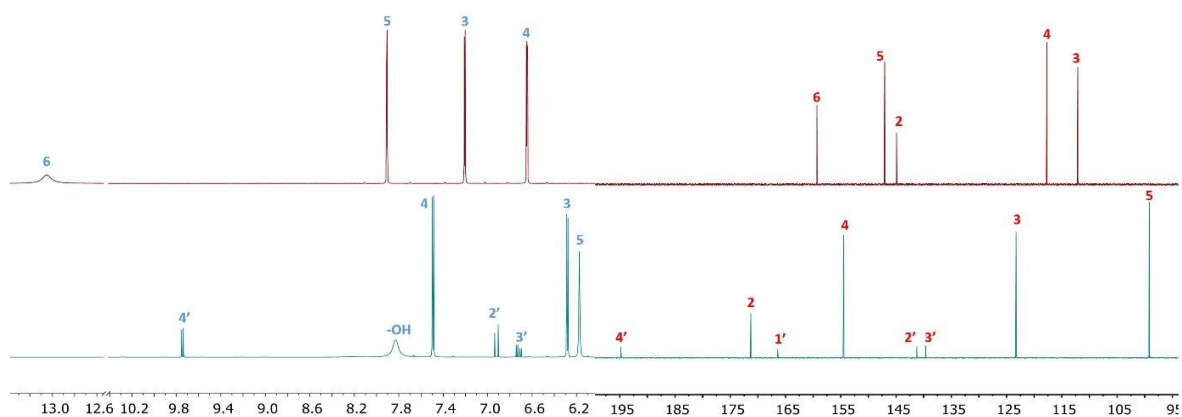Scheme 8.5 Reaction of furfural or furoic acid and singlet oxygen.

Fig. 8.5 (left) 500 MHz ^{1}H NMR spectrum and (right) 126 MHz ^{13}C NMR spectrum of a DMSO-d_6 solution of furoic acid (top) and a mixture of 5-hydroxyfuran(5H)-2-one and fumaraldehydic acid (bottom). See Scheme 8.5 for atom labelling.
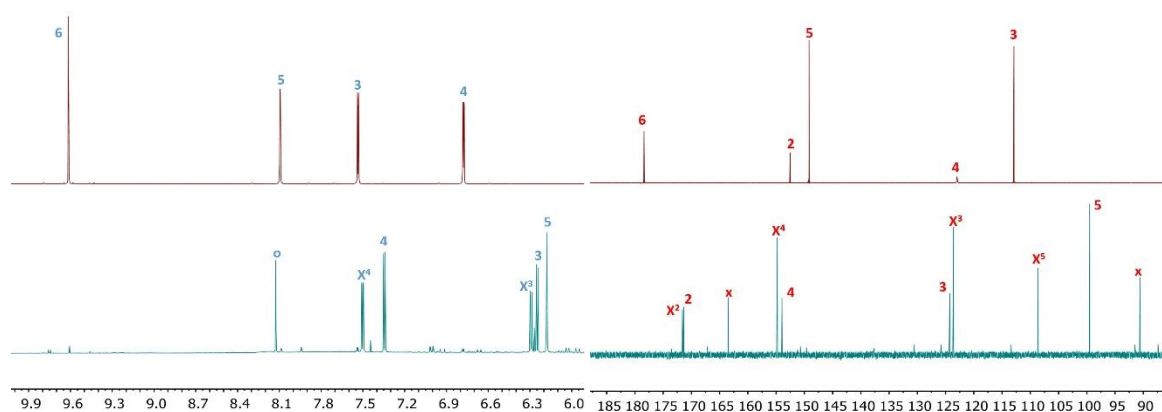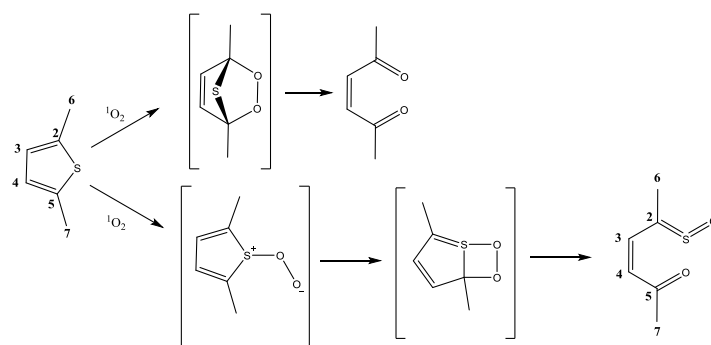

Fig. 8.6 (left) 500 MHz ^{1}H NMR spectrum and (right) 126 MHz ^{13}C NMR spectrum of a DMSO-d_6 solution of furfural (top) and 5-hydroxyfuran(5H)-2-one (bottom). "o" denotes a signal which does not give a COSY or NOESY cross peak to any other signal; "X" denotes a compound with spectral features similar to that of 5-hydroxyfuran(5H)-2-one, but whose identity is unknown. See Scheme 8.5 for atom labelling.

Passing from furan to thiophene has a deep effect on reactivity. As we know by now, singlet oxygen has a predilection for sulfur; in the case of 2,5-dimethylthiophene, this translates to two different modes of addition: the classical [4+2] cycloaddition and the formation of a persulfoxide (Scheme 8.6)[5]. The relative amount of the two products has been shown to vary depending on the solvent: chloroform gave 58% of *cis*-sulfine and 28% of diketone, while methanol gave 70% of the first and 2% of the second[5]. We performed the reaction in *d6*-DMSO and the NMR spectrum indicates complete conversion to a major species (Fig. 8.7).

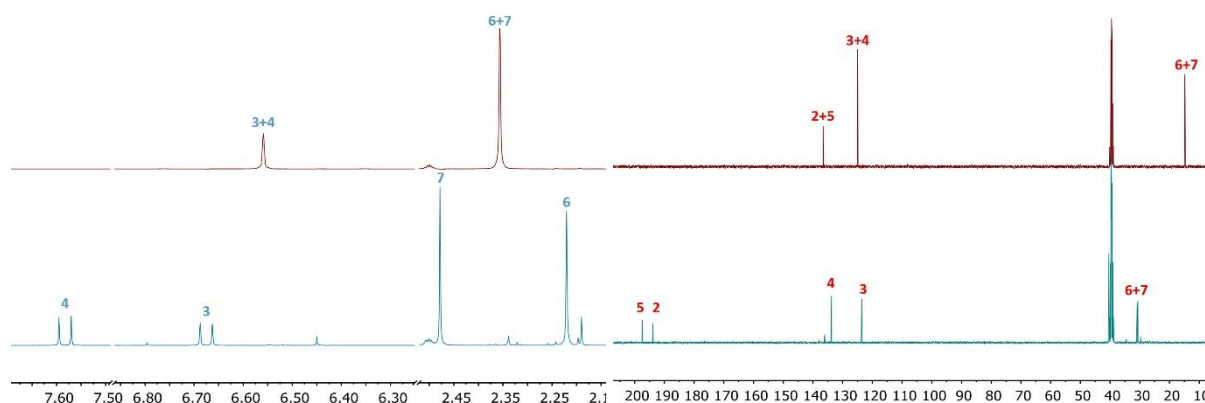Scheme 8.6 Reaction of 2,5-dimethylthiophene and singlet oxygen.

128

Fig. 8.7 (left) 400 MHz ^{1}H NMR spectrum and (right) 100 MHz ^{13}C NMR spectrum of a DMSO-d_6 solution of 2,5-dimethylthiophene (top) and the corresponding *cis*-sulfine derivative (bottom). See Scheme 8.6 for atom labelling.

The coupling constant *J* between H^3 and H^4 is 10 Hz; it perfectly matches that reported in literature and makes us confident to assign the structure to the *cis*-sulfine derivative shown in Scheme 8.6, bottom-right[5]. The major product derives from the attack of the peroxide to the alpha position, forming an intermediate dioxetane ring. Upon opening, one of the two oxygen atoms is retained on the sulfur, leading to the synthesis of a sulfine.

The reaction between anthracene and singlet oxygen has been used extensively to prove that different methods to generate singlet oxygen lead to the same product: anthracene endoperoxide (section 5.1). Scheme 8.7 shows the mechanism of the reaction for anthracene and 9,10-diphenylanthracene, but reactions involving 9,10-dimethylanthracene have been reported to react as well.
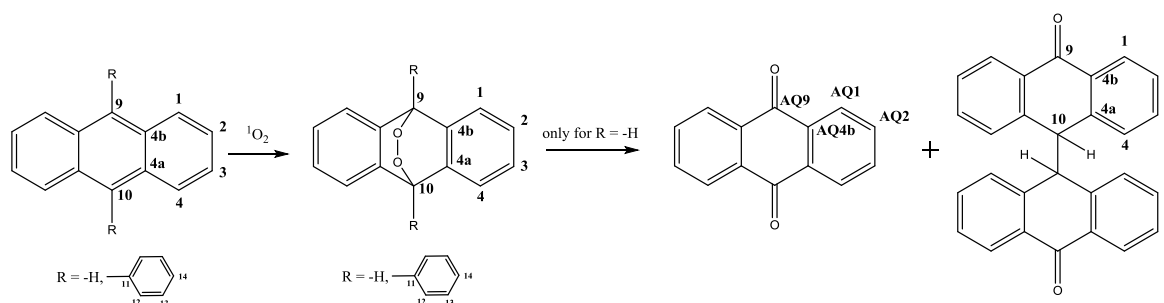
Scheme 8.7 Reaction of anthracene (R = H) or 9,10-diphenylanthracene (R = Ph) and singlet oxygen. In the case of anthracene, reaction goes on to anthraquinone and its dimeric form.

In our specific case it was possible to isolate the endoperoxide only when positions 9 and 10 bore a phenyl substituent (Fig. 8.8). For anthracene, the corresponding endoperoxide decomposed to two products (Fig. 8.9). One of the two was found to be anthraquinone: direct comparison with the ^{1}H NMR spectrum of anthraquinone matched part of the signals in our mixture. The second product is assigned as the dimeric quinone, with the two units connected through position 10. In fact, its NMR spectrum is consistent with positions 1 being different from 4 and 2 from 3. Dimerization is invoked to account for the loss of symmetry. Furthermore, it possess a quaternary carbon of carbonyl nature and an aliphatic proton. Anthrone (9(10H)-anthracenone) would possess both these characteristics, but direct comparison with the ^{1}H NMR spectrum of pristine material showed no match (data not shown). Unfortunately, it was not possible to find an NMR spectrum in the literature for direct comparison. From integration of the ^{1}H NMR spectrum of the mixture, we conclude

that anthraquinone is present in amounts that are 2.5 time less than that of the dimer (signal AQ1=4H results in 10H for position 1 of the dimer; if they were 1:1 I would have a ratio 4H:2H for these positions, correct?).
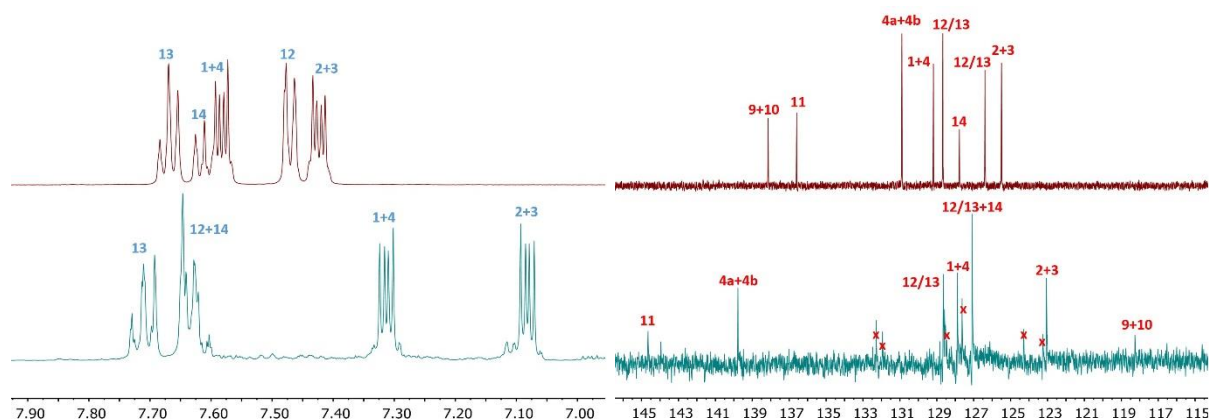

Fig. 8.8 (left) 400 MHz ^{1}H NMR spectrum and (right) 100 MHz ^{13}C NMR spectrum of a DMSO-d_6 solution of 9,10-diphenylanthracene (top) and 9,10-diphenylanthracene endoperoxide (bottom). Red crosses denote signal which did not show a cross peak in either HMBC or HMQC spectra of the product. See Scheme 8.7 for atom labelling.
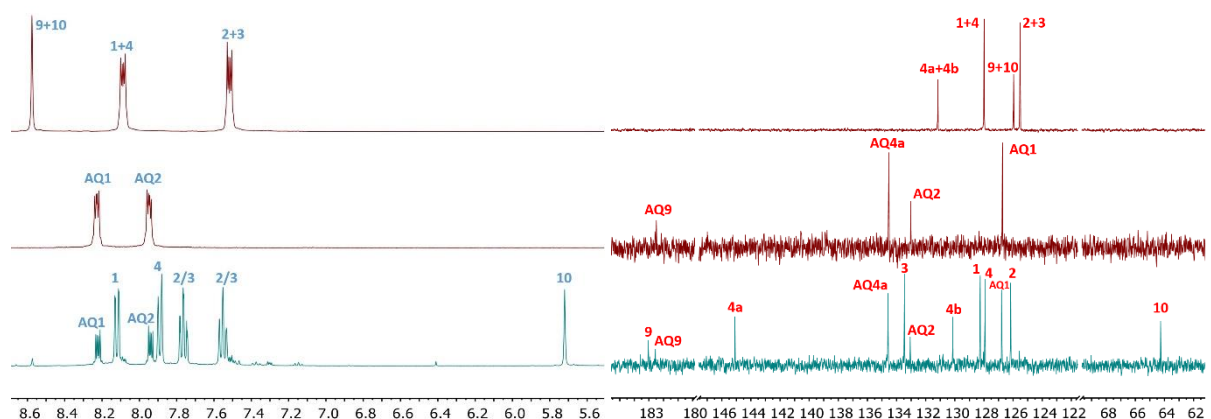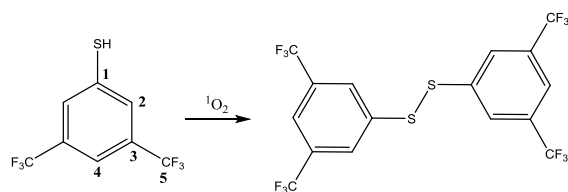

Fig. 8.9 (left) 400 MHz ^{1}H NMR spectrum and (right) 100 MHz ^{13}C NMR spectrum of a DMSO-d_6 solution of anthracene (top), anthraquinone (middle) and reaction mixture (bottom). See Scheme 8.7 for atom labelling.

As already discussed for cysteine and methionine (Chapter 6), reactivity of thiols and sulfides towards singlet oxygen differ in that thiols tend to form disulfides, while sulfides react to sulfoxides. Under the same conditions as for previous experiments, 3,5-bis(trifluoromethyl)benzenthiol was reacted with singlet oxygen and the resultant product was the disulfide (Scheme 8.8). The disulfide precipitates from the DMSO-d_6 solution as it is formed, but it can be redissolved in chloroform. Therefore, we present the NMR spectroscopic data for both the starting material and product in CDCl$_3$ (Fig. 8.10).

Scheme 8.8 Reaction of 3,5-bis(trifluoromethyl)benzenthiol and singlet oxygen.
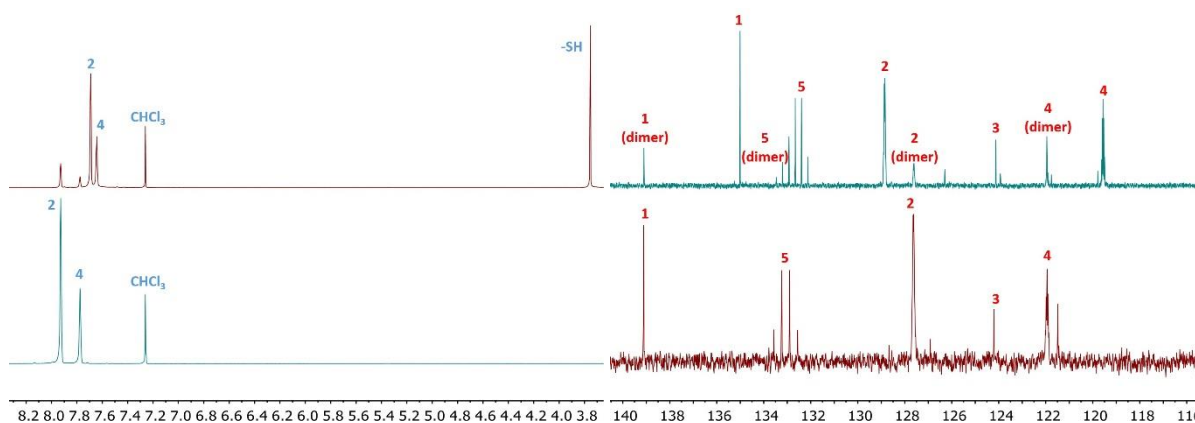
Fig. 8.10 (left) 400 MHz ^{1}H NMR spectrum and (right) 100 MHz ^{13}C NMR spectrum of a CDCl$_3$ solution of 3,5-bis(trifluoromethyl)benzenthiol (top) and di(3,5-bis(trifluoromethyl)phenyl) disulfide (bottom). See Scheme 8.8 for atom labelling.

For the first time, in all the photooxidations we have performed so far, the substrate had an effect on the catalyst. Specifically the colour of the DMSO-d_6 reaction mixture changed from red to emerald green upon irradiation at λ = 660 nm. The emerald colour is a direct consequence of the fact that the four Q bands of TPyCP are replaced by a broad absorption which spans all over the red part of the spectrum (Fig. 8.11). One of the possible assignment could be to a chlorin structure, in which one of the pyrrolyl double bonds has been reduced (Scheme 8.9). The evidence that the Soret band is completely lost made us discard this option since a chlorin still retains this feature; clearly more than one double bond is affected and the only ring current responsible for the transition is that leading to the red absorption.
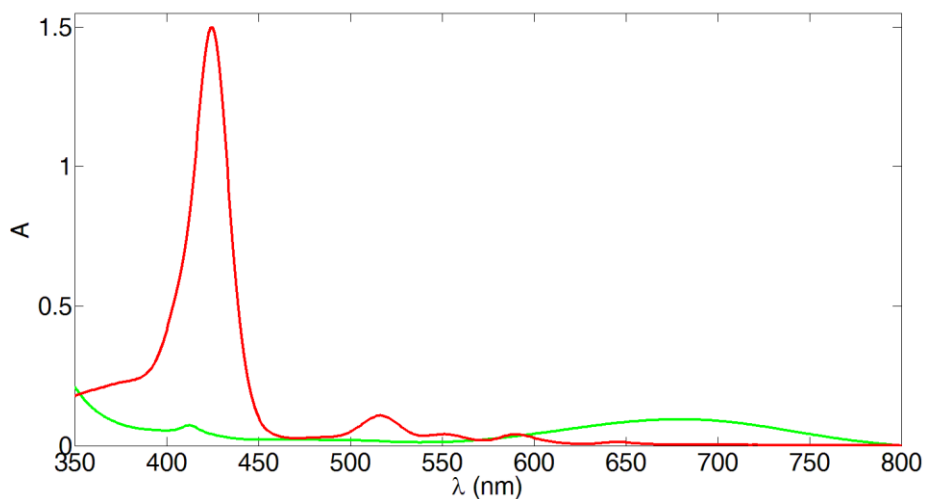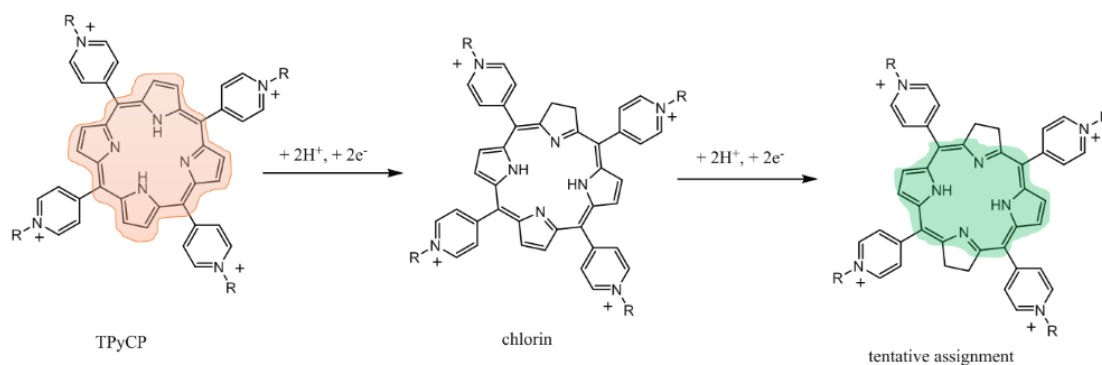

Fig. 8.11 Solution absorption spectrum of TPyCP and 3,5-bis(trifluoromethyl)benzenthiol (red) and of the reduced form of TPyCP (green). Solutions were made by mixing 100 µL of the DMSO-d_6 reaction mixture (pristine for red line and irradiated for green one) and 2.9 mL CH$_3$CN.

131

Scheme 8.9 Supposed mechanism for the reduction of TPyCP upon exposure to 3,5-bis(trifluoromethyl)benzenthiol. Shaded area underline the ring current.

With that being said, the reduced form of the catalyst is still active towards singlet oxygen generation. Two facts support this statement. First, TPyCP is present as 0.25 mol%, which translates to 1 mol% of 3,5-bis(trifluoromethyl)benzenthiol being consumed if we assume that a simple redox reaction takes place (Scheme 8.9) and that it requires 4 equivalents of reducing agent. Since the reaction goes on far beyond conversion of 1 mol% the catalyst is still active in its new form. Secondly, the absorption of the reduced form of TPyCP closely coincides with the LED emission spectrum; the overlap is better than that of TPyCP since it extends to the deep-red part of the spectrum. The experiment was repeated in dark conditions; again, the catalyst converts part of the thiol to disulfide and turns green. Once irradiated, the reaction mixture contains only disulfide. The ^{19}F NMR resonance is untouched by the chemical modification: the thiol finds itself δ -63.21 ppm and the disulfide at δ -63.29 ppm. This is not surprising because the CF_3 group is remote from the site of S–S oxidative coupling.

A second example of an aromatic thiol is 2-mercaptopyridine N-oxide (Scheme 8.10). Exposure to singlet oxygen results in a transformation assigned to the formation of the disulfide, based on comparison with literature data[6]. In DMSO-d_6, the ^{1}H spectrum of the starting material shows a resonance at δ 12.18 ppm (Fig 8.12). Considering that mercaptopyridines exist as two tautomers, this translates to that resonance belonging to a hydroxyl group connected to the nitrogen atom. In the ^{13}C NMR spectrum C^2 is the most shifted carbon atom, with a chemical shift of δ 168.2 ppm, typical of a thioketone (Fig 8.12). Such resonances disappear as the reaction takes place, which is a sign that the structure has been locked and tautomerism does not take place; the structure of a disulfide would meet this requirement.
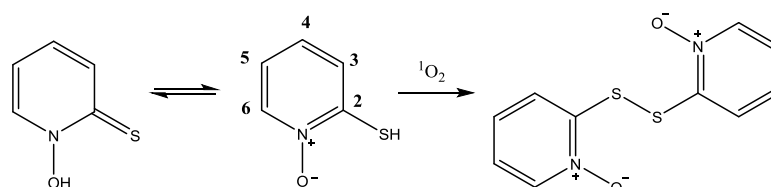
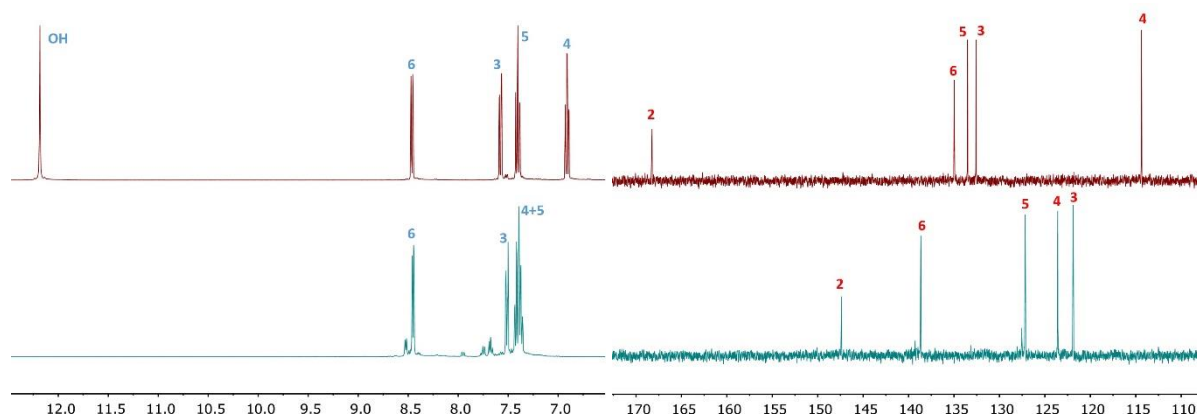Scheme 8.10 Reaction of 2-mercaptopyridine N-oxide and singlet oxygen.

Fig. 8.12 (left) 400 MHz ^{1}H NMR spectrum and (right) 100 MHz ^{13}C NMR spectrum of a DMSO-d_6 solution of 2-mercaptopyridine *N*-oxide (top) and bis(2-pyridoxydyl)disulfide (bottom). See Scheme 8.10 for atom labelling.

After the initial conversion is completed, a further transformation takes place. Later measurement of bis(2-pyridoxydyl)disulfide solution resulted in the NMR displayed in Fig. 8.13.
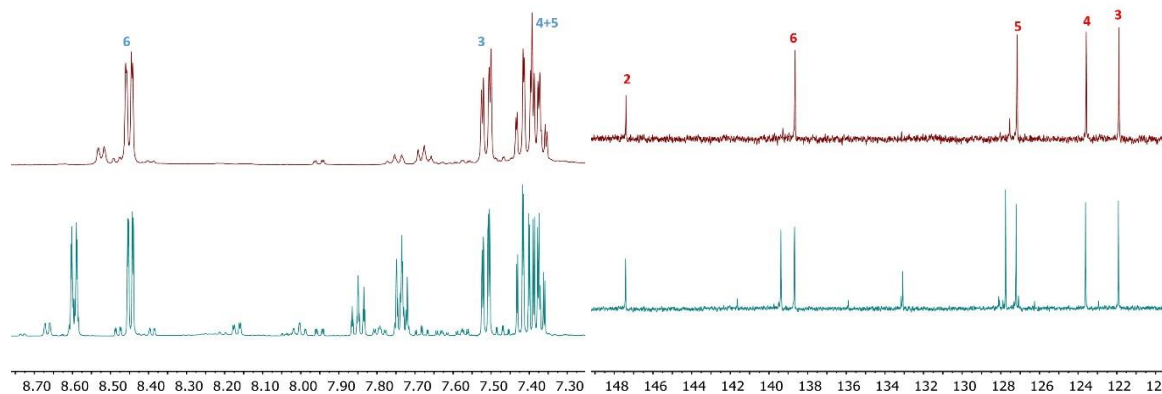

Fig. 8.13 (left) 400 MHz ^{1}H NMR spectrum and (right) 100 MHz ^{13}C NMR spectrum of a DMSO-d_6 solution of bis(2-pyridoxydyl)disulphide (top) and decomposition product (bottom). See Scheme 8.10 for atom labelling.

Last, we performed the oxidation on 2-(methylthio)pyridine. Being a liquid and being insoluble in water, we tried and succeeded in forming an emulsion in D$_2$O by sonication. The emulsion is off-white and stable under our experimental setup since continuous bubbling keeps the emulsion agitated. Two species exist in the emulsion. We start by assigning them to 2-(methylthio)pyridine as droplets (prefix A in Fig. 8.14 right) and as solubilized (prefix B in Fig. 8.14 right); they coexist in a 7:3 ratio. Fig. 8.14 left also shows that, after 90 min of irradiation, sulfoxide (prefix C) is slowly formed and stays in the aqueous phase. In fact, if the suspension is let separate, ^{1}H NMR of the aqueous phase only shows sulfoxide and dissolved starting material.
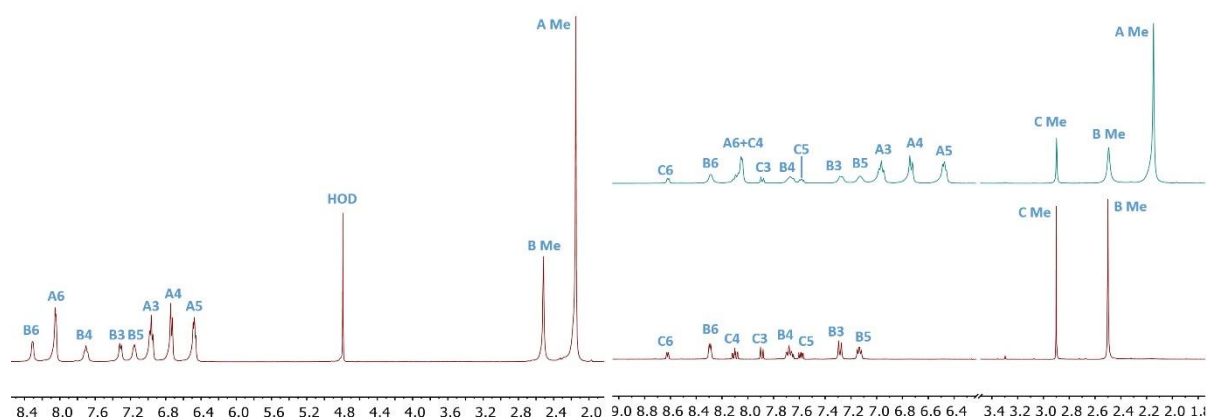
Fig. 8.14 400 MHz ^{1}H NMR spectrum of (left) a D$_2$O emulsion of 2-(methylthio)pyridine and (right) reaction mixture after 90 min of irradiation (top) and after separation of the droplets (bottom). Prefix A indicates the droplets, B the dissolved part and C the sulfoxide.

Mass-spectrometry confirms the presence of the sulfoxide. At the same time another species forms (prefix X in Fig. 8.15); its proton resonances are the most shifted, and it does not show up in the mass spectrum of the mixture. A structure for species X eludes elucidation, but we could collect three pieces of evidence on it. It is water soluble: when the reaction reaches completion, there is no longer an emulsion rather a homogeneous solution. The relative proportions of species C and X are stable over time: irradiation of the sulfoxide solution for 27 h did not result in conversion of C to X. Therefore, X does not represent a further transformation of C, but it is formed from A or B concurrently. If the photocatalyst is TPyCP C and X are formed in a proportion 98:2; if it is Rose Bengal, the proportion is C:X 85:15. In fact, the reaction was repeated with Rose Bengal (0.5 mol%) to check for possible effect of the photocatalyst. Irradiation was performed, with the usual LED setup, at 505 nm.
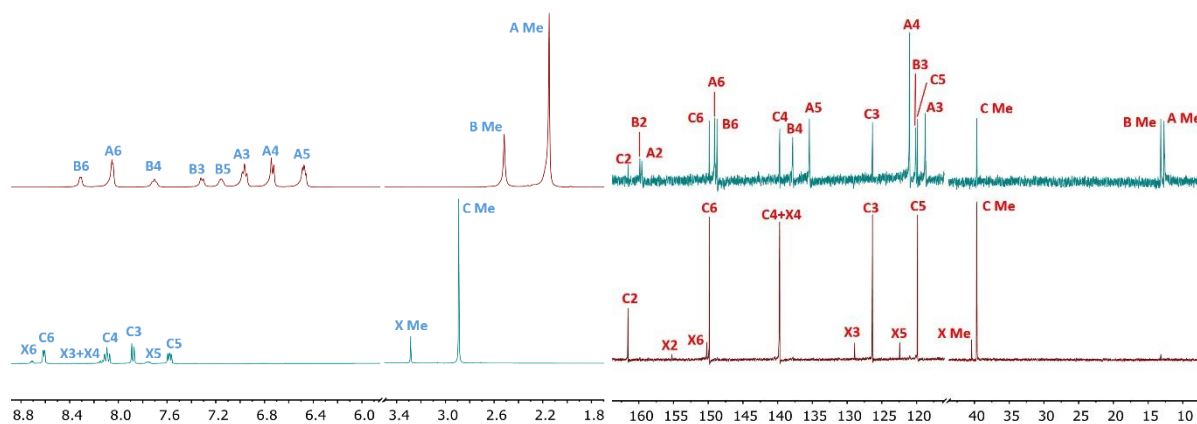

Fig. 8.15 (left) 400 MHz ^{1}H NMR spectrum and (right) 100 MHz ^{13}C NMR spectrum of a D$_2$O solution of 2-(methylthio)pyridine (top) and 2-(methylthio)pyridine sulfoxide. Prefix A indicates the droplets, B the dissolved part, C the sulfoxide and X the unknown species.

Concluding, application of singlet oxygen to aromatics has one major advantage over the reaction performed on aliphatic compounds and that is the variety of structures it is possible to target. On one hand singlet oxygen reacts with various aromatics, overcoming the limitation of possessing a sulfur atom, which is imposed to aliphatics; on the other hand, reactivity greatly differs from five- to six-membered heterocycles. Transformation of furan derivatives to lactones would be not easily achieved via common synthetic routes; the same applies to the transformation of 2,5-dimethyl-thiophene to a sulfine derivative. If it is true that conversion of thiols to disulfides broadens the spectrum of application of singlet

134

oxygen, it is also true that common oxidation procedures are effective as well. Therefore, we do not foresee singlet oxygen to become a competitor to well-established procedures targeting thiols.

8.3 NMR data

Ethyl vinyl sulfide. ^{1}H (DMSO-d_6, 500 MHz): 6.46 (dd, 1H, J_{HH} = 16.77 and 10.21 Hz, H^3), 5.19 (d, 1H, J_{HH} = 10.22 Hz, H^4), 5.07 (d, 1H, J_{HH} = 16.79 Hz, H^4), 2.72 (q, 2H, J_{HH} = 7.37 Hz, H^2), 1.22 (t, 1H, J_{HH} = 7.36 Hz, H^1). ^{13}C (DMSO-d_6, 126 MHz): 132.9 C^3, 110.8 C^4, 24.9 C^2, 14.6 C^1.

Ethyl vinyl sulfoxide. ^{1}H (DMSO-d_6, 500 MHz): 6.90 (dd, 1H, J_{HH} = 16.52 and 9.78 Hz, H^3), 5.98 (d, 1H, J_{HH} = 9.78 Hz, H^4), 5.84 (d, 1H, J_{HH} = 16.51 Hz, H^4), 3.20 (q, 2H, J_{HH} = 7.35 Hz, H^2), 1.34 (t, 3H, J_{HH} = 7.39 Hz, H^1). ^{13}C (DMSO-d_6, 126 MHz): 141.3 C^3, 121.0 C^4, 30.3 C^2, 6.4 C^1. NMR data match those reported in ref [7].

Phenyl ethyl sulfide. ^{1}H (DMSO-d_6, 400 MHz): 7.31 (m, 4H, H^{2+3}), 7.18 (m, 1H, H^4), 2.97 (q, 2H, J_{HH} = 7.33 Hz, H^5), 1.22 (t, 3H, J_{HH} = 7.32 Hz, H^6). ^{13}C (DMSO-d_6, 100 MHz): 136.2 C^1, 129.0 C$^{2/3}$, 127.9 C$^{2/3}$, 125.5 C^4, 26.0 C^5, 14.2 C^6.

Phenyl ethyl sulfoxide. ^{1}H (DMSO-d_6, 400 MHz): 7.59 (m, 5H, H^{2+3+4}), 2.99 (dq, 1H, J_{HH} = 13.41 and 7.34 Hz, H^5), 2.75 (dq, 1H, J_{HH} = 13.41 and 7.34 Hz, H^5), 1.02 (t, 3H, J_{HH} = 7.33 Hz, H^6). ^{13}C (DMSO-d_6, 100 MHz): 143.6 C^1, 130.7 C^4, 129.2 C^3, 124.2 C^2, 48.7 C^5, 5.4 C^6. NMR data match those reported in ref [8].

Benzyl methyl sulfide. ^{1}H (DMSO-d_6, 400 MHz): 7.31 (m, 4H, H^{2+3}), 7.25 (m, 1H, H^4), 3.58 (s, 2H, H^5), 1.94 (s, 3H, H^6). ^{13}C (DMSO-d_6, 100 MHz): 138.5 C^1, 128.8 C$^{2/3}$, 128.3 C$^{2/3}$, 126.7 C^4, 37.1 C^5, 14.3 C^6.

Benzyl methyl sulfoxide. ^{1}H (DMSO-d_6, 400 MHz): 7.34 (m, 5H, H^{2+3+4}), 4.12 (d, 1H, J_{HH} = 12.68 Hz, H^5), 3.94 (d, 1H, J_{HH} = 12.67 Hz, H^5), 2.46 (s, 3H, H^6). ^{13}C (DMSO-d_6, 100 MHz): 131.4 C^1, 130.3 C$^{2/3}$, 128.5 C$^{2/3}$, 127.8 C^4, 58.5 C^5, 37.3 C^6. NMR data match those reported in ref [9].

1,3-diphenylisobenzofuran. ^{1}H (DMSO-d_6, 500 MHz): 8.01 (m, 4H, H^7), 7.97 (m, 2H, H^4), 7.53 (m, 4H, H^8), 7.35 (m, 2H, H^9), 7.11 (m, 2H, H^5). ^{13}C (DMSO-d_6, 126 MHz): 143.0 C^2, 130.1 C^6, 129.3 C^8, 127.2 C^9, 125.8 C^7, 124.4 C^5, 121.6 C^3, 120.1 C^4.

1,2-phenylenebis(phenylmethanone). ^{1}H (DMSO-d_6, 500 MHz): 7.74 (dd, 2H, J_{HH} = 5.64 and 3.27 Hz, H^4), 7.68 (m, 4H, H^7), 7.63 (dd, 2H, J_{HH} = 5.68 and 3.28 Hz, H^5), 7.60 (m, 2H, H^9), 7.57 (m, 4H, H^8). ^{13}C (DMSO-d_6, 126 MHz): 195.9 C^2, 139.3 C^3, 136.6 C^6, 133.3 C^9, 130.8 C^4, 129.6 C^5, 129.5 C^7, 128.6 C^8. NMR data match those reported in ref [10].

Furoic acid. ^{1}H (DMSO-d_6, 500 MHz): 13.05 (s, 1H, H^6), 7.91 (dd, 1H, J_{HH} = 1.70 and 0.85 Hz, H^2), 7.21 (dd. 1H, J_{HH} = 3.46 and 0.83 Hz, H^4), 6.65 (dd, 1H, J_{HH} = 6.47 and 1.78 Hz, H^3). ^{13}C (DMSO-d_6, 126 MHz): 159.3 C^6, 147.1 C^5, 144.9 C^2, 117.7 C^4, 112.1 C^3.

Furfuraldehyde. ^{1}H (DMSO-d_6, 500 MHz): 9.61 (s, 1H, H^6), 8.09 (m, 1H, H^5), 7.53 (dd, 1H, J_{HH} = 3.61 and 0.79 Hz, H^4), 6.78 (dd, 1H, J_{HH} = 3.63 and 1.69 Hz, H^3). ^{13}C (DMSO-d_6, 126 MHz): 178.4 C^6, 152.5 C^5, 149.2 C^2, 123.0 C^4, 112.9 C^3.

5-hydroxy-2-(5H)-furanone. ^{1}H (DMSO-d_6, 500 MHz): 7.83 (s, 1H, H^{OH}), 7.49 (dd, 1H, J_{HH} = 5.67 and 1.18 Hz, H^4), 6.28 (dd, 1H, J_{HH} = 5.72 and 1.21 Hz, H^3), 6.18 (s, 1H, H^5). ^{13}C (DMSO-d_6, 126 MHz): 171.3 C^2, 154.5 C^4, 123.8 C^3, 99.2 C^5. NMR data match those reported in ref [11].

Fumaraldehydic acid. ^{1}H (DMSO-d_6, 500 MHz): 9.75 (d, 1H, J_{HH} = 7.59 Hz, H$^{4'}$), 6.92 (d, 1H, J_{HH} = 15.83 Hz, H$^{2'}$), 6.72 (dd, 1H, J_{HH} = 15.85 and 7.61 Hz, H$^{3'}$). ^{13}C (DMSO-d_6, 126 MHz): 194.8 C$^{4'}$, 166.4 C$^{1'}$, 141.2 C$^{2'}$, 139.7 C$^{3'}$. NMR data match those reported in ref [11].

2,5-dimethylthiophene. ^{1}H (DMSO-d_6, 400 MHz): 6.56 (s, 2H, H^{3+4}), 2.36 (s, 6H, H^{6+7}). ^{13}C (DMSO-d_6, 100 MHz): 136.6 C^{2+5}, 125.0 C^{2+3}, 14.8 C^{6+7}.

cis-sulfine. ^{1}H (DMSO-d_6, 400 MHz): 7.58 (d, 1H, 9.94 Hz, H^4), 6.68 (d, 1H, 9.94 Hz, H^3), 2.48 (s, 3H, H^7), 2.22 (s, 3H, H^6). ^{13}**C (DMSO-d_6, 100 MHz):** 197.5 C^5, 193.9 C^2, 133.8 C^4, 123.6 C^3, 30.8 C^{6+7}. NMR data match those reported in ref [5].

9,10-diphenylanthracene. ^{1}H (DMSO-d_6, 500 MHz): 7.67 (m, 4H, H^{13}), 7.62 (m, 2H, H^{14}), 7.58 (m, 4H, H^{1+4}), 7.47 (m, 4H, H^{12}), 7.43 (m, 4H, H^{2+3}). ^{13}**C (DMSO-d_6, 126 MHz):** 138.1 C^9, 136.6 C^{11}, 130.9 C^{4a+4b}, 129.2 C^1, 128.7 C$^{12/13}$, 127.8 C^{14}, 126.4 C$^{12/13}$, 125.5 C^{2+3}.

9,10-diphenylanthracene endoperoxide. ^{1}H (DMSO-d_6, 500 MHz): 7.71 (m, 4H, H^{13}), 7.63 (m, 6H, H^{12+14}), 7.31 (dd, 4H, J$_{HH}$ = 5.63 and 3.23 Hz, H^{1+4}), 7.09 (m, 4H, J$_{HH}$ = 5.61 and 3.24 Hz, H^{2+3}). ^{13}**C (DMSO-d_6, 126 MHz):** 144.7 C^{11}, 139.8 C^{4a+4b}, 128.7 C$^{12/13}$, 127.9 C^{1+4}, 127.1 C$^{12+13/14}$, 123.1 C^{2+3}, 118.2 C^{9+10}.

Anthracene. ^{1}H (DMSO-d_6, 400 MHz): 8.58 (s, 2H, H^{9+10}), 8.09 (dd, 4H, J$_{HH}$ = 6.48 and 3.32 Hz, H^{1+4}), 7.52 (dd, 4H, J$_{HH}$ = 6.5   8 and 3.19 Hz, H^{2+3}). ^{13}**C (DMSO-d_6, 126 MHz):** 131.2 C^{4a+4b}, 128.0 C^{1+4}, 126.0 C^{9+10}, 125.5 C^{2+3}.

Anthraquinone. ^{1}H (DMSO-d_6, 400 MHz): 8.23 (dd, 4H, J$_{HH}$ = 5.77 and 3.39 Hz, H^{AQ1}), 7.95 (dd, 4H, J$_{HH}$ = 5.79 and 3.29 Hz, H^{AQ2}). ^{13}**C (DMSO-d_6, 100 MHz):** 182.5 C^{AQ9}, 134.5 C^{AQ4a}, 133.0 C^{AQ2}, 126.7 C^{AQ1}. NMR data match those of commercially available anthraquinone.

Anthraquinone dimer. ^{1}H (DMSO-d_6, 500 MHz): 8.12 (dd, 8H, J$_{HH}$ = 7.79 and 1.41 Hz, H^1), 7.89 (m, 8H, H^4), 7.76 (td, 8H, J$_{HH}$ = 7.65 and 1.44 Hz, H$^{2/3}$), 7.55 (m, 8H, H$^{2/3}$), 5.72 (s, 2H, H^{10}). ^{13}**C (DMSO-d_6, 126 MHz):** 183.0 C^9, 145.1 C^{4a}, 133.5 C^3, 130.1 C^{4b}, 128.3 C^1, 128.0 C^4, 126.2 C^2, 64.3 C^{10}.

3,5-bis(trifluoromethyl)benzenthiol. ^{1}H (CDCl$_3$, 500 MHz): 7.69 (s, 2H, H^2), 7.64 (s, 1H, H^4). ^{13}**C (CDCl$_3$, 126 MHz):** 135.0 C^1, 132.5 (q, J$_{CF}$ = 33.5 Hz, C^5), 128.9 (m, C^2), 124.1 C^3, 119.6 C^4. ^{19}**F (CDCl$_3$, 470 MHz):** -63.21 F^5.
di(3,5-bis(trifluoromethyl)phenyl) disulfide. ^{1}H (CDCl$_3$, 500 MHz): 7.95 (s, 2H, H^2), 7.78 (s, 1H, H^4). ^{13}**C (CDCl$_3$, 126 MHz):** 138.9 C1, 132.6 (q, J$_{CF}$ = 35.3 Hz, C^5), 127.3 (m, C^2), 123.6 C3, 141.5 (m, C4). ^{19}**F (CDCl$_3$, 470 MHz):** -63.29 F^5. NMR data match those reported in ref [12].

2-mercaptopyridine N-oxide. ^{1}H (DMSO-d_6, 400 MHz): 12.18 (s, 1H, H^{OH}), 8.46 (ddd, 1H, J$_{HH}$ = 6.80, 1.55 and 0.61 Hz, H^6), 7.58 (ddd, 1H, J$_{HH}$ = 8.55, 1.85 and 0.61 Hz, H^3), 7.40 (ddd, 1H, J$_{HH}$ = 8.57, 7.08 and 1.55 Hz, H^5), 6.91 (td, 1H, J$_{HH}$ = 6.94 and 1.83 Hz, H^4). ^{13}**C (DMSO-d_6, 100 MHz):** 168.2 C^2, 134.9 C^6, 133.5 C^5, 132.5 C^3, 114.3 C^4.

Bis(2-pyridoxydyl)disulphide. ^{1}H (DMSO-d_6, 500 MHz): 8.45 (dd, 1H, J$_{HH}$ = 6.08 and 1.45 Hz, H^6), 7.51 (m, 1H, H^3), 7.40 (m, 2H, H^{4+5}). ^{13}**C (DMSO-d_6, 126 MHz):** 147.7 C^2, 138.7 C^6, 127.2 C^5, 123.6 C^4, 121.9 C^3. NMR data match those reported in ref [6].

2-(methylthio)pyridine, emulsion component. ^{1}H (D$_2$O, 400 MHz): 8.05 (d, 1H, J$_{HH}$ = 5.03 Hz, H^{A6}), 6.96 (m, 1H, H^{A3}), 6.73 (d, 1H, J$_{HH}$ = 8.19 Hz, H^{A4}), 6.47 (m, 1H, H^{A5}), 2.15 (s, 3H, Me^A). ^{13}**C (D$_2$O, 100 MHz):** 159.6 C^{A2}, 149.1 C^{A6}, 135.4 C^{A3}, 121.0 C^{A4}, 118.7 C^{A5}, 12.7 C^{MeA}.

2-(methylthio)pyridine, soluble component. ^{1}H (D$_2$O, 400 MHz): 8.31 (m, 1H, H^{B6}), 7.70 (t, J$_{HH}$ = 7.95 Hz, 1H, H^{B4}), 7.31 (d, J$_{HH}$ = 8.32 Hz, 1H, H^{B3}), 7.15 (m, 1H, H^{B5}), 2.52 (s, 3H, Me^B). ^{13}**C (D$_2$O, 100 MHz):** 159.9 C^{B1}, 148.7 C^{B6}, 137.9 C^{B4}, 121.0 C^{B3}, 120.2 C^{B5}, 13.1 C^{MeB}.

2-(methylsulfinyl)pyridine. ^{1}H (D$_2$O, 400 MHz): 8.61 (d, 1H, J$_{HH}$ = 4.73 Hz, H^{C6}), 8.11 (m, 1H, H^{C4}), 7.88 (d, J$_{HH}$ = 7.91 Hz, 1H, H^{C3}), 7.58 (dd, JHH = 7.59 and 4.91 Hz, H^{C5}), 2.89 (s, 3H, Me^C).). ^{13}**C (D$_2$O, 100 MHz):** 161.5 C^{C2}, 149.8 C^{C6}, 139.8 C^{C4}, 126.4 C^{C5}, 119.8 C^{C3}, 39.7 C^{MeC}. NMR data match those reported in ref [13].

Unknown compound. ^{1}H (D$_2$O, 400 MHz): 8.71 (d, 1H, J$_{HH}$ = 4.80 Hz, H^{X6}), 8.14 (m, 2H, H^{X3+X4}), 7.75 (m, 1H, H^{X5}), 3.29 (s, 3H, Me^X). ^{13}**C (D$_2$O, 100 MHz):** 155.2 C^{X2}, 150.2 C^{X6}, 139.8 C^{X4}, 128.9 C^{X5}, 122.5 C^{X3}, 40.4 C^{MeX}.

References

[1] C. S. Foote, J. W. Peters, *J. Am. Chem. Soc.,* 1, 93, 1971, 3795.

[2] F. Wilkinson, W. P. Helman and A. B. Ross, *J. Phys. Chem. Ref. Data* 24, 663, 1995.

[3] H. S. Ryang, C. S. Foote, *J. Am. Chem. Soc.*, 101, 1979, 6683.

[4] K. Gollnick and A. Griesbeck, *Tetrahedron*, 41, 11, 2057, 1985.

[5] C. N. Skold and R. H. Schlessinger, *Tetrahedron Lett.,* 10, 791, 1970.

[6] Saima, A. G. Lavekar, R. Kumar and A. K. Sinha, *J. Mol. Catal. B: Enzymatic* 116, 2015, 113.

[7] P. B. Page, B. R. Buckley, C. Elliott, Y. Chana, N. Dreyfus, F. Markend, *Synlett,* 2016, 27, 80.

[8] Y. Yuan, X. Shi and W. Liu, *Synlett*, 2011, 4, 559.

[9] X.-S. Zhang, Q.-L. Zhu, Y.-F. Zhang, Y.-B. Li and Z.-J. Shi, *Chem. Eur. J.*, 2013, 19, 11898.

[10] M. Bovenkerk and B. Esser, *Eur. J. Org. Chem.,* 2015, 775.

[11] A. G. Salles, S. Zarra, R. M. Turner, J. R. Nitschke, *J. Am. Chem. Soc.*, 2013, 135, 19143.

[12] R. R. Tata, C. S. Hampton, M. Hamata, *Adv. Synth. Catal*. 2017, 359, 1232.

[13] C. A. Dannenberg, L. Fritze, F. Krauskopf and C. Bolm, *Org. Biomol. Chem.*, 2017,15, 1086.

# Part III

Spectroelectrochemistry (emission)

9 SPECTROELECTROCHEMISTRY (emission)

9.1 State of the art

A commercial cell specifically designed for measuring the emission spectrum of an electrochemically generated species is not available as confirmed by discussions with sales representatives of analytical instrument companies at ILMAC2017 in Basel. At the atomic level, atomic emission spectroelectrochemistry has been developed by combining a three-electrode electrochemical flow cell with an inductively coupled plasma atomic emission spectrometer[1]. For molecules the situation is not that bright. The only devices in the literature able to perform such measurement are home-made cells. An example of this kind dates back to 1992 when Salbeck assembled a cell to perform simultaneously electrochemical and spectroelectrochemical measurements under thin-layer diffusion conditions[2]. In 1994 Kakiuchi and Takasu recorded the fluorescence of Eosin B as it crosses a polarized 1,2-dichloroethane/water interphase as a function of voltage[3]. In 2000 Girault *et al.* measured the fluorescence of zinc porphyrins at the same interphase by potential modulated fluorescence. A HeCd laser would hit the interphase and excite the Soret band of the dye, whose fluorescence would then be guided to the detector by total internal reflection[4]. Other strategies consist of immobilizing the compound of interest on a conducive film[5], performing in situ fluorescence microscopy[6] or working at a solid/liquid interphase as in spectrofluorometric hydrodynamic voltammetry[7]. Reports exist on the use of an OTTLE cell (optically transparent thin layer electrochemical cell)[8-10].

9.2 Experimental setup

An OTTLE cell design is presented in Scheme 9.1, together with a Cartesian coordinate system to help us define the orientation of the components. The face pointing towards the y-axis contains the optical windows and is transparent, while the face perpendicular to *x*-axis is opaque because consists of a plastic gasket embedding the dye solution. The design seems to make an OTTLE unfit for fluorescence measurements, given that the solution is enclosed between electrodes and polymeric material, opaque to radiation. Nevertheless, we will show in the remaining sections of this chapter that we could detect fluorescence and its changes over the electrochemical experiment. To do so, the cell is placed such that the excitation is performed along the *x*-axis. The excitation slit is opened to its maximum width (20 nm) to ensure illumination of the whole cell. The light-beam hits the lateral faces of the cell and is scattered in all directions by various plastic and metal parts. Scattering will ensure that a portion of light reaches the volume containing the solution; subsequent luminescence can be collected along the y-axis since it is transparent to radiation. Instrumentally, the sample holder of a fluorimeter is specifically designed for hosting cuvettes. In order to perform the experiments by means of an OTTLE cell, the holder was removed and the cell position was optimized in terms of its distance with respect to excitation and emission lenses to maximize the output fluorescence intensity. Electrical cables, linking each of the three electrodes to an external potentiostat, were passed through a pre-designed hole in the holder, along the *z*-axis.
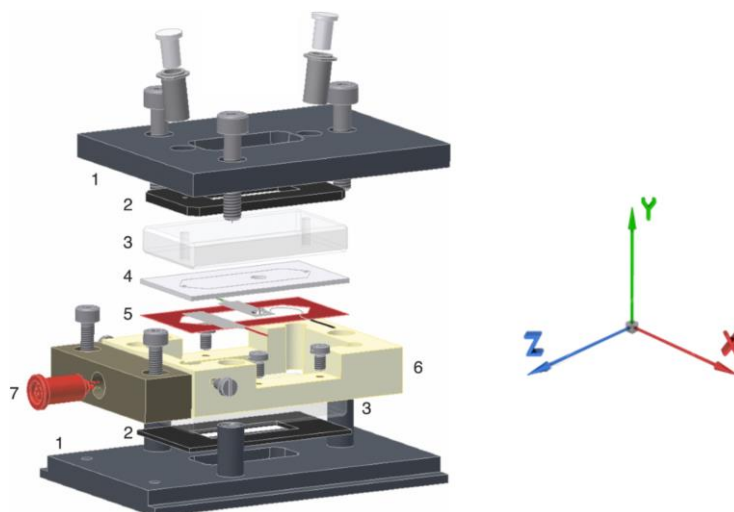
Scheme. 9.1 (left) exploded view of an OTTLE cell. 1) metal cover plates, 2) rubber gasket, 3) optical window, 4) polytetrafluoroethylene spacer, 5) electrodes, 6) protective frame, 7) electrode plug. Adapted with permission from S. Woutersen *et al.*, *An optically transparent thin-layer electrochemical cell for the study of vibrational circular dichroism of chiral redox-active molecules*, Review of Scientific Instruments, 2013[11]. Copyright AIP Publishing LLC.

An attempt was made to build a cylindrical cell (diameter 1 cm), which possesses similar features. A Pt-mesh electrode (working electrode) was deposited on a side of the round surface, while a Ag-wire (pseudo-reference electrode) and Pt-wire (counter electrode) wires were inserted from the top into the solution. Unfortunately, unlike the previous case, in which the working electrode was operating on hundreds of microliters, a cylindrical cell exposes millilitres of analyte to the electrode. The electro-generated species accounts for a fraction of the total population; even considering that it would successfully diffuse to the centre of the cell without reverting to its neutral state, its signal is lost in that of the neutral dye. This approach was discarded in favour of a quartz cell whose design takes into account the need for apposite slots for the electrodes.

Another option is a quartz cell, which can accommodate the three-electrode setup, and is commonly used in absorption spectroelectrochemical measurements. A picture of it is given in Scheme 9.2. Its section has the shape of a funnel, with the width decreasing from 10 to 1 mm as we move from top to bottom. A Pt-grid serves as working electrode and it is placed in the channel 1 mm wide. The counter electrode (Pt wire) is placed vertically along the *y*-axis next to the Pd-grid, being careful not to short circuit the electrodes. The third electrode is the silver pseudo-reference and is placed outside of the optical window, at the top of the "funnel", to close the electrical circuit. Once potential is applied, the redox species is generated at the interface of the grid electrode, in the central channel. If we placed the cell in the fluorimeter in such a way that the detector would be along the *x*-axis, then excitation would occur along the *z*-axis. It could be argued that the excitation beam will irradiate a channel 1 mm thick and 10 mm wide, in which two electrodes are placed, decreasing therefore the amount of solution which is successfully exposed to light. This configuration is not optimal, but anyhow better than the one with a cell excited along the longer side of the channel (x-axis) and whose fluorescence would be collected along the *z*-axis. Being the electrodes placed along *z*, they would scatter the fluorescence away from the direction of the detector.
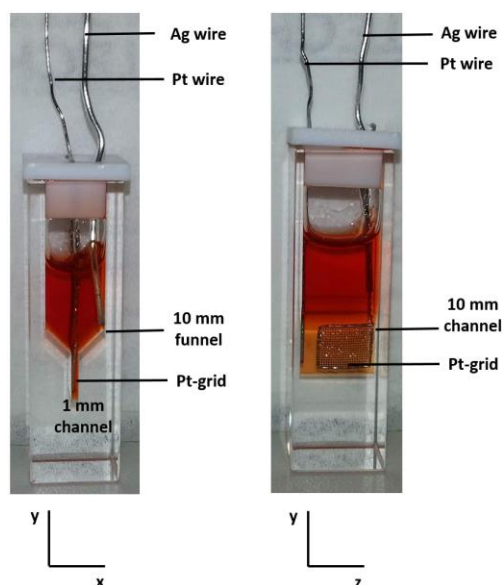
Scheme. 9.2 Spectroelectrochemical quartz cell along the (left) *z*-axis and (right) *x*-axis. The three-electrode setup is shown. The 1x10x5 mm channel constitutes the optical window, which is aligned with the instrumental optics.

The measurements we present were collected by means of an OTTLE cell; for the dye **P1** (Scheme 9.3), the OTTLE-induced scattering was such that it overlapped to the compound's fluorescence. The compound was therefore remeasured with the quartz cell setup; scattering persisted to a lesser extent, and it would make possible to interpret the spectra.
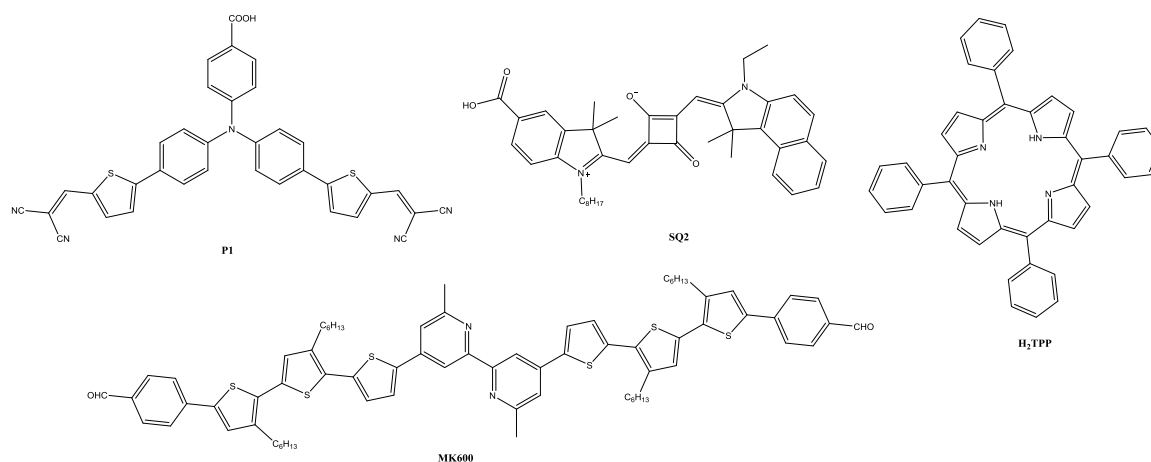
Scheme 9.3 Structures of **P1**, **SQ2**, **H₂TPP** and **MK600**.

9.3 P1

P1, IUPAC name 4-(Bis-{4-[5-(2,2-dicyano-vinyl)-thiophene-2-yl]-phenyl}-amino)-benzoic acid, is a commercial dye used in p-type solar cell applications (Scheme 9.3). It consists of a triarylamine core, from which two chromophoric dicyano-vinylthiophene rings depart. Triarylamines possess low oxidation potentials, a process that extracts one electron from the lone pair localized on the nitrogen atom. Generation of a radical cation gives rise to

a unique spectroscopic feature: an absorption band around 1100 nm[12]. Such absorption has helped scientists to detect electron transfer by transient absorption techniques, in which a transient radial cation is generated[13]. Our interest resides in the behaviour of **P1** under oxidative and reductive potentials, specifically we monitored its absorption and emission under chronoamperometry conditions.
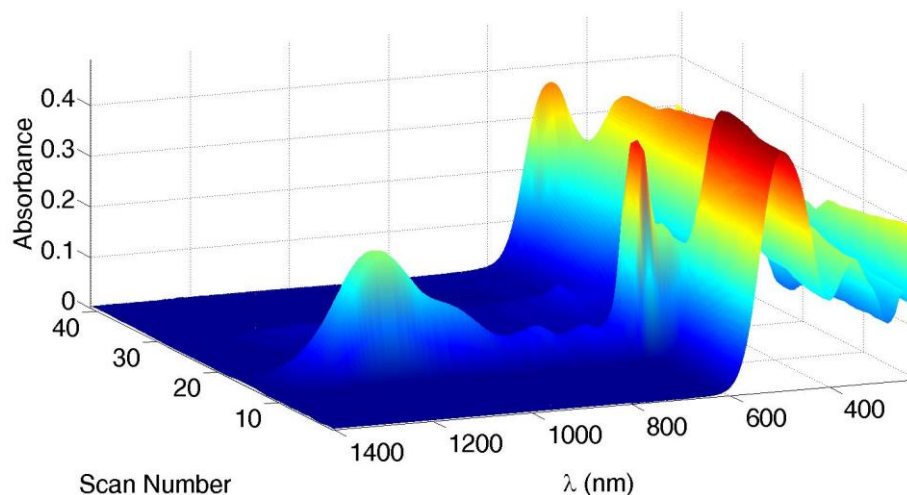

Fig. 9.1 Spectroelectrochemical data for the oxidative cycle of **P1** ($\approx$ 0.57 mM in propylene carbonate, [$^nBu_4N$][PF_6] supporting electrolyte). A spectrum was recorded every 0.1 V, starting from 0 V (Scan Number = 0) to +2.0 V (Scan Number = 21) and back to 0 V (Scan Number = 41). See caption to Fig. 3.1 for referencing to Fc/Fc$^+$.
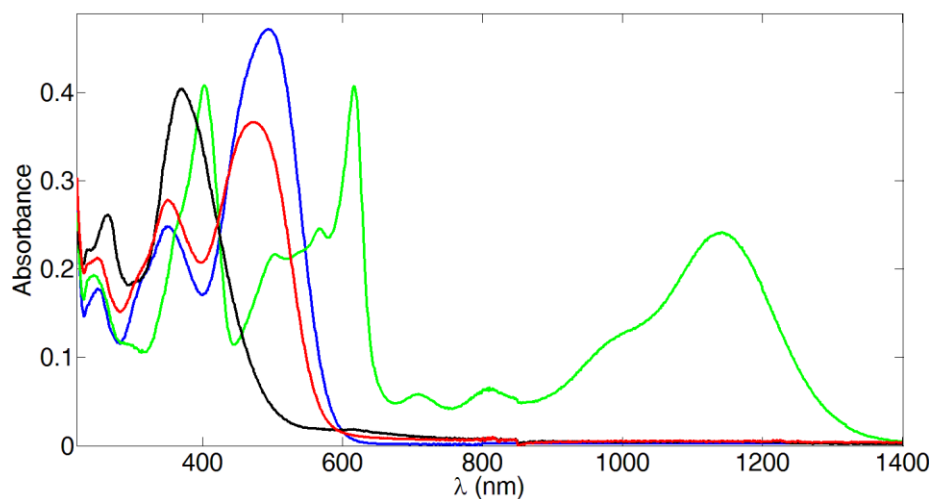
Fig. 9.2 Absorption spectra of neutral **P1** (blue), +1.4 V applied (green), +1.8 V applied (black) and back to 0 V (red) in propylene carbonate.

The absorption spectrum displays absorptions in the UV and green part of the spectrum (blue trace in Fig. 9.2). Both transitions are of (π,π^*) nature, with the high-energy band being associated with triphenylamine and the visible one with the conjugated thiophenes. Increasing the voltage to +1.4 V triggers the first process, which happens at the level of the triphenylamine; specifically a radical cation is formed, and this species is stabilized by resonating the charge over the whole surface of **P1** (green trace in Fig. 9.2). The broad band in the IR is associated with excitation of the hole[14], and both the UV and visible band at $\approx$500 nm move to the right, sign that the thiophenes are affected, too. Once the

142

voltage reaches +1.8 V the spectrum significantly simplifies (black trace in Fig. 9.2). The trace in the infrared is lost, as well as the absorptions in the visible; at this stage the compound should appear colourless to light-yellow. It is not immediate to assign this second oxidation process. It clearly involves the thiophene units since abstraction of a second electron from an already charged amine is unlikely to happen at a potential just 0.4 V higher. Reversing the potential back to 0 V restores the pristine absorption (red trace in Fig. 9.2). Some of the compound did not behave reversibly and therefore the absorbance is lower after one oxidative cycle, still the shape matches that of neutral **P1**.

While oxidation is a reversible process, the same cannot be said of reduction. Fig. 9.3 shows the reductive cycle of **P1** up to -2.0 V. Simple comparison of the spectrum before and after the redox cycle (inset Fig. 9.3) shows that a new species is dominant from +1.0 V on, and that such species is maintained throughout all the experiment. The absorption maximum shifts from ≈500 to ≈370 nm, with a tail still extending into the blue-green part of the spectrum.
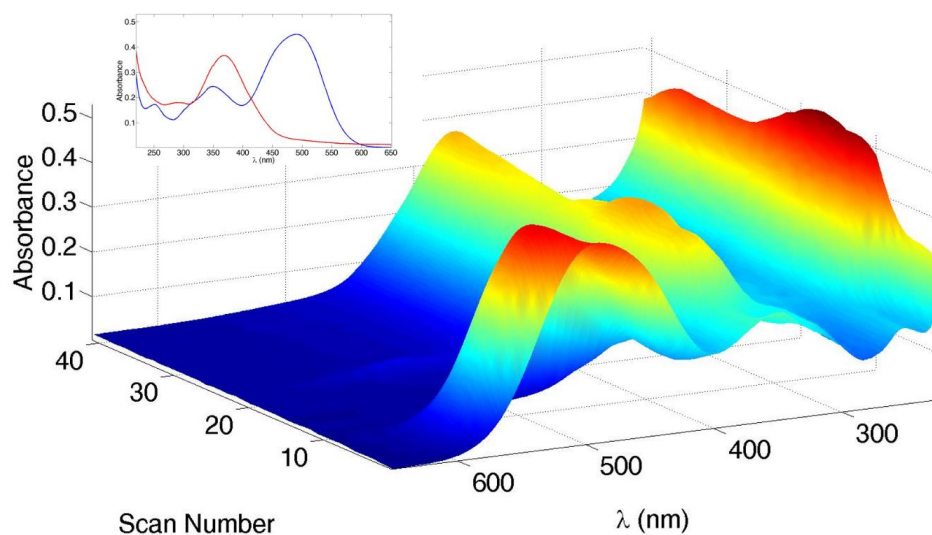

Fig. 9.3 Spectroelectrochemical data for the reductive cycle of **P1** (≈ 0.57 mM in propylene carbonate, [^{n}Bu$_4$N][PF$_6$] supporting electrolyte). A spectrum was recorded every 0.1 V, starting from 0 V (Scan Number = 0) to -2.0 V (Scan Number = 21) and back to 0 V (Scan Number = 41). See caption to Fig. 3.1 for referencing to Fc/Fc$^+$. (inset) Absorption spectra of **P1** before (blue) and after (red) application of -2.0 V.

The structure of **P1** is such that the electron-deficient region can be identified with the dicyano-vinyl arms. Reduction of this moiety affects thiophene absorption inducing a significant shift to lower wavelengths. As expected, the UV band of triphenylamine does not change significantly.

Fig. 9.4 reports the normalized plot for the absorption and emission of **P1** in propylene carbonate; and Fig. 9.5 shows the different emission pattern for excitation in the three main absorption bands. Excitation at 250 nm gives raise to three emission bands, of which one is due to emission of the triphenylamine unit[15]; excitation at 350 and 485 nm show a main emission band at 660 nm of probable intramolecular charge transfer character. It is in fact known that **P1** acts as a p-type sensitizer, extracting one electron from nanoparticulate NiO following excitation[13].
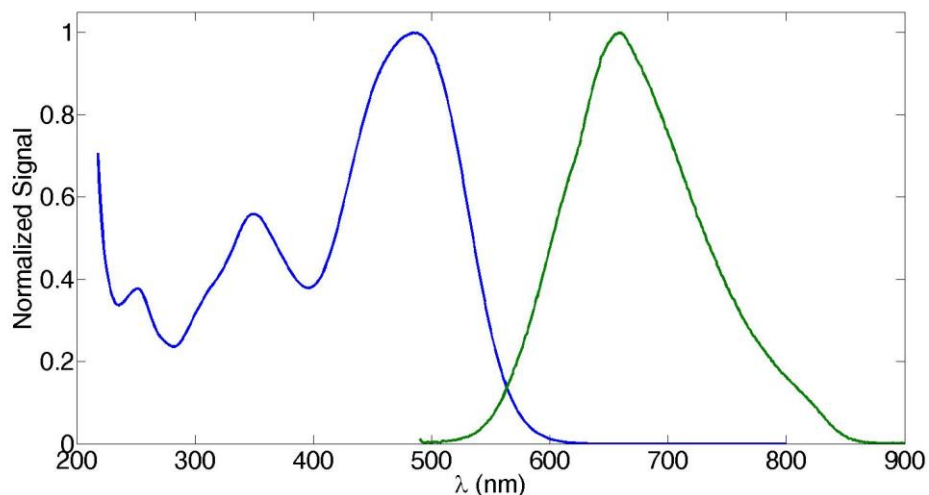
Fig. 9.4 (blue) solution absorption spectrum of a 57 μM propylene carbonate **P1** solution. (green) solution emission spectrum upon excitation at 485 nm.
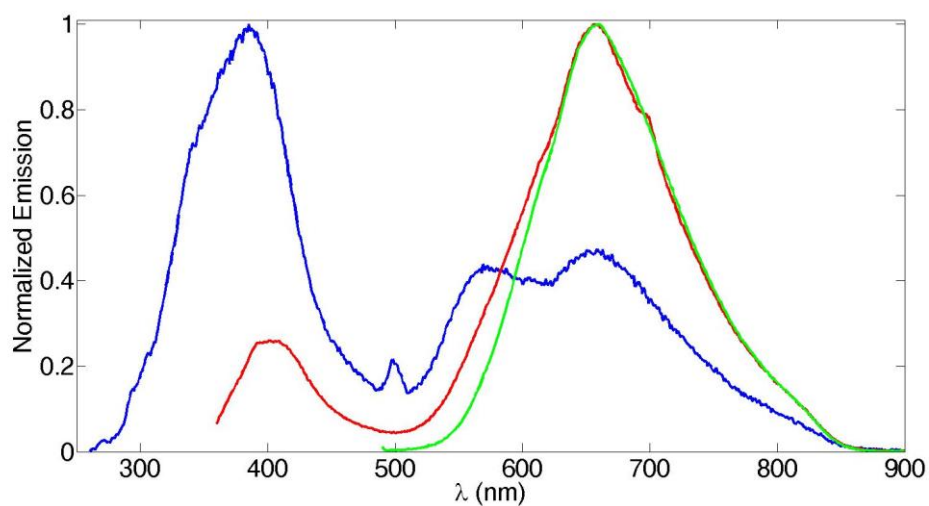

Fig. 9.5 Solution emission spectra of a 57 μM propylene carbonate **P1** solution when excited at (blue) 250 nm, (red) 350 nm and (green) 485 nm.

Once located the main emission band at 600 nm, the emission behaviour of **P1** has been studied upon excitation at 500 nm when exposed to oxidative (Fig. 9.6) or reducing (Fig 9.7) potentials. The contour plot of the 3D graph is reported as inset in the figures.
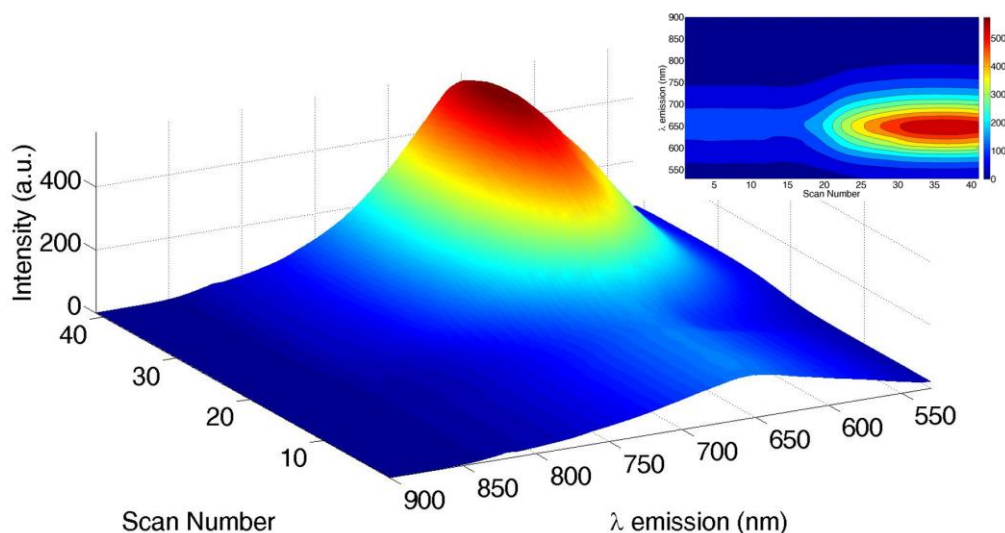
Fig. 9.6 Spectroelectrochemical data for the oxidative cycle of **P1** (≈ 0.15 mM in propylene carbonate, [$^nBu_4N$][PF_6] supporting electrolyte). A spectrum was recorded every 0.1 V, starting from 0 V (Scan Number = 0) to +2.0 V (Scan Number = 21) and back to 0 V (Scan Number = 41). See caption to Fig. 3.1 for referencing to Fc/Fc$^+$.
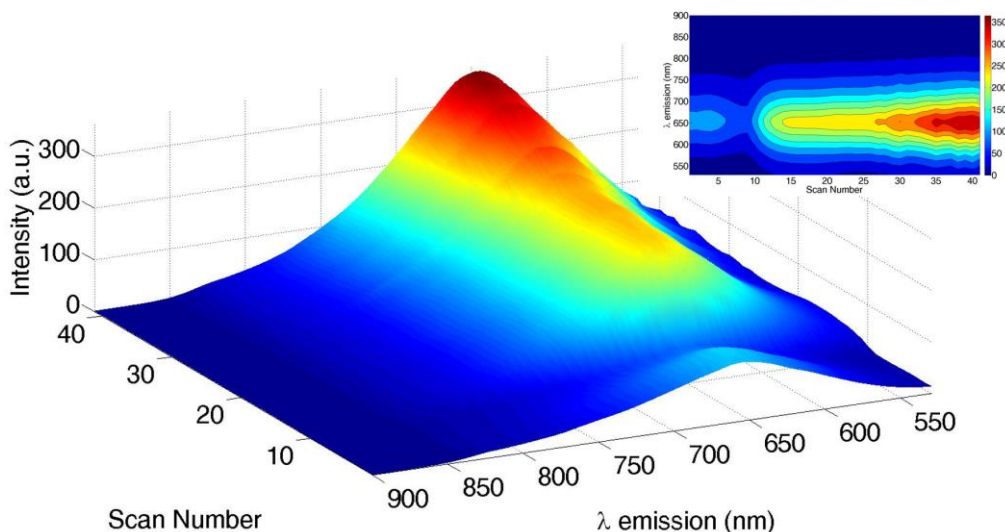

Fig. 9.6 Spectroelectrochemical data for the reductive cycle of **P1** (≈ 0.15 mM in propylene carbonate, [$^nBu_4N$][PF_6] supporting electrolyte). A spectrum was recorded every 0.1 V, starting from 0 V (Scan Number = 0) to +2.0 V (Scan Number = 21) and back to 0 V (Scan Number = 41). See caption to Fig. 3.1 for referencing to Fc/Fc$^+$.

9.4 SQ2

SQ2 is another commercial dye, which finds application in n-type solar cell (Scheme 9.1). It belongs to the family of squarylium dyes, a polymethine chain which passes through an oxocyclobutenolate ring and has at both ends a nitrogen atom. Its turquoise colour derives from an intense absorption band extending from the orange to the red part of the spectrum. Spectroelectrochemical experiments conducted on a propylene carbonate solution showed irreversible oxidation on the time scale investigated, both for potentials of +1.0 and +2.0 V. The data recorded for the cycle 0 V/+1 V/0 V are presented in Fig. 9.8. The

145

absorption decreases as the potential increases, until +1.0 V at which point none of the original material is left (green trace in the inset of Fig. 9.8). Going back to 0 V does not regenerate **SQ2**, but modifies the spectrum to its final shape (red trace in Fig 9.8).
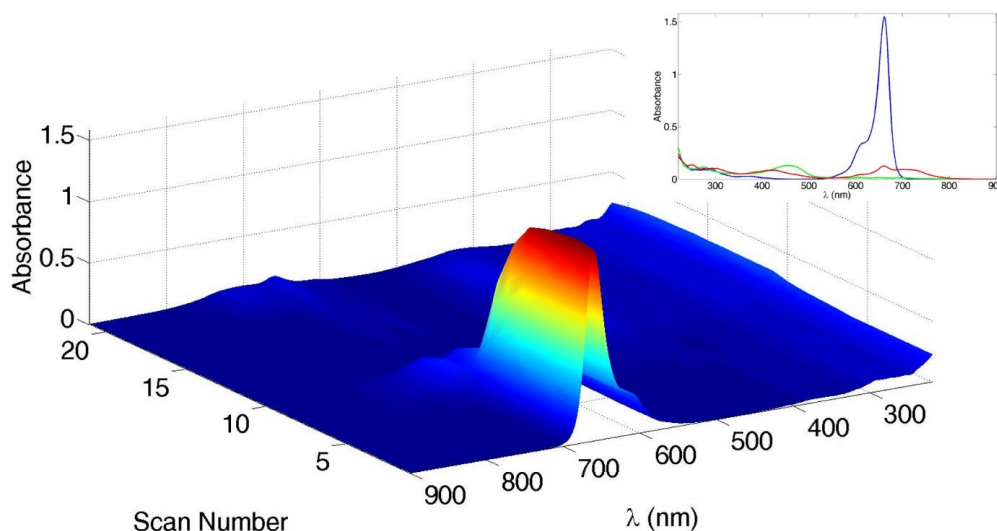

Fig. 9.8 Spectroelectrochemical data for the oxidative cycle of **SQ2** ($\approx$ 0.2 mM in propylene carbonate, [^{n}Bu$_4$N][PF$_6$] supporting electrolyte). A spectrum was recorded every 0.1 V, starting from 0 V (Scan Number = 0) to +1.0 V (Scan Number = 11) and back to 0 V (Scan Number = 21). See caption to Fig. 3.1 for referencing to Fc/Fc$^+$. (inset) Absorption spectra before (blue line), when +1.0 V is applied (green) and after (red line) the oxidative cycle.

The situation is quite different in reduction. A run until -1.5 V shows that the absorption spectrum is stable over the window 0 to -0.9 V and it is suddenly lost at -1.0 V. From this point over-reduction of the dye takes place and reverting the potential regenerates only partially **SQ2** (data not shown). We therefore run a second experiment, being careful to stop the reduction at -1.0 V (Fig. 9.9). Again, exactly at -1.0 V the spectrum changes to the green trace in Fig. 9.9 and going back to 0 V leads to a full recovery of **SQ2** absorption (red trace in Fig. 9.9).
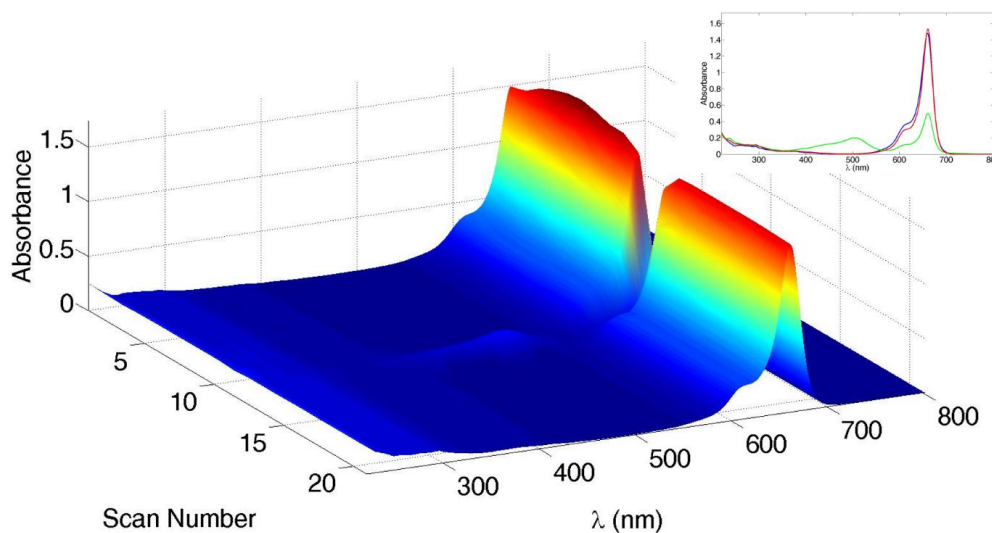

Fig. 9.9 Spectroelectrochemical data for the reductive cycle of **SQ2** ($\approx$ 0.2 mM in propylene carbonate, [^{n}Bu$_4$N][PF$_6$] supporting electrolyte). A spectrum was recorded every 0.1 V, starting from 0 V (Scan Number = 0) to -1.0 V (Scan Number = 11) and back to 0 V (Scan Number = 21). See caption to Fig. 3.1 for referencing to

Knowing absorption and emission spectral features of **SQ2** in solution simplifies our task when moving to emission spectroelectrochemistry (Fig. 9.10). Fig. 9.11 reports the emission behaviour of **SQ2** for an oxidative cycle 0 V/ +1.0 V/ 0V, exciting at 600 nm. As expected, the process is not reversible and emission decreases to a minimum point for +1.0 V, after which little material is recovered. To help visualization, a top-view (contour plot) is shown in the inset of Fig. 9.11.
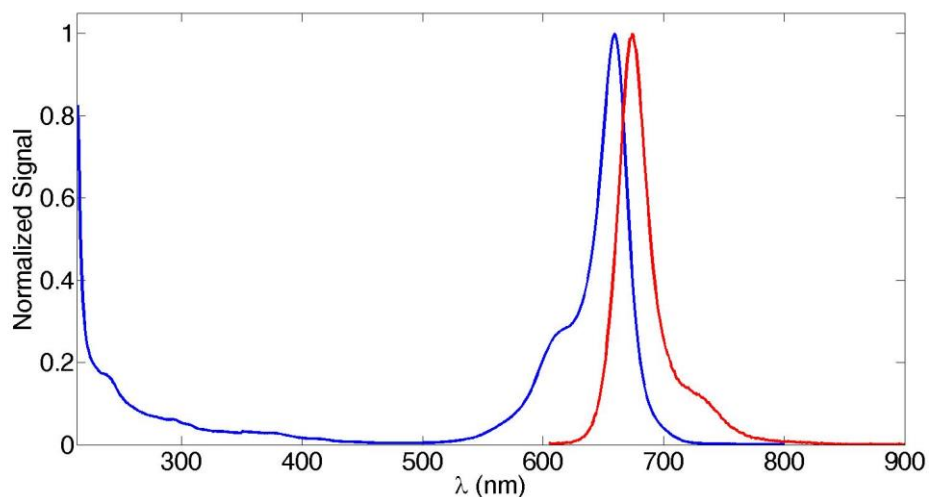

Fig. 9.10 (blue) solution absorption spectrum of a 6 µM propylene carbonate **SQ2** solution. (red) solution emission spectrum upon excitation at 600 nm (3 µM solution).
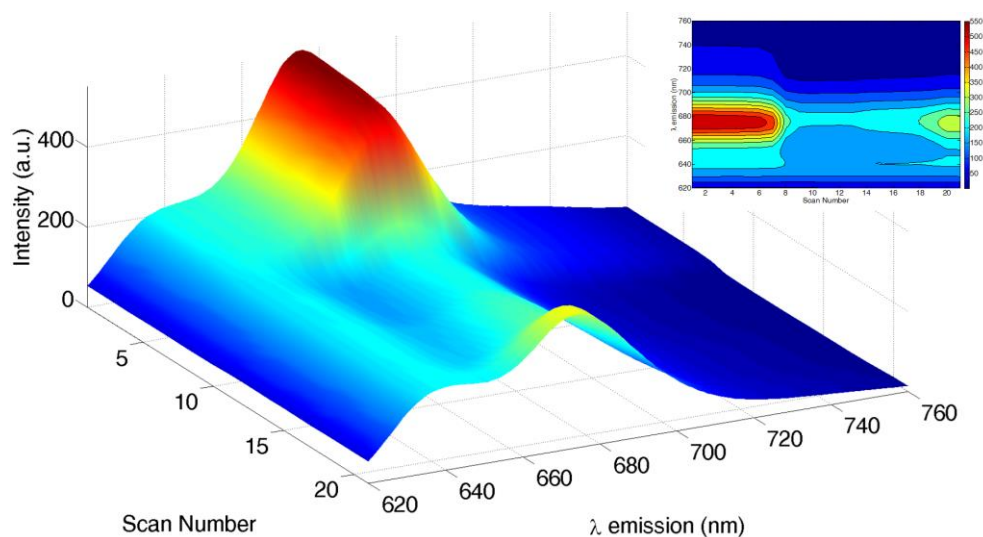

Fig. 9.11 Spectroelectrochemical data for the oxidative cycle of **SQ2** (≈ 0.2 mM in propylene carbonate, [$^nBu_4N$][PF_6] supporting electrolyte). A spectrum was recorded every 0.1 V, starting from 0 V (Scan Number = 0) to +1.0 V (Scan Number = 11) and back to 0 V (Scan Number = 21). See caption to Fig. 3.1 for referencing to Fc/Fc+. (inset) contour plot.

In reduction, the emission was monitored for excitation wavelengths of 500 and 600 nm; in fact, we previously detected a second species with absorption at 500 nm, which is generated upon reduction of **SQ2**. The cycle 0 V/ -1.0 V/ 0 V with excitation at 600 nm

showed no spectral change (data not shown). Puzzled by this evidence, we decided to increase the potential range, scanning to -1.5 V and exciting at 500 nm (Fig. 9.12). **SQ2** has virtually no absorption at 500 nm, nonetheless its emission spectrum could be recorded as a very weak emission. It is to be noted that with a slit width of 20 nm, enough of the lower energy radiation reaches and excite the samples, justifying the appearance of **SQ2** emission spectrum. The emission is lost in the potential range -1.1 to -1.5 V and from there back to -1.1 V (see contour plot). Apart for this, the spectrum does not appear different from that of pristine **SQ2** at any time of the scan**.**
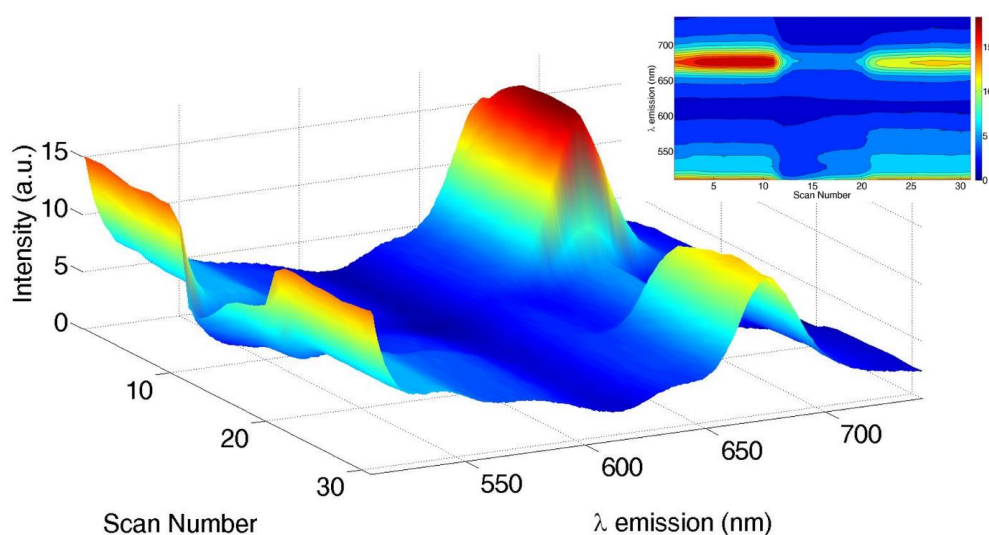

Fig. 9.12 Spectroelectrochemical data for the reductive cycle of **SQ2** ($\approx$ 0.2 mM in propylene carbonate, [^{n}Bu$_4$N][PF$_6$] supporting electrolyte). A spectrum was recorded every 0.1 V, starting from 0 V (Scan Number = 0) to -1.5 V (Scan Number = 16) and back to 0 V (Scan Number = 31). See caption to Fig. 3.1 for referencing to Fc/Fc$^+$. (inset) contour plot.

9.5 MK600

MK600 was prepared by MSc Max Klein (Scheme 9.1). It consists of a central bipyridine, functionlized with two terthiophene arms. Absorption behaviour of 2,2':5',2'' terthiopenes has already been reported[16]. This molecule can undergo two one-electron oxidation to its cationic and dication form, with absorption band arising 825 nm for the cation and at 643 nm for the doubly oxidized species[16]. The oxidative scan in Fig. 9.13 was recorded until 800 nm, and its spectroscopic signature matches that of the dication. Fig. 9.14 displays the major spectroscopic changes upon oxidation.
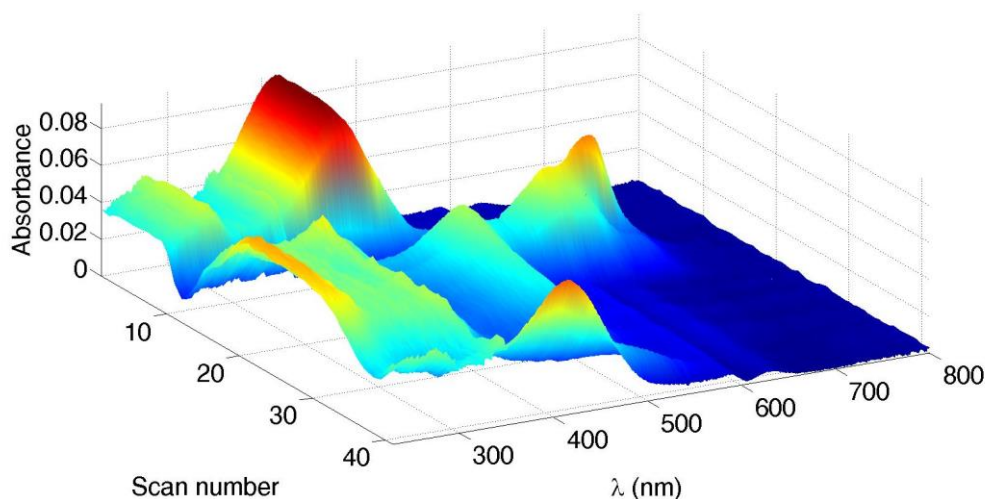
Fig. 9.13 Spectroelectrochemical data for the oxidative cycle of **MK600** (≈ 0.3 mM in propylene carbonate, [$^{n}Bu_4N$][PF_6] supporting electrolyte). A spectrum was recorded every 0.1 V, starting from 0 V (Scan Number = 0) to +2.0 V (Scan Number = 21) and back to 0 V (Scan Number = 41). See caption to Fig. 3.1 for referencing to Fc/Fc^{+}.
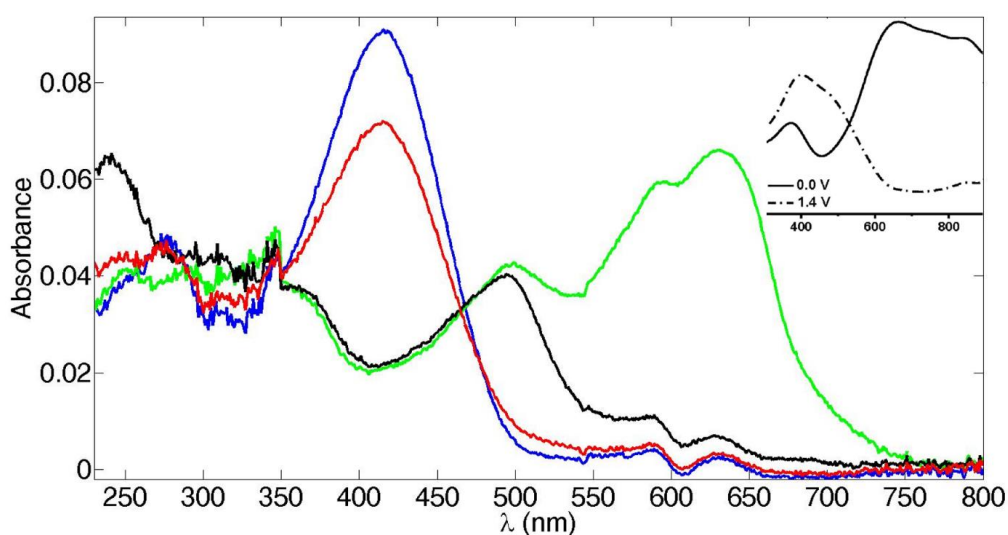

Fig. 9.14 Absorption spectra of **MK600** before (blue), +1.4 V applied (green), +1.9 V applied (black) and after (red) the oxidative scan (solvent: propylene carbonate). (inset) reference spectrum from ref. [16]. Adapted with permission from Y.-B. Shim at al., *Spectroelectrochemical and electrochromic behaviors of newly synthesized poly[3'-(2-aminopyrimidyl)-2,2':5',2''-terthiophene],* Electrochimica Acta, 2013. Copyright 2013 The Authors. Published by Elsevier Ltd.

The reductive behaviour of the compound is not of interest, spectroscopically. Fig. 9.15 shows how the absorption starts decreasing at -1.7 V, touches a minimum at -2.0 V and regains in intensity until the original value.
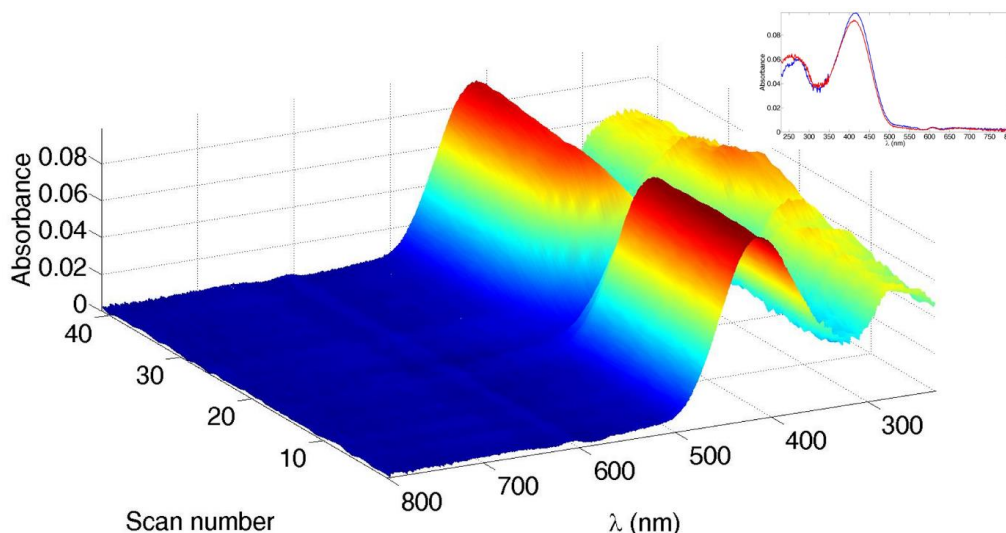
Fig. 9.15 Spectroelectrochemical data for the reductive cycle of **MK600** (≈ 0.2 mM in propylene carbonate, [^{n}Bu$_4$N][PF$_6$] supporting electrolyte). A spectrum was recorded every 0.1 V, starting from 0 V (Scan Number = 0) to -2.0 V (Scan Number = 21) and back to 0 V (Scan Number = 41). See caption to Fig. 3.1 for referencing to Fc/Fc$^+$. (inset) Absorption spectra before (blue line) and after (red line) the reductive cycle.

The emission behaviour simply consists of a loss of signal as the oxidation takes place. Fig. 9.16 shows three contour plots, reconstructed from the data recorded for scans up to +2.0, +1.0 and +0.5 V, respectively. The scan up to +2.0 V shows that reaching of +1.0 V kills all of the emission in an irreversible way. Scanning up to +1.0 V confirms it, so that we performed a third scan interrupting it at +0.5 V, in the middle of the irreversible process. The emission decreases again, but it stops at a value higher than zero. The experimental evidence gathered from emission properties supports an irreversible process, while absorption spectroelectrochemistry states the contrary.
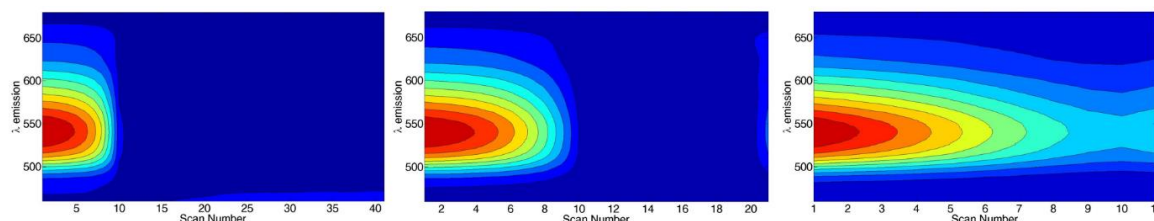

Fig. 9.16 Contour plot of the spectroelectrochemical data for the oxidative cycle of **MK600** (≈ 0.1 mM in propylene carbonate, [^{n}Bu$_4$N][PF$_6$] supporting electrolyte); excitation at 400 nm. A spectrum was recorded every 0.1 V, starting from 0 V (Scan Number = 0) to +2.0 V (left), +1.0 V (middle) or +0.5 V (right) (Scan Numbers = 21, 11 or 6, respectively) and back to 0 V (Scan Numbers = 41, 21 or 11, respectively). See caption to Fig. 3.1 for referencing to Fc/Fc$^+$.

In reduction, potentials as low as -2.0 V blueshift the emission band of 20 nm (Fig. 9.17). The effect is reversible, but most of the intensities is lost in the recovery of the original peak position. Scans up to -1.5, -1.0 and -0.5 V do not result in the same effect (Fig. 9.18).
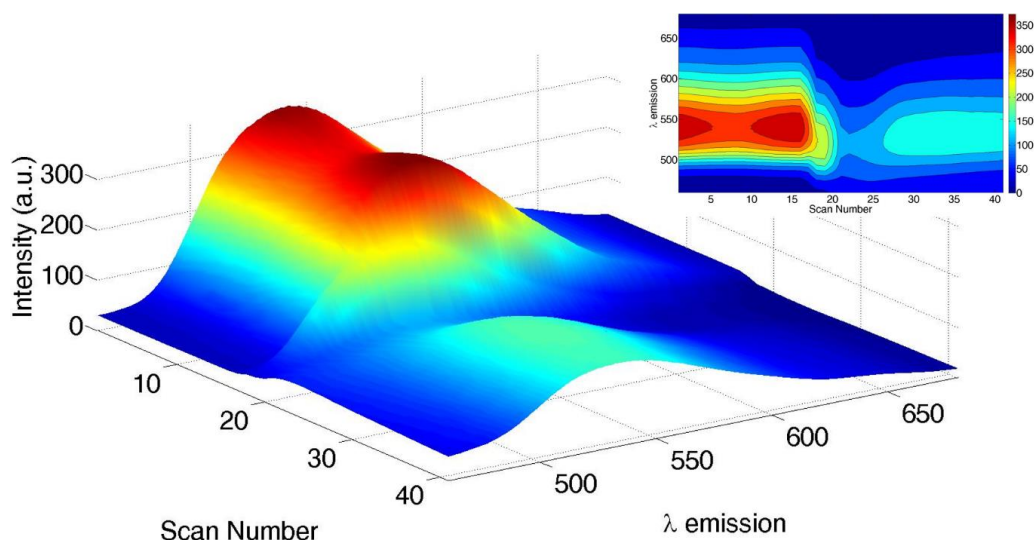
Fig. 9.17 Spectroelectrochemical data for the reductive cycle of **MK600** (≈ 0.1 mM in propylene carbonate, [^{n}Bu$_4$N][PF$_6$] supporting electrolyte). A spectrum was recorded every 0.1 V, starting from 0 V (Scan Number = 0) to -2.0 V (Scan Number = 21) and back to 0 V (Scan Number = 41). See caption to Fig. 3.1 for referencing to Fc/Fc^{+}. (inset) contour plot.
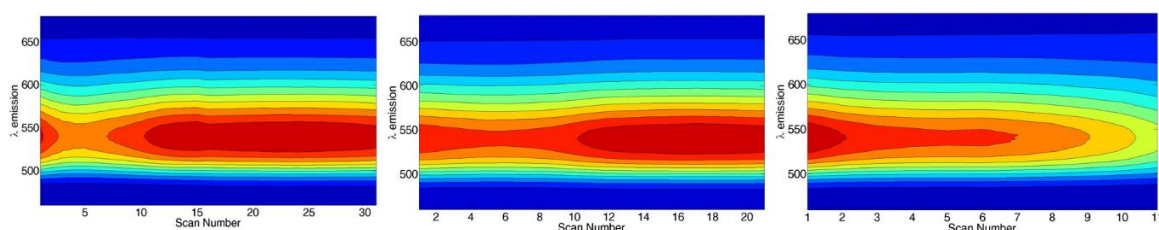

Fig. 9.18 Contour plot of the spectroelectrochemical data for the reductive cycle of **MK600** (≈ 0.1 mM in propylene carbonate, [^{n}Bu$_4$N][PF$_6$] supporting electrolyte); excitation at 400 nm. A spectrum was recorded every 0.1 V, starting from 0 V (Scan Number = 0) to -1.5 V (left), -1.0 V (middle) or -0.5 V (right) (Scan Numbers = 16, 11 or 6, respectively) and back to 0 V (Scan Numbers = 31, 21 or 11, respectively). See caption to Fig. 3.1 for referencing to Fc/Fc^{+}.

9.6 H$_2$TPP

The behaviour of H$_2$TPP has been studied in dichloromethane and dimethylformamide and has been found to profoundly differ in these two solvents. First, we present the absorption spectroelectrochemistry in oxidation (0 V/ +2.0 V/ 0 V, Fig. 9.19) and reduction (0 V/ -1.8 V/ 0V, Fig. 9.20) for the dichloromethane solution. The spectral changes are consistent with the general behaviour of porphyrins reported in Chapter 3.
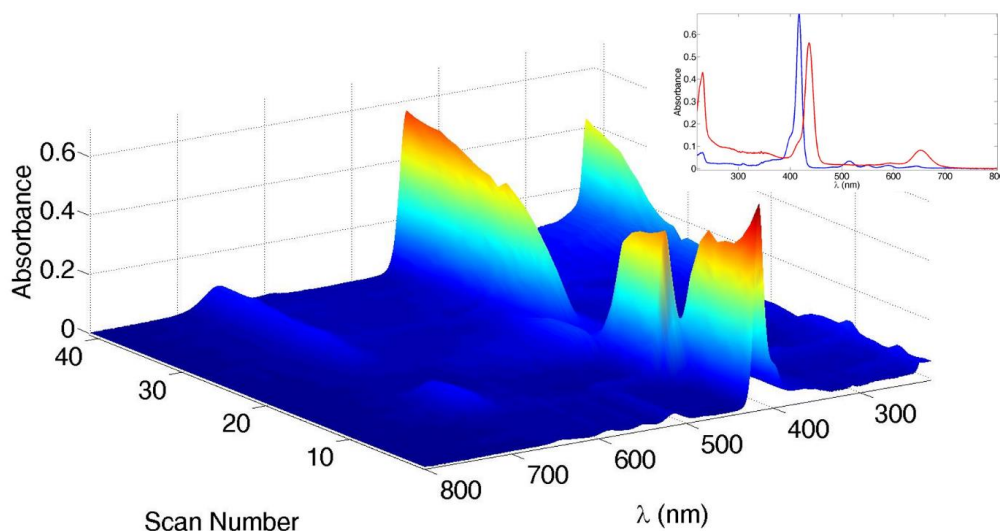
Fig. 9.19 Spectroelectrochemical data for the oxidative cycle of **H₂TPP** (≈ 40 μM in dichloromethane, [ⁿBu₄N][PF₆] supporting electrolyte). A spectrum was recorded every 0.1 V, starting from 0 V (Scan Number = 0) to +2.0 V (Scan Number = 21) and back to 0 V (Scan Number = 41). See caption to Fig. 3.1 for referencing to Fc/Fc⁺. (inset) Absorption spectra before (blue line) and after (red line) the oxidative cycle.

Fig. 9.20 Spectroelectrochemical data for the reductive cycle of **H₂TPP** (≈ 40 μM in dichloromethane, [ⁿBu₄N][PF₆] supporting electrolyte). A spectrum was recorded every 0.1 V, starting from 0 V (Scan Number = 0) to -1.8 V (Scan Number = 19) and back to 0 V (Scan Number = 37). See caption to Fig. 3.1 for referencing to Fc/Fc⁺. (inset) Absorption spectra before (blue line) and after (red line) the reductive cycle.
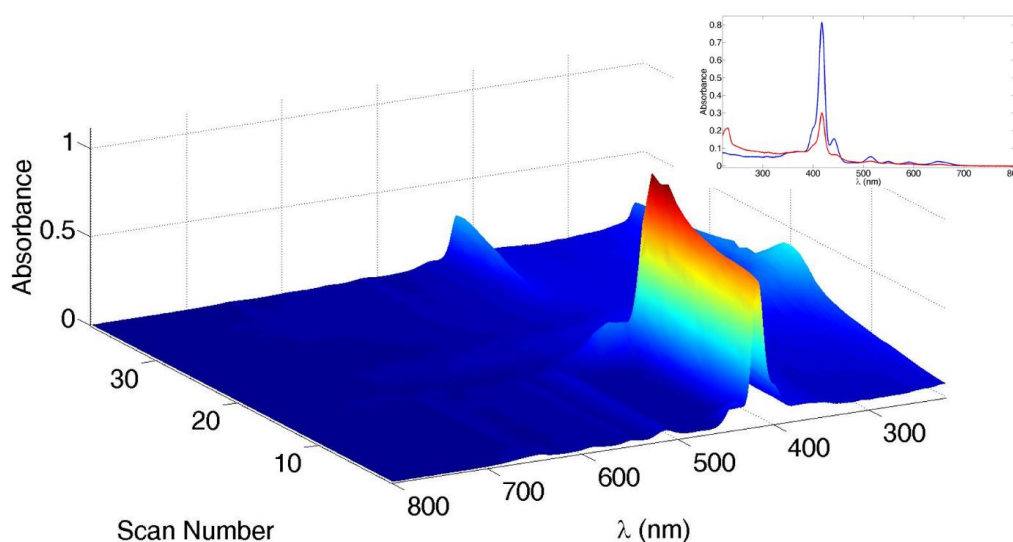
If the same compound is dissolved in dimethylformamide, oxidation is not reversible for +2.0 V (data not shown), but it becomes fully reversible if the scan is stopped at +1.5 V (Fig. 9.21). Reduction scans have been performed for potentials of -2.0, -1.5 and -1.0 V; none of the scans showed reversibility, but the amount of porphyrin which could be recuperated depends on the maximum potential applied (Fig. 9.22).
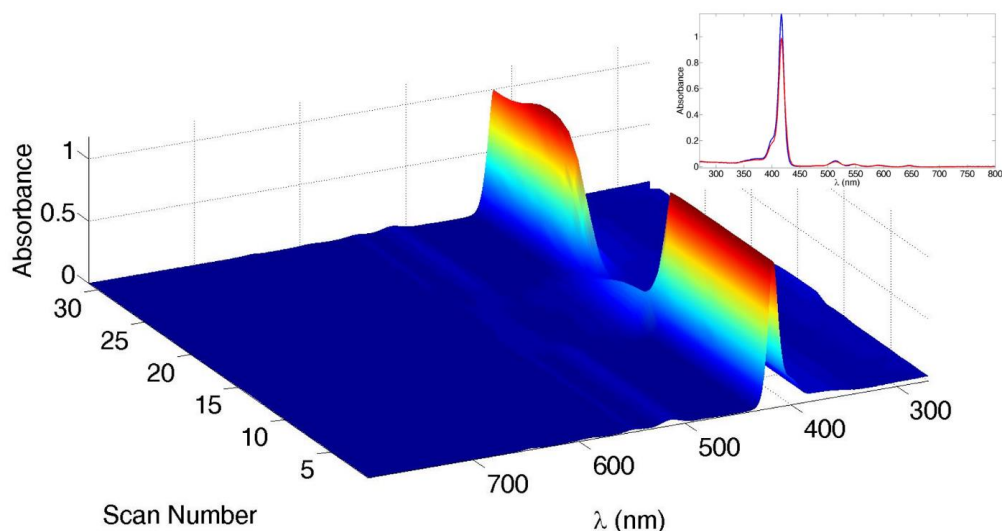
Fig. 9.21 Spectroelectrochemical data for the oxidative cycle of **H₂TPP** (≈ 180 μM in dimethylformamide, [ⁿBu₄N][PF₆] supporting electrolyte). A spectrum was recorded every 0.1 V, starting from 0 V (Scan Number = 0) to -1.8 V (Scan Number = 19) and back to 0 V (Scan Number = 37). See caption to Fig. 3.1 for referencing to Fc/Fc⁺. (inset) Absorption spectra before (blue line) and after (red line) the oxidative cycle.
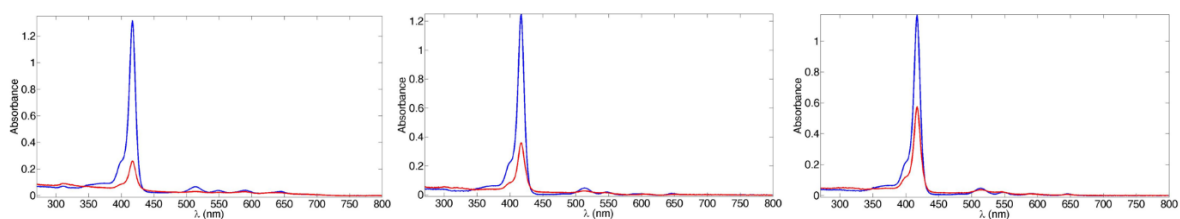

Fig. 9.22 Absorption spectra extracted from the spectroelectrochemical data for the reductive cycle of **H₂TPP** (≈ 180 μM in dimethylformamide, [ⁿBu₄N][PF₆] supporting electrolyte). Scans until (left) -2.0 V, (middle) -1.5 V and (right) -1.0 V, before (blue line) and after (red line) the reductive cycle.

Looking at the emission, Figs. 9.23 and 9.24 refer to oxidative and reductive cycles for the dichloromethane solution, excited in the Soret band. Already from the absorption, it was clear that oxidation generates a compound with different spectroscopic characteristics. This reflect in the emission spectrum, where a new peak appears in-between the classical free-base porphyrin emission (inset Fig. 9.23). This compound is stable in the sense that pristine H₂TPP is not regenerated upon application of 0 V. Reduction scan to -2.0 V decreases the fluorescence to the point that only one of the two porphyrin emission (the one at 650 nm) is visible. The author thinks that this is due to limited instrumental sensitivity and that the band at 720 nm is still present, but not of right intensity to be detected under our experimental conditions (inset Fig. 9.24).
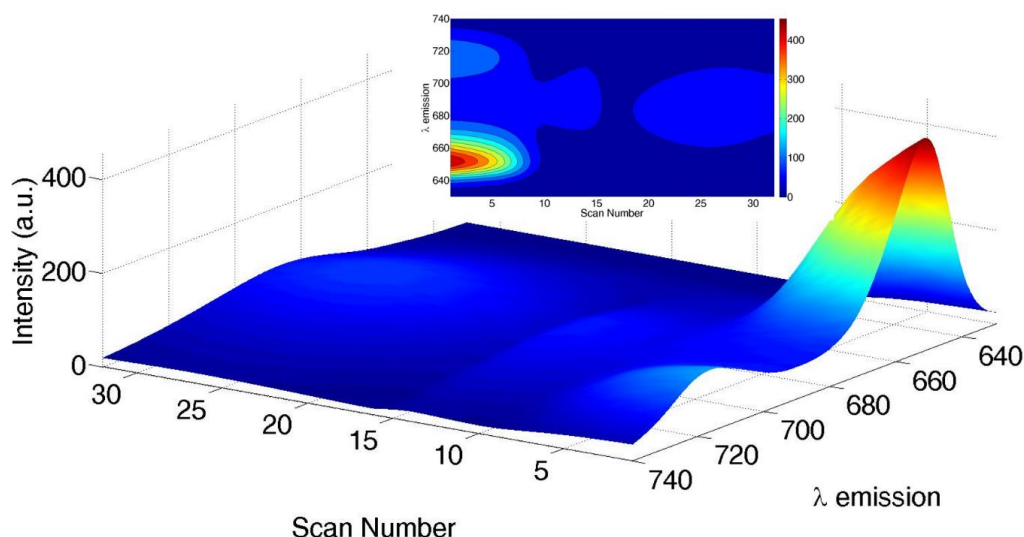
Fig. 9.23 Spectroelectrochemical data for the oxidative cycle of **H₂TPP** (≈ 40 µM in dichloromethane, [ⁿBu₄N][PF₆] supporting electrolyte). A spectrum was recorded every 0.1 V, starting from 0 V (Scan Number = 0) to +1.5 V (Scan Number = 16) and back to 0 V (Scan Number = 31). See caption to Fig. 3.1 for referencing to Fc/Fc⁺. (inset) contour plot.

Fig. 9.24 Spectroelectrochemical data for the reductive cycle of **H₂TPP** (≈ 40 µM in dichloromethane, [ⁿBu₄N][PF₆] supporting electrolyte). A spectrum was recorded every 0.1 V, starting from 0 V (Scan Number = 0) to -2.0 V (Scan Number = 21) and back to 0 V (Scan Number = 41). See caption to Fig. 3.1 for referencing to Fc/Fc⁺. (inset) contour plot.

The spectroelectrochemical experiments for the dimethylformamide solution are presented in Figs. 9.25 and 9.26. Contrary to what happens to the compound in dichloromethane, scan up to -2.0 V is fully reversible (Fig. 9.25). In oxidation, scan up to +1.5 V results in irreversibility, whilst a maximum potential of +1.0 V translates to no spectroscopic change (Fig. 9.26).

Fig. 9.25 Spectroelectrochemical data for the reductive cycle of **H₂TPP** (≈ 180 μM in dimethylformamide, [ⁿBu₄N][PF₆] supporting electrolyte). A spectrum was recorded every 0.1 V, starting from 0 V (Scan Number = 0) to -2.0 V (Scan Number = 21) and back to 0 V (Scan Number = 41). See caption to Fig. 3.1 for referencing to Fc/Fc⁺. (inset) contour plot.
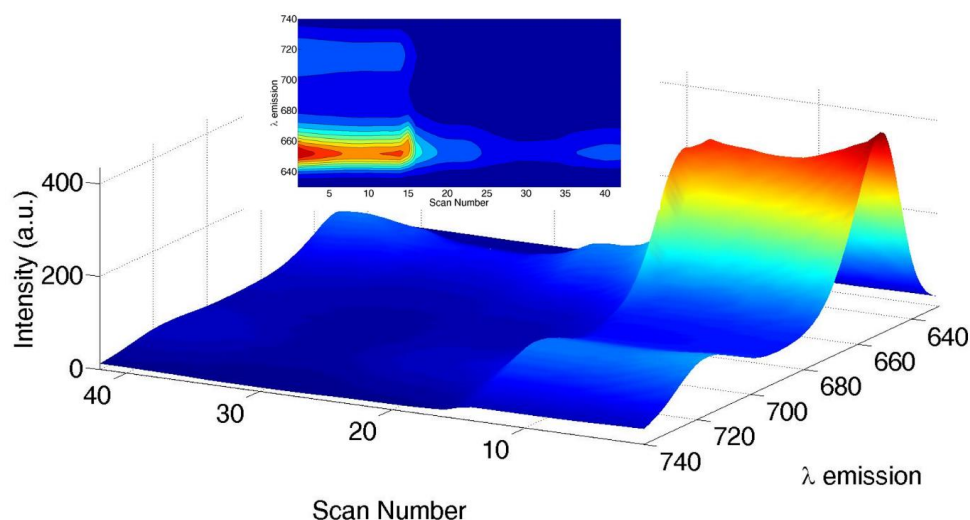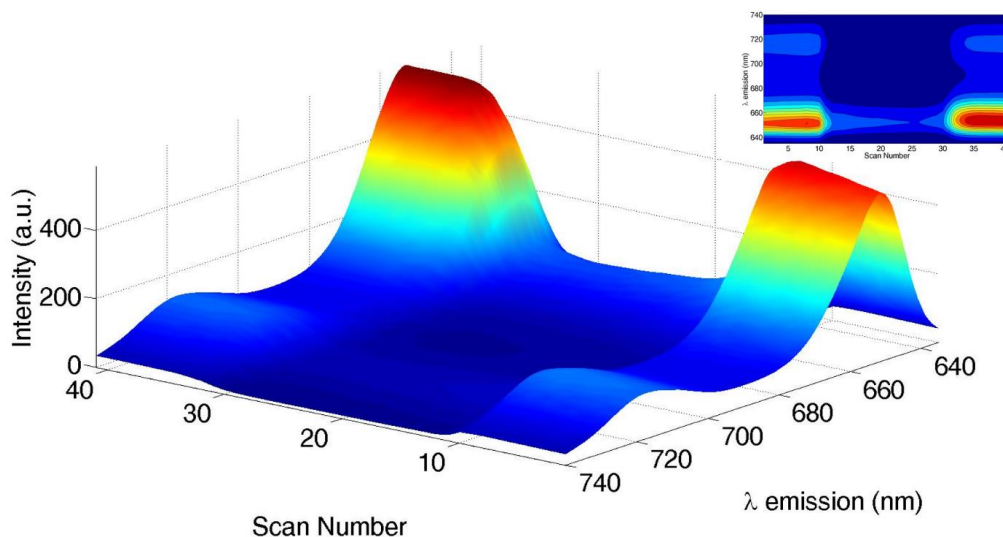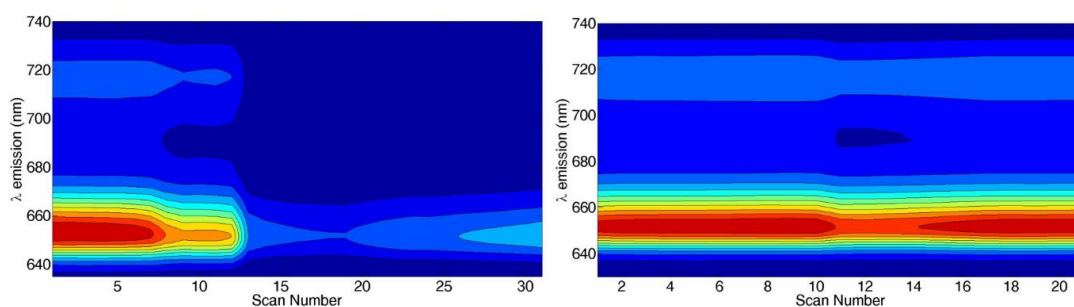

Fig. 9.26 Contour plot of the spectroelectrochemical data for the oxidative cycle of **H₂TPP** (≈ 180 μM in dimethylformamide, [ⁿBu₄N][PF₆] supporting electrolyte); excitation at 420 nm. A spectrum was recorded every 0.1 V, starting from 0 V (Scan Number = 0) to +1.5 V (left) or +1.0 V (right) (Scan Numbers = 16 or 11, respectively) and back to 0 V (Scan Numbers = 31 or 21, respectively). See caption to Fig. 3.1 for referencing to Fc/Fc⁺.

Absorption spectroelectrochemistry is a well-established field, mainly because changes in the absorption spectrum can be directly correlated to redox changes in the chemical structure of the dye. We ourselves have seen how specific chromophores, e.g. triarylamine or terthiopenes, possess characteristic spectral features according to their oxidation state.

We wish the situation is remotely maintained when it comes to luminescence. Emission is a more complex process than absorption, and while a wide range of molecule absorbs, those which emit are a small portion. One major cause for the lack of luminescence is quenching, a general term indicating the dissipation of electronic excitation energy into vibrational and torsional molecular modes. The ability of a molecule to luminesce is quantified by its quantum yield, defined as the ratio between the radiative constant and the non-radiative one. While luminescence is the sole process contributing to the radiative constant, all of the other processes that bring the excited compound back to the ground state contribute to the non-radiative one and their contribution adds up arithmetically.

The examples we reported in this last chapter are representative and they show that the most common feature in an emission spectroelectrochemical experiment is the quenching of the emission upon application of an oxidative/reducing potential. From then, depending on the reversibility of the electrochemical process, the emission can be regenerate to resemble that of the pristine dye; more rarely new bands appear, as for H_2TPP in dichloromethane. For this particular compound, fluorescence at a different wavelength should not surprise since the oxidation process is irreversible and the newly generated species possess a totally different absorption spectrum. What we are detecting is therefore the emission of a neutral and chemically different species, and not the emission of an excited charged-state of H_2TPP. Additional confirmation comes from the experiment run on the same dye in a polar solvent as dimethylformamide. Solvent-stabilization of the charged state prevents the compound from undergoing modifications, as confirmed by the complete dye recovery.

Turning our attention back to the non-radiative constant, it is clear that the abstraction/injection of one electron introduces a new quenching pathway. In fact, a radical anion/cation is less stable than its neutral counterpart, and therefore less emissive. The only reason why we can generate and maintain such species in solution is because of their proximity to the electrodes, which provide the right potential for them to exist as charged species. If on the one hand the electrodes stabilize the dye, they cannot influence its emission properties, which are purely related to its chemistry. Having said that, we recognize that a major limitation exists in applying spectroelectrochemistry to emission spectroscopy. It is opinion of the author that only the identification of a fluorescent dye, whose charged/radical state is stable could serve as benchmark for testing the true power of the technique. Experimentally, an OTTLE cell has proven adequate to perform such measurement, with scattering being the only instrumental limitation. Attenuation of the scattering is achieved by modulation of the excitation wavelength, slit openings and relative position of the cell with respect to the lenses in the sample-holder, which represent the "degrees of freedom" the experimenter can play with. A three-electrode setup quartz cell proved trickier to handle, but it still remains a valid option for cases in which an OTTLE cell cannot be used.

References

[1] K. Ogle, *Corrosion ad Materials*, 37, 2012, 58.

[2] J. Salbeck, *J. Electroanal. Chem*. 340, 1992, 169.

[3] T. Kakiuchi, Y. Takasu, *Anal. Chem*. 66, 1994, 1853.

[4] H. Nagatani, R. A. Iglesias, D. J. Fermín, P.-F. Brevet, H. H. Girault, *J. Phys. Chem. B,* 2000, 104, 6869.

[5] P. Jennings, A.C. Jones, A.R. Mount, *Phys. Chem. Chem. Phys*., 2, 2000, 1241.

[6] R. Stoodley, D. Bizzotto, *Analyst,* 128, 2003, 552.

[7] R.G. Compton, J. Winkler, D.J. Riley, S.D. Bearpark, *J. Phys. Chem*., 98, 1994, 6818.

[8] I. Taniguchi, T. Fujiwara, M. Tominaga, *Chem. Lett*., 12, 1992, 1217.

[9] C. Farren, C. A. Christensen, S. FitzGerald, M.R. Bryce, A. J. Beeby, *Org. Chem*., 67, 2002, 9130.

[10] X. Hu, Q. Wang, P. He, Y. Fang, *Anal. Sci.,* 18, 2002, 645.

[11] S. R. Domingos, H. Luyten, F. van Anrooij, H. J. Sanders, B. H. Bakker, W. J. Buma, F. Hartl and S. Woutersen, *Review of Scientific Instruments*, 84, 033103, 2013.

[12] A. G. Bonn and O. S. Wenger, *Phys.Chem.Chem.Phys*., 2015, 17, 24001.

[13] Lei Zhang PhD thesis, *Exploring Electron Transfer Dynamics of Novel Dye Sensitized Photocathodes*, Uppsala University.

[14] C.-Y. Huang and Y. O. Su**,** *Dalton Trans***.**, 2010, 39**,** 8306.

[15] H. Tian, X. Yang, J. Pan, R. Chen, M. Liu, Q. Zhang, A. Hagfeldt, L. Sun, *Adv. Funct. Mater*. 2008, 18, 3461.

[16] D.-M. Kim, K.-B. Shim, J. I. Son, S. S. Reddy, Y.-B. Shim, *Electrochim. Acta*, 104, 2013, 322.

Conclusions and outlook

The first part of the thesis focused on the preparation of a porphyrin-ruthenium polypyridine dyad as dye for solar cell applications. Although such a dyad could be prepared and characterized, it performed poorly when tested in DSC. The reason for the virtually non-existing electron injection efficiency resides in a quenching process that happens between the two units in the dyad. The triplet states of [Zn(TPP)] and {Ru(tpy)$_2$} are of right energy to allow an energy flow from the latter to the first, with a kinetic constant higher than 10^{10} s^{-1}. The energy transfer process is so fast that accounts for quenching of all the charge-separated states generated upon excitation of the ^{1}MLCT absorption band of the dyad; no electron injection can therefore result.

If efforts are to be put in the preparation of a better performing dyad, we suggest to move from the investigated architecture porphyrin/ruthenium/anchor to one of the kind anchor/porphyrin/ruthenium. Only in such case the excitation energy, which collects on the porphyrin after energy transfer, is accessible to the semiconductor.

Moving to photocatalysis, the triplet state of our porphyrin dye **TPyCP** could be used for molecular oxygen sensitization to its singlet state. Singlet oxygen proved able to react with a wide class of substrates, ranging from amino acids to aliphatic sulfides to aromatics.

Two experimental evidences collected on sulfides call for further investigation. First, the electronic nature of the carbon atoms to the left and to the right of the sulfur dictates the rate of reaction. A sulfide of the type C(sp^2)-S-C(sp^2) is unreactive, while C(sp^3)-S-C(sp^2) is moderately reactive and C(sp^3)-S-C(sp^3) represents the most reactive sulfide of the series. It would be of interest to deepen our knowledge of the dependence existing between the reaction kinetic rate and molecular electronic properties.

Secondly, being the sulfur atom of a sulfide a prochiral centre, we investigated singlet oxygen addition on sulfides possessing pre-existing chiral centres. Cyclic sulfides have been chosen to limit the possibility of attack to the situations on top and down the molecular plane. It was found that they acted as chiral auxiliaries and directed the insertion of molecular oxygen in a way that privileged the formation of a sole diastereoisomer (isothiocineole, cephalexin, 2-methyl-4-propyl-1,3-oxathiinane) or induced an enantiomeric excess (lamivudine and emtricitabine).

Photocatalytic preparation of sulfoxides applied to chiral substrates holds promises if we consider than the reaction requires inexpensive molecular oxygen and light, plus a catalyst that is not even chiral. The author believes the procedure could be applied to industrial synthesis of derivatives of drugs that exist nowadays as sulfides, as we have shown by performing the transformation of the drugs lamivudine, emtricitabine and cephalexin.

Last, recording of the emission spectrum of a spectroelectrochemically generated species proved far from trivial. The main process upon reduction/oxidation of the dye is the systematic quenching of the luminescence. The emergence of a new emission spectrum was detected only for those dyes that underwent partial or irreversible chemical modification upon voltammetry experiment. The solvent seemed to play an important role in the case of H$_2$TPP, whose charged state decomposed in dichloromethane, but not in dimethylformamide; an evidence that points in the direction of solvent stabilization.

We stand by the opinion that only a dye, whose charged/radical state remains stable will serve as benchmark for testing the technique and its limitations.

Curriculum Vitae

Personal information

Angelo Lanzilotto
Pfirtergasse 14, Basel, CH-4054, Switzerland
+41 78 6529 6829
angelolanzilotto@gmail.com
04.05.1989, Maglie (Italy), Italian

Education

2014 - 2017	**PhD** in Chemistry, Department of Inorganic Chemistry, University of Basel. Supervision of Prof. Dr. Catherine Housecroft and Prof. Dr. Edwin Constable

Research projects on:
i. Synthesis of porphyrin-ruthenium polypyridine dye for dye-sensitized solar cells.
ii. Synthesis of sensitizer for singlet oxygen generation; application in photo-oxidation of organic compounds.
iii. Synthesis of a sensitizer for photodynamic therapy: demonstrated antimicrobial activity.

Teaching experience
- Practicum General Chemistry I-II:
- Teaching assistant for Inorganic Chemistry I-II-III

2011 - 2013	**Master's** Degree in Photochemistry and Molecular Materials, Alma Mater Studiorum, Bologna, Italy 110/110 cum laude
2008 - 2011	**Bachelor's** Degree in Chemistry Università degli Studi Aldo Moro, Bari, Italy 110/110
Language skills	Italian (native) English (fluent) German (basic) French (advanced) Spanish (advanced)